



## City Research Online

### City, University of London Institutional Repository

---

**Citation:** van Bokhorst, E. (2018). Forcing of the primary and secondary crossflow instability. (Unpublished Doctoral thesis, City, University of London)

This is the accepted version of the paper.

This version of the publication may differ from the final published version.

---

**Permanent repository link:** <https://openaccess.city.ac.uk/id/eprint/20151/>

**Link to published version:**

**Copyright:** City Research Online aims to make research outputs of City, University of London available to a wider audience. Copyright and Moral Rights remain with the author(s) and/or copyright holders. URLs from City Research Online may be freely distributed and linked to.

**Reuse:** Copies of full items can be used for personal research or study, educational, or not-for-profit purposes without prior permission or charge. Provided that the authors, title and full bibliographic details are credited, a hyperlink and/or URL is given for the original metadata page and the content is not changed in any way.

# **Forcing of the primary and secondary crossflow instability**

**Evelien van Bokhorst**

**Thesis submitted as part of the requirement for the fulfilment of  
a degree of Doctor of Philosophy**

**School of Engineering and Mathematical Sciences  
Research centre for aerodynamics and flow control  
City, University of London**

**May 2018**



# Contents

<b>Acknowledgements</b>	<b>v</b>
<b>Summary</b>	<b>vi</b>
<b>Nomenclature</b>	<b>viii</b>
<b>1. Background</b>	
1.1. Introduction . . . . .	2
1.2. Overview of transition paths . . . . .	5
1.3. Hydrodynamic stability . . . . .	6
1.4. Reynolds-Orr equation . . . . .	9
1.5. Primary modes . . . . .	10
1.5.1. Görtler instability . . . . .	10
1.5.2. Tollmien-Schlichting wave . . . . .	10
1.5.3. Crossflow instability . . . . .	11
1.5.4. Attachment line contamination and instability . . . . .	13
1.6. $e^N$ -method . . . . .	14
1.7. Motivation and objectives . . . . .	15
1.8. Thesis outline . . . . .	16
<b>2. Experimental set-up and instrumentation</b>	
2.1. Introduction . . . . .	18
2.2. Wind tunnel facility . . . . .	18
2.3. Design of experimental model . . . . .	19
2.3.1. Model configuration . . . . .	19
2.3.2. Design of the displacement body . . . . .	20
2.3.3. Design of the flat plate . . . . .	28
2.3.4. Coordinate systems . . . . .	31
2.4. Hot-wire anemometry . . . . .	32
2.4.1. Working principle . . . . .	32

2.4.2.	Setting up the hot-wire . . . . .	35
2.4.3.	Hot-wire calibration . . . . .	36
2.4.4.	Data analysis . . . . .	37
2.5.	Traverse and laser positioning system . . . . .	41
2.5.1.	Wall avoidance . . . . .	41
2.6.	Freestream velocity and temperature measurement . . . . .	45
2.7.	Static pressure measurement . . . . .	46
2.8.	LabVIEW system . . . . .	47
<b>3.</b>	<b>Baseline measurements</b>	
3.1.	Freestream disturbance measurements . . . . .	50
3.2.	Static pressure distribution . . . . .	53
3.3.	Displacement body wake measurements . . . . .	61
3.4.	Repeatability . . . . .	64
<b>4.</b>	<b>Forcing of the primary crossflow instability</b>	
4.1.	Introduction . . . . .	68
4.2.	Background . . . . .	68
4.2.1.	Influence of roughness . . . . .	69
4.2.2.	Influence of freestream turbulence . . . . .	78
4.2.3.	Influence of acoustic disturbances . . . . .	81
4.3.	Aim of current study . . . . .	81
4.4.	Design of the roughness distributions . . . . .	82
4.4.1.	Spanwise spacing, $\lambda$ . . . . .	82
4.4.2.	Roughness height, $k$ . . . . .	84
4.4.3.	Diameter, $D$ . . . . .	85
4.4.4.	Fourier coefficients . . . . .	85
4.5.	Data analysis . . . . .	86
4.6.	Results . . . . .	93
4.6.1.	YZ-scans . . . . .	93
4.6.2.	x-scans . . . . .	108
4.7.	Conclusions on forcing of the primary instability . . . . .	111
<b>5.</b>	<b>Secondary instability and breakdown to turbulence</b>	
5.1.	Introduction . . . . .	114
5.2.	Background . . . . .	114
5.2.1.	Origin and development of the secondary instability . . . . .	114
5.2.2.	Receptivity of the secondary crossflow instability . . . . .	119

5.3. Aim of the current study . . . . .	121
5.4. Design of excitation mechanism . . . . .	121
5.4.1. Wall-forcing . . . . .	121
5.4.2. Freestream forcing . . . . .	124
5.5. Measurements and data analysis . . . . .	127
5.5.1. Coordinate systems . . . . .	127
5.5.2. Analysis of the exciter signal . . . . .	129
5.6. Results: development of the secondary instability . . . . .	130
5.6.1. Development of the mean and fluctuating flow . . . . .	131
5.6.2. Early development of the secondary crossflow instability . . . . .	141
5.6.3. The secondary instability in the non-linear growth stage . . . . .	145
5.6.4. Conclusions: development of the secondary instability . . . . .	158
5.7. Results: wall-forcing . . . . .	159
5.7.1. Conclusions: wall-forcing . . . . .	169
5.8. Results: freestream forcing . . . . .	170
5.8.1. Conclusions: freestream forcing . . . . .	173
<b>6. Conclusions and recommendations</b>	
6.1. Main objectives . . . . .	178
6.2. Experimental design and data analysis . . . . .	178
6.3. Experiments on forcing of the primary instability . . . . .	180
6.4. Experiments on forcing of the secondary instability . . . . .	182
<b>Appendices</b>	<b>189</b>
<b>Appendix A. Computational analysis</b>	<b>189</b>
A.1. Linear stability analysis . . . . .	189
A.2. DLR-TAU analysis . . . . .	190
A.3. Piecewise linear velocity profiles . . . . .	198
<b>Appendix B. Hess-Smith panel code</b>	<b>203</b>
B.1. Introduction . . . . .	203
B.2. Principle of panel code . . . . .	203
B.3. Definition of matrix A for different cases . . . . .	206
B.3.1. Single body . . . . .	206
B.3.2. Two bodies . . . . .	206
B.3.3. Standard method of images . . . . .	208
B.3.4. Method of images with a single body . . . . .	208

B.4. Validation of panel code . . . . .	209
B.5. Improvements of panel code . . . . .	210
B.5.1. Flap angle, $\alpha_f$ . . . . .	210
B.5.2. Increased resolution at leading edge . . . . .	211
<b>Appendix C. LabVIEW system</b>	<b>212</b>
<b>Appendix D. Freestream turbulence measurements</b>	<b>215</b>
<b>Appendix E. Uncertainty analysis</b>	<b>219</b>
E.1. Error propagation . . . . .	219
E.2. Pressure measurements . . . . .	220
E.3. Hot wire measurements . . . . .	221
<b>Bibliography</b>	<b>223</b>

# Acknowledgements

During my PhD project I got help from many people, who I would like to thank here. First of all thanks to my first supervisor Chris Atkin for his advice and guidance throughout my PhD project. I also would like to thank him for the opportunities he gave me to go to several conferences abroad and to spend a few weeks at Airbus to carry out a computational analysis. I also would like to thank my second supervisor Michael Gaster for his advice on the experimental procedures and numerical analysis and also for sharing his immense knowledge and experience on boundary layer stability in general. Next, I would like to thank Marco for discussing my experiments and for giving feedback on my conference papers and thesis. I also would like to thank Ricky for his feedback throughout the project and for reviewing parts of the thesis. Thanks to Barry for making the electronics part of the project work. Also thanks to Isabella and Barry for their help during stressful experiments, even at unusual hours. I also would like to thank them and Dhamo for discussing results, data processing methods and thoughts which often helped me to understand the subject more thoroughly. For technical support I would like to thank Richard, Keith and Phil for their help. Zumba lessons, fly your ideas, a vegan chocolate class, escape rooms and a treasure hunt; thanks to Isabella, Judit and Weimiao for all these funny memories I now have about my time in London.

Furthermore, I would like to thank my parents for always being interested in what I am doing and for worrying if I am still eating and sleeping well. Finally thanks to my boyfriend for his support throughout the project and for his understanding that Sunday night at 10pm is the perfect time to set up a new hot-wire.

# Summary

With fossil fuels diminishing and fuel prices rising the development of more efficient aeroplanes is needed from an economical and environmental point of view. One possibility to increase the aerodynamic efficiency is to reduce the skin friction. This reduction can be achieved by having large areas of laminar flow. To be able to design laminar flow wings a thorough understanding of the transition from laminar to turbulent flow on a swept wing is needed.

The current experimental investigation focusses on the influence of environmental disturbances on the development of the crossflow instability. In order to study this influence, in the low turbulence wind tunnel at City University of London, an experimental model had to be designed. It was chosen to have a 45 degrees swept flat plate with a displacement body placed above it which created a favourable pressure gradient on the plate. With the sweep angle and favourable pressure gradient the conditions to have a transition process dominated by the crossflow instability were met. To characterize the flow detailed single hot-wire scans were carried out with a custom made data acquisition system in LabVIEW.

Prior to the experiments on the crossflow instability, measurements to characterize the freestream environment and to obtain the pressure distribution on the flat plate were carried out. The turbulence intensity was found to be around 0.02% for freestream velocities from 10 to 18m/s. The pressure distribution was obtained with two methods, with static pressure ports embedded in the plate and with a custom made pressure belt which spanwise location could easily be varied. Both methods gave comparable results and showed that a moderate favourable pressure gradient was created on the plate compared to other studies. The pressure belt results and panel code results were compared to a three-dimensional RANS computation of the set-up. A similar pressure gradient was found for all three pressure distributions. The magnitude of the pressure coefficient obtained from the panel code was slightly higher due to the inviscid character of this code.

The main experiments focussed on two stages of the transition process, the development of the primary and secondary crossflow instability. The goal of the primary crossflow instability experiments was to investigate the influence of the wavelength content of different roughness distributions while previous studies focussed more on the roughness height. A cylindrical and pyramidal roughness elements were studied for this purpose. The roughness elements were spaced at a spanwise distance of  $\lambda$ , which was the wavelength of the most amplified stationary crossflow wave following linear stability analysis. From the calculation of the Fourier coefficients it followed that the pyramidal roughness distribution had stronger forcing at  $\lambda$  and weaker forcing at  $\lambda/n$  compared to the cylindrical roughness distribution.

The experiments on the secondary instability first investigated the characteristics of this instability during different stages of its development. While in previous studies the characteristics in the early growth stage were studied here the characteristics of the secondary instability during breakdown are reported. Next, the experiments focussed on excitation of the secondary instability by wall-forcing and freestream forcing. The secondary instability was forced from the wall with a small speaker. The results with different amplitudes of the excitation signal showed that the secondary instability is receptive for wall-forcing. The secondary instability was forced from the freestream through a small pipe which was connected to a speaker placed in the displacement body. The first experiments showed that the freestream forcing did not interact with the secondary instability in the boundary layer. Analogously to the travelling primary instability a thin roughness strip was placed on the swept flat plate at the location where the secondary instability started to grow. With the roughness in place an interaction between the freestream disturbances and secondary instability did occur and the phase structure of the secondary instability could be obtained.

# Nomenclature

## Latin Symbols

$A_1, A_2$  Amplitude of the stationary crossflow wave

$A_n, B_n, C_n$  Fourier coefficients

$c$  Chord length of the plate (m)

$c$  Wave speed (m/s)

$C_f$  Skin friction coefficient

$C_p$  Pressure coefficient

$c_{DB}$  Chord length of the displacement body (m)

$D$  Diameter of the roughness element (m)

$E$  Hot-wire voltage (V)

$F$  Forcing by environmental disturbances

$f$  Frequency (Hz)

$f_c$  Cut-off frequency (Hz)

$f_s$  Sampling frequency (Hz)

$f_{exc}$  Excitation frequency (Hz)

$h_{DB}$  Distance from the trailing edge of the displacement body to the flat plate (m)

$k$  Roughness height (m)

$L, H, W$  Length, height and width of the wind tunnel (m)

$M$  Number of samples

---

$Nu$	Nusselt number
$P_\infty, P_s, P_d$	Total static and dynamic pressure (N/m <sup>2</sup> )
$R$	Receptivity coefficient
$Re$	Reynolds number based on the chord length of the model
$Re_k$	Reynolds number based on the roughness height
$Re_{\theta, AL}$	Reynolds number based on the momentum thickness at the attachment line
$S$	Temporal and spatial power spectrum (u <sup>2</sup> /Hz and u <sup>2</sup> m)
$T_f$	Fluid temperature (°)
$T_w$	Hot-wire temperature (°)
$Tu$	Turbulence intensity
$u', v', w'$	Disturbance velocities in the x, y and z direction (m/s)
$u'_{BP}$	Bandpass filtered velocity (m/s)
$U_\infty$	Freestream velocity (m/s)
$U_e$	Edge velocity (m/s)
$U_s, V_s, W_s$	Mean velocities in the in the x <sub>s</sub> , y <sub>s</sub> and z <sub>s</sub> direction (m/s)
$u_{ph}$	Phase-averaged velocity (m/s)
$U, V, W$	Mean velocities in the in the x, y and z direction (m/s)
$x_s, y_s, z_s$	Streamline coordinates
$X, Y, Z$	Model coordinates
$x, y, z$	Wind tunnel coordinates

### Greek Symbols

$\alpha_i, \alpha_r$	Real and imaginary part of the streamwise wavenumber (m <sup>-1</sup> )
$\alpha_{DB}$	Angle of attack of the displacement body (°)
$\beta_i, \beta_r$	Real and imaginary part of the spanwise wavenumber (m <sup>-1</sup> )

---

$\chi$	Azimuthal angle ( $^{\circ}$ )
$\delta$	Boundary layer thickness (m)
$\Delta\lambda$	Resolution in the spatial power spectrum (m)
$\delta^*$	Displacement thickness (m)
$\epsilon$	Height ratio
$\gamma$	Elevation angle ( $^{\circ}$ )
$\lambda$	Spanwise wavelength (rad/s)
$\Lambda, \Lambda_{eff}$	Geometric and effective sweep angle ( $^{\circ}$ )
$\mu$	Viscosity (Pa s)
$\omega$	Angular frequency (rad/s)
$\phi$	Phase (rad)
$\phi$	Wedge spreading angle
$\Psi$	Streamline angle ( $^{\circ}$ )
$\rho$	Density ( $\text{kg/m}^3$ )
$\tau_w$	Shear stress (Pa)

### Acronyms

CTA Constant temperature anemometer

DB Displacement body

DLR-TAU Reynolds averaged Navier-Stokes solver developed by DLR

LSA Linear stability analysis

PB Pressure belt





**1**

**Background**

## 1.1. Introduction

About 115 years ago the Wright brothers managed to keep the first powered aeroplane in the air for 12 seconds covering a distance of about 30 metres (Anderson, 1997). They could not have imagined that 115 years later, over 800 people at the time<sup>1</sup> are transported at heights above 10 kilometres for million times a year<sup>2</sup>. While in the early days of aircraft development increasing height and range might have been the major challenges, nowadays the efficiency of aeroplanes receives most attention. With fossil fuels diminishing, fuel prices rising and global warming linked to CO<sub>2</sub> emissions, every possible improvement in aircraft efficiency is needed from an economical and environmental point of view.

In Figure 1 the direction of the four main forces acting on an aeroplane in flight are sketched. For an aeroplane to move forward the thrust has to overcome the drag.

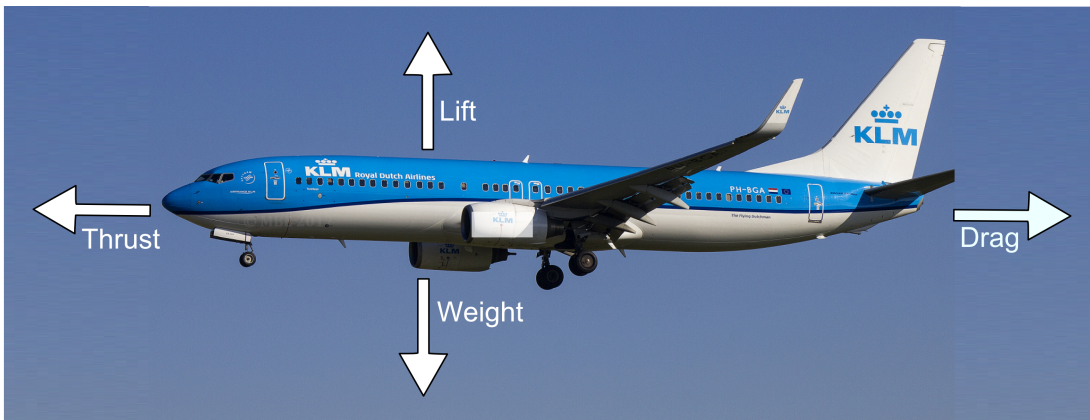


**Figure 1.** Direction of the four main forces acting on an aeroplane. Picture from <https://planefinder.net/data/airline/KL>

One way of increasing the aerodynamic efficiency of an aeroplane is reducing the drag such that less fuel is needed to propel an aeroplane forward for a certain distance. On a commercial aircraft, such as the Boeing 737, more than half of the total drag is attributed to skin friction (Goldhammer and Plendl, 2013). Skin friction is caused by the friction between the surface of the aeroplane wing and air above it. The skin friction coefficient is defined as:

$$C_f = \frac{\tau_w}{\frac{1}{2}\rho U_\infty^2}, \quad (1.1)$$

<sup>1</sup>[en.wikipedia.org/wiki/Airbus\\_A380](https://en.wikipedia.org/wiki/Airbus_A380)

<sup>2</sup>[www.statista.com/statistics/564769/airline-industry-number-of-flights/](https://www.statista.com/statistics/564769/airline-industry-number-of-flights/)

where  $\rho$  is the density of the fluid,  $U_\infty$  the speed and  $\tau_w$  the shear stress at the surface of the wing. The wall shear stress in a fluid is written as:

$$\tau_w = \mu \left. \frac{dU}{dy} \right|_{y=0}, \quad (1.2)$$

where  $\mu$  is the viscosity,  $y$  the coordinate normal to the surface and  $dU/dy|_{y=0}$  the gradient of the velocity profile at the wall. The magnitude of this velocity gradient differs for laminar and turbulent flow. Laminar flow is characterized as organized, parallel and predictable while turbulent flow is chaotic and unpredictable. In Figure 2 a laminar and turbulent boundary layer are shown. Where the boundary layer is the region close to the surface where viscous effects are important, in contrast to the inviscid flow region where viscous effects can be neglected.

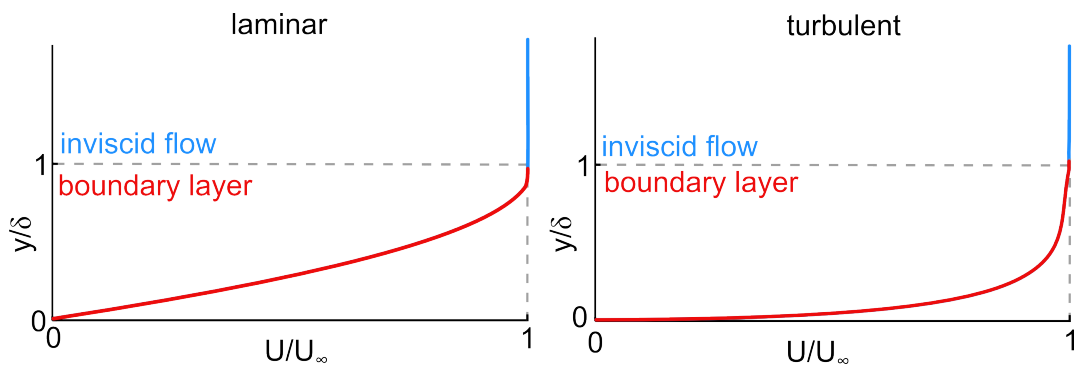


**Figure 2.** Schematic of a laminar (left) and turbulent (right) boundary layer. Where  $\delta$  represents the boundary layer thickness.

Due to mixing in the turbulent boundary layer there is more momentum close to the wall compared to the laminar boundary layer. Because of this the velocity gradient at the surface,  $dU/dy|_{y=0}$ , is larger for a turbulent boundary layer than for a laminar boundary layer. Consequently, through Equations 1.1 and 1.2, the skin friction for a turbulent boundary layer will be higher than for a laminar boundary layer. Estimations have shown that for laminar flow aeroplane wings, the skin friction can be reduced by 6 to 7% (Atkin, 2004). For this reason there is and has been an interest from industry to develop wings with large areas of laminar flow. The first aeroplane specifically designed to have large areas of laminar flow was the P-51 Mustang in the second world war<sup>3</sup>. The airfoil shape of the P-51 was optimized to get a significant amount of laminar flow. Eventually, an efficient aeroplane was built, however, it is thought that its high efficiency was due to the high surface quality of the wings instead of the designed shape (Anderson, 1997). Prior to the development of the

<sup>3</sup>[www.aviation-history.com/theory/lam-flow.htm](http://www.aviation-history.com/theory/lam-flow.htm)

P-51, in the 1930s, the first experiments on laminar flow control were carried out by the use of suction (Braslow, 1999) through slits in the wing. The purpose of laminar flow control is to keep the flow laminar where it would naturally transition to turbulence. In the case of suction the thickness of the boundary layer is reduced resulting in a more stable boundary layer. Throughout the years, with varying interest from industry (Atkin, 2008), laminar flow control techniques were further developed and this eventually led to the test flight of the Airbus BLADE (Breakthrough Laminar Aircraft Demonstrator in Europe) in September 2017<sup>4</sup>. For an extensive review on laminar flow control techniques and developments up to the end of the 1990's Joslin (1998) should be consulted. While the quest for laminar flow wings has started about 80 years ago, scientists and engineers have been interested in the transition process from laminar to turbulent flow for much longer. In Hagen (1839) and Hagen (1854) the distinction between laminar and turbulent flow in a pipe was first made (Anderson, 1997). The purpose of the now famous pipe flow experiment by Osborne Reynolds (Reynolds, 1883) was to find a parameter which would determine if the flow was laminar or turbulent. He found that if the magnitude of a non-dimensional group exceeded a certain limit the flow became turbulent. The non-dimensional group is now known as Reynolds number and is defined as:

$$Re = \frac{\rho U_{\infty} D}{\mu}, \quad (1.3)$$

where  $D$  is a length scale of the object through which or over which the fluid flows. Reynolds number represents the ratio between inertial and viscous forces. If Reynolds number is high viscous effects are negligible compared to the inertial effects and vice versa. For very controlled experiments such as a flat plate or pipe flow experiment, Reynolds number might be sufficient to predict if the flow is laminar or turbulent. However, in less controlled environments other factors influence the transition process and Reynolds number is not sufficient to predict whether the flow is laminar or turbulent. While up to now no universal model has been developed to take all other factors into account to predict the transition location correctly, previous studies have shown that the transition path from laminar to turbulent flow depends on the level of environmental disturbances such as roughness and freestream turbulence. In the following section an overview of these transition paths is given.

---

<sup>4</sup>[http://www.airbus.com/newsroom/press-releases/en/2017/09/airbus\\_-\\_blade\\_-laminar-flow-wing-demonstrator-makes-first-fligh.html](http://www.airbus.com/newsroom/press-releases/en/2017/09/airbus_-_blade_-laminar-flow-wing-demonstrator-makes-first-fligh.html)

## 1.2. Overview of transition paths

In Figure 3 an overview of the different paths from laminar to turbulent flow are shown.

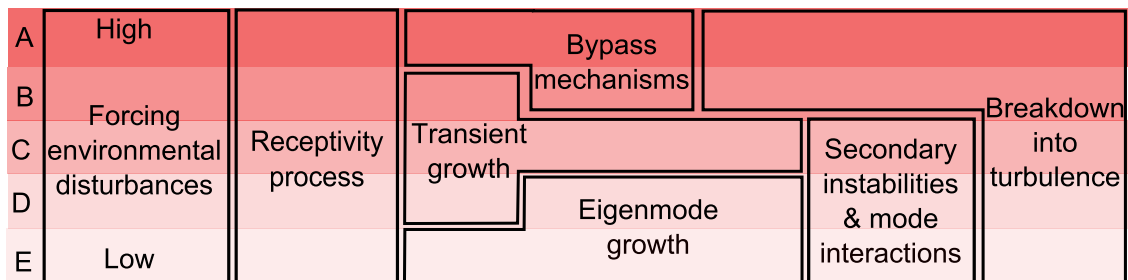


**Figure 3.** Overview of transition paths for different levels of environmental disturbances (modified from Morkovin et al. (1994)).

The first stage of all transition paths is the receptivity process. Here, perturbations are generated from environmental disturbances, such as freestream turbulence or surface roughness. When the level of disturbances is high the bypass path is followed (Path A). After the receptivity process, the flow breaks immediately down into turbulence. It is believed that the step of eigenmode growth is bypassed or alternatively taking place over a very short distance such that it is difficult to be observed. Next, there are three paths where transient growth plays a role (Path B,C, and D). Transient growth is caused by the non-orthogonality of eigenmodes. This means two modes which decay with different rates in time, can still generate algebraic growth over a short amount of time (Schmid and Henningson, 2001). While mathematically the concept for transient growth is understandable, it is more difficult to imagine a flow configuration where such situation actually occurs. It has been shown that by optimizing the disturbance energy for maximum transient growth an optimal perturbation for transient growth can be found. In flat plate boundary layers this optimal perturbation manifest itself as streamwise vortices. The most amplified perturbation, has been found to be streamwise streaks which are forced by these streamwise vortices (Fransson et al., 2004). In experiments it is found that streaks develop when the freestream turbulence levels are elevated (Matsubara and Alfredsson, 2001). Even though, no critical threshold for which transient growth becomes relevant has been defined in literature, in the current experiment the external disturbances ( $Tu \approx 0.02\%$ ) are low compared to transient growth studies ( $Tu \approx 1\%$ ). Therefore, it is expected that transient growth will not play a major role in the current study. For an extensive review on the subject of transient growth Schmid and Henningson (2001) could be consulted. Finally, when the environmental disturban-

ces are low, Path E is followed. After the receptivity process, primary instabilities start to grow. The nature of the primary instability depends on characteristics of the model such as sweep, curvature and pressure gradient. Because the initial disturbances are small this part can be described with linear theory. After the wave amplitude reaches a certain threshold the instabilities grow in a non-linear manner and a secondary instability is created. Explosive growth of the secondary instability and non-linear mode interactions lead eventually to breakdown of the flow into turbulence. In the current set-up the environmental disturbances are small and therefore it is expected that transition path E is followed. In Section 1.5 the primary modes occurring on different geometries will be discussed. Now, first the concept of hydrodynamic stability is described.

### 1.3. Hydrodynamic stability

The Navier-Stokes equations describe the motion of viscous fluid flow. The equations are derived from a momentum balance over a small fluid element and write:

$$\rho \frac{D\mathbf{u}}{Dt} = -\nabla p + \mu \nabla^2 \mathbf{u} + \mathbf{f}, \quad (1.4)$$

where  $\mathbf{u}$  represent the velocities in the  $x, y$  and  $z$  direction and  $p$  the pressure. The terms on the left represent the change in momentum while the right hand side represents the pressure, viscous and external forces respectively. While the Navier Stokes equation describe the motion of fluids it does not directly give any information about the stability of a flow. Hydrodynamic stability theory deals with the response of small disturbances on the flow. The first step to get from the Navier-Stokes equations to stability equations is therefore to write the velocity and pressure as  $\mathbf{u} = \mathbf{U} + \mathbf{u}'$  and  $p = P + p'$ , where  $\mathbf{U}$  and  $P$  are the mean and  $\mathbf{u}'$  and  $p'$  the fluctuating components of the velocity and pressure. For small disturbances the linearised disturbance equations are then derived and given by:

$$\begin{aligned} \frac{\partial u'}{\partial x} + \frac{\partial v'}{\partial y} + \frac{\partial w'}{\partial z} &= 0, \\ \rho \left( \frac{\partial u'}{\partial t} + U \frac{\partial u'}{\partial x} + v' \frac{\partial U}{\partial y} + W \frac{\partial u'}{\partial z} \right) &= -\frac{\partial p'}{\partial x} + \mu \left( \frac{\partial^2 u'}{\partial x^2} + \frac{\partial^2 u'}{\partial y^2} + \frac{\partial^2 u'}{\partial z^2} \right), \\ \rho \left( \frac{\partial v'}{\partial t} + U \frac{\partial v'}{\partial x} + W \frac{\partial v'}{\partial z} \right) &= -\frac{\partial p'}{\partial y} + \mu \left( \frac{\partial^2 v'}{\partial x^2} + \frac{\partial^2 v'}{\partial y^2} + \frac{\partial^2 v'}{\partial z^2} \right), \\ \rho \left( \frac{\partial w'}{\partial t} + U \frac{\partial w'}{\partial x} + v' \frac{\partial W}{\partial y} + W \frac{\partial w'}{\partial z} \right) &= -\frac{\partial p'}{\partial z} + \mu \left( \frac{\partial^2 w'}{\partial x^2} + \frac{\partial^2 w'}{\partial y^2} + \frac{\partial^2 w'}{\partial z^2} \right). \end{aligned}$$

For this derivation it is assumed that the flow is parallel i.e.  $U = U(y)$ ,  $V = 0$  and  $W = W(y)$ . Next, the disturbances are written as exponentials in the form  $q'(x, y, z, t) = q(y)e^{i(\alpha x + \beta z - \omega t)}$ . Where  $\alpha$ ,  $\beta$  and  $\omega$  are complex and represent the streamwise wave number, spanwise wave number and temporal frequency respectively. Substituting this into the linearized disturbance equations and defining  $k^2 = \alpha^2 + \beta^2$  gives the Orr-Sommerfeld equation:

$$\frac{d^4 v}{dy^4} - 2k^2 \frac{d^2 v}{dy^2} + k^4 v - iRe \left[ (\alpha U + \beta W - \omega) \left( \frac{d^2 v}{dy^2} - k^2 v \right) - \left( \alpha \frac{d^2 U}{dy^2} + \beta \frac{d^2 W}{dy^2} \right) v \right] = 0 \quad (1.5)$$

The Orr-Sommerfeld is an eigenvalue problem and for known mean velocity profiles  $U$  and  $W$  the equation can be solved. The Orr-Sommerfeld equation is complex and so are  $\alpha$ ,  $\beta$  and  $\omega$  of which the real and imaginary part are sketched in Figure 4.

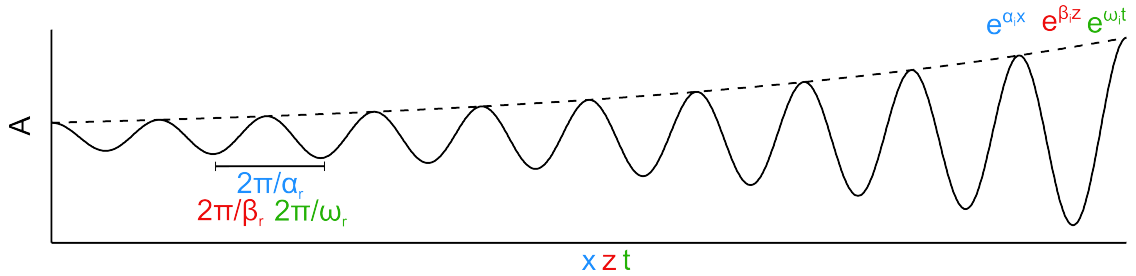


**Figure 4.** Representation of waves growing in space and time.

The imaginary part of  $\alpha$ ,  $\beta$  and  $\omega$  denoted with  $\alpha_i$ ,  $\beta_i$  and  $\omega_i$  determine if the solution is unstable. For local temporal stability analysis it is assumed that the wavenumbers  $\alpha$  and  $\beta$  are real and  $\omega$  is the eigenvalue to be found. If  $\omega_i$  is positive the disturbances grow in time and the flow is temporally unstable. In local spatial stability analysis it is assumed that  $\omega$  and  $\beta$  are real such that the eigenvalue to be found is  $\alpha$ . This represents a case where disturbances do not grow in time and in the spanwise direction but can grow in the streamwise direction as is the case for Tollmien-Schlichting waves and crossflow instabilities, discussed in the following section. By observing Equation 1.5 it is clear that the equation is simpler to solve for  $\omega$  than for  $\alpha$  or  $\beta$ . If the amplification rates are sufficiently small and the parameters of interest are close to the neutral stability curve it can be shown that through Gaster's transformation the temporal disturbances can be converted to spatial ones (Gaster, 1962). With Squire's theorem it is shown that a two dimensional perturbation is most unstable and therefore the Orr-Sommerfeld equation can be solved as a two-dimensional problem (Squire, 1933). If the Orr-Sommerfeld equation is solved for a lot of different Reynolds numbers a neutral stability curve can be obtained as presented in Figure 5.

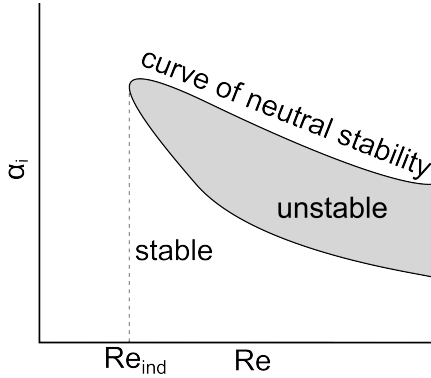


**Figure 5.** Sketch of a neutral stability curve.

The curve is the boundary for the stable and unstable region and the most left point on the curve represents the indifference Reynolds number which is the lowest Reynolds number for which the flow can become unstable.

Inviscid instabilities can be considered separately if the Orr-Sommerfeld equation is taken in the limit of large Reynolds numbers:

$$(U - c) \left( \frac{d^2 v'}{dy^2} - \alpha^2 v' \right) - \frac{d^2 U}{dy^2} v' = 0, \quad (1.6)$$

where  $c = \omega/\alpha$  is the complex wave speed and the spanwise direction is omitted here. When Equation 1.6 is multiplied by its complex conjugate and integrated over  $y$  it can be shown that the imaginary part of the equation reads:

$$c_i \int_{y_1}^{y_2} \frac{1}{(U - c_r)^2 + c_i^2} \frac{d^2 U}{dy^2} |\hat{v}|^2 dy = 0. \quad (1.7)$$

If  $c_i > 0$  it follows that  $\frac{d^2 U}{dy^2} = 0$  somewhere in between  $y_1$  and  $y_2$ . This statement is known as Rayleighs criterion and it means that an inflection point in the mean velocity profile is a necessary condition for the presence of amplified waves caused by an inviscid mechanism.

The main assumptions underlying the Orr-Sommerfeld equation are that the disturbances are small and that the base flow is parallel. In the start of the transition process these assumptions might hold and the growth of the instabilities will be predicted correctly. However, further in the transition process different methods are required to obtain correct predictions. Non-parallel effects are included by solving the parabolised stability equations, of which the development is described in [Herbert \(1997\)](#). Large disturbances, i.e. non-linear effects, can also be included in these equations. In [Saric et al. \(2003\)](#) it is shown that the solution of the non-linear parabolised stability equations predicts the growth of the crossflow instability well.

In the current thesis, computational methods were used to design the experimental model. For this purpose, the characteristics of the instabilities in the linear development stage were required. The linear stability characteristics in this thesis are

obtained from CoDS<sup>5</sup> which solves the compressible laminar boundary layer equations. For more details of the computational methods used in this thesis Appendix A should be consulted.

## 1.4. Reynolds-Orr equation

The Orr-Sommerfeld equation gives insight in the growth of the hydrodynamic instabilities. The mechanisms by which these instabilities grow are shown with the Reynolds-Orr equation which are the kinetic disturbance energy equations. These equations are obtained from integrating the nonlinear disturbance equations (Schmid and Henningson, 2001) and write (Malik et al., 1999):

$$\frac{dE}{dt} = P - D, \quad (1.8)$$

where  $E$  is the kinetic energy,  $P$  the production term and  $D$  the production term given by:

$$E = - \int_0^{2\pi/\alpha} \int_0^\infty \int_0^{2\pi/\beta} \left( \frac{u_i u_i}{2} \right) dx_1 dx_2 dx_3, \quad (1.9)$$

$$P = - \int_0^{2\pi/\alpha} \int_0^\infty \int_0^{2\pi/\beta} u_i u_j \left( \frac{\partial U_i}{\partial x_j} \right) dx_1 dx_2 dx_3. \quad (1.10)$$

and

$$D = - \int_0^{2\pi/\alpha} \int_0^\infty \int_0^{2\pi/\beta} \frac{1}{Re} \left( \frac{\partial u_i}{\partial x_j} \right) \left( \frac{\partial u_i}{\partial x_j} \right) dx_1 dx_2 dx_3. \quad (1.11)$$

These equations show that the production terms of the velocity fluctuations are expected to be large where the spanwise and wall-normal shear terms  $\partial U/\partial x_3$  and  $\partial U/\partial x_2$  are large. This is used in previous studies to define the secondary crossflow instability as will be discussed more thoroughly in Chapter 5.

---

<sup>5</sup>Qinetic (unpublished)

## 1.5. Primary modes

### 1.5.1. Görtler instability

The Görtler instability is an inviscid centrifugal instability which occurs in shear flows over curved surfaces. The necessary condition for such instability is the Rayleigh circulation criterion which states that  $d\Gamma^2/dr < 0$  somewhere in the flow, where  $\Gamma = rV$  with  $r$  the radial coordinate and  $V$  the tangential velocity. In Figure 6, stable and unstable cases are shown for a convex and concave surface. On a swept wing the Görtler instability is not dominating the transition process and therefore not relevant in the current experimental investigation. A review of studies on this instability is given by Saric (1994).

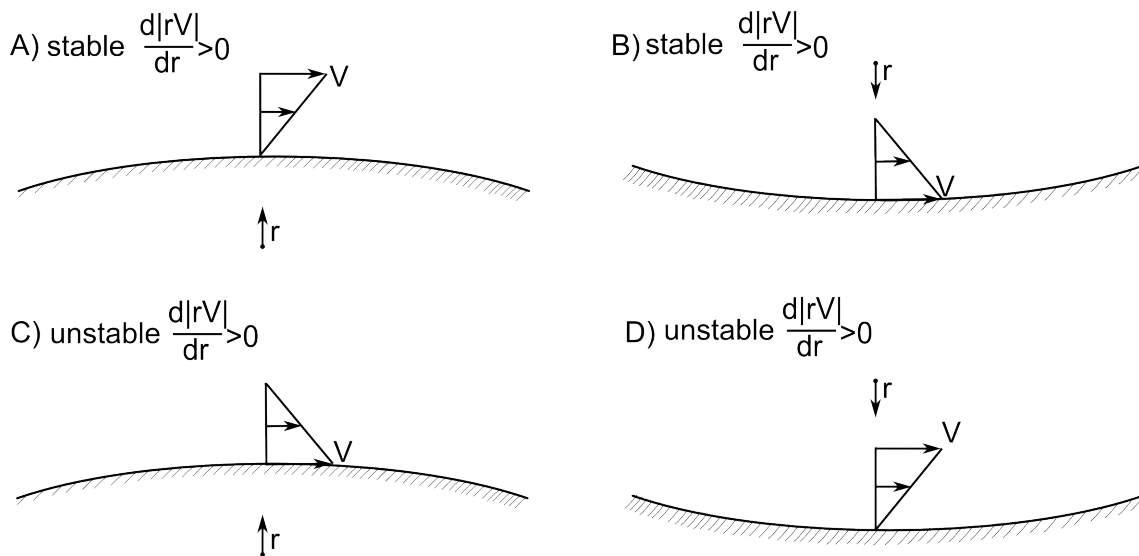


**Figure 6.** Flow configurations which are stable (left) and unstable (right) to the Görtler instability (Modified from Figure 1 in Saric (1994)).

### 1.5.2. Tollmien-Schlichting wave

A two-dimensional zero-pressure-gradient laminar boundary layer does not exhibit inviscid instabilities since Rayleigh's inflection point criterion, is not satisfied. Since it is known that the boundary layer is unstable, there is a mechanism where viscosity works as a destabilizing force. A Tollmien-Schlichting wave is such viscous two-dimensional instability. For a two-dimensional base state the non-linear disturbance equation in terms of the energy disturbance equation for a one dimensional base

state writes (Saric, 2008):

$$\frac{DE}{Dt} = - \int_V u'v' \left( \frac{dU}{dy} \right) - \frac{1}{Re} \int_V (\nabla \overline{v'})^2. \quad (1.12)$$

It is assumed that the disturbance vanishes on the boundaries of control volume  $V$ . The last term on the right side is always stabilizing and represents diffusion of energy through viscosity. The first term represents the Reynolds stress and can be stabilizing or destabilizing depending on the phase between the two disturbance. From this equation it is clear that a uniform flow ( $\frac{dU}{dy} = 0$ ) will always be stable. By looking at the inviscid and viscous solutions of the Orr-Sommerfeld equations it can be shown that for the inviscid solutions the  $u'$  and  $v'$  component are 90 degrees out of phase and therefore the Reynolds stress distribution is 0. For the viscous solution it can be found that the Reynolds stress distribution is always positive. This implies that the first term in Equation 1.12 is always positive and therefore destabilizing. The mathematical prove of this viscous instability was first given by Tollmien (1929) and then by Schlichting (1933). The experimental proof of the Tollmien-Schlichting wave was given by Schubauer and Skramstad with very accurate hot-wire measurements (Schubauer and Skramstad, 1948). In their experiment it was also found that there was increased amplification for adverse pressure gradients and increased damping for favourable pressure gradients.

### 1.5.3. Crossflow instability

The crossflow instability is an inviscid instability which occurs on a swept body with a pressure gradient. In Figure 7 the influence of the favourable pressure gradient and sweep angle, on the direction of the inviscid streamlines is shown. At the attachment line the velocity vector is aligned with the leading edge. From the attachment line the streamwise velocity increases due to a favourable pressure gradient. This leads to a curvature of the inviscid streamlines. When the pressure gradient weakens the curvature decreases, eventually, when the pressure gradient vanishes, the inviscid streamlines align with the freestream velocity,  $Q_\infty$ . The Navier-Stokes equation in streamline coordinates  $(s, n, y)$  with  $\overline{U} = [U_s, 0, 0]$  show that for a steady inviscid parallel flow the pressure gradient normal to the streamline writes:

$$\frac{\partial p}{\partial n} \Big|_{inv} = \frac{\rho U_s^2}{R}. \quad (1.13)$$

From an order of magnitude analysis of the full y-momentum equation it follows, that for  $Re \gg 1$ , the pressure gradient in the wall-normal direction,  $\frac{\partial p}{\partial y}$ , is equal to

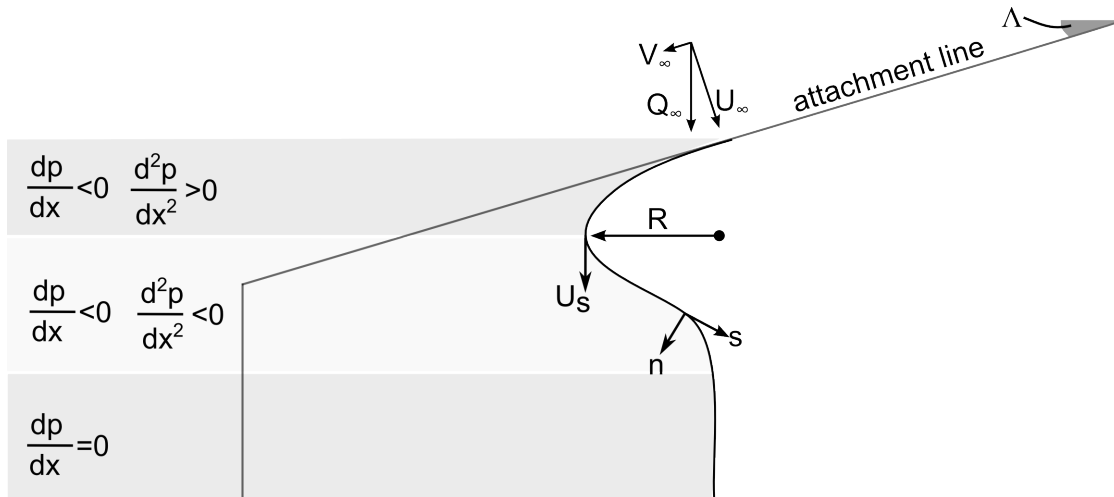


**Figure 7.** Origin of the crossflow instability.

zero. This indicates that the pressure is constant in the wall normal direction, such that the pressure gradient normal to the streamline outside the boundary layer is equal to the pressure gradient inside the boundary layer i.e.  $\frac{\partial p}{\partial n}|_{inv} = \frac{\partial p}{\partial n}|_{BL}$ . However, inside the boundary layer the balance between the pressure gradient and centripetal acceleration does not exist, since the streamwise velocity,  $u_s$ , decreases towards the wall due to the action of viscosity (Saric et al., 2003). This imbalance drives the crossflow which is defined as the flow perpendicular to the streamline. The crossflow component is zero at the wall and the edge of the boundary layer and therefore the crossflow velocity profile has an inflection point which is a source for the inviscid instability following the Rayleigh inflection point criterion. The instability manifests itself as steady and unsteady co-rotating vortices which are almost aligned to the potential flow direction. Gray (1952) first observed that the sweep angle influenced the stability of a laminar boundary layer. The vortex structure on a rotating disk was clearly shown by Gregory et al. (1955) who used a china-clay technique. Poll (1985) showed the vortex structure as streamwise streaks even more clearly on a cylinder with varying yaw angles as is shown on the front of this thesis.

With linear stability analysis it is found that the most amplified disturbance is the travelling crossflow wave ((Malik and Poll, 1985; Dagenhart, 1992)). However, it depends on the environmental disturbances if the stationary or traveling wave will dominate the transition process, as will be discussed in Chapter 4. For extensive reviews about research on the crossflow instability Bippes (1999) and Saric et al. (2003) can be consulted.

### 1.5.4. Attachment line contamination and instability

The attachment line, is the three-dimensional equivalent of the stagnation point. At the attachment line, the velocity has only a component parallel to the leading edge, i.e. the streamwise velocity is zero. There are two mechanisms by which the attachment line can become turbulent, which are both presented in Figure 8. Tran-

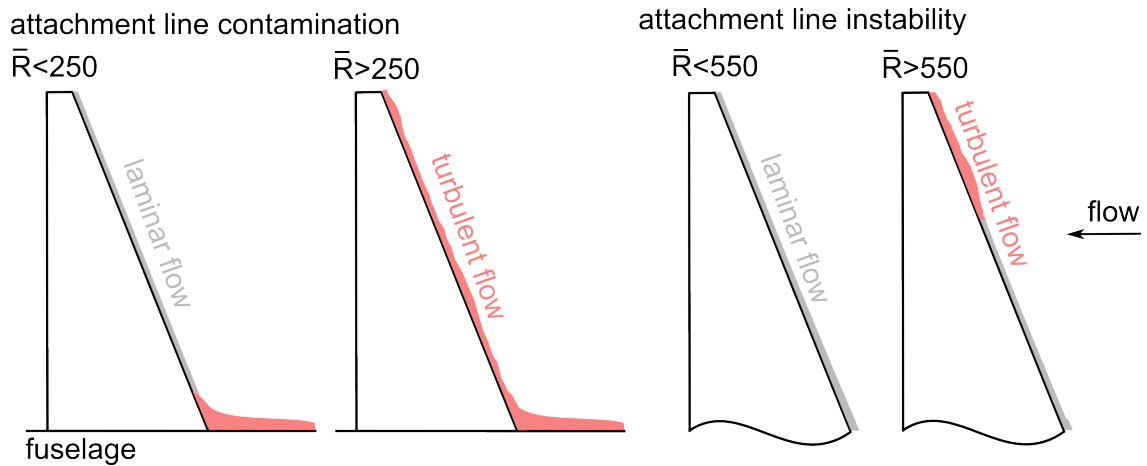


**Figure 8.** Flow configurations where attachment line contamination (left) and the attachment line instability (right) occurs (Modified from Figure 5.15 in Gowree (2014)).

sition to a turbulent attachment line can occur naturally through the attachment line instability. Poll (1979) found that the first bursts of turbulence occurred around  $\bar{R}=550$  where  $\bar{R}$  is the Reynolds number based on the velocity gradient at the attachment line. The attachment line contamination occurs when turbulent flow from the fuselage, is convected inside the attachment line boundary layer and instantly creates a turbulent boundary layer over the wing. The attachment line contamination is not an instability by itself and is therefore not classified as a primary mode. Nevertheless, it should be taken into account in practical applications such as aeroplane or experimental design. The turbulent disturbances, due to contamination, propagate along the attachment line once the Reynolds number exceeds a certain limit. In literature the Reynolds number, based on the momentum thickness of the attachment line boundary layer,  $Re_{\theta,AL}$  and  $\bar{R}$  are used. Pfenninger (1977) and Gaster (1967) found a limit of  $Re_{\theta,AL}=90-100$  and Poll (1979) a limit of  $\bar{R}=250$ . Several solutions have been proposed to maintain a laminar attachment line, where the Gaster bump has been effective (Gaster, 1965). The Gaster bump is a small fairing placed closely to the wing root. The shape of the bump is optimized such that the contaminated layer is brought to rest at one side while a clean laminar boundary layer is generated at the other side. Gaster showed that the mechanism is effective up to  $Re_{\theta,AL} = 420$ . For an extensive review of attachment line instability studies Reed and Saric (1989)

and [Gowree \(2014\)](#) can be consulted.

In this section an overview of the different transition paths and primary instabilities has been given. In flight conditions it is expected that environmental disturbances are sufficiently small to follow transition path E. Furthermore, if it is assumed that the attachment line instability is controlled, the crossflow instability is expected to dominate the transition process over a swept wing with some possible influence of Tollmien-Schlichting waves. In the introductory sections of [Chapter 4](#) and [Chapter 5](#) further details on the growth of the crossflow instability are given.

## 1.6. $e^N$ -method

Since wind tunnel tests are expensive and time consuming, there is a need from industry for quick methods to obtain an indication of the transition location. One of the main methods used by industry is the  $e^N$ -method which was simultaneously but independently developed by [van Ingen \(1956\)](#) and [Smith and Gamberoni \(1956\)](#). The method follows directly from the Orr-Sommerfeld equation and is therefore only valid in the linear regime. The amplitude of the disturbance at location  $x$  is defined as  $A = e^{-\alpha_i x}$  and is equal to  $A + dA = e^{-\alpha_i(x+dx)}$  at  $x + dx$ . The ratio between the two gives if and how much the wave has grown and is given by:

$$\frac{A + dA}{A} = e^{-\alpha_i(x+dx)}, \quad (1.14)$$

or,

$$\ln(A + dA) - \ln(A) = d\ln(A) = -\alpha_i dx, \quad (1.15)$$

When this equation is integrated from  $x_0$  which is the position where the instability starts to grow to location  $x$  the expression for the N-factor is given by:

$$N = \ln(A/A_0) = \int_{x_0}^x -\alpha_i dx. \quad (1.16)$$

The idea of the  $e^n$ -method is that when  $N$  is above a certain threshold the flow becomes turbulent. Since the  $e^N$ -method is linear it only gives an indication of where transition occurs. In [van Ingen \(2008\)](#) it is stated that the method works well for 2D incompressible flows with low environmental disturbances since a large part of the transition process can be described with only linear effects. To include environmental

disturbances such as roughness and freestream turbulence the  $e^N$ -method has been extended through empirical methods (Crouch and Ng, 2000; Borodulin et al., 2017), however, a general theory has not been obtained so far.

## 1.7. Motivation and objectives

In this thesis the transition process from laminar to turbulent flow over an model with characteristics of an aeroplane wing is studied experimentally. For a swept wing with a favourable pressure gradient the crossflow instability dominates the transition process. Previous studies have shown that the development of the crossflow instability is influenced by the sweep angle, pressure gradient, surface roughness and freestream environment, however, a more thorough understanding of these parameters is needed to be able to predict transition for a given environment. Next to transition prediction, it is thought that with deeper knowledge of the influence of environmental disturbances on the transition process more efficient strategies can be developed to control the crossflow instability. This is of large interest for aeroplane manufactures in the development of next generation laminar flow aeroplanes. A more detailed motivation for the experiments carried out in this thesis are given in Chapter 4 and 5.

At the start of the current project the research group was built up and no experimental model or data acquisition system was in place. Therefore the objectives of this project have aspects related to the influence of disturbances on the transition process, as well as, aspects related to the design of the experimental set-up in general. By keeping this in mind the aims of the project were formulated as followed:

- To design an experimental model where the transition process is dominated by the crossflow instability.
- To develop a data acquisition system and experimental procedure which makes it possible to continuously take detailed hot-wire measurements up to several days.
- To better understand the parameters influencing the different stages of the transition process dominated by the crossflow instability. In the first experiments the focus is on the primary crossflow instability while in a later stage the secondary crossflow instability is studied in detail.

## 1.8. Thesis outline

After this introductory chapter the design of the experimental set-up is described together with an overview of the instrumentation used in the experiments. In Chapter 3 the freestream turbulence measurements of the empty wind tunnel are discussed together with the static pressure measurements and the hot-wire measurements in the wake of the displacement body.

The two main chapters of the thesis are focusing on the development of the primary crossflow instability, Chapter 4, and the secondary crossflow instability, Chapter 5. Each of these chapters is structured as a stand-alone report. It starts with a background section, after which the experimental design and data analysis tools specific to the primary and secondary instability experiments are discussed. Next, the results and discussion are given followed by a conclusion. Following the two main chapters, the overall conclusions are drawn in Chapter 6. Finally, the appendices contain information about the computational methods used to design the experimental set-up and support the experimental results. Furthermore, the freestream turbulence measurements are given as well as an uncertainty analysis on the data obtained from the experiments.





# 2

## **Experimental set-up and instrumentation**

## 2.1. Introduction

A substantial part of the PhD project was involved with the design of the experimental set-up and data acquisition system. An overview of the system is shown in Figure 1. In the following sections all the components of the system will be discussed.

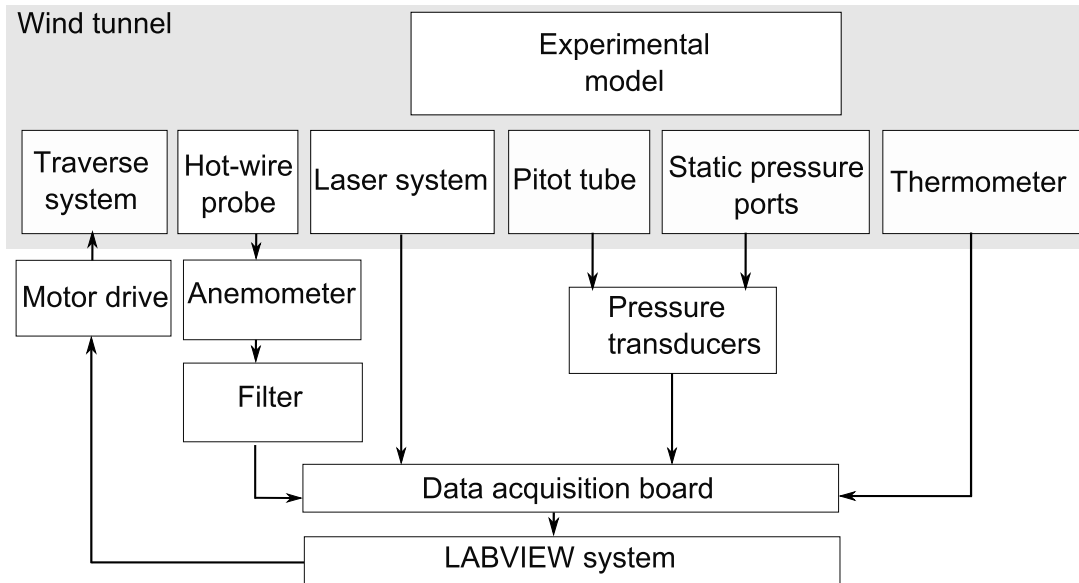


Figure 1. Overview of the experimental set-up.

## 2.2. Wind tunnel facility

All experiments were conducted in the UK National Low Turbulence wind tunnel facility at City, University of London (Figure 2). The characteristics of the closed loop tunnel are given in Table 2.1. The tunnel has low freestream turbulence levels, which makes it an excellent facility to study boundary layer transition following the natural transition path. The freestream turbulence levels quoted in Table 2.1 are an indication, in Section 3.1 a more detailed characterization of the freestream environment is given.

Table 2.1. Specifications UK National Low Turbulence wind tunnel.

Maximum flow speed	45m/s
Reynolds number range	$0.34 \times 10^6 - 3.1 \times 10^6$
Turbulence intensity	<0.01% (up to 20 m/s)
Contraction ratio	6.75:1
Mach number	up to 0.13



**Figure 2.** UK National Low Turbulence wind tunnel at City, University of London.

## 2.3. Design of experimental model

### 2.3.1. Model configuration

The experimental model should have ideal characteristics to study the development of the crossflow instability, i.e. a sweep angle and favourable pressure gradient. In previous experimental crossflow instability studies a swept aerofoil (Saric and Yeates, 1985; Dagenhart, 1992; Radeztsky et al., 1999; Saric et al., 1998; White and Saric, 2005; Serpieri and Kotsonis, 2016b) and a swept flat plate with a displacement body (Nitschke-Kowsky, 1987; Kawakami et al., 1999; Eppink, 2014) have been employed (Figure 3).

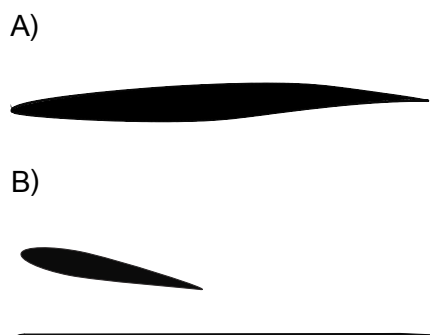


**Figure 3.** A) Swept aerofoil and B) displacement body configuration.

The swept aerofoil has a maximum thickness at large  $x/c$  values, to create the favourable pressure gradient over a large part of the model. For the displacement body arrangement, the favourable pressure gradient is created on the swept flat plate by a suitable orientation of the displacement body. The advantage of the swept aerofoil is that the flow can be measured at all chord-wise locations, since it is not blocked by a displacement body. The advantage of the displacement body arrangement is that the measurements are carried out on a flat surface, avoiding problems

with the alignment of a hot-wire on a curved surface. Furthermore, there is more

flexibility with the displacement body arrangement, compared to the swept aerofoil. Once the aerofoil is chosen, the pressure distribution is fixed, while on the flat plate the pressure gradient can be changed, by varying the parameters of the displacement body. In the current study, it is essential to take detailed measurements over a large spanwise and streamwise region. It is concluded that for the system in place, these measurements would be most effectively carried out on a flat surface. Furthermore, the designed set-up could be used in future swept wing studies which might require a different pressure distribution. By considering all advantages and disadvantages, it was determined that, for the current wind-tunnel set-up, the swept flat plate with a displacement body is preferred.

### 2.3.2. Design of the displacement body

In order to design the displacement body (DB), a two dimensional Hess-Smith panel code was developed in MATLAB (Appendix B), to obtain an approximation of the pressure distribution on the flat plate. It must be noted that, given the inviscid character of the panel code, both separation and boundary layer growth are not taken into account. Therefore, the panel code results are not expected to fully match

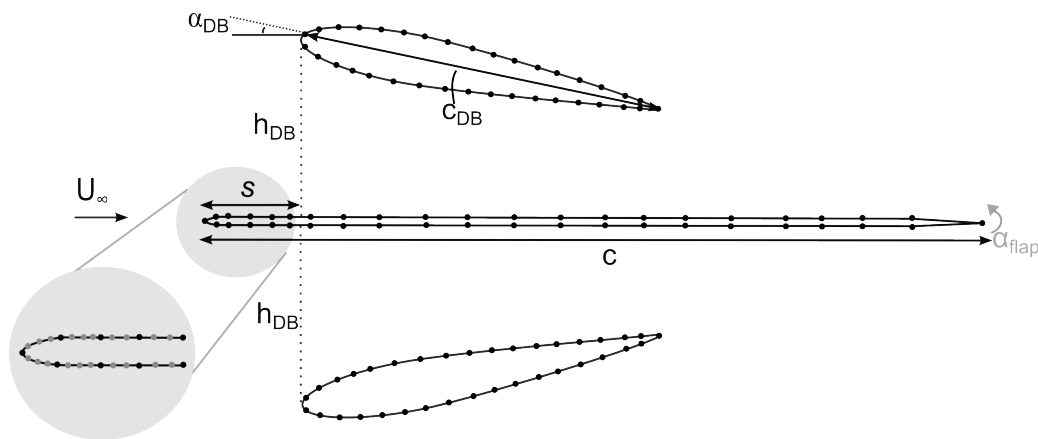


**Figure 4. Configuration of the panel code.** In black all variables which were varied in the parametric study are shown. In grey improvements of the initial panel code are shown.

the experimental results. The comparison of the pressure distribution obtained with the panel code, with the experimental data and RANS computations are shown in Section 3.2 and Appendix A. The lay-out of the panel code is shown in Figure 4 where the black dots indicate the edges of the panels. To avoid large circulation in the wind tunnel, it was chosen to have a symmetric set-up with two displacement bodies. The variables, which are varied in the panel code, are the distance of the trailing edge of the displacement body above the plate ( $h_{DB}$ ), the angle of attack of

the displacement body ( $\alpha_{DB}$ ), the size of the displacement body ( $c_{DB}$ ) and finally, the shift of the displacement body with respect to the flat plate leading edge ( $s$ ). The pressure coefficient on the plate, in the direction perpendicular to the leading edge, was computed as:

$$C_{p,2D} = 1 - (u_{tan}/U_\infty)^2, \quad (2.1)$$

where  $u_{tan}$  is the velocity tangential to the panel.

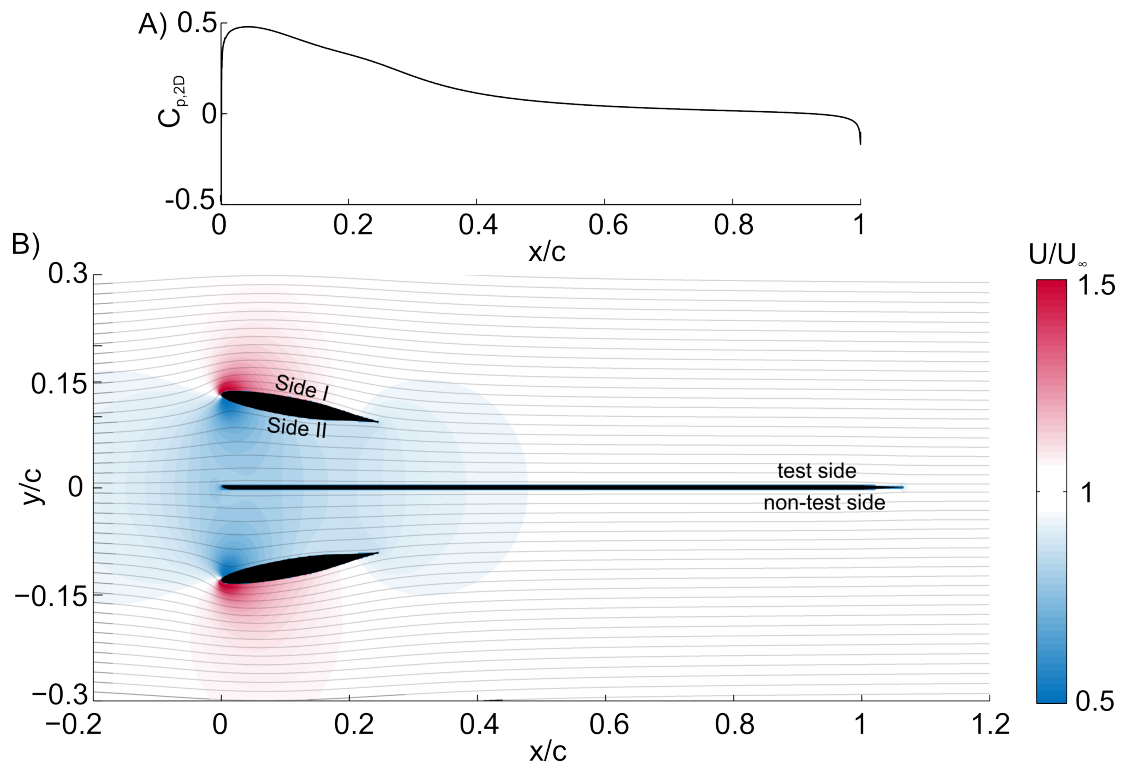


**Figure 5.** Velocity distribution around the flat plate and displacement bodies obtained from the panel code.

First, the general characteristics of the velocity and pressure distribution, obtained from the panel code are discussed. In Figure 5 the velocity distribution and streamlines around the displacement body and flat plate are shown together with the pressure distribution at the test side of the plate, where the measurements are carried out. In the presented case the flap angle is zero degrees, and the displacement bodies have a positive angle of attack. Even though a converging channel is created between the flat plate and the displacement body, the velocity underneath the displacement body is decreased compared to the freestream velocity. This is caused by the lifting effect of the airfoil, which diverges the streamlines creating a decelerated flow region on side II of the displacement body and an accelerated flow region at side I of the displacement body. While the velocity decreases with respect to the freestream it

increases over the flat plate creating a favourable pressure gradient, as also shown in Figure 5. A close up of the pressure distribution in the leading edge region is shown in Figure 6. The negative  $x/c$  represents here the non-test side the plate. It is shown

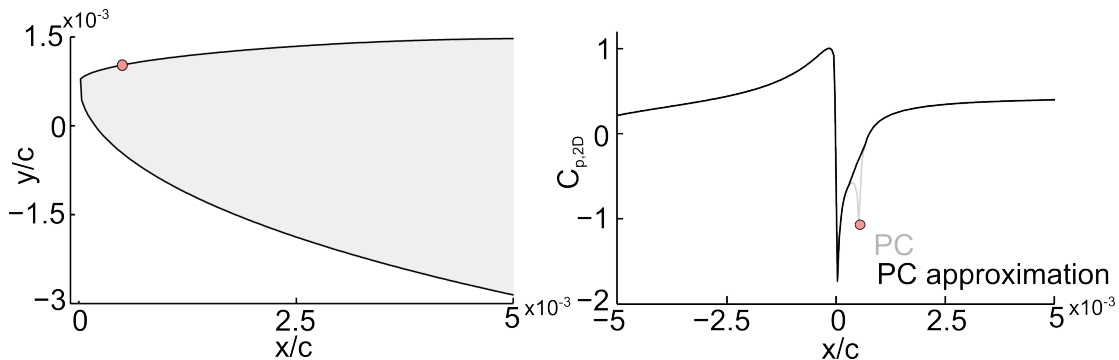


**Figure 6.** Pressure distribution at the leading edge obtained from the panel code.

that the stagnation point is just at the non-test side of the plate creating a suction peak at the test side of the plate after which the pressure recovers. From the results of the panel code a small secondary suction peak was observed around  $x/c=0.0005$ . The original smooth shape of the leading edge is discretized in the panel code. This discretization leads to local changes in the curvature creating the small suction peak at  $x/c=0.0005$ . This was confirmed by changing the number of panels on the leading edge, which consequently changed the location and magnitude of the secondary suction peak. The design of the displacement body was carried out with a flap angle of zero degrees. However, to have closer agreement with the experiment, an angle of the trailing edge flap  $\alpha_{flap}$  were added to the panel code set-up. Furthermore, the number of panels at the flat plate leading edge were increased. In Appendix B the influence of these improvements on the flat plate pressure distribution are discussed.

Next, the optimal values of the variables defined in Figure 4 were determined with a parametric study. The optimal pressure distribution was characterised as followed:

- A large extent of favourable pressure gradient over the flat plate. The favourable pressure gradient is essential for the growth of the crossflow instability.
- No region of strong adverse pressure gradient close to the leading edge. The adverse pressure gradient in vicinity of the neutral stability point will promote the growth of Tollmien-Schlichting waves.
- The gradient of the pressure distribution should be similar to previous crossflow studies, such as Nitschke-Kowsky (1987) and Dagenhart (1992), to ensure there is significant crossflow growth on the flat plate.

First, all the parameters were varied one by one to understand which range of parameters needed to be assessed in the parametric study. In Figure 7 the effect of changing these parameters on the pressure distribution on the flat plate is shown.

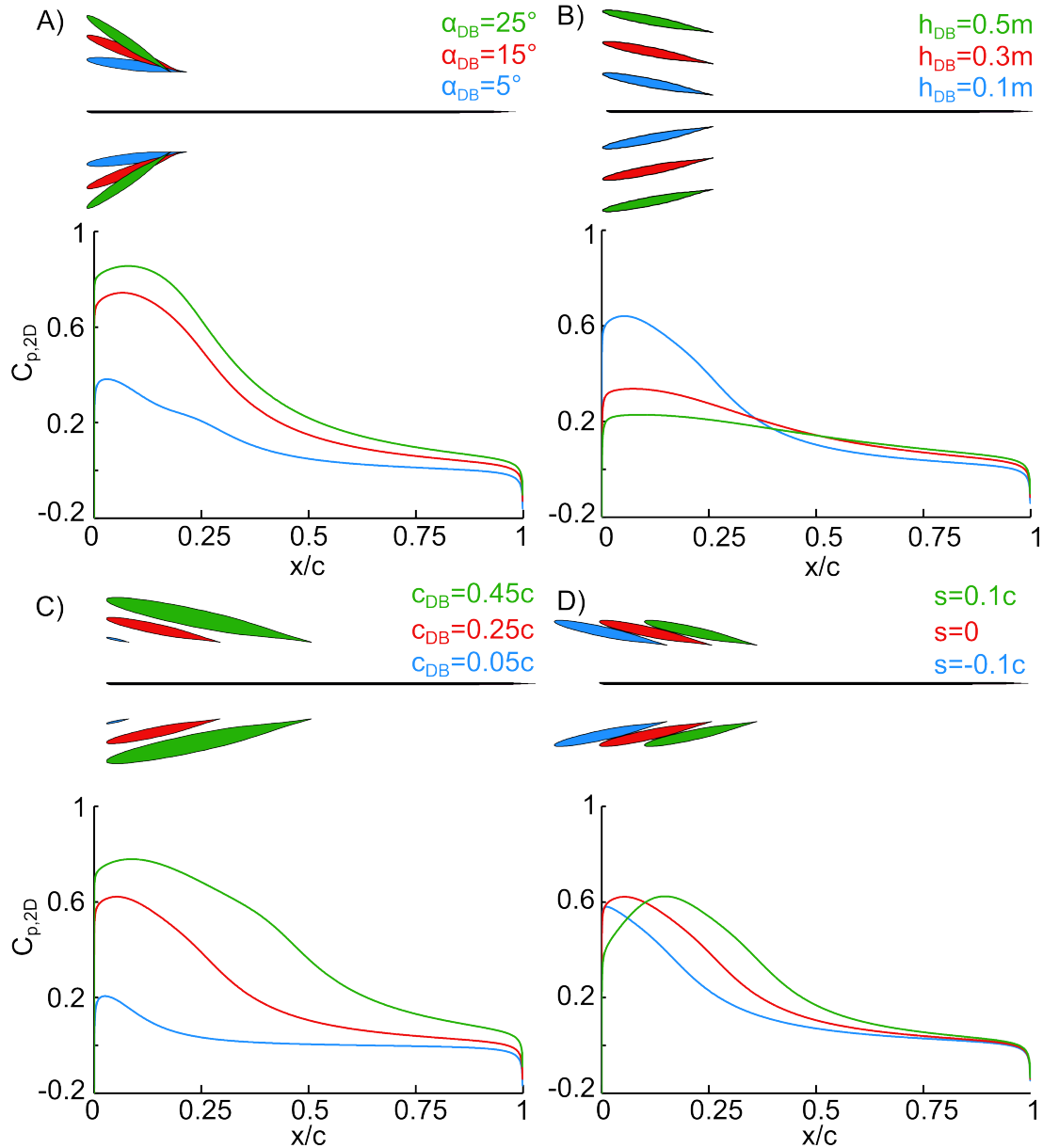


**Figure 7. Variation of pressure distribution on the flat plate for different displacement body configurations** A) Variation of angle of attack,  $\alpha_{DB}$ . B) Variation of height above the plate  $h_{DB}$ . C) Variation of the size of the displacement body  $c_{DB}$ . D) Variation of the shift of the displacement body with respect to the leading edge,  $s$ .

When the angle of attack increases (Figure 7A), the pressure gradient increases, since a converging channel is created between the plate and the displacement body, which accelerates the flow more strongly. When the angle of attack is too high se-

paration will occur, which will not be predicted correctly by the panel code. In the experiments large separation should be avoided since the produced wake might interact with the boundary layer on the flat plate. Furthermore, extra disturbances are introduced in the freestream, which instabilities in the boundary layer might be receptive to (Chernoray et al., 2005). From a viscous analysis in XFOIL (Drela, 1989) it was estimated around which angle of attack separation would occur. In Figure 8 the growth of the computed displacement thickness on top of the aerofoil is shown for different angles of attack. For an angle of attack of 10 degrees significant separation

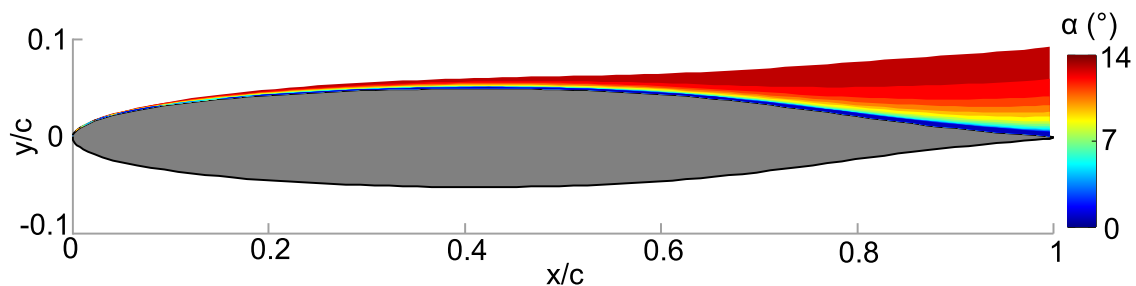


**Figure 8.** Displacement thickness growth over the lwk80100 aerofoil for different angles of attack computed by XFOIL.

ration occurs at the trailing edge of the model. Even though, in the experiment a swept wing is used which might change the separation characteristics, it was decided to investigate angles of attack from 0 to 10 degrees in the parametric study.

When the displacement body is placed closely to the plate, the pressure gradient is strongest, while going further from the plate the pressure gradient becomes weaker (Figure 7B). Placing the body too close will lead to an interaction of the boundary layer on the plate, with the boundary layer or wake of the displacement body. Therefore, the parametric study focusses on distances from 0.1 to 0.3m.

Varying the size of the displacement body, presented in Figure 7C, changes the pressure gradient as expected; for larger bodies the pressure gradient is stronger and sustained for a larger distance over the plate. The size of the displacement body is limited by the blockage ratio of the wind-tunnel cross-section. The maximum blockage ratio is defined as:

$$BR = \frac{W_{DB}}{W_{tot}}, \quad (2.2)$$

where  $W_{tot}$  is the width of the wind tunnel and  $W_{DB}$  the total length which is blocked by the displacement bodies and flat plate. The total length is defined as:

$H_b = 2H_{DB} + H_{pl}$ , where  $H_{DB}$  and  $H_{pl}$  are the thickness of the displacement body and plate, at the chordwise location where the local thickness is maximum. Large blockage will lead to flow deceleration and consequently, leading to unwanted unsteadiness and separation. As a rule of thumb the blockage ratio should stay below 0.2<sup>1</sup>. It was found that if  $c_{DB} \approx 0.25c$ , a favourable pressure gradient is sustained on half of the plate, while the blockage ratio is below 0.1. Therefore, values for this chord length are studied in more detail in the parametric study.

Finally, the influence of the shift of the displacement body, in the streamwise direction, on the flat plate pressure distribution is shown in Figure 7D. When the body is placed downstream of the flat plate leading edge ( $s=0.1c$ ), there is an adverse pressure gradient up to  $x/c=0.2$ . When the displacement body is placed in front of the leading edge ( $s=-0.1c$ ) this adverse pressure gradient vanishes. This can be understood with the velocity distribution shown in Figure 5. Upstream of the displacement body, upto  $x/c=-0.2$ , the velocity decreases leading to an increasing pressure coefficient. When the leading edge of the displacement body is aligned with the plate this effect will hardly be shown on the flat plate. While when the displacement bodies are moved upstream the increase in pressure coefficient will be shown as presented in Figure 7D. The strong adverse pressure gradient is not preferred since it will promote the growth of Tollmien-Schlichting waves. In the parametric study, no shift and small negative values of the shift are tested.

The different constraints together with the range used in the parametric study are summarised in Table 2.2.

**Table 2.2.** Constraints on different parameters in displacement body design.

	Constraint	Range
$c_{DB}$	Large $c_{DB}$ leads to high blockage value. Small $c_{DB}$ will not create a strong pressure gradient.	0.2-0.3c
$\alpha_{DB}$	Large $\alpha_{DB}$ will lead to separation. Small $\alpha_{DB}$ will not create a strong pressure gradient.	0-10°
$h_{DB}$	Large $h_{DB}$ will lead to a weak pressure gradient. Small $h_{DB}$ might lead to boundary layer interaction between the boundary layers of the plate and the displacement body.	0.1-0.3m
$s$	Positive shift will lead to a strong adverse pressure gradient in the leading edge region.	-0.1-0c

For the parametric study three different aerofoils were chosen, with the airfoilttools

<sup>1</sup>Personal communication with Prof. Michael Gaster



**Figure 9.** Airfoil shapes used in the parametric study.

website<sup>2</sup>, which are presented in Figure 9. The *NACA0010* is a simple symmetric aerofoil which gave promising pressure distributions in initial tests. The *lwk80100* and *bell540* aerofoils have a similar thickness to the *NACA0010* aerofoil, however, the minimum pressure coefficient is at different chordwise locations leading to different pressure distributions on the plate.

From the parametric study it was found that the parameters which gave the optimal pressure distribution, as defined earlier in this section, were similar for each aerofoil with  $\alpha_{DB}=8-9^\circ$ ,  $c_{DB}=0.25c$ ,  $h_{DB}=0.1m$  and  $s=0m$ . In Figure 10B the pressure distributions at the flat plate are shown for the tested aerofoils together with the results of the displacement body used in [Bippes and Muller \(1990\)](#) (designed in [Nitschke-Kowsky \(1987\)](#)) and the swept aerofoil used in [Saric et al. \(1998\)](#) (designed in [Dagenhart \(1992\)](#)) amongst other studies. For the computations the pressure gradient on the swept wing is used which is calculated from the 2D pressure coefficient,  $C_{p,2D}$  with:

$$C_{p,3D} = C_{p,2D} \cos(\Lambda)^2, \quad (2.3)$$

where  $\Lambda$  is the geometric sweep angle. The *lwk80100* aerofoil is able to sustain the pressure gradient for the largest distance. The pressure gradients from the panel code and the previous studies are similar between  $x/c=0.1$  and  $x/c=0.4$ . In the leading edge region the pressure gradient on the swept aerofoil ([Dagenhart, 1992](#)) is significantly stronger. Therefore the crossflow vortices will develop more slowly on the present model compared to the experimental study of ([Dagenhart, 1992](#)) and other studies using this experimental model ([Saric et al., 1998](#); [Radeztsky et al., 1999](#); [Hunt and Saric, 2011](#)). Since in the current study hot-wire measurements were not taken below the displacement body, a slower development of the flow is beneficial. Because the pressure gradient is favourable for most part of the plate, it is still expected that the flow will be crossflow dominated.

<sup>2</sup><http://airfoiltools.com/airfoil/>

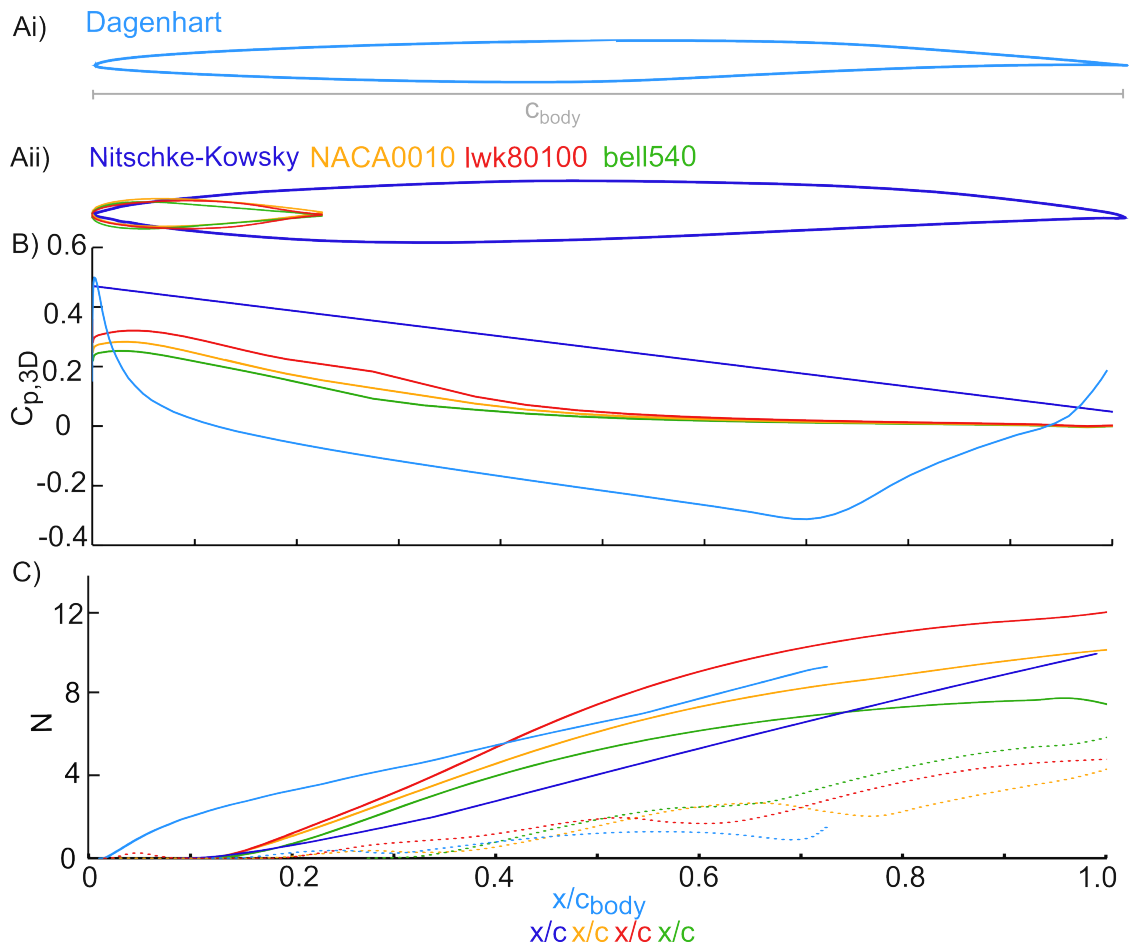


**Figure 10. Displacement body design.** Ai) Swept wing designed in Dagenhart (1992). Aii) Displacement bodies used in the parametric study (NACA0010, bell540, lwk80100 and the displacement body designed in Nitschke-Kowsky (1987)). The chord length of the displacement bodies are scaled with the chord length of the flat plate,  $c$  where the displacement bodies are placed above. B) The pressure distributions found with the optimal parameters from the parametric study and of previous investigations. Where the displacement body studies show the pressure distribution on the plate, while the swept airfoil shows the pressure distribution on the airfoil itself. C)  $N$  factor growth for the crossflow instability (solid lines) and Tollmien Schlichting waves (dashed lines).

In order to study for which pressure distribution the crossflow growth was maximized, a linear stability analysis (Appendix A) was carried out with the pressure distributions from Figure 10B. The results are presented in Figure 10C, which shows the N-factor curves for both the crossflow instability and Tollmien-Schlichting waves. The travelling crossflow waves are omitted here, since with the low freestream turbulence levels in the wind-tunnel, it is expected that the flow will be dominated by the stationary crossflow waves as discussed in more detail in Chapter 4. The N-factor curves show that the Tollmien-Schlichting waves grow slowly and the transition process over all models is crossflow dominated. Of the tested displacement bodies, the *lwk80100* shows the strongest crossflow growth. The *bell540* aerofoil shows weakest crossflow growth, together with the strongest growth of Tollmien-Schlichting waves. These results were also expected from the pressure distributions, since for the *lwk80100* and *bell540* the favourable pressure gradient sustain the largest and smallest chordwise distance respectively.

From the discussed analysis it follows that the *lwk80100* aerofoil will be most suitable to create a crossflow dominated flow. With the chosen parameters the displacement body has a thickness of 3.8cm which leads to a total blockage of 8.6cm which is 9.4% of the wind tunnel width. The displacement body is manufactured from foam and stiffened with steel rods. It is finished with a smooth plastic to ensure low surface roughness.

### 2.3.3. Design of the flat plate

A 45 degrees swept flat plate was available from previous studies and used in this experimental study. The dimensions and main characteristics of the flat plate are shown in Figure 11.

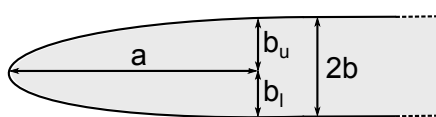


**Figure 12.** Leading edge parameters. Figure adapted from Hanson et al. (2012).

The plate consists of three parts, which are connected together with screws at the bottom and top of the plate. Previous studies have found that discontinuities in the leading edge are a source of receptivity (Reed and Saric, 2014). Lin et al. (1992) found that the discontinuities vanish by using a modified super ellipse as a leading edge geometry, which is the geometry used in the current study.

The parameters defining this super ellipse are given in Figure 12. For the current study the chosen values were:  $\epsilon = a/b=9.52$ ,  $a=45.36\text{mm}$ ,  $b_h=4.76\text{mm}$ ,

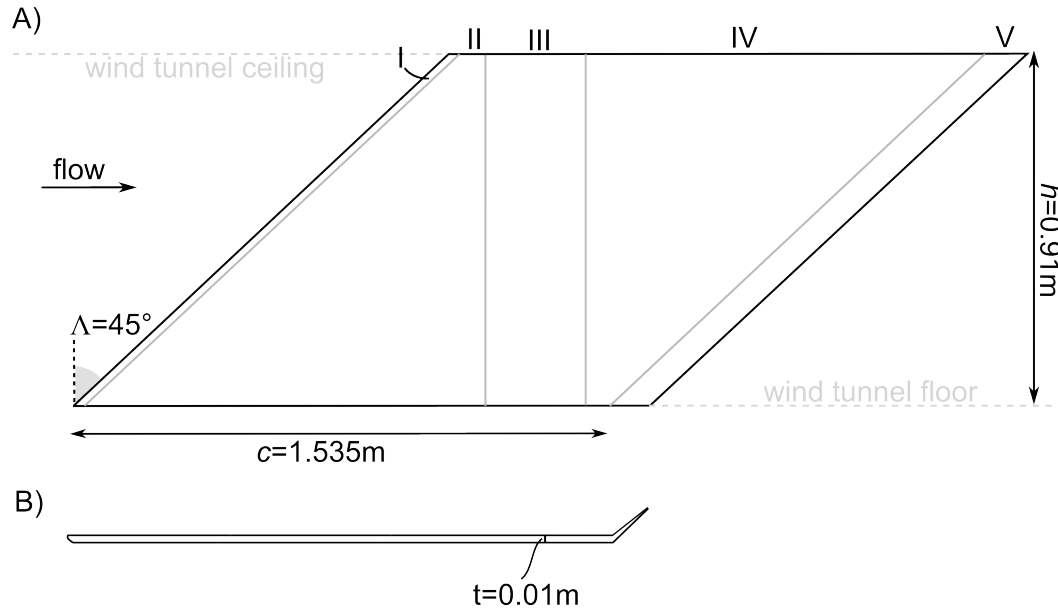


**Figure 11. Flat plate lay-out.** A) Side view of the plate which consists of five parts. Part I is the detachable leading edge and part V the trailing edge flap. Part II,III and IV are the main part of the body. Part II has three rows of pressure taps (dashed lines) B) Cross-section along the chord of the flat plate.

$b_u = 3/12b = 1.19\text{mm}$ ,  $b_l = 9/12b = 3.57\text{mm}$ , which were derived from an optimization carried out by [Hanson et al. \(2012\)](#). The designed leading edge was manufactured from aluminium, using a CNC machine. A trailing edge flap was designed to be able to adjust the location of the attachment line. The attachment line at the bottom of the plate should be avoided since it will lead to a small separation bubble at the top of the plate leading to early transition. Due to manufacturing constraints a small flap of 12 cm was designed and connected to the flat plate with a hinge mechanism.

The design and geometry of the swept leading edge determines if the attachment line boundary layer will be contaminated by disturbances from the turbulent boundary layer on the wind-tunnel wall. A turbulent attachment line should be avoided, since no transition process from laminar to turbulent flow over the swept flat plate could be studied. As discussed in Section 1.5, [Gaster \(1967\)](#) found that the Reynolds number based on the momentum thickness of the attachment line,  $R_{\theta AL}$  should stay below 100 to avoid attachment line contamination. From the solution of the Falkner-Skan-Cooke equation for swept Hiemenz flow, the Reynolds number is calculated with:

$$R_{\theta AL} = 0.4042 \sqrt{\frac{U_{\infty} r \sin \Lambda \tan \Lambda}{\nu(1 + \epsilon)}}, \quad (2.4)$$

where  $\epsilon$  is the ellipticity of the leading edge. With a sweep angle,  $\Lambda$ , of 45 degrees and freestream velocity of 16m/s,  $R_{\theta AL}=16$  which ensures that the attachment line boundary layer will not be contaminated.

To ensure a high-surface quality, the plate was progressively polished with sandpaper grits increasing from P400 to P1200. Small scratches were filled with car body

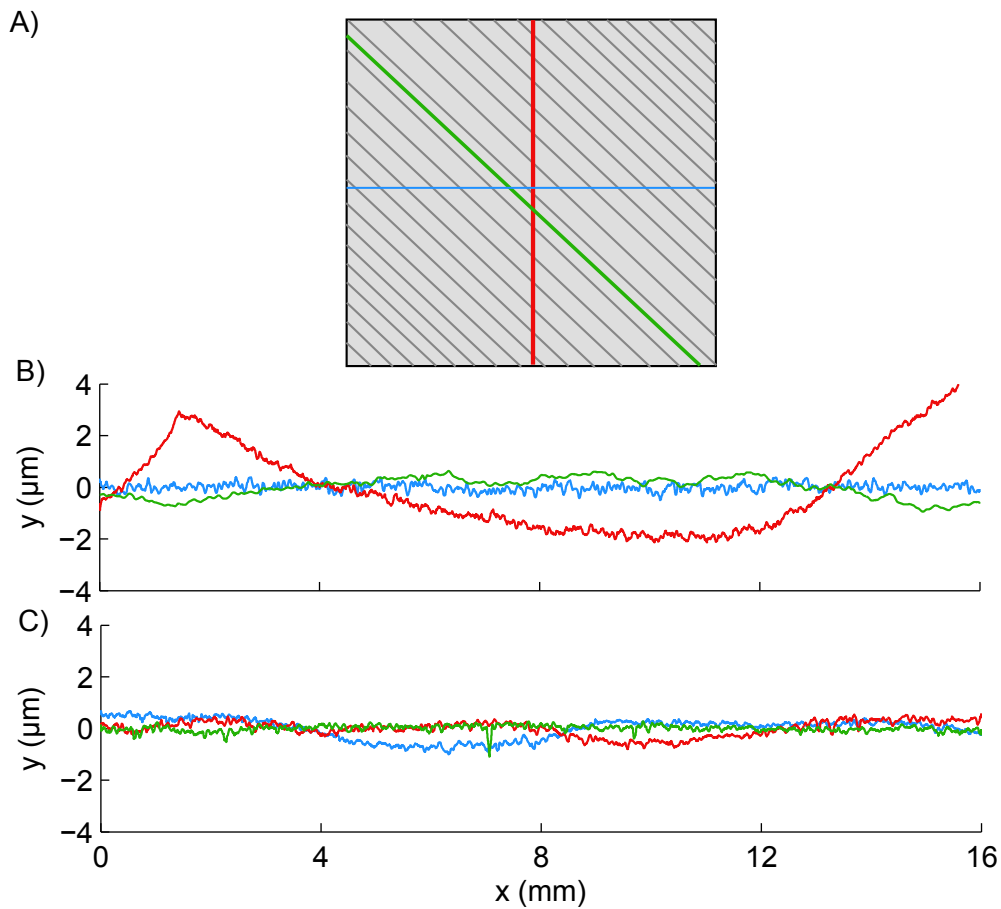


**Figure 13. Flat plate roughness measurements.** A) Roughness measurements were taken in three different measurement directions (coloured lines) to detect any influence of the machining ridges (grey lines). B) Roughness measurements on the unpolished surface. C) Surface measurements on the polished surface.

filler (Simoniz spray putty) until seemingly embedded in the plate. The connection between the leading edge and plate was filled with a similar procedure. The surface roughness of the flap was measured before and after polishing with a profilometer (Mitutoyo SJ-410). In the samples the machining lines were visible and therefore surface measurements were taken in three different directions (Figure 13). The results (Figure 13) show that polishing created a more uniform surface while the surface

roughness is similar for both cases. The surface roughness was determined with:

$$R_q = \sqrt{\frac{1}{n} \sum_{i=1}^n y_i^2} \quad (2.5)$$

A value of  $R_q = 0.2\mu\text{m}$  was measured which is similar to surface roughness values in other crossflow receptivity studies (Radeztsky et al., 1999; Hunt and Saric, 2011; Eppink, 2014)

### 2.3.4. Coordinate systems

The designed experimental set-up is shown in Figure 14. Two main coordinate systems are used. The traverse oriented coordinate system is denoted with  $x,y,z$ . The  $x$ -direction is aligned with the streamwise velocity,  $U_\infty$ . The model oriented coordinate system is aligned parallel ( $Z$ ) and perpendicular ( $X$ ) to the leading edge of the flat plate while the wall-normal direction ( $Y$ ) coincides with the  $y$ -direction of the traverse oriented system. Throughout the thesis the  $Z$ -direction is also denoted

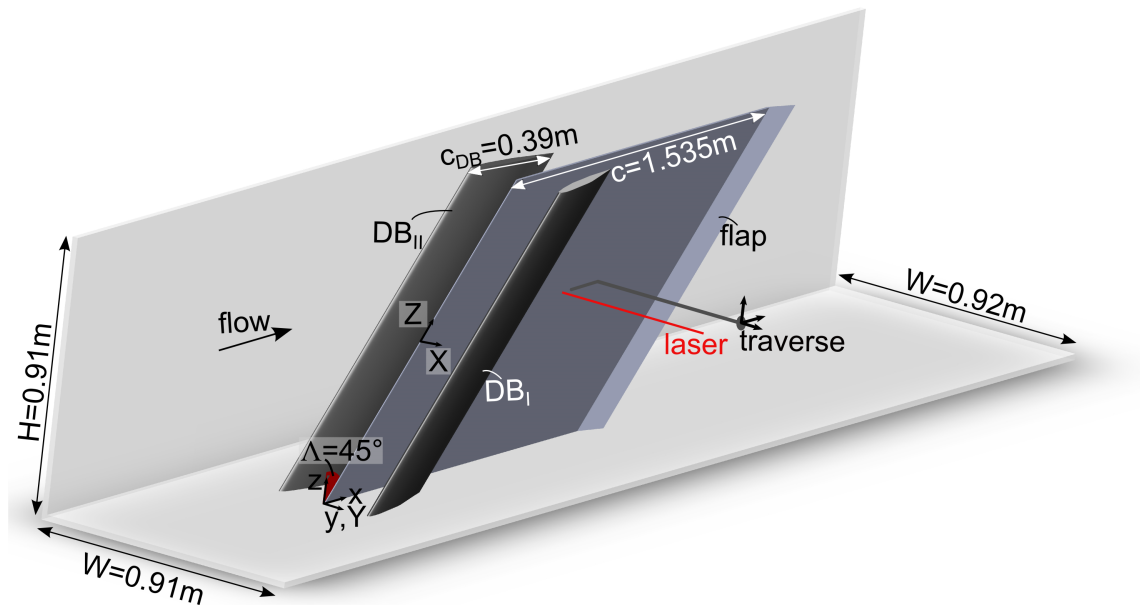


**Figure 14.** Designed experimental set-up. With two displacement bodies ( $DB_I$  and  $DB_{II}$ ) placed on each side of the plate.

as the spanwise direction. The origin of the wall-normal coordinate is at the surface of the plate, while the streamwise coordinate starts at the leading edge of the flat plate. For the spanwise coordinate,  $Z$ , the origin is aligned with the hot-wire scans and will therefore differ for the experiments described in Chapter 4 and Chapter 5

## 2.4. Hot-wire anemometry

### 2.4.1. Working principle

The development of the stationary and travelling crossflow instabilities is tracked with single hot-wire anemometry measurements. Hot-wire anemometry allows for high spatial and temporal resolution measurements, which are essential in the current investigation. In this section the governing equations and principle of Constant Temperature Anemometry (CTA) are explained following Tropea et al. (2007) and Scarano (2012). In Figure 15 a sketch of a hot-wire is shown.

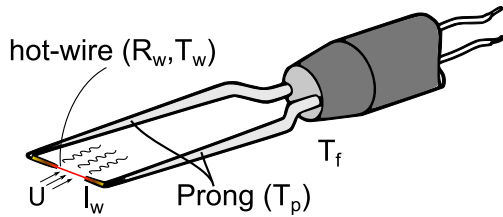


**Figure 15.** Schematic of a hot-wire.

The hot-wire probe is made of an electric conducting material such as Tungsten or nickel. When a current is sent through the hot-wire it wire will heat up, due to the Joule effect, with an amount of  $I_w^2 R_w$  where  $I_w$  is the current through the wire and  $R_w$  the wire resistance. At the same time heat is transferred to the surroundings by convection, con-

duction and radiation denoted by  $Q_{conv}$ ,  $Q_{cond}$  and  $Q_{rad}$  respectively. The change in the wire temperature,  $T_w$ , can thus be written as:

$$m_w c_w \frac{dT_w}{dt} = I_w^2 R_w - (Q_{conv} + Q_{cond} + Q_{rad}), \quad (2.6)$$

where  $m_w$  is the mass of the wire and  $c_w$  the specific heat of the sensor material. The heat transfer terms  $Q_{rad}$ ,  $Q_{cond}$  and  $Q_{conv}$  are described with:

$$Q_{rad} = \epsilon \sigma A (T_w^4 - T_f^4), \quad (2.7)$$

where  $\epsilon$  is the emissivity of the hot-wire surface,  $\sigma$  the Stefan-Boltzmann coefficient and  $A$  the heat transfer area and  $T_f$  the temperature of the fluid. Due to the small surface area of the wire and low emissivity, this term is negligible compared to the other heat transfer terms. The conductive heat transfer terms writes:

$$Q_{cond} = -k_w A \frac{dT_w}{dx}, \quad (2.8)$$

where  $k_w$  is the conductivity coefficient of the hot-wire material and  $dT_w/dx$  the temperature gradient along the wire. In the middle of the hot-wire probe the temperature is constant, however, at the end of the wire there is a large temperature

difference between the prong and the hot-wire. To minimize the effects of heat conduction a wire with a high length over diameter ratio should be used. Finally, the convective heat transfer term is written as:

$$Q_{conv} = hA(T_w - T_f), \quad (2.9)$$

Where  $h$  is the convective heat transfer coefficient. For a Tungsten wire, with a diameter of  $5\mu\text{m}$ , and wire length of  $1.25\text{mm}$  the conductive heat losses,  $Q_{cond}$ , correspond to around 15% of the total heat transfer (Bruun, 1995). This shows that the convective heat losses dominate the temperature change in the wire and in the following analysis the radiation and conduction terms are neglected. Furthermore, it is assumed that the temperature of the wire does not change with time. With these assumptions Equation 2.6 simplifies to:

$$I_w^2 R_w = Q_{conv} = hA(T_w - T_f). \quad (2.10)$$

Nusselts number,  $Nu$ , describes the ratio between the convective and conductive heat transfer between the wire and fluid. With Nusselts number the heat transfer coefficient writes  $h = Nuk_f/d$  where  $k_f$  is the heat conductivity of the fluid and  $d$  the diameter of the wire. For subsonic flow in the forced convection regime, which is considered in the current study, the Nusselt number can be written as a function of Reynolds number as:  $Nu = A_1 + B_1 Re^n = A_2 + B_2 U^n$ . Filling this expression in Equation 2.10 and using Ohms law ( $E = I_w R_w$ ) King's law is derived:

$$E^2 = A + BU^n. \quad (2.11)$$

King's law shows that when the voltage drop over the wire,  $E$ , is measured the velocity  $U$  can be determined. The coefficients  $A$  and  $B$  are dependent on the properties of the wire and fluid flowing around it. With the total velocity  $U$ , the fluctuating velocity  $u$  can be determined. If  $E = \bar{E} + e$  and  $U = \bar{U} + u$ , where  $(\bar{\quad})$  denotes the mean, is substituted in Equation 2.11 it can be shown that for small fluctuations the velocity fluctuations are written as:

$$u' = \frac{2\bar{E}}{Bn\bar{U}^{n-1}}e = \left(\frac{d\bar{E}}{d\bar{U}}\right)^{-1} e. \quad (2.12)$$

The resistance of the wire,  $R_w$ , is a function of the temperature of the wire  $T_w$  as:

$$R_w = R_0[1 + \alpha_0(T_w - T_0)], \quad (2.13)$$

where  $R_0$  denotes the resistance of the wire taken at a reference temperature of  $T_0$ . The non-dimensional temperature rise of the wire is defined with the overheat ratio  $OHR$ :

$$OHR = \frac{R_w}{R_0} = 1 + \alpha_0(T_w - T_0). \quad (2.14)$$

In a constant temperature anemometer (CTA) the temperature of the wire is kept constant, by keeping the resistance constant with a Wheatstone bridge which is shown in Figure 16.

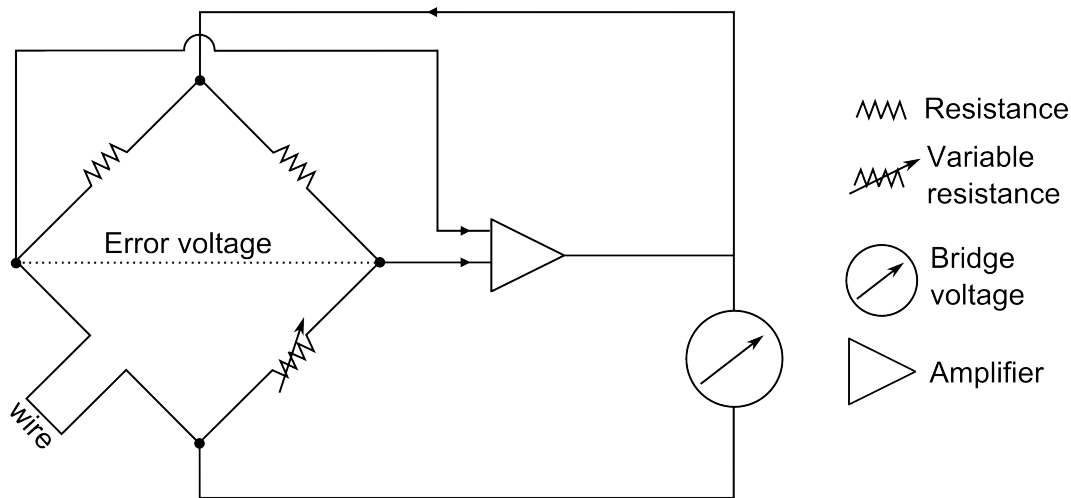


**Figure 16.** Configuration of a Wheatstone bridge to keep the wire temperature or current constant.

For CTA the Wheatstone bridge works as follows. First, the bridge is balanced by changing the variable resistance such that the error voltage is equal to zero. When the velocity increases the wire temperature and consequently the wire resistance decreases resulting in an unbalanced bridge. The amplifier detects this imbalance and sends a current through the wire which causes the wire to heat up, increase the wire resistance and restore the balance in the bridge. Alternatively, a constant current anemometer (CCA) could be used, by allowing the temperature to change and varying the voltage drop with a Wheatstone bridge. In most applications, including the current investigation, a CTA is used because the CCA has a slower frequency response due to thermal inertia and furthermore there is a possibility of burning out the wire since the temperature is not kept constant.

### 2.4.2. Setting up the hot-wire

In the experiments a Tungsten wire is used with a diameter of  $5\mu\text{m}$  and length of  $1.25\text{mm}$ . To operate the hot-wire first the reference resistance,  $R_0$  is measured when the hot-wire is connected to the anemometer and the fluid velocity is zero. The resistance measured includes the resistance of the prongs and connector from the hot-wire sensor to the anemometer. Next, the overheat ratio is chosen and the wire resistance is calculated with Equation 2.14. The overheat ratio is usually set to 1.5 leading to a wire temperature of around  $159^\circ\text{C}$  which is well below the oxidizing temperature of Tungsten of  $350^\circ\text{C}$  (Bruun, 1995).

To assess the frequency response of the wire, a square-wave test is performed. In this test a square-wave signal is applied to the top of the Wheatstone bridge, which creates an unbalanced bridge. The time it takes to rebalance the bridge is then representative for the frequency response of the wire. The response of a constant temperature hot-wire to a square wave signal has been obtained theoretically by (Freymuth, 1977) and has the characteristics shown in Figure 17. The cut-off frequency  $f_c$ , is the maximum frequency which can be measured with the hot-wire. When the gain of the amplifier in the Wheatstone bridge is set too high, the feedback loop is unstable and ringing can occur leading to an unstable dynamic system, and distorted hot-wire signal. The response of the hot-wire in a square-wave test with ringing is shown in red in Figure 17.

In the current experiment a square wave signal was applied to the top of the bridge, when the wind tunnel velocity was set to the measurement velocity. The gain of the amplifier was then changed until the response of the hot-wire had similar characteristics as the green line in Figure 17. From this a time delay,  $\tau$ , of approximately  $10\mu\text{s}$  was obtained, which led to a cut-off frequency of  $100\text{kHz}$  by using  $f_c = 1/1.3\tau$ . To determine the sampling frequency, the frequencies

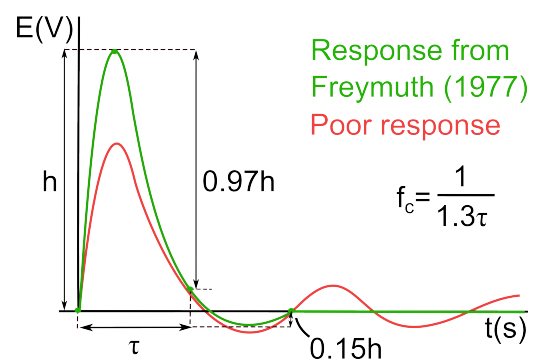


**Figure 17.** Response of a hot-wire to a square-wave test (From Bruun (1995)).

of the travelling waves in the boundary layer had to be estimated. The secondary instability was expected to have the highest frequency which needed to be measured. In previous studies, the secondary crossflow instability had frequencies of  $1\text{kHz}$  to  $5\text{kHz}$  (Kawakami et al., 1999; White and Saric, 2005; Serpieri and Kotsonis,

2016b) at similar freestream velocities as used in the current experiment. In these experiments a sampling frequency of 20kHz to 40kHz has been used. To reduce the amount of data created it was chosen to have a sampling frequency of 20kHz in the current experiment. With this sampling frequency, disturbances with frequencies up to 10kHz can be resolved as is depicted by the Nyquist theorem. The sampling frequency is well below the cut-off frequency of 100kHz determined with the square-wave test. The sampling time for each individual hot-wire measurement is optimized for the different experiments. To obtain the optimum measurement time, the flow fields were compared for different sampling times. The optimum sampling time was chosen as the time where the mean flow field characteristics did not vary when the sampling time was increased.

The raw hot-wire signal is passed through a high- and low-pass filter. The high-pass filter is set to 2Hz. With this frequency the DC component is removed as well as low frequencies which do not relate to flow instabilities. The low-pass filter is set to 10kHz to avoid aliasing of frequencies above 10kHz.

### 2.4.3. Hot-wire calibration

Prior to each hot-wire scan, a calibration was carried out, to determine the coefficients  $A, B$  and  $n$  defined in Equation 2.11. To carry out the calibration the hot-wire was brought close to the Pitot tube placed ahead of the leading edge, to have a similar velocity at both sensors. The wind-tunnel speed was changed from 2 to 18m/s in 2m/s increments. After each velocity change, a waiting time of 30 seconds was set to ensure that a constant velocity was reached. Next, the mean velocity from the Pitot tube,  $U$  and mean voltage of the hot-wire probe,  $E$ , were measured simultaneously. When all velocities were measured the coefficients were determined by fitting a line through  $E^2$  and  $U^{\hat{n}}$ , where  $\hat{n}$  was varied from 0.2 to 1.2 in 0.01 increments. For each  $\hat{n}$  the coefficients  $\hat{A}$  and  $\hat{B}$  were calculated and the voltage,  $\hat{E}$ , was calculated with Equation 2.11. Next the root mean square error  $R$  was calculated with:

$$R = \sqrt{\sum_{i=1}^N (\hat{E}_i - E_i)^2}. \quad (2.15)$$

Repeating these steps for all  $\hat{n}$ , the final  $n$  was determined as the  $\hat{n}$  where  $R$  was minimum, as presented in Figure 18. The coefficients  $A$  and  $B$  then followed from the linear fit of  $E^2$  and  $U^n$ . Throughout the experiments values of  $n$  of 0.3-0.45 were found. The large range of  $n$  was due to the different hot-wire probes used and the

varying ambient temperature throughout the year. After the hot-wire calibration

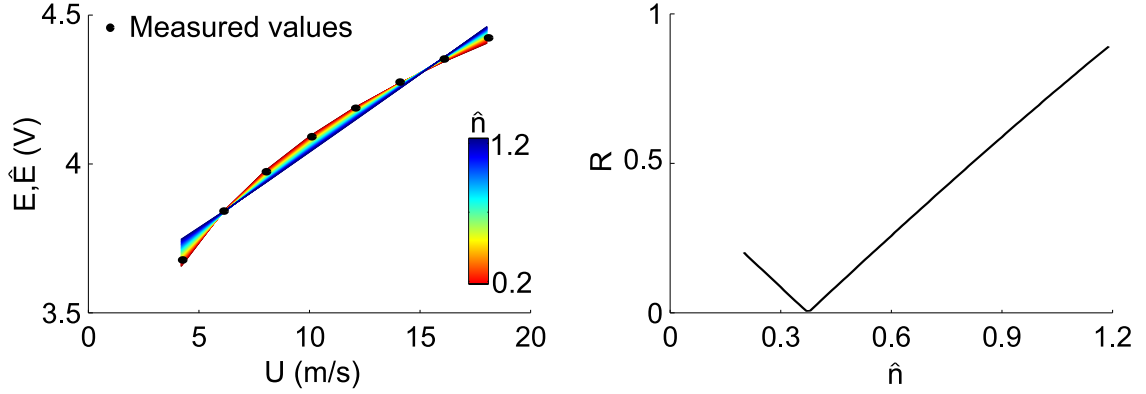


**Figure 18.** Hot-wire calibration curve for different  $n$  (left). Error between estimation and measured values for different  $n$  (right).

was carried out a hot-wire scan was started. During the hot-wire scan the ambient temperature slightly changed compared to the temperature at which the calibration was carried out ( $\Delta T \approx 1-3^\circ$ ). The consequences of this temperature difference are illustrated with the following example. Suppose there are two hot-wire measurements, MI and MII measuring a velocity  $U$  which is equal for both measurements. MI is carried out at the calibration temperature,  $T_{a,r}$  while MII is carried out at a temperature of  $T_{a,r} + \Delta T$ . The voltage measured in MI and MII will differ due to the different ambient temperatures. For MI the actual velocity,  $U$  will be measured while for MII a velocity of  $U + \Delta U$  will be measured resulting in an error between the actual velocity and measured velocity. To minimize this error the hot-wire voltage is adjusted for the variation in ambient temperature. The voltage,  $E_w$ , measured at ambient temperature,  $T_a$ , is transformed to voltage,  $E_{w,r}$  at the ambient temperature during the calibration  $T_{a,r}$ . The transformation is written as followed:

$$E_{w,r} = E_w \sqrt{\frac{T_w - T_{a,r}}{T_w - T_a}}, \quad (2.16)$$

where the wire temperature,  $T_w$ , is determined with Equations 2.13 and 2.14.

#### 2.4.4. Data analysis

The first step in the data analysis process is to understand how to detect the travelling and stationary crossflow waves. For the travelling crossflow wave the amplitude and frequency can be obtained from the power spectrum of the hot-wire signal. The detection of the stationary crossflow waves from the streamwise velocity is less straightforward. In Figure 19 it is shown how a Blasius boundary layer is deformed by a

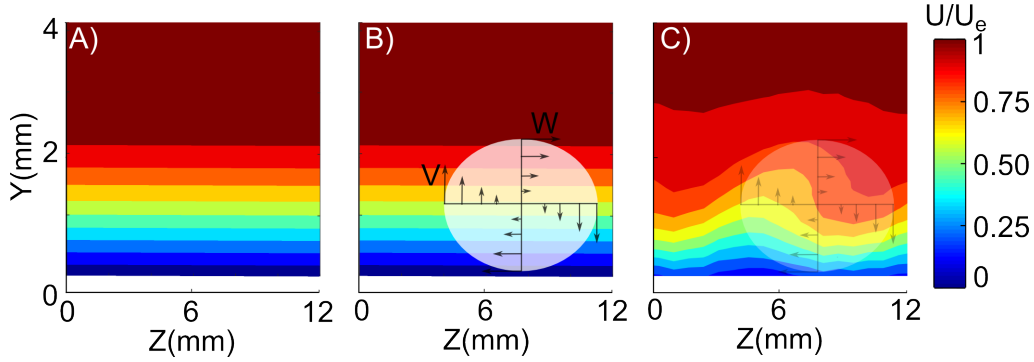


**Figure 19.** A) Mean streamwise velocity distribution showing a spanwise uniform Blasius boundary layer. B) Structure of a stationary crossflow vortex on top of the Blasius boundary layer. C) Deformation of the mean streamwise velocity field due to the stationary crossflow vortex.

streamwise vortex. The stationary vortex has velocity components in the spanwise and wall-normal direction which act on the fluid particles passing by in the streamwise direction. Because of the stationary character of the vortex, the fluid particles are continuously deflected resulting in regions of downwelling and upwelling fluid, as shown in the mean streamwise velocity distribution presented in Figure 19C. When a large spanwise extent is measured different vortex structures can be observed and the wavelength and amplitude of the stationary crossflow waves can be obtained.

To interpret the hot-wire measurements correctly it is important to understand which velocity components are measured. Since the hot-wire is aligned in the streamwise direction it will measure the streamwise velocity,  $U$ , as well as the wall-normal velocity  $V$ . The strength of the stationary vortex determines the magnitude of the wall-normal velocity,  $V$ . Since it is expected that  $V \approx W$ , the value of  $W$  found in previous studies can be used to estimate the magnitude of  $V$ . In [Deyhle and Bippes \(1996\)](#) the velocity components  $U$  and  $W$  were measured with a v-probe when the stationary vortices were fully developed. They found that at the wall-normal location where the spanwise velocity was maximum,  $W=8\%$  and  $U=55\%$  of the freestream velocity. Similar ratios were found by [Kurian et al. \(2011\)](#) and [Serpieri and Kotsionis \(2016b\)](#). In the current set-up, where the single hot-wire is aligned with the streamwise direction, the measured velocity,  $U_{meas}$ , would be:

$$U_{meas} = \sqrt{U^2 + V^2}. \quad (2.17)$$

For a freestream velocity of 16m/s, the streamwise, spanwise and wall-normal velocity are  $U=8.80\text{m/s}$ ,  $W \approx V=1.28\text{m/s}$  respectively. This gives  $U_{meas}=8.89\text{m/s}$ , which

shows that  $U_{meas} \approx U$ . Therefore the velocities measured with the hot-wire in the present study can be interpreted as streamwise velocities, keeping in mind that a small fraction is caused by the wall-normal velocity  $V$ . Throughout the thesis the measured velocity is denoted by  $U$ .

The data analysis of the hot-wire data described in this section relates to all hot-wire measurements in general, while in Section 4.5 and Section 5.5 the specific analysis for each experiment is given. Two streams of raw hot-wire data are obtained. The first stream  $E$ , is obtained directly from the anemometer while the second stream,  $e$ , is obtained from the analogue bandpass filter (2-10000Hz). With  $E_{w,r}$  calculated, from the temperature correction shown in the previous section, the velocities  $U_{raw}$  and  $u_{raw}$  are determined with King's law given with Equations 2.11 and 2.12. The mean velocity  $U$  and rms fluctuation velocity  $u'$  are calculated from the time signal with  $M$  samples as:

$$U = \frac{1}{M} \sum_{m=1}^M U_{raw}[m], \quad (2.18)$$

$$u'_{TD} = u'_{rms} = \sqrt{\frac{1}{M} \sum_{m=1}^M |u_{raw}[m]|^2}, \quad (2.19)$$

where TD denotes the time domain. The rms fluctuation velocity of the time signal is denoted by  $u'_{rms}$  throughout the thesis. The power spectra of the fluctuating velocity component are calculated to understand which temporal frequencies are present in the flow. First, the signal is divided into  $N$  blocks with each  $M_b$  samples to have a frequency resolution,  $\Delta f$  of 10Hz. This frequency resolution was sufficient to resolve the travelling waves which have frequencies in the range from 100Hz to 5kHz and is similar to the frequency resolution used in previous investigations (White and Saric, 2005). The number of samples per block is initially determined as:

$$M_{b,init} = \frac{2f_s}{\Delta F}, \quad (2.20)$$

this number is then altered such that it satisfies  $M_b = 2^p$  where  $p$  is an integer which is determined from  $2^p \leq M_{b,init}$ . This last step is carried out to speed up to fast Fourier algorithm. With the number of samples per block known the number of

blocks,  $N$  is determined with:

$$N = M/M_b. \quad (2.21)$$

Where  $N$  is then rounded to the nearest integer less or equal to  $N$ . Each block of samples is then multiplied by a Hanning window to reduce spectral leakage. The Hanning window is described with:

$$w(m) = 0.5 \left( 1 - \cos \left( 2\pi \frac{m}{M_b} \right) \right) \quad 0 \leq m \leq M_b. \quad (2.22)$$

The frequency spectrum,  $F_N$ , is then calculated for each block of windowed samples with a Fast Fourier Transform algorithm implemented in MATLAB. The block-averaged frequency spectrum is obtained with:

$$F = \frac{1}{N} \sum_{n=1}^N F_N. \quad (2.23)$$

The frequency spectrum is normalised such that Parseval's theorem holds. Parseval's theorem states that the energy of the signal,  $E = u'^2$ , in the time domain should be equal to the energy of the spectrum in the frequency domain (Bracewell, 1986). The main purpose of scaling the spectra is to be able to calculate the rms value of velocity fluctuations within specific frequency bands as will be discussed in more detail in Chapter 4. In the current case, Parseval's theorem writes:

$$\sum_{m=1}^M u'[m]^2 = \frac{\zeta N}{M_b} \sum_{m=1}^{M_b} F[m]^2, \quad (2.24)$$

where  $\zeta$  is the correction factor due to windowing which is 8/3 for a Hanning window. The root mean square velocity of the fluctuations for all frequencies can now be obtained from the power spectrum ( $S^* = F^2$ ), by using Equations 2.19 and 2.23, with:

$$u'_{FD} = \sqrt{\frac{\zeta}{M_b^2} \sum_{m=1}^{M_b} S^*[m]}. \quad (2.25)$$

This leads to the scaled power spectrum:

$$S = \frac{\zeta}{M_b^2} S^*. \quad (2.26)$$

which is used throughout the thesis. The unit of the power spectrum is equal to  $\text{m}^2/\text{s}^2\text{Hz}$  which will be denoted as  $u'^2/\text{Hz}$ .

## 2.5. Traverse and laser positioning system

The 3-axis traverse system, shown in Figure 20, determines the x,y and z position of the hot-wire probe. The resolution in the x and z direction is  $10\mu\text{m}$ . For the wall normal direction (y) the motor was changed during the course of the project to improve the resolution in the wall-normal direction. Therefore for the hot-wire scans described in Chapter 5 the resolution is  $1.25\mu\text{m}$  while the scans described in Chapter 4 the resolution is  $12.5\mu\text{m}$ .

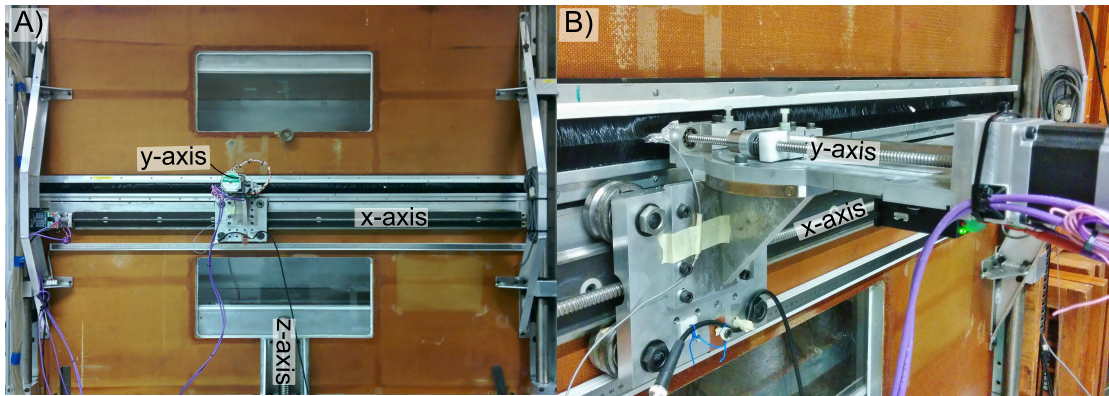


**Figure 20.** A) Overview of traverse system installed on the test section with each of the axes defined. B) Detailed view of the part of the traverse controlling the y-axis.

The laser positioning system (micro-epsilon optoNCDT1700) is attached to the traverse stand. A laser beam is sent to the experimental model, reflects off it and sent back to the receiver. From the time difference between sending and receiving the laser beam, the distance to the model is determined with an accuracy of  $0.5\mu\text{m}$ . The positioning system prevents the hot-wire probe from hitting the wall as explained in the following section.

### 2.5.1. Wall avoidance

Prior to each hot-wire scan the hot-wire probe is brought as close as possible to the wall (judged by eye). Possible undulations or small inclinations of the flat plate, or a slightly misaligned traverse system could cause the hot-wire probe to hit the wall during a hot-wire scan. Since the hot-wire is fragile any contact with the wall should be avoided. In the LabVIEW program there are several methods implemented to

achieve this (Figure 21). At the start of each hot-wire scan a table with  $x, y$  and  $z$

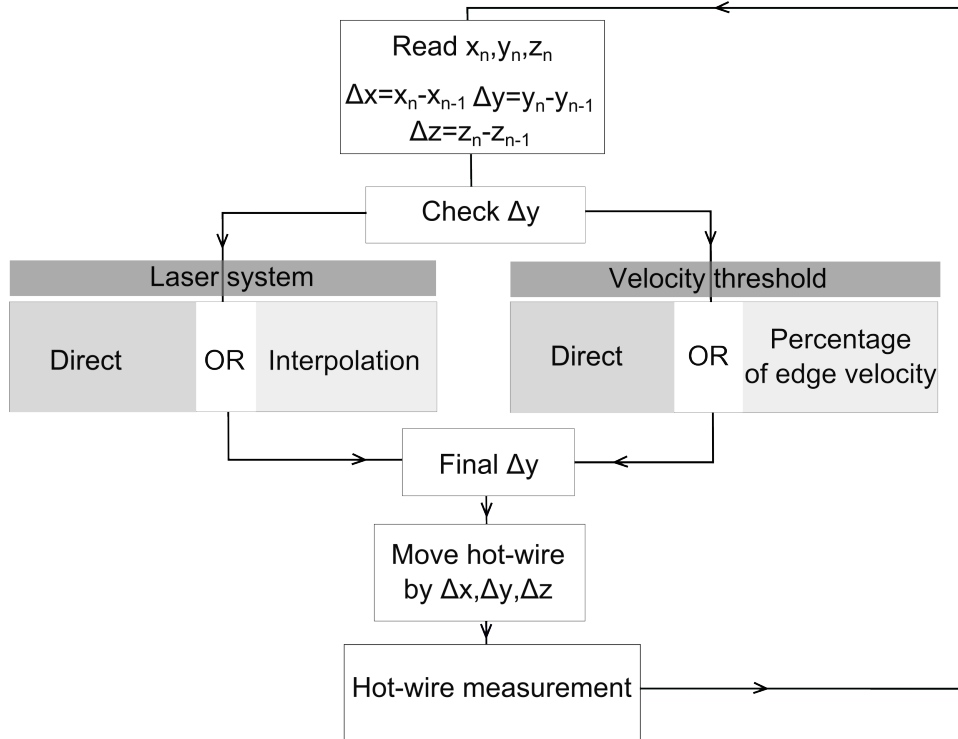


**Figure 21.** Overview of methods implemented in LabVIEW to avoid contact of the hot-wire probe with the inclined flat plate wall.

coordinates is uploaded to the LabVIEW system. From this table it is determined to which locations the hot-wire should move. After each individual hot-wire measurement the new hot-wire location,  $x_n, y_n$  and  $z_n$  is read from the table. The distance by which the  $x, y$  and  $z$  traverse should move, denoted by  $\Delta x$ ,  $\Delta y$  and  $\Delta z$ , are then calculated from the previous hot-wire location;  $x_{n-1}, y_{n-1}$  and  $z_{n-1}$ . The distance by which the  $y$ -traverse should move is then checked with two possible methods which can be used separately or in parallel. The first method uses the laser system and the second method uses a velocity threshold. When the laser system method is activated there are two possible options. The direct laser method is sketched in Figure 22. The first step in this method is to measure the distance from the laser to the wall surface of the flat plate, denoted by  $d_{ref}$ . At this location the wall is determined, i.e.  $y=0$ , by bringing the hot-wire as close as possible to the wall judged by eye. Next the hot-wire scan starts at location 1 and a hot-wire measurement is carried out. Then a new entry,  $x_2, y_2$  and  $z_2$ , is read from the table and the traverse moves in the  $x$  and  $z$  direction. After this, a new laser measurement is carried out to measure the distance from the laser to the surface of the flat plate, denoted by  $d_1$ . In the current example, the flat plate has an inclination such that  $d_1 \neq d_{ref}$ . Finally, the hot-wire is moved in

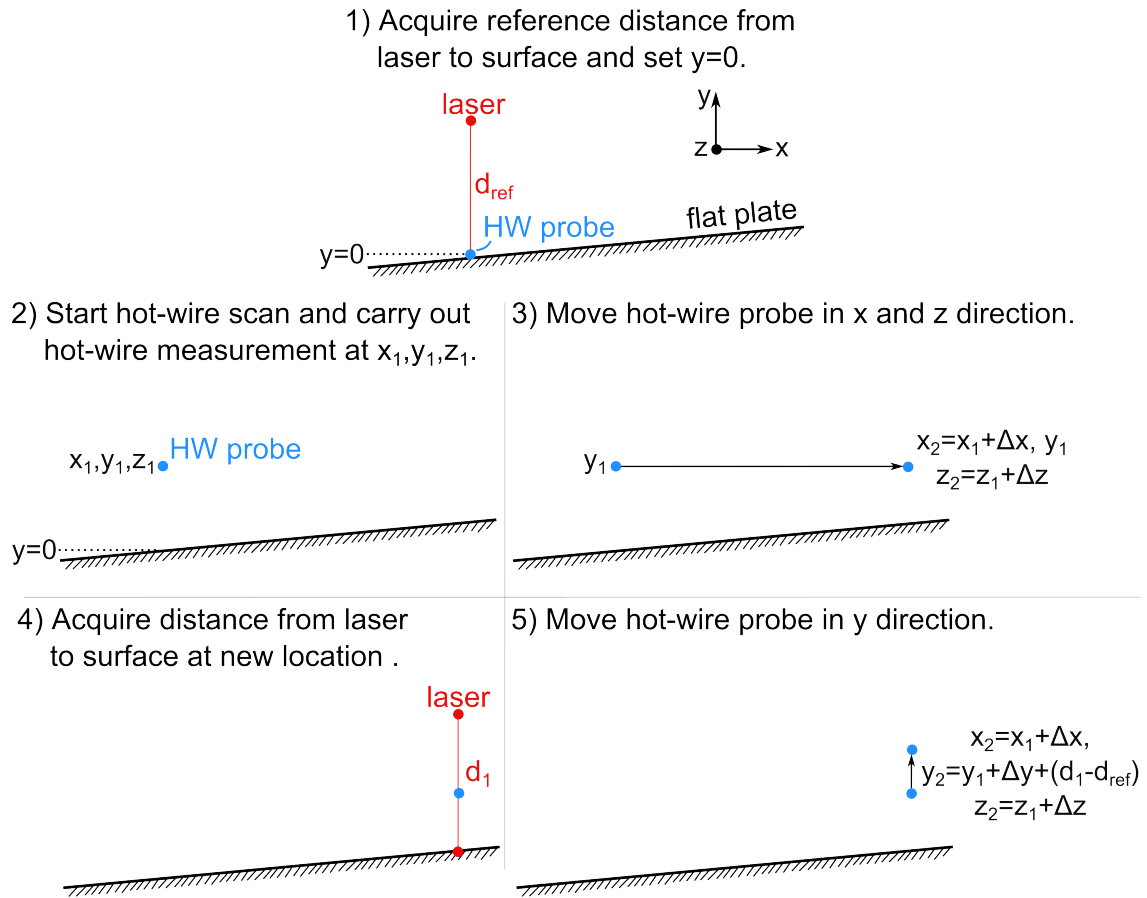


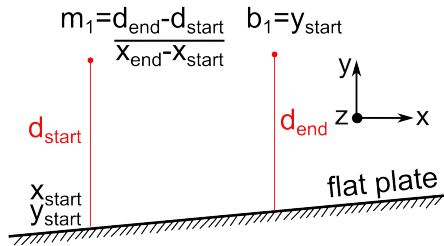
**Figure 22.** Steps taken in the direct laser method to avoid the hot-wire probe getting in contact with the flat plate wall.

the y-direction according to the difference between  $d_{ref}$  and  $d_1$  and  $\delta y$  obtained from the table entries. With the direct laser method a laser measurement is carried out for each measurement point.

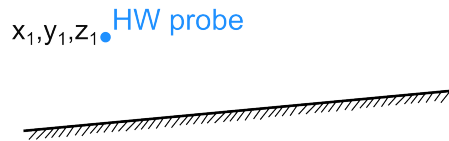
For the interpolation method, presented in Figure 23 for a two-dimensional case, it is assumed that the flat plate has a small inclination in the x and z direction which can be described with two lines,  $y = m_1(x - x_{start}) + b_1$  and  $y = m_2(z - z_{start}) + b_2$ . To find the coefficients  $m_1, m_2, b_1$  and  $b_2$ , the distance from the laser to the surface of the wall is measured at the edges of the measurement region. For example if a hot-wire scan is carried out over a surface spanning from  $x=0$  to 100mm and  $z=0$  to 20mm, laser measurements are carried out at  $x_{start}, z_{start}=(0,0)$ ,  $x_{end}, z_{start}=(100,0)$   $x_{start}, z_{end}=(0,20)$  prior to the hot-wire scan. During the hot-wire scan the location to the wall is determined with these equations for each measurement point and the hot-wire probe is moved accordingly in the wall-normal location.

The laser positioning system should have an accuracy of  $0.5\mu\text{m}$  however during the

1) Acquire distances from the laser to the surface of the flat plate.



2) Start hot-wire scan and carry out hot-wire measurement at  $x_1, y_1, z_1$ .



3) Move hot-wire probe in x, y and z direction.

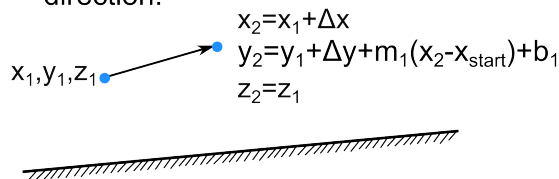


**Figure 23.** Steps taken in the direct laser method to avoid the hot-wire probe getting in contact with the flat plate wall.

experiments it was observed that this decreased to around  $50\mu\text{m}$  due to electronic noise. To achieve an accuracy of  $0.5\mu\text{m}$ , the laser signal should be acquired for a longer sampling time. In the direct method the laser measurement is carried out for each measurement point and therefore longer sampling times can lead to a significant increase of measuring time, considering that a hot-wire scan can consist of 10000 individual measurements. For the interpolation method the sampling time can be easily increased since only 3 points are measured for each scan. The interpolation method was developed at the end of the project and therefore the experiments described in 4 use the direct method while the experiments described in 5 use the interpolation method.

The other method implemented in LabVIEW to avoid the wall is with a velocity threshold which can be used in parallel with the laser methods described above. For the velocity threshold method there are again two possibilities. For the direct method the threshold is set as an absolute velocity. In the other method a percentage of the edge velocity is chosen as threshold. The edge velocity is set each time the traverse moves in x or z to a new boundary layer. When the hot-wire probe measures a value below these thresholds it will not move and  $\Delta y = 0$  while if it is above the threshold  $\Delta y$  is as given i.e.  $\Delta y = y_n - y_{n-1}$ .

## 2.6. Freestream velocity and temperature measurement

The freestream velocity,  $U_\infty$ , is measured with a static Pitot tube placed ahead of the experimental model, as shown in Figure 24. The pressure transducer (SETRA 239), connected to the Pitot tube, measures the difference between the total pressure  $P_\infty$  and static pressure  $P_{s,\infty}$  with an accuracy of 0.1Pa.

Since  $P_\infty = P_{s,\infty} + P_{d,\infty}$  where  $P_{d,\infty}$  is the dynamic pressure the velocity  $U_\infty$  is calculated with:

$$U_\infty = \sqrt{\frac{2(P_\infty - P_{s,\infty})}{\rho}}. \quad (2.27)$$

The density  $\rho$  is determined with the ideal gas law:

$$\rho = \frac{P}{RT}. \quad (2.28)$$

The barometric pressure  $P$  is measured with a barometric pressure sensor (SETRA 270).

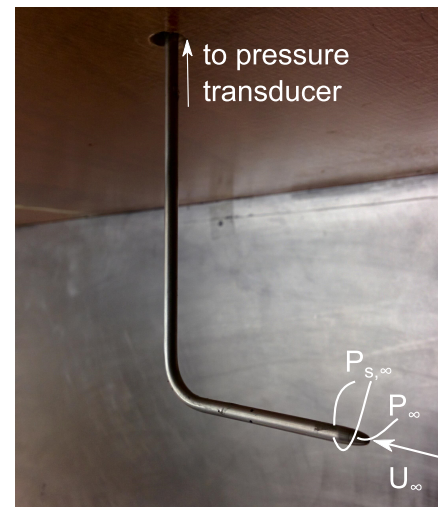


Figure 24. Pitot tube parameters.

The wind-tunnel speed is controlled from LabVIEW through serial communication between the wind-tunnel motor and computer. The input to the wind-tunnel motor is the number of revolutions per minute (rpm). To relate the rpm to an approximate wind tunnel speed, a calibration was carried out, by varying the rpm and getting the velocity from the Pitot tube. In the experiment changing the wind-tunnel speed consisted of the following steps:

- A wind tunnel speed (m/s) was chosen in LabVIEW.
- The velocity was converted to rpm with the calibration.
- After the wind tunnel speed was constant it was measured with the Pitot tube and the error between the set velocity and measured velocity was determined.
- If the velocity was not within the set error bound the rpm of the wind tunnel motor was changed by an amount which scales with the error.
- When the velocity was within the error bounds the velocity adjustment is stopped.

The temperature was measured at each measurement location with a temperature sensor placed inside the test section at the bottom of the tunnel with an accuracy

of  $0.1^\circ$ . Another temperature sensor was placed at the top of the tunnel to monitor any temperature gradient between the top and bottom of the tunnel.

## 2.7. Static pressure measurement

The pressure distribution on the plate was measured with two methods. With the first method, the pressure was obtained from the static pressure ports ( $d=0.5\text{mm}$ ) embedded in the plate at three spanwise locations (Figure 25). The location of the pressure ports was predetermined since an existing set-up was used.

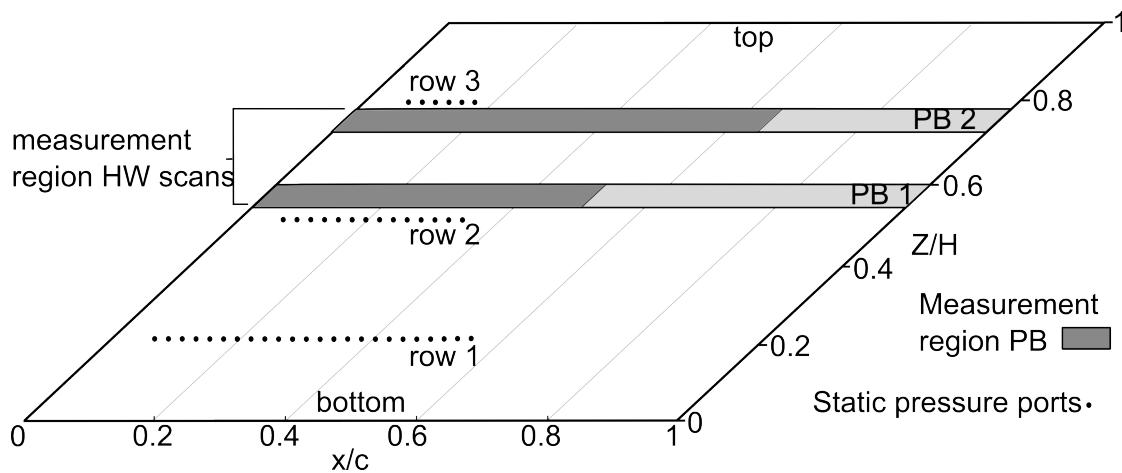


**Figure 25.** Location of static pressure ports and the pressure belt (PB) on the plate.

Secondly, a pressure belt, as described in [Eppink \(2014\)](#), was manufactured to obtain measurements more closely to the leading edge and at a chosen spanwise location. The pressure belt consisted of 30 silicon tubes which were held together by custom designed 3D printed slotting mechanisms. The tubes had an inner diameter of 1mm and outer diameter of 2mm. From previous investigations it is known that diameter of the tube does not change the pressure distribution ([Rivers et al., 2001](#)) when the pressure belt is wrapped around a large part of the plate. 3D printed sleeves with a 0.5mm hole on top served as static pressure ports. The pressure belt was wrapped around the leading and trailing edge of the flat plate. In [Figure 26](#) the pressure belt installed on the flat plate is shown. In order to measure the spanwise uniformity in the measurement region of the hot-wire scans the pressure belt measurements were taken at two spanwise locations. The first pressure port was located at 11mm from the leading edge which corresponds to 0.007% chord. The next 10 pressure ports are placed as closely as possible to each other to resolve the leading edge region with maximum resolution. After that the ports are distributed such that the last port is around 50% and 65% chord for the pressure belt on the top and bottom

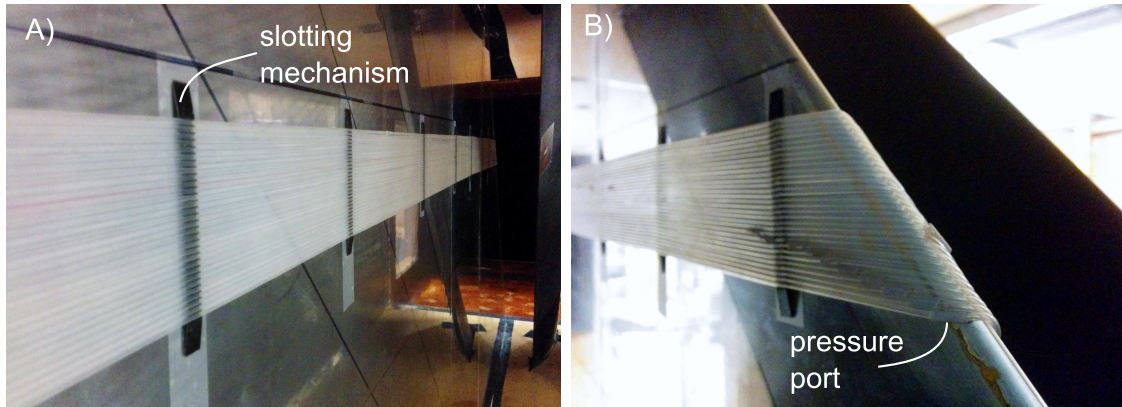


**Figure 26. Pressure belt installed on the flat plate.** A) View from the middle of the flat plate. B) View from the leading edge of the plate.

part of the plate respectively. The pressure ports from both methods measure the static pressure,  $P_s$ . With the static pressure from the Pitot tube,  $P_{s,\infty}$  the pressure coefficient is calculated.

$$C_p = \frac{P_s - P_{s,\infty}}{\frac{1}{2}\rho U_\infty^2} \quad (2.29)$$

The pressure difference  $P_s - P_{s,\infty}$  is measured with a differential pressure transducer (Furness Control 560). The pressure coefficient  $C_p$  corresponds to  $C_{p,3D}$  defined earlier in this chapter.

## 2.8. LabVIEW system

The control of the windtunnel speed and the traverse system together with all data acquisition is carried out in one integrated custom made user interface in LabVIEW (National Instruments). In Appendix C an overview of the user interface is shown and a more detailed description of the system's architecture is described. There were specific parts to start a hot-wire scan, change the wind-tunnel speed or manually move the traverse. The LabVIEW system made it possible to carry out hot-wire scans which could take several days without being interrupted. This time efficient system allowed to obtain large amounts of data which were necessary for the current investigation.



**3**

**Baseline  
measurements**

### 3.1. Freestream disturbance measurements

The overall disturbance level of the wind tunnel was assessed by taking single hot-wire measurements in an empty wind tunnel. In Figure 1, the measurement locations

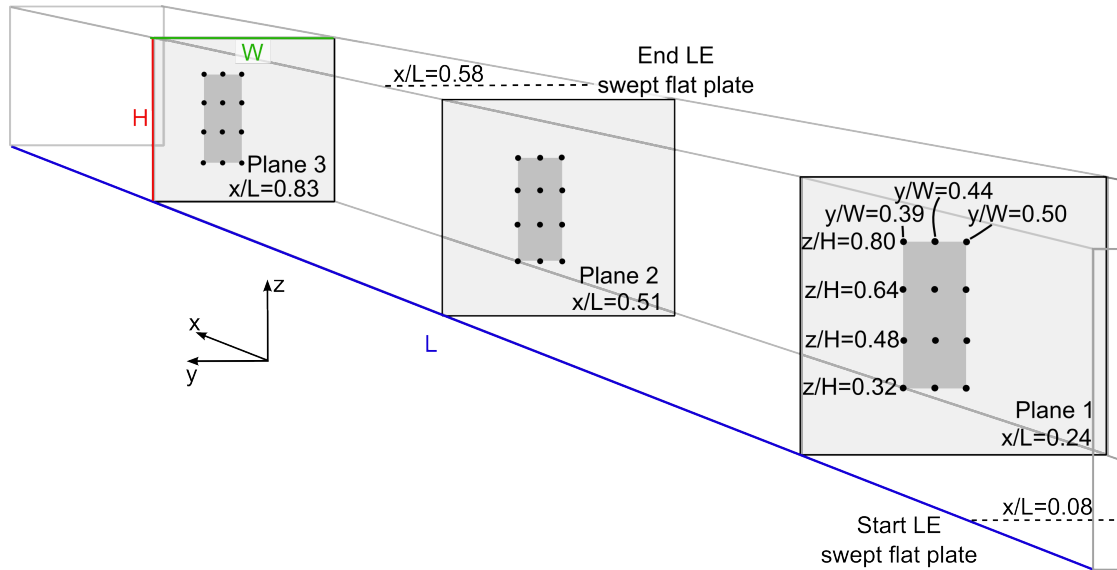


**Figure 1.** Measurement locations (black dots) at which the freestream disturbance level is assessed.

are shown. At each location the disturbance level was measured for freestream velocities from 10 to 18m/s. Long samples of 60s with a sampling frequency of 20kHz, were taken and filtered with the analogue filter between 0.002 and 10kHz. The signal was amplified with the analogue filter such that the signal spanned the full -5 to 5V range. Ideally, the fluctuations in all three directions should be measured (Hunt, 2012), however the experimental set-up in place did not support such measurements.

i2.4.4. The disturbance level is calculated as:

$$Tu = \frac{u'_{rms}}{U_{\infty}}, \quad (3.1)$$

where  $U_{\infty}$  is the velocity measured with the Pitot tube and  $u'_{rms}$  is calculated with Equation 2.19. The fluctuations measured by the hot-wire are caused by the flow through turbulent fluctuations and acoustic noise, as well as, by electronic noise. The turbulent fluctuations have a three-dimensional nature while the acoustic fluctuations are two-dimensional. By correlating two hot-wire signals the two types of fluctuations can be separated as performed by Hunt (2012) amongst others. In this early stage of the project these measurements were not carried out, however, in Placidi et al. (2017) the measurements can be found for the Gaster wind tunnel when

the model is placed inside the test section. In order to distinguish between the flow fluctuations, turbulent and acoustic, and electronic noise, the disturbance levels were measured with the motors, controlling the traverse axis and wind tunnel, switched off. In Figure 2 the results of these tests show that the motor controlling the z-axis created considerable high frequency noise. The amplitude of the peaks around 50 and 150Hz are not affected by the motors and are due to the mains electricity<sup>1</sup>. It

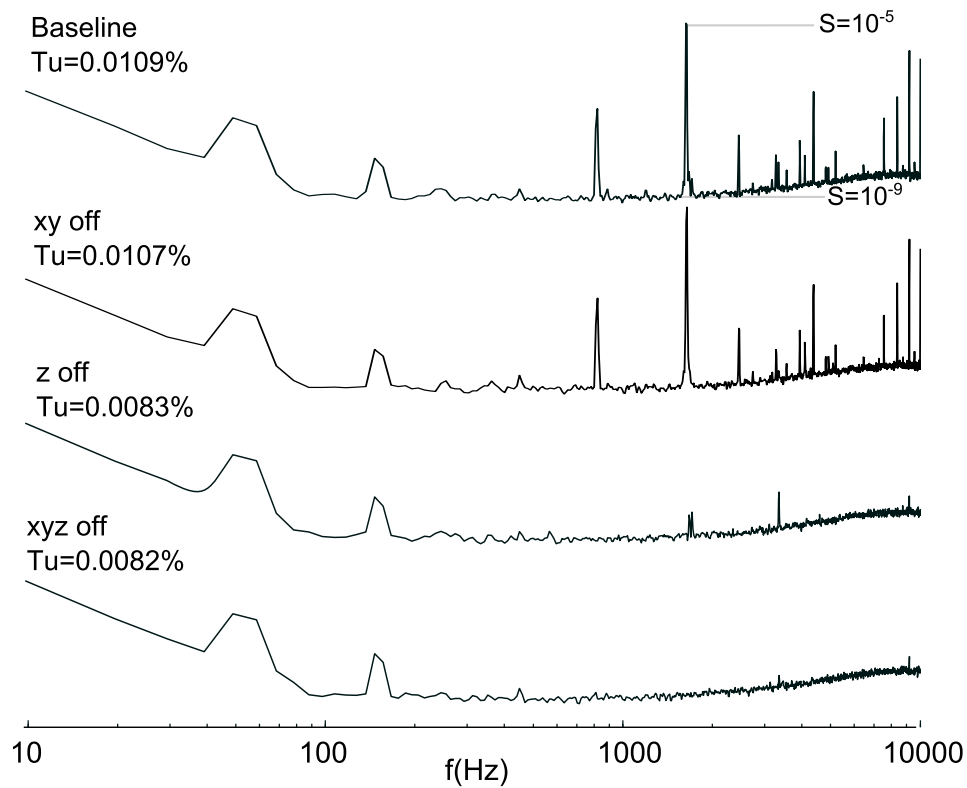


**Figure 2.** Power spectra with the motors, powering the traverse system, turned on and off ( $U_\infty=16\text{m/s}$ ,  $\Delta f=10\text{Hz}$ ).

was chosen to report the disturbance levels with the electronic noise included, however, it was estimated that the electronic noise accounts for around 20-30% of the disturbance levels reported hereafter. The results of all freestream disturbance measurements are tabulated in Appendix D. The measured freestream disturbance levels are below 0.02% for all measurement locations. The results show that the disturbance level decreases with increasing freestream velocity. In Hunt (2012) extensive flow-quality measurements show that the streamwise disturbance levels increase with the freestream velocity. This was attributed to an increase in low frequency acoustic noise at higher velocities. In Figure 3 it is shown that the fluctuations in the flow increase proportional to the freestream velocity in the entire power spectrum, while

<sup>1</sup><http://www.worldstandards.eu/electricity/plug-voltage-by-country/>

the magnitude of the electronic noise stays constant. When the noise was removed manually in the post-processing stage for this set of measurements, the resulting disturbance levels stayed approximately constant with increasing freestream velocity. Next, the disturbance level was measured with the experimental model inside

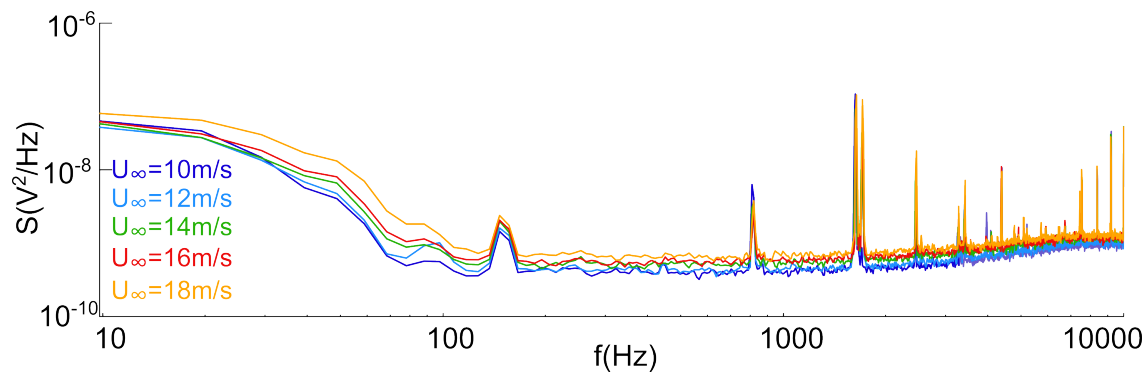


**Figure 3.** Power spectra for different freestream velocities ( $\Delta f=10\text{Hz}$ ).

the wind tunnel. In Figure 4 the power spectra in an empty tunnel are compared to the spectra with the model inside the wind tunnel. The frequency resolution in these spectra is set to 1Hz, to clearly show differences in specific frequency bands. The energy in the low frequency band (1-100Hz) increases when the model is placed

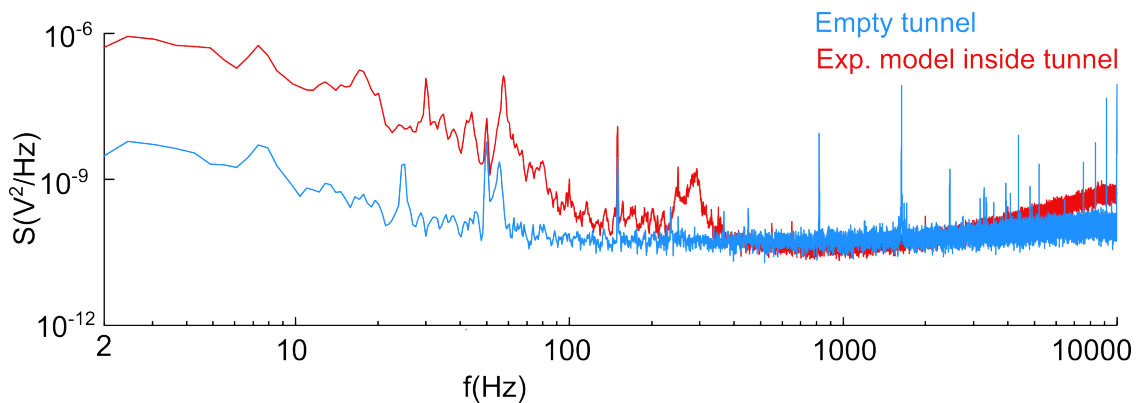


**Figure 4.** Power spectra for the empty wind tunnel compared to when the experimental model is placed inside the wind tunnel ( $\Delta f=1\text{Hz}$ ).

inside the wind tunnel. The nature of these low-frequency travelling waves in the present experimental set-up were investigated by [Placidi et al. \(2017\)](#). By correlating two hot-wire signals they separate the vortical and acoustic freestream fluctuations. They found that the energy in the low frequency band is mostly related to acoustic noise and vibrations of the hot-wire probe. Due to the blockage by the displacement bodies the unsteadiness in the flow increases, leading to increased acoustic noise and vibrations compared to the empty tunnel.

Next to the increase of energy in the low-frequency band, it is shown in Figure 4 that the high frequency noise caused by the z motor disappeared. This is believed to be due to several improvements made on the entire experimental set-up. For example, the voltage supply for the hot-wire anemometer was separated from the voltage supply of the motors. Furthermore, the motors were placed inside a box and placed further away from the hot-wire anemometer. Throughout all experimental sessions presented in this thesis the high frequency noise, such as shown in Figure 2, was not observed.

To assess the uniformity of the disturbance environment along the leading edge, several hot-wire scans were carried out for velocities of 16 and 18m/s. For 500 individual measurement parallel to the leading edge from  $Z/H=0.53$  to  $Z/H=0.75$ , the variation in disturbance levels was 0.001%, ensuring a uniform incoming disturbance field. Throughout all experimental runs the freestream disturbance level was measured at one point in front of the leading edge after each calibration of the hot-wire. The freestream disturbance level varied between 0.0214-0.0255% for all tests, ran over a time period of two years. Other stationary crossflow receptivity studies quote freestream disturbance levels of 0.08% (Deyhle and Bippes, 1996), below 0.05% (Hunt and Saric, 2011) and approximately 0.05% (Eppink, 2014). This shows that even though disturbance levels increased by a factor of about 2.5 when the model was placed inside the tunnel, the levels can still be considered low and well below the limit where travelling crossflow instabilities dominate the flow (Deyhle and Bippes, 1996; Downs, 2012; Schrader et al., 2009).

## 3.2. Static pressure distribution

The static pressure was measured with the static-pressure ports and pressure belt, as described in Section 2.7. The top and the bottom pressure belts refer to the larger and smaller  $z/H$  location as defined in Figure 25 in Chapter 2. The test side of the plate is the side where the static-pressure ports are placed and the hot-wire measurements are carried out. The uncertainty in the static pressure measurements is determined in Appendix E. It is shown that the  $C_p$  has an error of about 1%.

First, the pressure distributions of the two methods were compared for both spanwise locations, as presented in Figure 5, while the spanwise uniformity is discussed later in this section. The row of static-pressure ports closest to the respective pres-

sure belt are shown here, i.e. for PB1 and PB2, row 2 and 3 in Figure 25 in Chapter 2 respectively. The spanwise location of the pressure belt is defined at the middle of the pressure belt. The pressure distribution is very similar for both methods, at

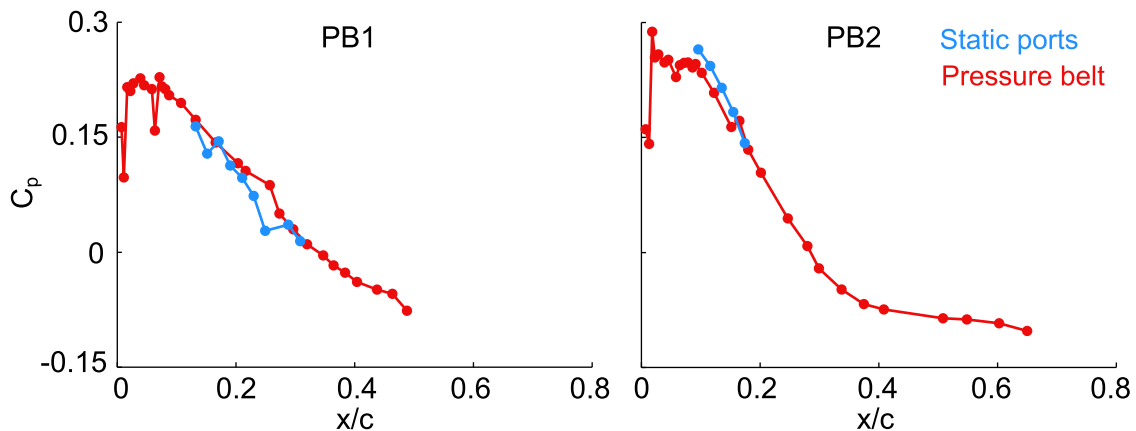


**Figure 5.** Comparison of the pressure distribution taken with the static-pressure ports and pressure belt.

both spanwise locations. For  $x/c < 0.15$ , there are no static pressure measurements to compare to. In this region the effect of the presence of the pressure belt is expected to be largest due to the thin boundary layer. Later in this section the behaviour of the pressure distribution close to the leading edge will be discussed in more detail. From Figure 5 it is concluded that outside the leading-edge region the presence of the pressure belt does not influence the results significantly, and that the pressure-belt measurements are representative for the actual pressure distribution on the plate.

In previous investigations the experimental model was designed such that a spanwise uniform flow was achieved and the infinite swept condition was met (Deyhle and Bippes, 1996; Reibert et al., 1996; White and Saric, 2005). Meeting this condition is especially important when comparing experiments with computations, since in the latter a uniform pressure distribution is prescribed in the spanwise direction. The variation of the pressure distribution in the spanwise direction of the flat plate in the current experiment is shown in Figure 6 for two different flap angles. It is observed that the flow is not spanwise uniform. The different pressure gradients in the spanwise direction, might lead to a variation of the stability characteristics along the span. To obtain a measure of this variation, the pressure distributions at  $\alpha_f = 20^\circ$  were smoothed and used as an input for the linear stability analysis, where the N-factor curves for the stationary crossflow and Tollmien-Schlichting waves were obtained. The results of the linear stability analysis depend on the effective sweep angle which is determined from the pressure at the attachment line. The shape of the

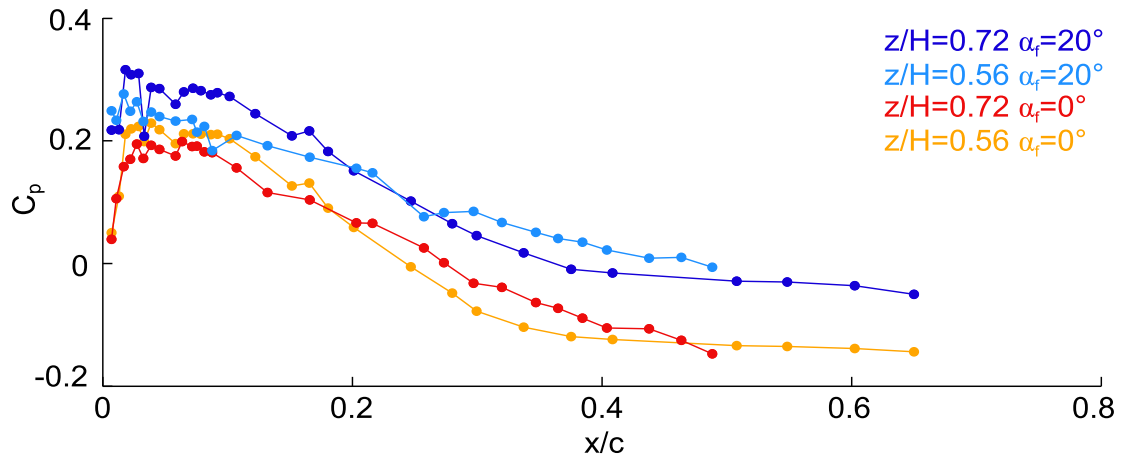


**Figure 6.** Comparison of the pressure distribution taken at different spanwise locations.

pressure distribution close to the attachment line is obtained from the DLR-TAU computations as shown in Figures 10 and 12.

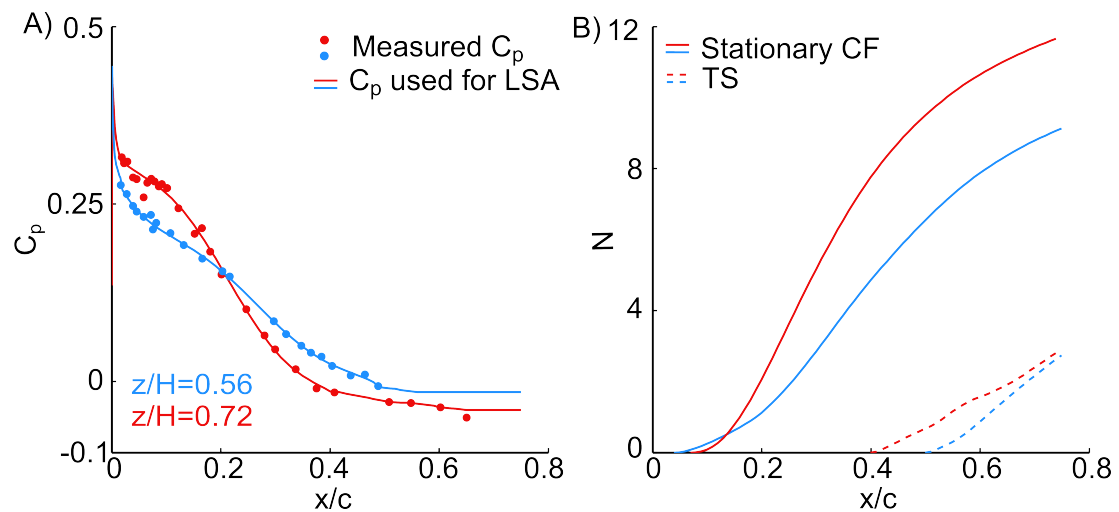


**Figure 7.** A) Measured pressure distribution together with the pressure distribution used for the linear stability analysis. B) Results of the linear stability analysis.

The linear stability analysis results show that the stronger favourable pressure gradient, at  $z/H=0.72$ , generates stronger growth of the stationary crossflow waves as presented in Figure 7. The Tollmien-Schlichting waves start to grow slightly earlier at  $z/H=0.72$ . The wavelength, of the most unstable stationary crossflow wave, are in range of 8-13mm and 10-14mm for  $z/H=0.56$  and  $z/H=0.72$  respectively. Furthermore, the neutral stability point is found to be at  $x/c=0.05$  at  $z/H=0.56$  and at  $x/c=0.07$  for  $z/H=0.72$ . These aspects are important for the excitation of the primary instability as will be discussed in more detail in Chapter 4. From the pressure distributions at the two spanwise locations, it is concluded that in the current experiment it will not be possible to obtain a fully spanwise uniform flow. Howe-

ver, the largest spanwise region measured in the experiments is 80mm while the distance between the middle of PB1 and PB2 is 146mm. This means that in the measurements the variation of the pressure distribution in the spanwise direction will be at most half of the variation shown in Figure 6. When comparing the experimental results to computations the nonuniformity in the spanwise direction is not ideal since a spanwise varying pressure distribution has to be modelled in the computation. Furthermore, due to the spanwise variation in the growth of the cross-flow instabilities, the  $x/c$  location where transition occurs will vary along the span. Since the detailed pressure measurements were carried out in a later stage of the project it was chosen to not optimize the experimental set-up further and to carry on with the small spanwise variation in the pressure distribution. When the pressure distribution characteristics are compared to pressure distributions on current aeroplane wings the spanwise varying pressure distribution might be more realistic. An aeroplane wing is connected to the fuselage at the wing base and has a free end at the wing tip, this leads to a spanwise variation in the pressure distribution such that the infinite swept condition is not met. It should be noted that recently the possibilities of infinite swept wings in flight are being investigated (Tufts et al., 2014) which suggests that on future aeroplanes with a spanwise uniform pressure distributions might become the standard.

The influence of the flap angle, as defined in Figure 8, on the pressure distribution is shown in Figure 9.

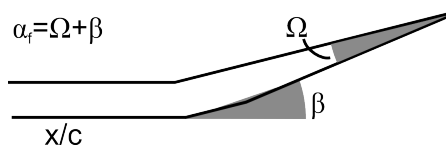


**Figure 8.** Definition of the flap angle,  $\alpha_f$

Even though, the flap has length of only 7% chord, it changes the pressure distribution over the flat plate significantly. The increase in pressure with increasing flap angle is expected. The flap angle gives the flat plate a small negative angle of attach which creates a high and low pressure region, at the test side and non-test side

respectively. The main purpose of varying the flap angle is to ensure that the attachment line is at the top of the plate. In Figure 10 the pressure distribution in the leading edge region is shown after the pressure belt is at the upper part of the plate (PB2). For two flap angles nine pressure ports were placed at the non-test side of the plate. The resolution of the measurements is not high enough to define the location of the attachment line and to obtain the stagnation pressure. However, for a flap angle of zero degrees the pressure distribution is almost symmetric around the leading edge, indicating that the attachment line is close to  $x/c=0$ . The results of

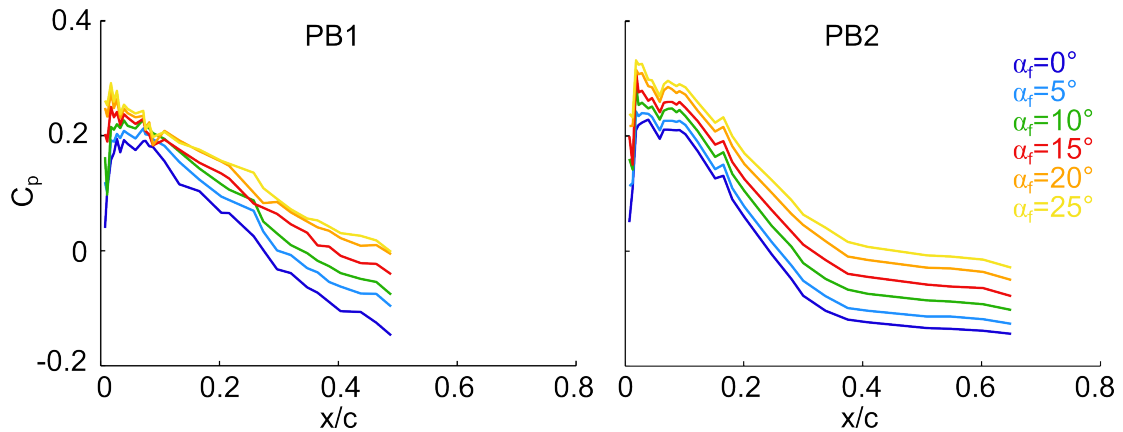


**Figure 9.** Pressure distributions of both pressure belts for different flap angles.

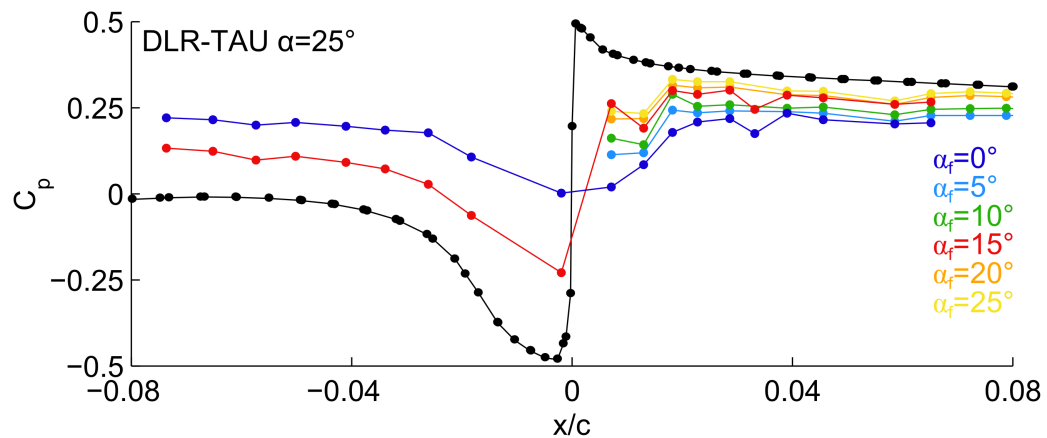


**Figure 10.** Pressure-belt measurements close to the leading edge at the non-test side (negative  $x/c$ ) and test side (positive  $x/c$ ) for different flap angles.

the DLR-TAU computations, which are discussed later in this section, show that for  $\alpha_f=25^\circ$  the attachment line is at the test side of the plate creating the suction peak at the non-test side. For  $\alpha_f=15^\circ$  a similar behaviour is observed. From the suction peak at the non-test side of the plate for  $\alpha_f=15^\circ$  it is expected that the attachment line is at the test side of the plate. This hypothesis was confirmed by listening to the flow on the plate with a stethoscope. Turbulent flow was observed at small flap angles while for higher angles the flow was laminar for a large part of the plate.

The sensitivity of the flap angle on the pressure distribution was only measured in one of the final experimental runs, when the pressure belt was manufactured. Therefore, the experiments described in Chapter 4 and Chapter 5 have slightly different pressure distributions. In Figure 11 the pressure distributions obtained from the static-pressure ports for the different tests are shown at the three spanwise locations. In the measurement region at the top part of the plate the distributions are

almost identical. The pressure distributions correspond to a flap angle of approximately 15-20 degrees in the set-up where the pressure belt was used. For this flap angle the attachment line is on top of the plate as was also confirmed with stethoscope measurements taken during each experimental session.

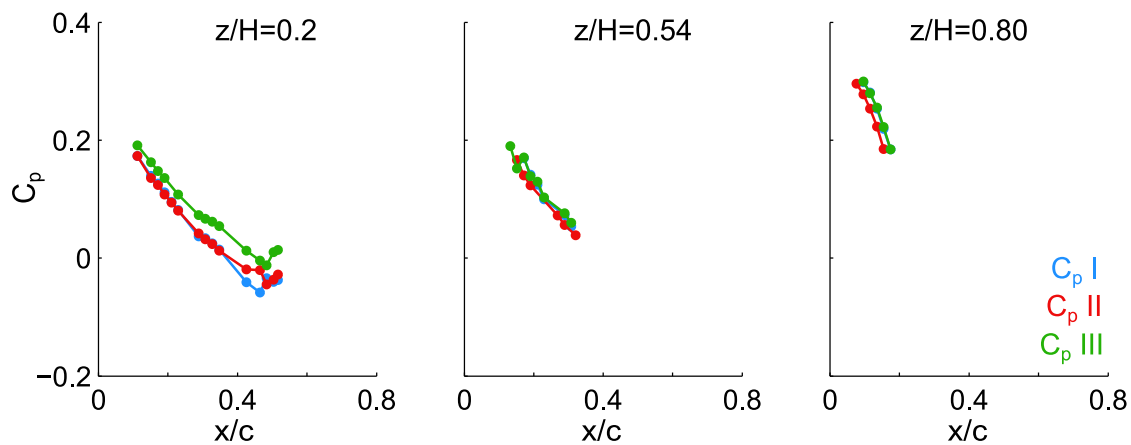


**Figure 11.** Static pressure distributions measured for the different experimental sessions.

Next, the obtained pressure distributions for  $\alpha_f = 25^\circ$  were compared with the two-dimensional inviscid panel code (Chapter 2) and the full three-dimensional viscid turbulent flow solver TAU (Appendix A). The corresponding pressure distributions are shown in Figure 12. The 2D pressure coefficient from the panel code is converted to the three-dimensional equivalent with the effective sweep angle from DLR-TAU at the middle of the plate. The magnitude of the pressure coefficients obtained from the panel code are significantly higher than the pressure coefficients obtained in the experiment. This can be attributed to the two main differences between the computation and experiment. Firstly, the panel code calculations are inviscid while in the experiment the flow is viscous. The growing boundary layers on the plate, displacement body and tunnel walls will change the effective shape of the bodies leading to a different pressure distribution. Furthermore, flow separation on the flap, which is not modelled in the inviscid panel code, makes the flap less effective leading to a more accelerated flow and consequently a lower pressure in the experiment. Secondly, the panel code is two-dimensional while in the experiment three-dimensional effects lead to a variation in the the pressure distribution in the spanwise direction as shown in Figure 6.

Figure 12 shows that the pressure distribution obtained from the DLR-TAU computations still gives slightly higher pressure coefficients compared to the experiment, even though three-dimensional effects and viscous effects are taken into account in these computations. The pressure gradient is very similar between both pressure

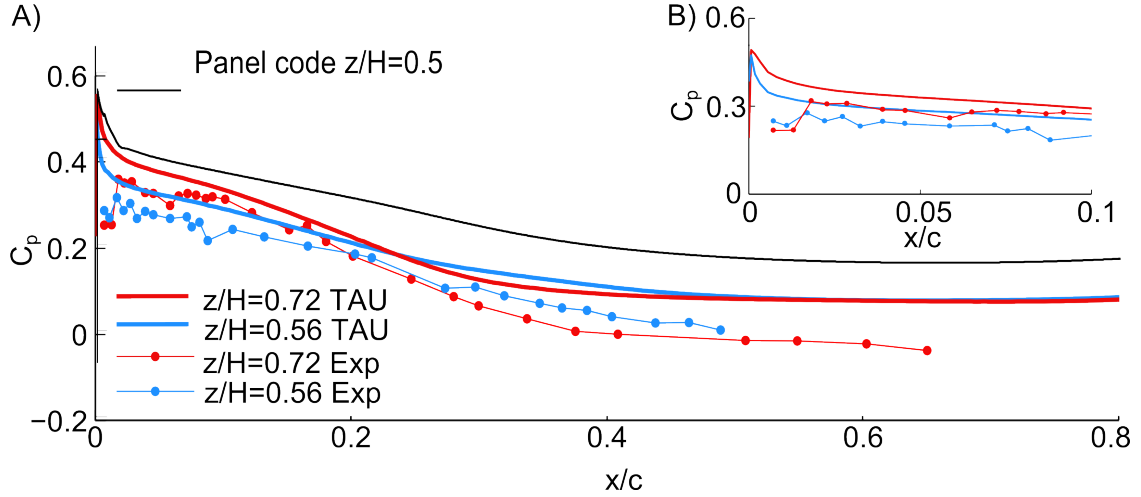


**Figure 12.** Comparison between the pressure distribution obtained from the experiment, panel code and DLR-TAU code.

distributions, as well as the streamwise location where the pressure distributions of  $z/H=0.72$  and  $z/H=0.56$  cross each other. The main cause for the different in magnitudes is expected to be the different freestream conditions as discussed in Appendix A. The correction applied to the original data from the DLR-TAU code might have a slightly different  $U_{Pitot}/U_\infty$  ratio leading to different corrected pressure coefficients. Small differences in magnitude between the computations and experiment can also be caused by a slightly different flap angle and flap-angle geometry, as well as differences in the location and orientation of the displacement bodies. Furthermore, in the computation, the flow is considered to be completely turbulent, while in the experiment the flow is laminar. A turbulent flow will adhere to the surface longer and result in a smaller region of separation. Even though trip wires are placed on the non-test side of the plate and at both displacement bodies, the separated region in the experiment might be considerably larger. Large separation at the flap will lead to a smaller effective flap angle and a more accelerated flow and consequently a lower pressure coefficient. Considering all these small differences and uncertainties, it is thought that the pressure distribution of the experiment and DLR-TAU computation compare quite well. The pressure coefficients in the leading edge region, presented in Figure 12B, show that the pressure-belt measurements do not capture the behaviour in proximity of the stagnation point correctly, as also concluded from Figure 10. Therefore, it was chosen to estimate the effective sweep angles in the experiment from the computational results. From the attachment line pressure of

the DLR-TAU results the effective sweep angle is calculated with:

$$\Lambda_{eff} = \cos^{-1} \left( \sqrt{C_{p,AL}} \right), \quad (3.2)$$

which gives  $\Lambda_{eff}=46.5^\circ$  and  $\Lambda_{eff}=45.3^\circ$  for  $z/H=0.56$  and  $z/H=0.72$  respectively. Since the shape of the pressure distribution is similar for the computation and experiment outside the leading edge region, it is assumed that this is also the case in the leading edge region. This gives estimated effective sweep angles in the experiment of  $\Lambda_{eff}=48.84^\circ$  and  $\Lambda_{eff}=47.65^\circ$  for  $z/H=0.56$  and  $z/H=0.72$  respectively. The values are reasonably close to the geometrical sweep angle for 45 degrees. The stability characteristics obtained from the pressure distribution at the bottom part of the plate for  $\alpha_f=25^\circ$ , are compared to the stability characteristics obtained from the computational pressure distributions. Figure 13 shows that the N-factor growth for both the stationary crossflow waves and Tollmien-Schlichting waves is similar for all cases. Table shows the neutral stability point (NSP) and the wavelengths of the amplified stationary crossflow waves  $\lambda_{CF}$  for all three cases. The neutral stability point is at a similar streamwise location for all three cases. Furthermore, stationary crossflow waves with a similar wavelength are amplified.

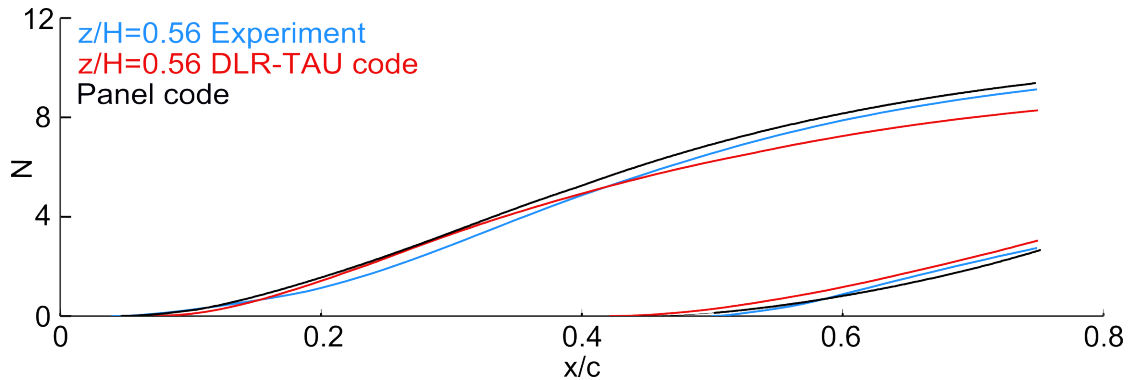


**Figure 13.** N-factor curves for the experimental and computational pressure distributions at the top and bottom of the flat plate.

**Table 3.1.** Stability characteristics obtained from the experimental and computational pressure distributions.

Dataset	NSP	$\lambda_{CF}$ (mm)
$z/H=0.56$ Exp	0.05	7.5-13.25
$z/H=0.56$ TAU	0.07	9.5-13.75
Panel code	0.05	7.5-14

In the current study the panel code was used to predict the pressure distribution

on the swept plate and consequently the characteristics of the amplified stationary crossflow waves. The similarity in the linear stability characteristics between the experiment and the panel code suggest that the panel code is suitable as such design tool, given that the pressure distribution is predicted at a location where three-dimensional effects are small. The similarity between the linear stability characteristics between the DLR-TAU code and experiments indicate that the high resolution pressure distributions from the DLR-TAU code could be used in further computational studies. While it was not in the scope of the current project, the pressure distributions could be used to compute the flow characteristics and compare them with the detailed hot-wire measurements.

### 3.3. Displacement body wake measurements

Hot-wire measurements in the wake of the displacement body were taken to understand the possible interaction between the wake and the boundary layer on the flat plate. The measurements were taken at three chordwise locations at  $z/H=0.73$  as outlined in Figure 14. The chordwise locations span the entire measurement domain of the hot-wire scans carried out in Chapter 4 and Chapter 5. The mean velocity

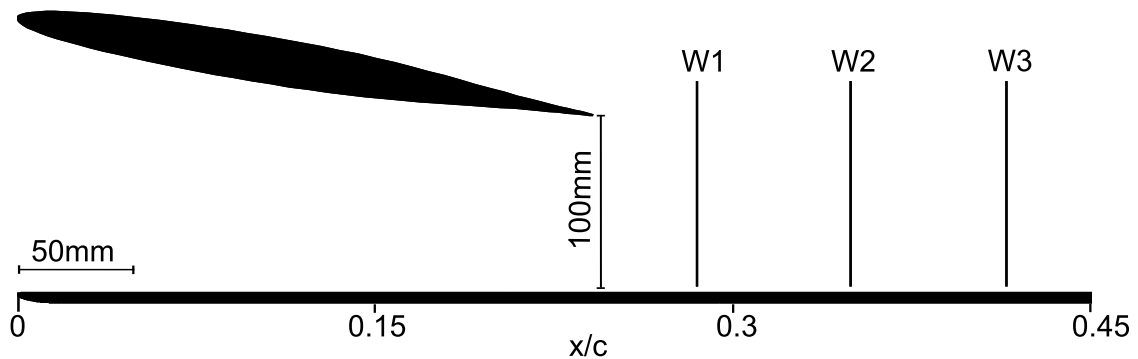


**Figure 14.** Chordwise locations where the hot-wire measurements in the wake of the displacement body were performed.

profiles normalised by the edge velocity of the boundary layer,  $U_e$ , show that the wake is not impinging on the plate (Figure 15). The mean velocity can be considered constant when approaching the boundary layer. The wake thickness increases slightly downstream and the strength, measured by the velocity deficit, decreases. Because the displacement bodies have an angle of attack the asymmetric wake profiles are expected. The broad wake above 100mm indicates that some separation has occurred on the displacement body, as was also predicted by the DLR-TAU code (Appendix A). The streamwise fluctuation profiles, shown in Figure 16, have high

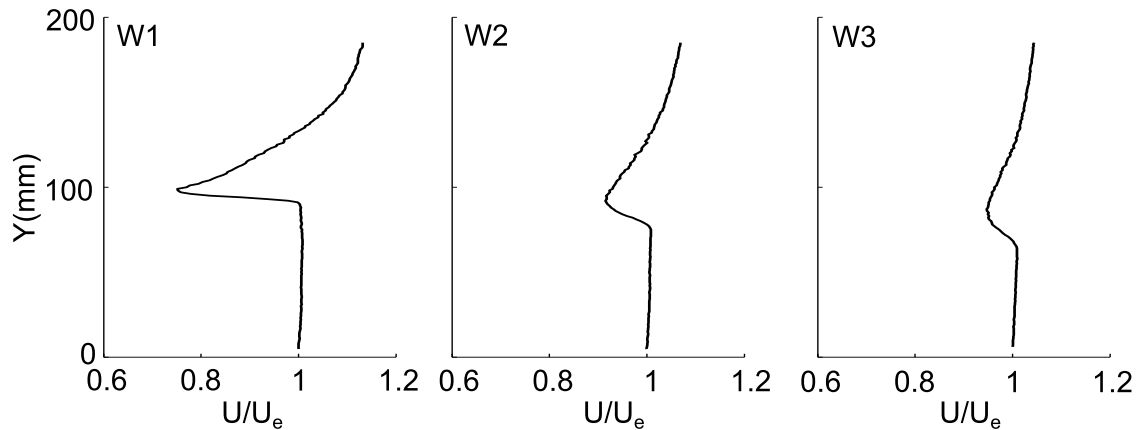


**Figure 15.** Mean velocity profiles inside the wake of the displacement body at three different chordwise locations.

fluctuations in the wake, which indicates that the wake is turbulent. When the boundary layer is approached the fluctuation level becomes constant. To ensure there is

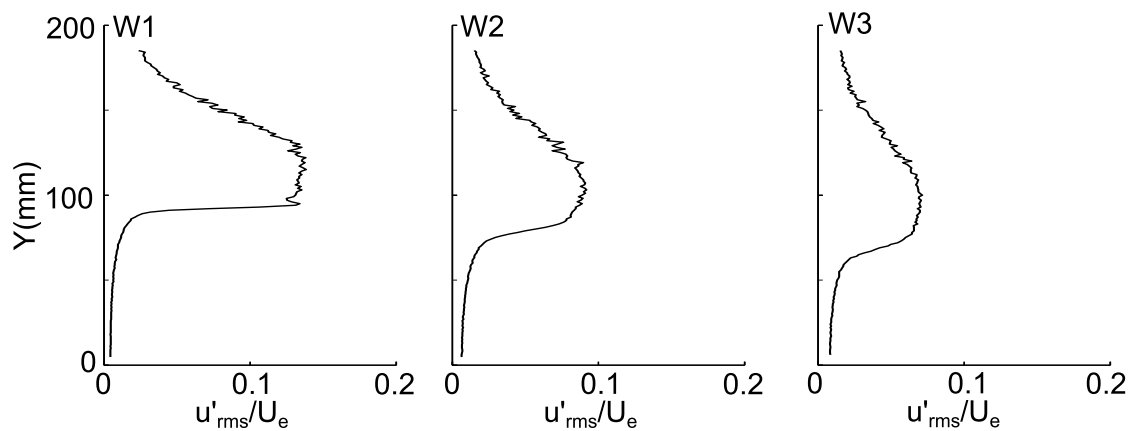


**Figure 16.** Streamwise velocity fluctuations inside the wake of the displacement body at three different chordwise locations.

no interaction between the wake and boundary layer, the power spectra in and outside the wake are considered, as presented in Figure 17. For brevity, only the first measurement location is shown here, since for the other two locations a similar behaviour is observed. Inside the wake the spectra are turbulent. Moving closer to the plate results in a large decrease in energy in the high frequency band indicating that the flow is laminar. From  $Y=20\text{mm}$  to  $Y=5\text{mm}$  the spectra are identical, showing that the fluctuation levels and frequencies inside the freestream are constant when approaching the boundary layer. There are no clear peaks in the power spectra suggesting that there will be no travelling waves from the freestream interacting with the disturbances inside the boundary layer. The freestream disturbance level just above the boundary layer at  $x/c=0.28$  was around 0.4-0.8% while in front of the

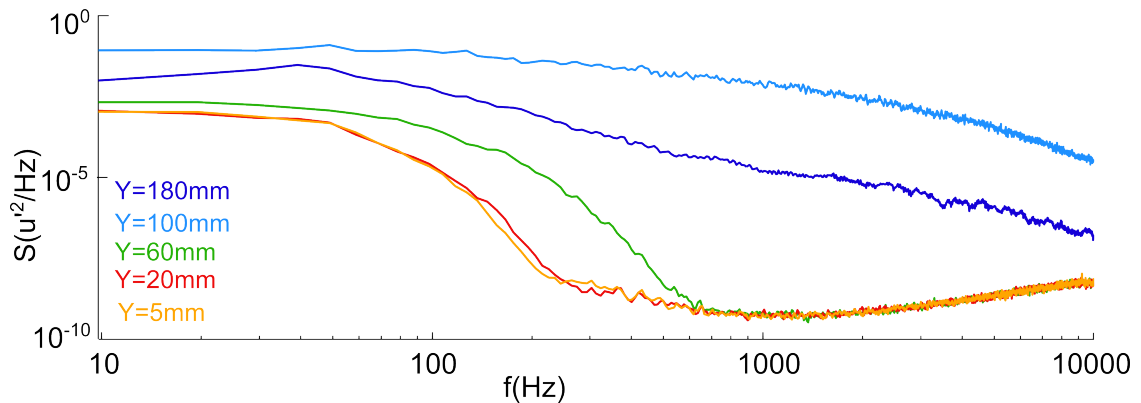


**Figure 17.** Power spectra at different wall-normal locations at  $x/c=0.28$ .

leading edge a value of around 0.02% was measured. This is a large difference and since the freestream disturbance level is expected to change the receptivity process, it is important to understand the origin of this variation. In Figure 18, the power spectra at the edge of the boundary layer at  $x/c=0.28$  and in front of the leading edge measurement location are shown. The high frequency content is identical for both locations, however, the low frequency content increased significantly for the measurement location behind the displacement body. In Section 3.1 it is explained that the low-frequency are caused by acoustic noise and unsteadiness in the flow. The high energy of these low frequency fluctuations might complicate the detection of any waves appearing in the boundary layer with the same frequency. However, from the linear stability analysis it is found that travelling waves with a frequency below 100Hz are not expected (see Chapter 4). For the same reason it is expected that the low frequency energy will not influence the transition process directly. From both the mean and fluctuating velocity measurements it is concluded that there is no interaction of the wake disturbances from the displacement body with the boundary layer on the plate.

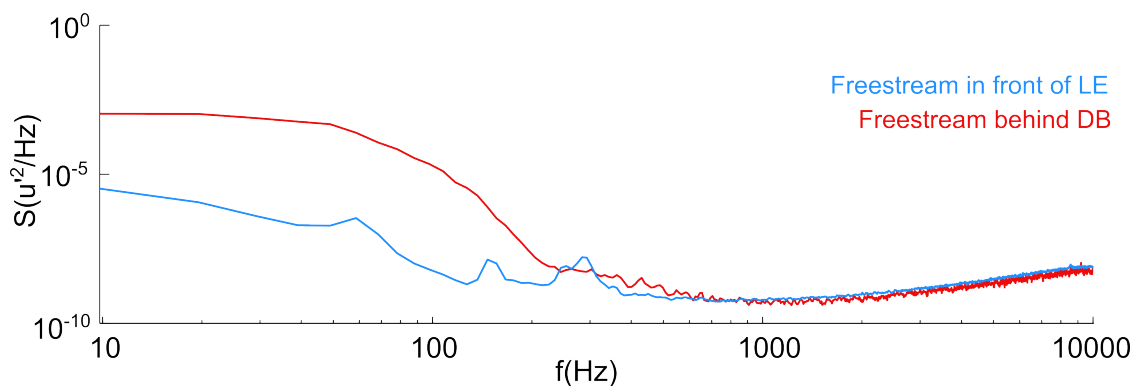


**Figure 18.** Power spectra in front of the leading edge ( $x/c=-0.07$ ) and behind the displacement body ( $x/c=0.285$ ) just outside the boundary layer.

### 3.4. Repeatability

This chapter on the baseline measurements ends with this small section on the repeatability of the results obtained during the thesis. As shown in Figure 25 the plate consists of several parts. Part I,II and III were fixed in the test section, while part IV and V were taken out after each experimental session because the test section had to be taken out such that other members of the research group could do measurements. Because of this there were small changes in the set-up between experimental sessions. Therefore it was not possible to compare the results quantitatively between experiments of different experimental sessions. Qualitatively, the results were similar. The transition location was at a similar location throughout the tests which indicated that the transition process occurred in a similar fashion between experimental sessions. Nevertheless, the results of the experiments in Chapter 4 are taken in one experimental session to not include the uncertainty caused by the change of the test sections. The results of the experiments in Chapter 5 are from two experimental sessions where it is clearly indicated which experimental session corresponds to which results.





**4**

**Forcing of the  
primary crossflow  
instability**

## 4.1. Introduction

The primary crossflow instability manifests itself as both stationary and travelling vortices which grow in space. The forcing of the instabilities is influenced by the environmental disturbances such as roughness, freestream turbulence and sound. In this chapter experiments on the influence of different roughness distributions on the growth of the stationary crossflow instability are described. The chapter starts with a literature review, after which the design of the roughness distributions is explained in Section 4.4. From the experiments large volumes of hot-wire data were obtained. The analysis of this data is explained in Section 4.5. Finally, the results are discussed and conclusions are drawn.

## 4.2. Background

The transition from laminar to turbulent flow follows different paths, depending on the level of environmental disturbances, as explained in Section 1.2. The freestream turbulence measurements presented in Section 3.1 show that in the current study the disturbances will be small, such that the natural transition path (Path E) will be followed. The first step of this transition path is the receptivity process. Here, instability waves are generated from the environmental disturbances, such as roughness or freestream turbulence. In Figure 1 a diagram of the receptivity process is presented. The boundary layer, just downstream of the forcing mechanism acts as a filter,

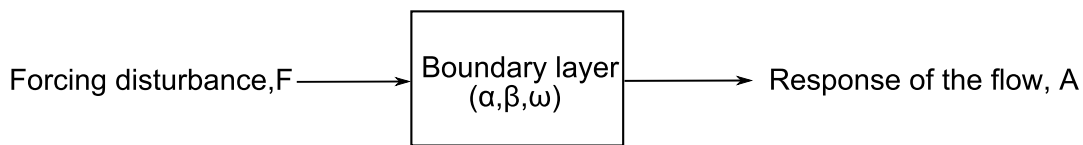


**Figure 1.** Schematic representation of the receptivity process.

where the band-pass wavenumbers and frequencies are represented by the unstable eigenvalues  $\alpha$ ,  $\beta$  and  $\omega$  following from linear stability analysis. From this simple diagram a receptivity coefficient,  $R$ , is defined as:

$$R = \frac{A}{F}. \quad (4.1)$$

The receptivity coefficient will be high, if there is coupling of the disturbances with the flow. On the other hand, the receptivity coefficient will be low, if there is no coupling between the disturbances and the flow. Conceptually, the receptivity coefficient is easy to understand. However, the variables  $A$  and  $F$  can be defined in

several ways, which makes comparison of receptivity studies across literature difficult. Computational and theoretical studies focus on the response of the flow close to the forcing mechanism. In these studies, the forcing  $F$ , is defined as a Fourier representation of the roughness or freestream turbulence, discussed in more detail in the following section. Furthermore,  $A$  is referred to as the receptivity amplitude and often defined as the initial amplitude of an instability, at, or close to, the forcing mechanism. In experimental studies, the response of the flow can often not be measured close to the forcing mechanism, since the instabilities have small length scales and magnitudes. Therefore, these studies focus on the influence of forcing on the flow further downstream. Here the receptivity amplitude is defined as the amplitude of an instability far from the forcing mechanism, or as a transition location. The forcing amplitude,  $F$ , is defined as a roughness height or freestream turbulence level.

Acknowledging, the different perspectives on the receptivity process across literature, in the following a review of both experimental and computational receptivity studies is given. The receptivity of roughness, freestream turbulence and acoustic disturbances on the crossflow instability are discussed consecutively.

#### 4.2.1. Influence of roughness

In computational studies it is found that roughness is the most efficient in exciting the stationary crossflow vortices, compared to other environmental disturbances such as freestream turbulence (Choudhari, 1994; Schrader et al., 2009). The nondimensional roughness height is described with the roughness Reynolds number  $Re_k$ , defined as,

$$Re_k = \frac{\rho k U_k}{\mu}, \quad (4.2)$$

where  $k$  is the roughness height and  $U_k$  the undisturbed streamwise velocity at height  $k$ . Or the roughness is described with a height ratio:

$$\epsilon = k/\delta^*, \quad (4.3)$$

where  $\delta^*$  is the displacement thickness of the undisturbed boundary layer. If the roughness Reynolds number exceeds a critical roughness height,  $Re_{k,crit}$ , the flow transitions quickly into turbulence and the natural transition path (Chapter 1 is not followed. For swept wing flows a critical Reynolds number of around 500-600 has been found (Kurz and Kloker, 2016; Brynjell-Rahkola et al., 2017). Studies on

the receptivity of roughness to the crossflow instability mostly focus on micron-sized cylindrical roughness elements where  $Re_k < 10$ . These roughness elements are placed periodically in the spanwise direction, on the swept wing model (Deyhle and Bippes, 1996; Saric et al., 1998; Radeztsky et al., 1999; Hunt and Saric, 2011). The location where the roughness elements are placed determines the effectiveness of the receptivity process. Deyhle and Bippes (1996) and Radeztsky et al. (1999) found that roughness elements placed close to the neutral stability point are more effective in moving the transition front forward. Upstream of the neutral stability point disturbances decay and therefore the forcing amplitude  $F$  is small leading to a smaller response of the flow. Placing the roughness elements downstream of the the neutral stability point two effects seem to play a role. Firstly, the disturbances caused by the coupling of the natural surface roughness with the flow have already grown, decreasing the effectiveness of the placed roughness elements. Secondly, since the boundary layer has grown, the non-dimensional roughness height,  $\epsilon$ , would be smaller leading to a smaller response of the flow. Studies of the flow structures, responsible for the receptivity between the discrete micron roughness elements and the stationary crossflow instability, are scarce. Experimental measurements on the generation of crossflow vortices close to the roughness elements are difficult to obtain, since the disturbances are often too small to measure. From computational studies it has been found, that for large roughness elements,  $Re_k=200-400$ , a horseshoe vortex system is formed of which one leg develops into an amplified stationary crossflow vortex (Kuruz and Kloker, 2016; Brynjell-Rahkola et al., 2017). For micron-sized roughness elements such mechanism does not exist (Rizzetta et al., 2010). From a mathematical point of view, it has been found that, for small roughness elements, the response of the flow can be computed using Fourier theory (Choudhari, 1994; Bertolotti, 2000; Schrader et al., 2009). In these studies the forcing amplitude,  $F$ , is calculated from the Fourier transform of the roughness distribution. The response of the flow is dominated by the least stable eigenmode having the same spanwise wavenumber  $\beta$  and  $\omega$  as the roughness distribution (Bertolotti, 2000). The Fourier coefficients  $A_n, B_n$  and  $C_n$  for a spanwise roughness distribution  $h(z)$  are calculated as:

$$A_n = \frac{2}{\lambda} \int_0^\lambda h(z) \cos \frac{2n\pi z}{\lambda} dz, \quad (4.4)$$

$$B_n = \frac{2}{\lambda} \int_0^\lambda h(z) \sin \frac{2n\pi z}{\lambda} dz, \quad (4.5)$$

$$C_n = \sqrt{A_n^2 + B_n^2}. \quad (4.6)$$

Here,  $1/\lambda$  represents the spatial frequency or wavenumber, in the spanwise direction. By varying  $n$ , the forcing expressed with  $C_n$  at a wavenumber of  $n/\lambda$  is evaluated. This wavenumber corresponds to a wavelength of  $\lambda/n$ , which indicates that for  $n=1,2,3,4$  the forcing at a wavelength of  $\lambda$ ,  $\lambda/2$ ,  $\lambda/3$  and  $\lambda/4$  is calculated. For a cylindrical roughness distribution, shown in Figure 2, with diameter,  $D$ , roughness height,  $k$  and spanwise spacing,  $\lambda$  the Fourier coefficients  $A_n$  and  $B_n$  are:

$$A_n = \frac{k}{n\pi} \sin \frac{2n\pi D}{\lambda}, \quad (4.7)$$

$$B_n = \frac{k}{n\pi} \left( 1 - \cos \frac{2n\pi D}{\lambda} \right). \quad (4.8)$$

A number of studies have been devoted to the influence of the height, diameter and spanwise spacing of the discrete roughness elements. In the following, the results of these studies will be illustrated with the Fourier coefficient spectra. An example of a spectrum is presented in Figure 2. The Fourier coefficient  $C_n$  is shown for cylindri-

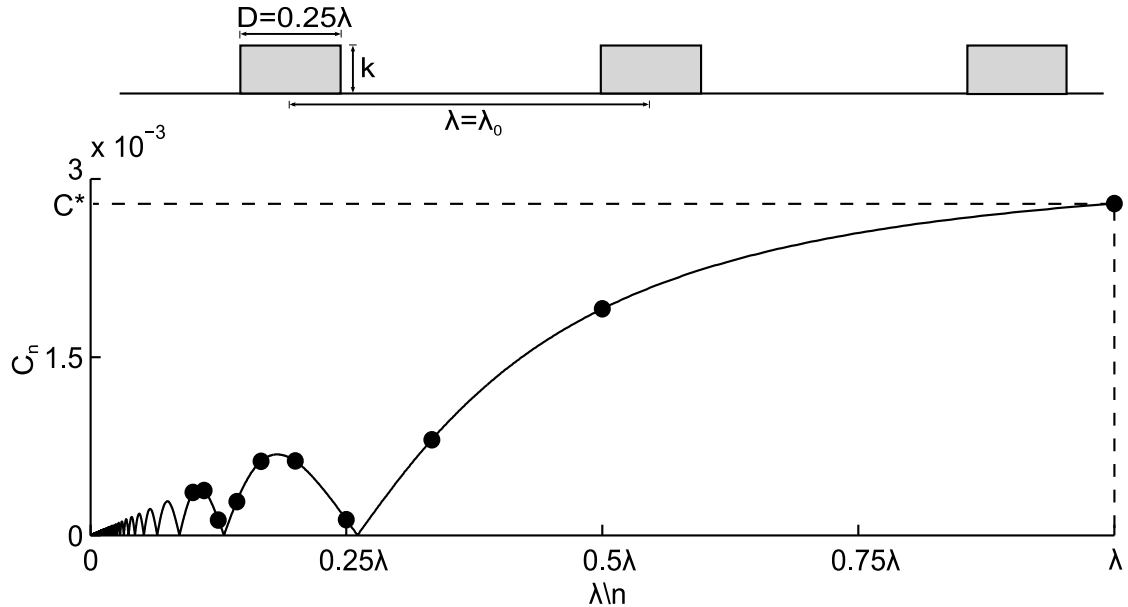


**Figure 2.** Wavelength representation of a typical roughness distribution with cylindrical roughness elements.

cal roughness elements, with diameter,  $D = 0.25\lambda$  height,  $k$  and spanwise spacing  $\lambda = \lambda_0$ . Here  $\lambda_0$  is defined as the wavelength of the stationary crossflow instability most unstable in the flow. The forcing at the harmonics,  $\lambda/2$ ,  $\lambda/3$  to  $\lambda/10$ , is highlighted with circles. The Fourier coefficients shown throughout the rest of this chapter are scaled with  $C^*$ , which is the forcing at wavelength  $\lambda$ , of the roughness distribution defined in Figure 2.

### *Roughness amplitude*

In this section the focus is on small roughness. Based on Fourier theory, increasing the height would increase the forcing in a linear manner as shown in Figure 3. Consequently, the response of the flow,  $A$ , would also increase linearly with roughness height. In Figure 3 the forcing at a wavelength  $\lambda_0$  ( $n=1$ ) and the harmonics  $\lambda_0/2$ ,  $\lambda_0/3$ ,  $\lambda_0/4$  and  $\lambda_0/5$  ( $n=2-5$ ) are presented, as a function of the height  $k_i$ , normalised over the height  $k$  of the standard roughness distribution. The forcing would be largest at  $\lambda_0$  ( $n=1$ ) and decrease with increasing  $n$ . In computational studies it has

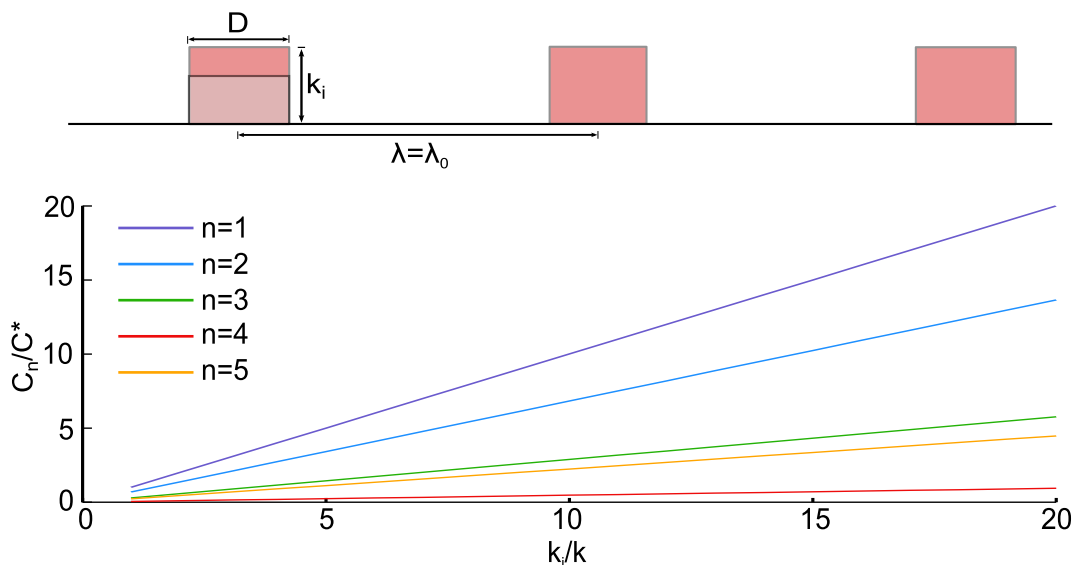


**Figure 3.** Scaled Fourier coefficients for different roughness heights,  $k_i$ .

been found that the Fourier theory only holds when the roughness height is below a certain limit. In these studies the roughness height is defined with the height ratio,  $\epsilon$ , defined in Equation 4.3. The response of the flow,  $A$ , is defined as the amplitude of the excited stationary crossflow wave at the streamwise location of the roughness element. Schrader et al. (2009) stated that the relationship between the amplitude of the roughness and the response of the flow was linear when the roughness height remained below 5% of the local displacement thickness. In Tempelmann et al. (2012) a limit at a height ratio of 10% has been found. The DNS study of Kurz and Kloker (2014) found that for a bump element, similar as used in Schrader et al. (2009) and Tempelmann et al. (2012), the non-linear effects are non-negligible when the height ratio is above 7%. In all computational studies the trend is similar, however, the height limit varies across the different investigations. As mentioned before, each study uses different definitions of their receptivity amplitude as well as different geometries of their roughness elements. Furthermore, the threshold defining if a response is linear or nonlinear has not been quantified in these studies. The variations

of all these variables across studies will most probably lead to the differences in the height limit, however, only a comparative study would give a decisive answer on this. The experiments carried out by [Hunt and Saric \(2011\)](#), showed that the initial amplitude of the stationary crossflow waves does increase linearly with roughness height. Here the amplitude was measured at  $0.15x/c$  approximately  $0.22m$  from the roughness elements. In this study the ratios between the height and displacement thickness are not mentioned. Therefore the displacement thickness is found from a boundary layer solver (BL2D <sup>1</sup>) with the flow parameters given in [Hunt and Saric \(2011\)](#). From this it is found that a linear relationship between the roughness height and stationary crossflow amplitude is found for height ratios of 2 to 16%. From the computational results a nonlinear response would be expected for this range of height ratios. The discrepancy between the experiment and computations might be caused by the different definitions of the response of the flow,  $A$ . In the experiment the response of the flow is defined at the roughness element, while, in the experiment, the response of the flow is measured far downstream of the roughness elements. It is expected that further downstream, next to the roughness height, the eigenmodes appearing in the natural flow would influence the amplitude of the stationary crossflow vortex. The effect of the different definitions of  $A$ , on the height limit for which non-linear effects start to play a role are difficult to predict.

The studies on the validity of the Fourier theory for different roughness heights show that theory holds up to a certain limit. In the several computational studies this limit has been defined around 5-10% of the local displacement thickness. In the only experimental study on this subject a linear relationship was found for all roughness heights tested, while the estimated height ratio was 16%. To understand this discrepancy between the experiment and computations an experimental and computational study should be carried out, where the definitions of the forcing and response of the flow are the same for both investigations.

Several experimental studies focussed on the influence of roughness height on the transition location. For a single discrete roughness element, an increase in roughness height leads to an earlier transition location ([Radeztsky et al., 1999](#)). For periodically placed roughness elements, the transition location did not change in some studies ([Reibert et al., 1996](#)) while in other cases a strong dependency was found ([Hunt and Saric, 2011](#)). These two studies were carried out in wind tunnels with different freestream turbulence levels. In [Hunt and Saric \(2011\)](#) it is argued that the initial

---

<sup>1</sup>QinetiC (unpublished)

amplitude of the crossflow instability is influenced by the turbulence intensity. When the turbulence intensity is higher, the roughness becomes less effective in forcing the flow. Consequently, there is no dependence of small differences in roughness height on the transition location. In Section 4.2.2 the influence of the freestream turbulence is discussed in more detail. For natural surface roughness, a strong dependency of average roughness height on the transition location has been found (Deyhle and Bippes, 1996; Radeztsky et al., 1999). The larger the average roughness height, the earlier transition occurred. It is noted that in these studies the power spectral density of the roughness distributions are not calculated, despite the fact that the latter influences the response of the flow as will be discussed hereafter.

From the previous studies it has been found that for low-turbulence environment the increasing roughness amplitude moves the transition location forward. When the turbulence intensity is increased this effect is not observed and the transition location is not influenced by the roughness amplitude.

#### *Wavelength content of the roughness distribution*

In this paragraph the influence of the wavelength content of the roughness distribution is discussed. Depending on the study the Fourier representation of the roughness distribution is described with the wavelength or wavenumber ( $1/\text{wavelength}$ ) content. In the current study the spanwise spacing  $\lambda$  is varied and therefore it is chosen to represent the Fourier coefficients as function of their wavelength.

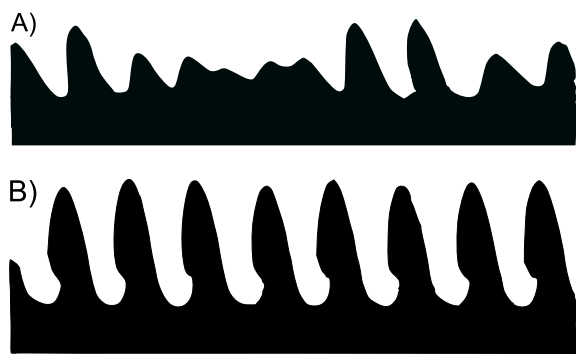


**Figure 4.** Primary crossflow vortices with (B) and without (A) roughness elements (adapted from Reibert (1996)).

In Figure 2 it is shown that the strongest forcing is obtained at a wavelength of  $\lambda_0$  which corresponds to a wavenumber of  $1/\lambda_0$ . The forcing decreases when the wavelength decreases. The dependency of the forcing on the wavelength is used in experimental studies to focus the energy of the flow in specific modes. It has been found that, without the roughness elements, the flow is not uniform in the spanwise direction, since the vortices are forced by the irregular sur-

face roughness that characterises the experimental model (Deyhle and Bippes, 1996). When the roughness elements are spaced at a wavelength of  $\lambda_0$ , the wavelength of the most unstable stationary crossflow instability in the flow, the flow is forced to

be spanwise uniform [Reibert et al. \(1996\)](#), as presented in Figure 4. The spanwise uniformity is experimentally an advantage, since the flow can be studied by focusing on a small number of vortices, instead of a large spanwise extent.

The wavelength content of the roughness distribution can be altered by changing the diameter,  $D$  and spanwise spacing,  $\lambda$ . When the ratio of  $D/\lambda_0$  is changed, it is shown in Figure 5, that the strongest forcing at  $\lambda_0$  ( $n=1$ ) is maximum for  $D/\lambda=0.5$ , following Fourier theory. This indicates that the strongest response of the flow would

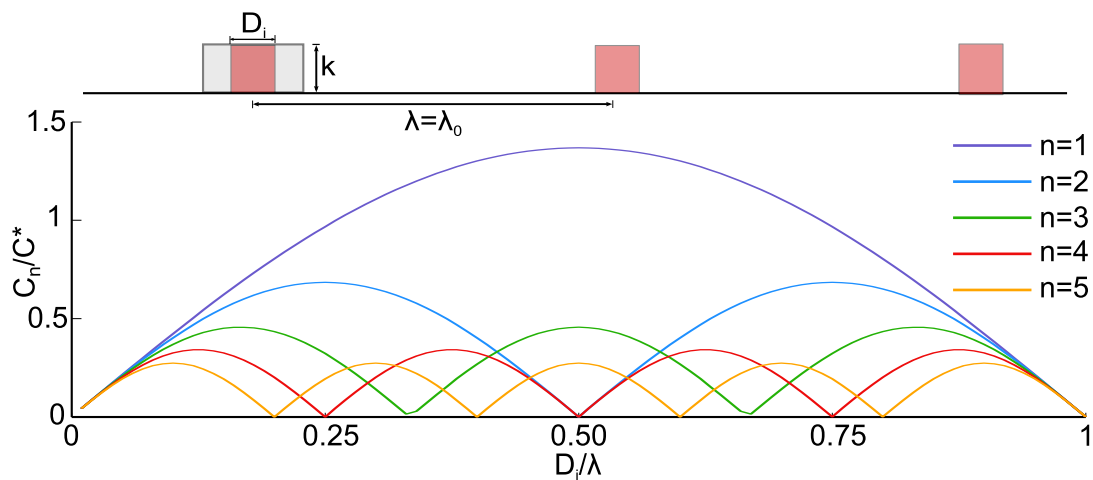


**Figure 5.** Scaled Fourier coefficients for different roughness diameters,  $D_i$ .

be at this  $D/\lambda_0$  ratio. In previous studies it was found that, for a single roughness element, there was no effect on the transition location when the ratio  $D/\lambda_0$  is small ([Radeztsky et al., 1999](#)). When the ratio increased upto  $D/\lambda_0=0.5$  the Reynolds number where transition occurred moved upstream which would support the Fourier model of forcing and Figure 5. [Choudhari \(1994\)](#) related the results of [Radeztsky et al. \(1999\)](#) to the Fourier spectrum of the roughness elements and came to the same result. This also explains results from [Deyhle and Bippes \(1996\)](#) and [Radeztsky et al. \(1999\)](#), who found there was no influence on transition location on a swept model of a two-dimensional strip with constant height in the spanwise direction ( $k = 6\mu m$ ). This kind of roughness would not have any coupling through its Fourier spectrum ( $D/\lambda_0=1$ ) since no specific frequency is excited. Of course, this result is only limited to small roughness heights, for larger heights a two-dimensional strip could trip the boundary layer directly into turbulence.

When  $\lambda$  is increased, the forcing extends to wavelengths larger than  $\lambda_0$  (Figure 6). Furthermore, the forcing is more constant over a larger wavelength domain. The

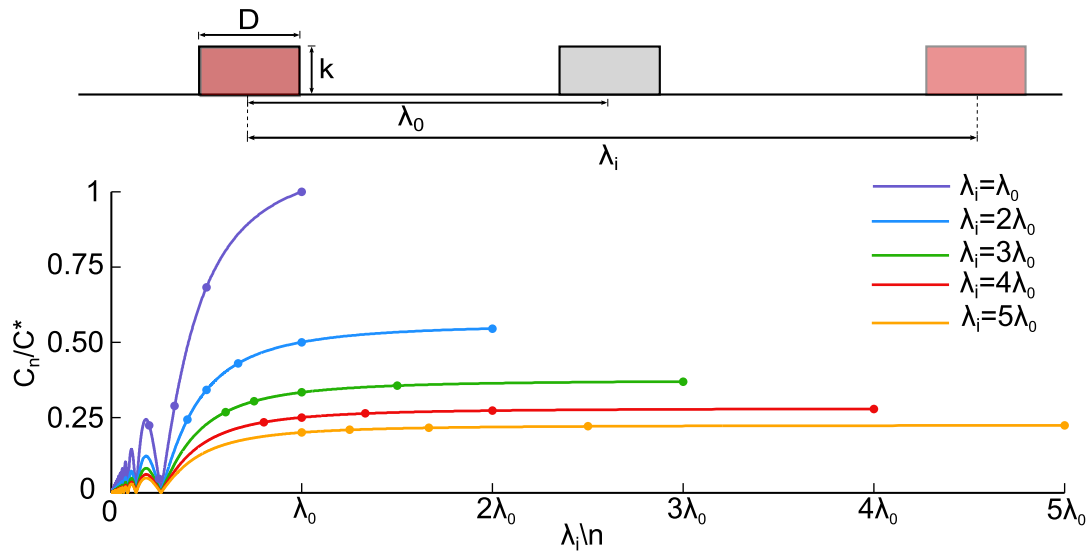


**Figure 6.** Scaled Fourier coefficients for different spanwise spacings,  $\lambda_i$ .

forcing at the spanwise spacing,  $\lambda_i$ , is lower since increasing the spanwise spacing decreases the  $D/\lambda_i$  ratio. Reibert et al. (1996) studied the influence of changing the spanwise spacing in detail and found that only modes with a wavelength of  $\lambda_i/n$  are excited i.e. harmonics in wavenumber space. Furthermore, he found that if the spanwise spacing is tuned, such that it is  $n$  times larger than the most unstable wavelength in the flow, i.e.  $\lambda = n\lambda_0$ , the transition location moves forward due to non-linear interactions occurring between multiple modes, excited by the roughness distribution. Saric et al. (1998) used this mechanism to achieve transition delay. In their study roughness elements were placed at  $2/3$  of the most unstable wavelength, such that the most unstable wavelength would not be excited. More recently, Serpieri et al. (2017) showed that the same transition delay mechanism can be achieved with plasma actuators. The working principle and its application was confirmed by DNS studies of Wassermann and Kloker (2002). However, Woodruff et al. (2011) showed that the effectiveness of this transition delay method does depend on the level of the freestream turbulence. A change of turbulence intensity from 0.04% to 0.02% made the method less effective. In the DNS study of Wassermann and Kloker (2002) the effect of freestream turbulence was not investigated. Flight tests carried out by Carpenter (2010) investigated the effectiveness of the method for different angles of attack. Varying the angle of attack varies the pressure distribution on the wing and therewith the stability characteristics. Carpenter (2010) showed that the degree of transition delay was highly dependent on small changes ( $1^\circ$ ) in angle of attack.

Next to transition delay it is also found that when the flow is excited by roughness

elements placed at  $\lambda = \lambda_0$ , the ratio between the amplitude of the harmonics,  $\lambda = \lambda_0/n$ , and the fundamental mode,  $\lambda = \lambda_0$ , depends on the Reynolds number (Reibert et al., 1996; Hunt and Saric, 2011). This is explained by the fact that the Reynolds number changes the stability properties of the boundary layer (Equation 1.5) and, therefore, the modes excited in the natural flow.

The wavelength content associated with the roughness distribution has been studied directly by Kurz and Kloker (2014). In their DNS study two different roughness elements are studied, which are denoted by a bump element and a spectrally reduced element as presented in Figure 7. The roughness elements are placed at a wavelength  $\lambda_0$ , such that they force the most unstable wavelength in the flow.

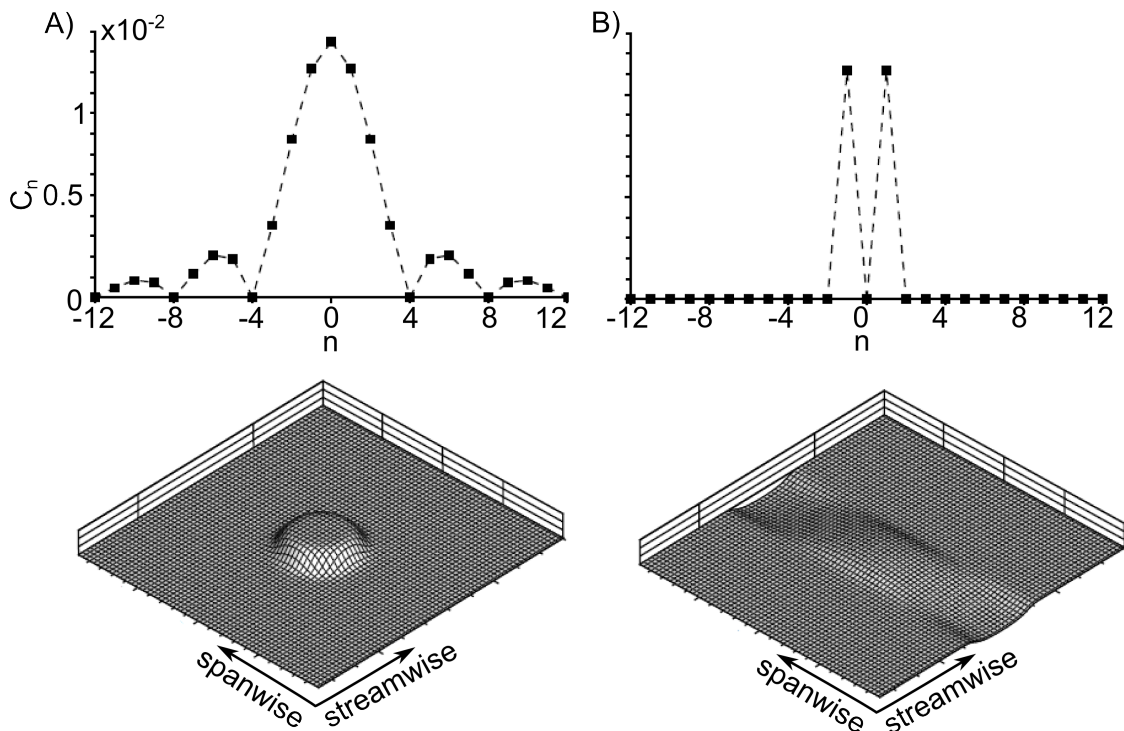


**Figure 7. Roughness elements used in Kurz and Kloker (2014). The picture is modified from Kurz and Kloker (2014).** A) Fourier coefficients and roughness shape of the bump roughness element. B) Fourier coefficients and roughness shape of the spectrally reduced roughness element.

In the Fourier spectrum of the bump element the mean height, denoted with  $n = 0$ , and all  $\lambda_0/n$  modes have a non-zero magnitude. For the spectrally reduced element, only the magnitude of the mode with a wavenumber of  $1/\lambda_0$  is non-zero in the Fourier spectrum. The response of the flow,  $A$ , is determined as the disturbance velocity of the stationary mode at the roughness element. The results show that for small roughness heights,  $\epsilon \leq 0.03$ ,  $A$  is very similar for the bump and spectrally reduced

element. For larger heights, the response of the flow is stronger for the bump element. To understand this, the zeroth and second mode,  $n=1$  and  $n=2$  in Figure 7, were mathematically added to the spectrally reduced element. The zeroth mode represents the mean height of the roughness distribution and therefore relates to the blockage of the flow caused by the roughness elements, while the second mode represents the forcing at a wavenumber of  $2/\lambda_0$ . Adding these two wavenumbers to the roughness shape now showed an identical response for both roughness elements for all height ratios ( $\epsilon=0$  to 0.15). This study shows subtle differences in the spectral content of the roughness distribution influences the initial amplitude of the crossflow instability. The importance of the wavelength content of the roughness distribution has also been shown by [Mughal and Ashworth \(2013\)](#). In their study the response of the flow of measured natural surface roughness distributions is evaluated. Their results show that roughness distributions which have a higher rms height can have a smaller effect on the flow than a roughness distribution with a smaller rms height. This is caused by the stronger forcing at the most unstable wavelengths in the flow for the roughness distribution with the smaller rms height. This argument is only valid upto a certain roughness amplitude. Above this limit the roughness will change the base flow and its stability characteristics directly as discussed in the start of this section.

The variation in wavelength content of a roughness distribution has been studied in several experimental and computational investigations. The effect of changing the diameter and spanwise spacing of the roughness elements on the development of the stationary crossflow waves can be understood with Fourier theory. While in computational studies the shape of the roughness elements was varied to change the wavelength content directly, in experimental studies the spanwise spacing and diameter was varied to obtain a similar effect.

#### 4.2.2. Influence of freestream turbulence

The freestream disturbance environment consists of vortical and acoustic components. Previous studies on the freestream turbulence level have focussed on the vortical part of the disturbances, which will be discussed in this section. In the next section the influence of the acoustic disturbances will be discussed. As shown in the previous section, a receptive boundary layer exists when the Fourier representation of the roughness distribution is similar to the wavenumbers of the eigenmode in the boundary layer. It has been found that often the freestream does not have the

same wavenumber content as the disturbances in the flow and, therefore, another mechanism is necessary to couple the disturbances with the boundary layer. This conversion process was first proposed by Goldstein (1983), Goldstein (1985) and Ruban (1985). They showed mathematically that a freestream turbulence wave with a large wavelength can generate Tollmien-Schlichting waves with a much smaller wavelength. The mechanisms by which this conversion is caused, can be a small surface non-uniformity or the fast accelerating flow due to the curvature of the leading edge. Schrader et al. (2009) showed that, for a three-dimensional boundary layer, there was no direct resonance between the freestream and the travelling crossflow waves, since the wavenumber and frequency content is not matched. When small roughness elements were added a response of the flow is found and the roughness seemed to address the length scale conversion. In Borodulin et al. (2013) a similar result was found. In their experimental study, traveling crossflow waves were excited by generating freestream vortices using a vibrating ribbon. With a single roughness element the amplitudes of the excited traveling crossflow waves were too small to measure since the freestream disturbances did not couple with the flow inside the boundary layer. When roughness elements were used with appropriate spanwise and streamwise length scales to focus the energy from the surface roughness in a few defined modes, the travelling waves were excited and their amplitudes could be measured.

The first parametric study on the influence of freestream turbulence on the crossflow instability was carried out by Bippes (1990) and Bippes and Muller (1990). Two different wind tunnels were used, and turbulence levels of 0.12 – 0.15%, 0.15% and 0.3% were tested. The turbulence intensity in these studies is defined as  $Tu = u'_{rms}/U_e$  where  $u'_{rms}$  is the magnitude of the streamwise fluctuating component measured with a hot-wire and  $U_e$  the streamwise velocity at the edge of the boundary layer. It was shown that the stationary modes were dominating the transition process at low turbulence levels, while at higher levels the travelling modes caused transition from laminar to turbulent flow. The main results were confirmed by a similar but more detailed follow-up study done by Deyhle and Bippes (1996). They showed that the freestream turbulence has a strong effect on the nature and growth of the crossflow instability. Experiments were performed in the same wind tunnel for turbulence intensities of 0.15% and 0.27%. Comparison of the frequency spectra for the low and high turbulence levels showed that the overall amplitude of the fluctuations increased with increasing turbulence intensity, while no difference at distinct frequencies were found. Therefore the temporal frequency content of the freestream did not cause the observed differences on the nature and growth of the crossflow instability.

The experimental study carried out by Downs (2012) showed that increasing turbulence levels ( $Tu=0.02\%$  to  $Tu=0.19\%$ ) led to a decrease of the stationary crossflow amplitude and increase of the travelling crossflow mode, in the region where the instability had grown significantly. The initial stationary crossflow amplitude was not influenced by the freestream turbulence level. This indicates that the increased freestream turbulence levels does not only cause the travelling mode to dominate the transition process, it also slows down the growth of the stationary crossflow instability directly. Downs (2012) showed that at  $Tu=0.19\%$  the transition process was dominated by the travelling crossflow instabilities. Kurian et al. (2011) tested five different grid generated turbulence levels and showed that the threshold for the travelling waves to dominate the flow is about  $Tu>0.2\%$ . The general trends for the influence of the freestream turbulence were confirmed by Schrader et al. (2009), however, they stated that the limit for travelling waves to dominate the flow is about  $Tu=0.5\%$ . The first reason for these different levels could be that the studies were only carried out at a few turbulence intensity levels. When more levels would be tested the limit could be determined with higher accuracy. Furthermore, the height and wavelength content of the surface roughness varies across studies. As discussed earlier the surface roughness will determine the initial amplitude and growth of the stationary crossflow instability as well the coupling between the freestream and boundary layer flow. The definition of the freestream turbulence might also influence the limit. In experimental studies the freestream turbulence is defined as the velocity fluctuations in a frequency band from 2Hz to 5kHz to 10kHz. In the computational study by Schrader et al. (2009), the freestream environment was modelled by adding a single continuous eigenmode to the boundary layer flow. Finally, in experimental studies the magnitude of the turbulence intensities can be influenced by electronic and acoustic noise, which will not interact with the disturbances in the boundary layer. In those cases the effective forcing would be lower than the quoted freestream disturbance level, leading to a lower limit. The limit for which the nature of the dominating crossflow instability changes from travelling to stationary crossflow waves is of importance when relating the development of the crossflow instability occurring in wind tunnel tests to the development of the crossflow instability in flight. Measurements of atmospheric turbulence showed that the turbulence intensity is below 0.05% (Riedel and Sitzmann, 1998). From the previous studies it is expected that in flight the stationary crossflow instability would dominate the transition process.

The studies on the freestream turbulence show that the freestream turbulence level determines if the stationary or travelling crossflow mode is dominating the transition

process. The limit for which travelling crossflow modes dominate the flow varies from 0.2 to 0.5%.

### 4.2.3. Influence of acoustic disturbances

Computational studies carried out by [Crouch \(1992\)](#) and [Choudhari \(1994\)](#) showed that the travelling waves are receptive for acoustic freestream disturbances. When roughness elements were added the receptivity to travelling crossflow increased. The receptivity of acoustic disturbances to stationary waves was found to be small in these computational studies. In experiments carried out by [Deyhle and Bippes \(1996\)](#) the acoustic environment was changed by introducing sound waves in the flow. The speaker, producing the sound, was placed at the wall of the settling chamber upstream of the test section. The emitted waves covered a range of frequencies, attempting to excite the travelling waves in the flow. The results showed that sound did not influence the growth of the travelling or stationary waves. [Radeztsky et al. \(1999\)](#) followed a similar approach. They varied the sound level and amplitude of a speaker placed upstream of the experimental model. Again they found no influence of sound on the transition location. In both experimental studies the surface roughness of the experimental model was small and the transition process was dominated by the stationary crossflow instability. From the computational studies of [Crouch \(1992\)](#) and [Choudhari \(1994\)](#) it is predicted that for such environment the acoustic disturbances are ineffective in exciting the stationary crossflow waves.

## 4.3. Aim of current study

From the literature review it was found that most experimental studies were performed on circular roughness elements with uniform height  $k$ , diameter  $D$  and evenly spaced at wavelength  $\lambda$ . Surface roughness on aeroplane wings is far more complex with heterogeneous heights, spanwise spacings and shapes. While in computational studies, natural surface roughness distributions are investigated using statistical methods, in experimental studies several steps have to be made to understand the effects of these complex roughness distributions in detail. It has been found that in industry the focus is mostly on the height of the surface ([Goldhammer and Plendl, 2013](#)), however, from experimental and computational studies it has been found that the Fourier spectrum of the roughness distribution is strongly coupled to the response of the boundary layer ([Choudhari, 1994](#); [Bertolotti, 2000](#); [Schrader et al., 2009](#)). Experimentally, this has been verified with discrete roughness elements by [Radeztsky](#)

et al. (1999) (who varied the diameter of the discrete roughness elements) and by Reibert et al. (1996) (who varied the spanwise spacing of the roughness elements). However, more complex distributions with stronger forcing of the most unstable wavelength have not been tested up to date. Therefore it is chosen to study the effect of spanwise wavelength content of the roughness distribution on the growth of the crossflow instability in detail, in the current experimental study. For this purpose two different roughness distributions with the same height but different spanwise wavelength content were tested in the UK National Low Turbulence wind tunnel at City, University of London. From the freestream turbulence measurements discussed in Chapter 3 an average turbulence intensity of 0.02% is found. This is well below the limits for which a travelling crossflow dominated transition process was found (Deyhle and Bippes, 1996; Kurian et al., 2011; Downs, 2012) and therefore it is expected that in the current experiment the transition process will be dominated by the stationary crossflow instability. In this freestream environment it is also expected that the receptivity to acoustic noise will be low.

## 4.4. Design of the roughness distributions

In the current experiment a step function roughness distribution is compared to a distribution mimicking a sine wave. It is expected that the sine wave element should have stronger forcing at the most unstable wavelength and would therefore force the flow more severely. The sine wave is a three-dimensional roughness element, which is sinusoidal in the spanwise direction and has a smoothed step in the streamwise direction. Preferably, the roughness distributions would be machined on the plate surface, however, this is a costly and lengthy procedure.

Therefore, it is chosen to discretise a sine wave, such that, it can be constructed of different layers of discrete roughness elements. The sine wave elements resembles a pyramid and will be called pyramidal roughness distribution throughout the thesis. For both roughness distributions, the geometry is shown in Figure 8, where the height ( $k$ ), diameter ( $D$ ) and spanwise spacing ( $\lambda$ ) are the design parameters.

### 4.4.1. Spanwise spacing, $\lambda$

The spanwise spacing is determined such that it amplifies the most unstable stationary crossflow wave in the flow. The neutral stability point and wavelength of the most amplified wave are found through linear stability analysis discussed in Appendix A. Because the roughness elements were designed and printed prior to the

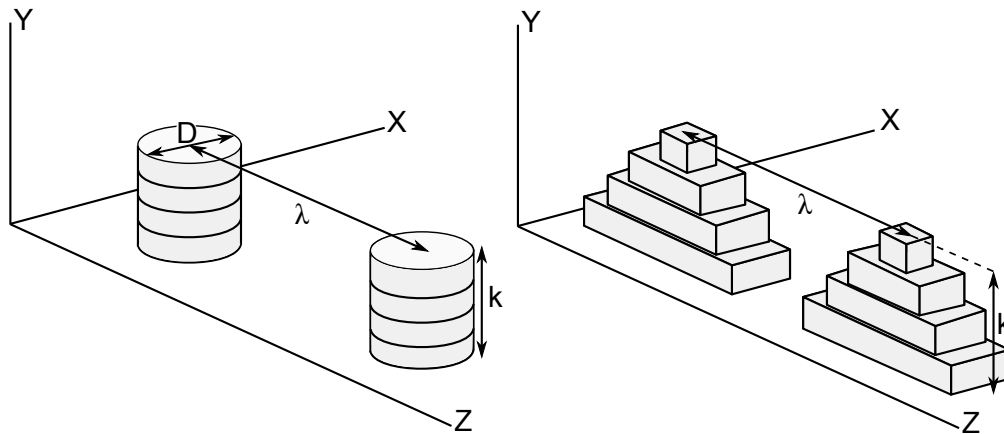


**Figure 8.** Design parameters for cylindrical (left) and pyramidal (right) roughness distributions.

experiments, the linear stability analysis to obtain the wavelength of the most amplified stationary crossflow wave was carried out with a pressure distribution obtained from the panel code. In Figure 9A the N-factors of the stationary crossflow waves are shown together with the Tollmien-Schlichting waves with different frequencies. Stationary crossflow waves with a wavelength of 11.5-15mm show strong growth in the measurement region, without significant differences between the waves. The Tollmien-Schlichting waves only start growing significantly outside the measurement region. From these results it is chosen to have a spanwise spacing of 11.5mm between roughness elements. Next, the linear stability analysis was repeated with the experimental pressure distribution at  $Z/H=0.56$ , presented in Section 3.2. The N-factor results obtained from the experimental pressure distribution, presented in Figure 9B show that crossflow waves with a similar wavelengths are amplified, as found from the linear stability carried out with the pressure distribution from the panel code. From this, it is concluded that the pressure distribution used in the design of the roughness elements gives similar stability characteristics as the pressure distribution obtained from the experiments. Therefore the chosen spanwise spacing of 11.5mm will force the unstable mode in the flow. From previous studies it is found that the roughness elements are most effective when they are placed close to the neutral stability (Deyhle and Bippes, 1996; Radeztsky et al., 1999). From the linear stability analysis the neutral stability point is found to be at  $x/c=0.04$  which is where the roughness elements are placed.

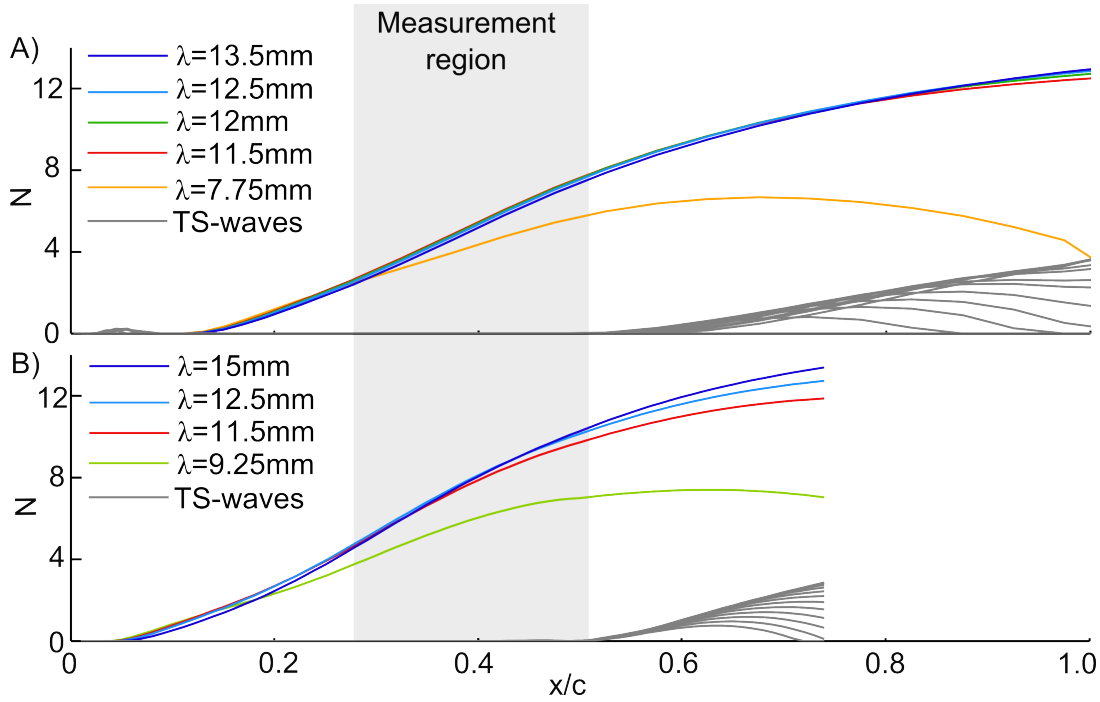


**Figure 9.** A) N-factor curves for the stationary crossflow (CF) waves and Tollmien Schlichting (TS) waves obtained from the pressure distribution used in the design process. The light grey area corresponds to the measurement region. B) A) N-factor curves for the stationary crossflow (CF) waves and Tollmien Schlichting (TS) waves obtained from the experimental pressure distribution. The light grey area corresponds to the measurement region.

#### 4.4.2. Roughness height, $k$

In the current sets of experiments it is required to have roughness well below the critical roughness height,  $Re_{k,crit}$  (see Section 4.2.1), since the main objective is to study the development and growth of the crossflow instability. Appliqué roughness elements of  $6\mu\text{m}$  were chosen which are the same as used in previous studies (Hunt and Saric, 2011; Eppink, 2014; Serpieri and Kotsonis, 2016b). The roughness elements can be stacked on top of each other to manage the total height. Here it is chosen to have  $k=24\mu\text{m}$  for both the cylindrical and pyramidal roughness distribution. From the BL2D boundary layer solver (Appendix A) the displacement thickness,  $\delta^*$  and the velocity at  $y=24\mu\text{m}$  was found at  $x/c=0.04$  where the roughness elements were placed. From this a height ratio,  $\epsilon$ , of 4.7% of the displacement thickness was calculated and a roughness Reynolds number,  $Re_k$ , of 0.05. The height ratio is below the limit for which non-linear receptivity has been found in computational studies (Schrader et al., 2009; Tempelmann et al., 2012; Kurz and Kloker, 2014). The roughness Reynolds number is well below  $Re_{k,crit}$ . Compared to other roughness receptivity studies the Reynolds number has a similar order of magnitude (Reibert

et al., 1996; Radeztsky et al., 1999).

#### 4.4.3. Diameter, $D$

From previous research it was found that the diameter of the roughness elements also influences the transition location (Braslow, 1960; Radeztsky et al., 1999; Eppink, 2014).

When the diameter is normalized with the wavelength of the dominant stationary crossflow wave,  $\lambda_0$ , it is found that the critical Reynolds number decreases when the normalized diameter increases (Radeztsky et al., 1999). To be sure that the effect of roughness is significant, a value of  $D/\lambda_0=0.2-0.4$  should be chosen.

For the cylindrical roughness elements a diameter of 3mm is chosen which gives a  $D/\lambda_0$  ratio of 0.26. For the pyramidal roughness distribution the diameter follows from the discretization of the sine wave (Figure 10). A sine wave is discretised with four layers of  $6\mu\text{m}$ , to keep the total height fixed across cases. The cross-section with the sine wave is found, determining the diameters for each of the four layers.

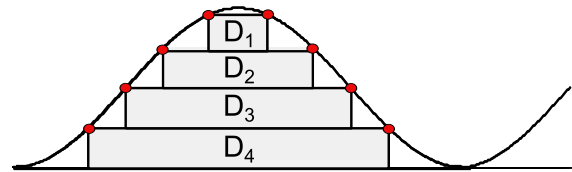


**Figure 10.** Definition of diameters of the different layers of the pyramidal roughness element.

#### 4.4.4. Fourier coefficients

The difference in forcing of both roughness distribution is evaluated with the Fourier spectrum. To obtain the Fourier coefficients for the pyramidal distribution, the pyramid is divided in 7 rectangles as shown in Figure 11.

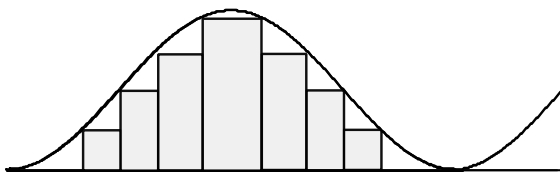


**Figure 11.** Division of pyramidal roughness element to calculate Fourier coefficients.

The coefficients  $A_n$  and  $B_n$  are calculated for each rectangle with Equations 4.7 and 4.8 and summed after which  $C_n$  is calculated. The results for  $C_n$  are shown in Figure 12. It is clear that the forcing for the pyramid is concentrated around  $\lambda$ , while the modes with a wavelength of  $\lambda/n$  are not as strongly forced

as for the cylinder. From this it would be expected that the stronger forcing at  $\lambda$  through the pyramidal roughness distribution will lead to a larger response of the flow at this wavelength.

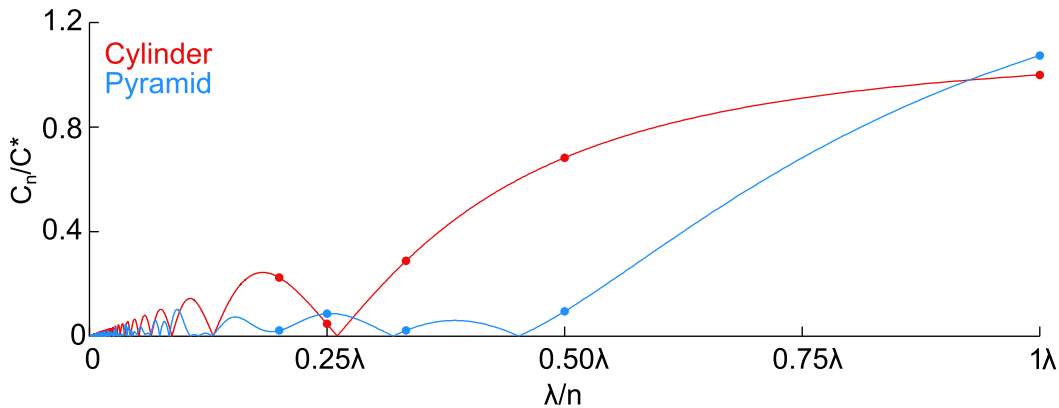


**Figure 12.** Scaled Fourier coefficients for the cylindrical and pyramidal roughness distribution.

The roughness elements were manufactured by Redd Europe Ltd, printed on an A4-size transfer paper and applied close to the neutral stability point, parallel to the leading edge of the plate. The shape of the roughness distribution was measured with a profilometer (MITUTOYO SJ-410) and the results are shown in Figure 13. The measured roughness distributions resemble the designed roughness elements

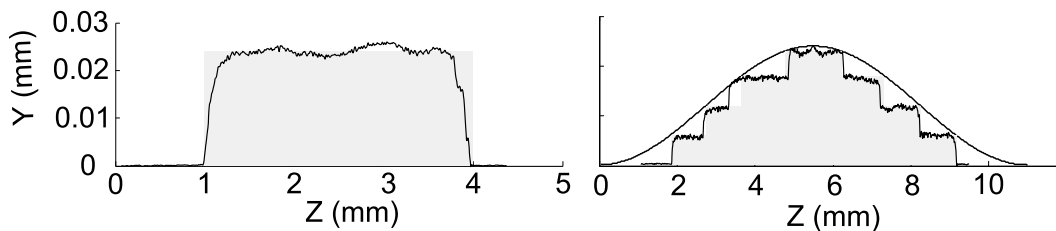


**Figure 13.** Designed roughness elements (light gray) superimposed with profilometer measurements (black line).

very well. The height of both elements is the same such that forcing is only determined by their shape.

## 4.5. Data analysis

Detailed hot-wire measurements were carried out to follow the development of the stationary and travelling crossflow waves. A single probe hot-wire was aligned in the x-direction to measure the streamwise velocity. Inevitably, the wall-normal velocity was measured as well as explained in section 2.4.4. The sampling frequency was set to 20kHz with an analog bandpass filter of 2-10000Hz. In Figure 14 the coordinate systems and orientation of the different hot-wire scans are shown. The coordinate system aligned with the traverse axis is denoted with the lower case letters x, y and z. The model coordinate system is oriented parallel (Z) and perpendicular (X) to

the leading edge. The wall-normal directions  $y$  and  $Y$  coincide for both coordinate systems

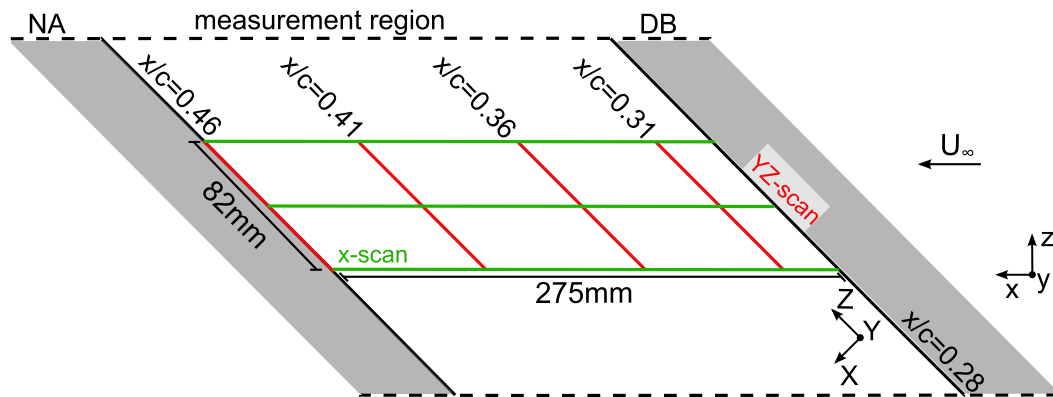


**Figure 14. Definitions of hot wire scans and coordinate systems.** The measurement region is limited by the displacement body (DB) and the region which is not accessible (NA) with the traverse system.

With the traverse system in place it was not possible to measure underneath the displacement body. Therefore the first streamwise location where measurements were taken was at  $x/c=0.285$ . Two types of hot-wire anemometry scans were carried out. For the YZ-scans, 82 boundary layer profiles were taken parallel to the leading edge with a spanwise spacing, of 1mm and a sampling time of 10 seconds for each data point. Each boundary layer profile has 40 points between  $0 < Y < 12\text{mm}$ . The YZ-scans were carried out at different chordwise locations and tracked the development of the stationary and travelling instabilities. The x-scans were taken at constant wall-normal location with  $\Delta x=5\text{mm}$ . With these scans the development of the travelling waves was determined at high streamwise resolution. In both scans the mean velocity, fluctuating velocity and bandpass filtered velocity are analysed. The fluctuating velocity signal is directly obtained by filtering the signal passed via an analog filter, while the bandpass filtered velocity is digitally filtered in the post processing stage. The data analysis of carried out in MATLAB (MathWorks).

The analysis of the hot-wire measurements discussed in the following section is illustrated with the measured data shown in Figure 15. Here a YZ-scan at  $x/c=0.31$  is shown for the cylindrical roughness distribution. The Figure shows the individual velocity profiles as well as the contour plot of the streamwise velocity.

### *Determination of wall*

During the measurements, the laser system described in Section 2.5 ensured that the distance to the wall was constant for all boundary layers. Prior to each hot-wire

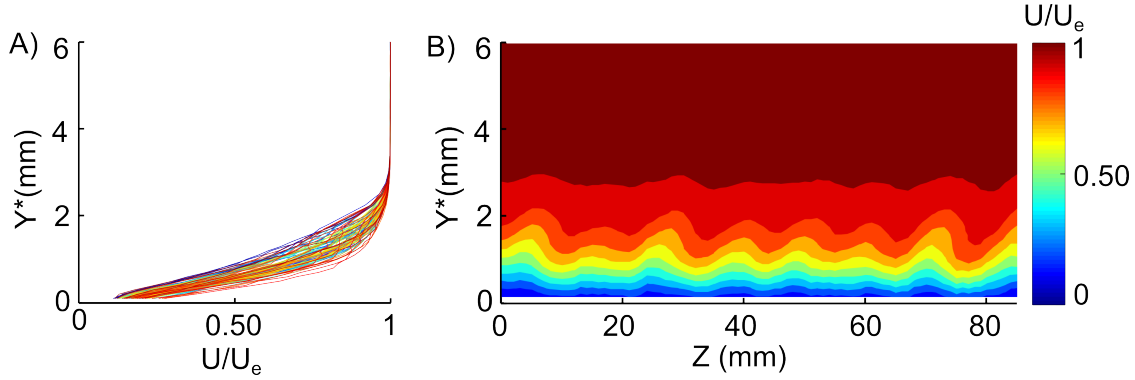


**Figure 15. Experimental data to illustrate the data analysis methods.** A) Streamwise velocity profiles taken at different spanwise location. B) Streamwise velocity distribution in the spanwise direction.

scan the hot-wire was positioned in proximity to the wall by eye and by using the measured velocity as an indicator. At this location the reference ( $Y^*=0$ mm) was set and the hot-wire measurements were carried out. Inevitably, there was a difference between the determined wall location and the actual wall location. This is shown in Figure 15 where the velocity profiles do not go through the origin for  $U/U_e=0$ , instead the y-axis would be crossed at  $Y^* < 0$ . To obtain the physical location of the wall a shift,  $\Delta Y$ , was applied to the boundary layer profiles in the post-processing stage, as presented in Figure 16.

The shift was obtained by linear interpolation of the velocity profile close to the wall, which assumes that the velocity profile in this region is linear. This is generally the case, however, when the profiles are strongly distorted, as is the case in a crossflow dominated flow, this linear region can become small resulting in an error in  $\Delta Y$ . Furthermore, due to electronic noise on the laser signal, another error was introduced which is estimated to be  $50\mu\text{m}$ . To minimize these errors,  $\Delta Y$  was averaged over the span at each chordwise location. For the data presented in Figure 15,  $\Delta Y \approx 0.2\text{mm}$ .

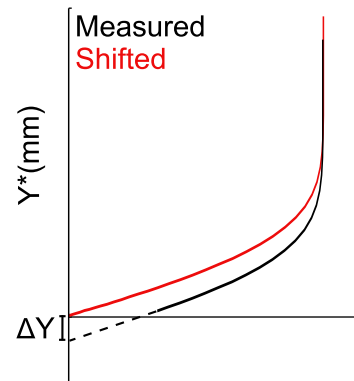


**Figure 16.** Definition of measured and shifted velocity profiles.

### *Mode shape and amplitude*

The boundary layer YZ-scans consisted of  $N$  boundary layer profiles taken across the span for each  $x/c$  location. The mode shape of the stationary crossflow wave was

determined with:

$$U^*(Y) = \sqrt{\frac{1}{N} \sum_{i=1}^N \left( \frac{U_i(Y) - \bar{U}(Y)}{U_{e,i}} \right)^2}, \quad (4.9)$$

where  $\bar{U}$  is the time-averaged velocity  $U$  averaged in the spanwise direction calculated with:

$$\bar{U}(Y) = \sum_{i=1}^N U_i(Y). \quad (4.10)$$

In Figure 17 the different quantities to calculate the mode shape  $U(Y)^*$  and  $U(Y)^*$  itself are shown for the data from Figure 15. In order to track the growth of the

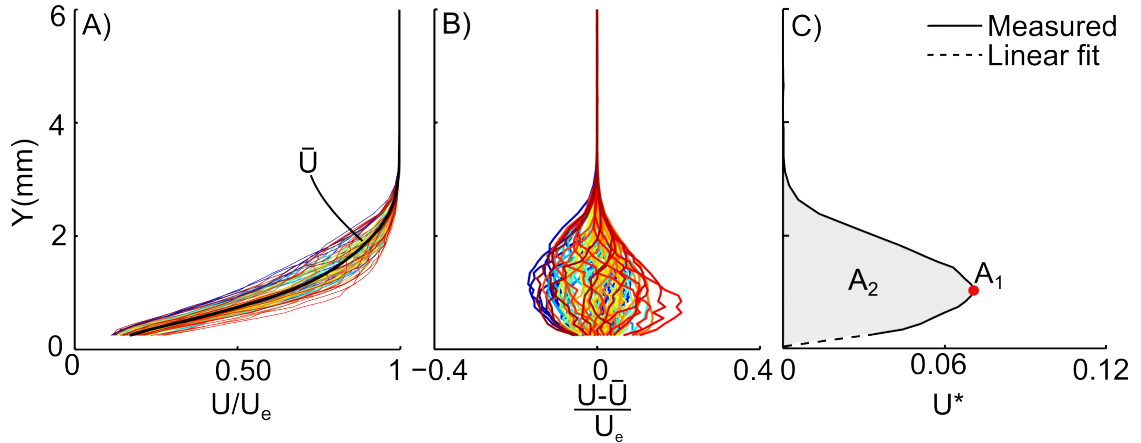


**Figure 17.** A) Streamwise velocity profiles at each spanwise direction in color and the spanwise averaged velocity profile,  $\bar{U}$  in black. B) The deviation of the spanwise averaged velocity profile at each spanwise location. C) The mode shape and amplitudes  $A_1$  and  $A_2$  of the stationary mode.

stationary crossflow wave the amplitude was determined for all  $x/c$  locations. The amplitude was calculated with two different methods (Figure 17C) by:

$$A_1 = \max_Y (U^*(Y)), \quad (4.11)$$

$$A_2 = \frac{1}{\delta} \int_0^\delta U^*(Y) dY. \quad (4.12)$$

The same procedure was followed to calculate the mode shape and of the fluctuating velocity component.

### ***Spatial power spectra***

The spatial power spectra were calculated to determine if instabilities with a certain

wavelength were dominant in the flow. The spatial power spectra were calculated from the time averaged velocity signal at each wall-normal location, shown in Figure 18A for  $Y=1\text{mm}$ . After the window function was applied to reduce spectral leakage,

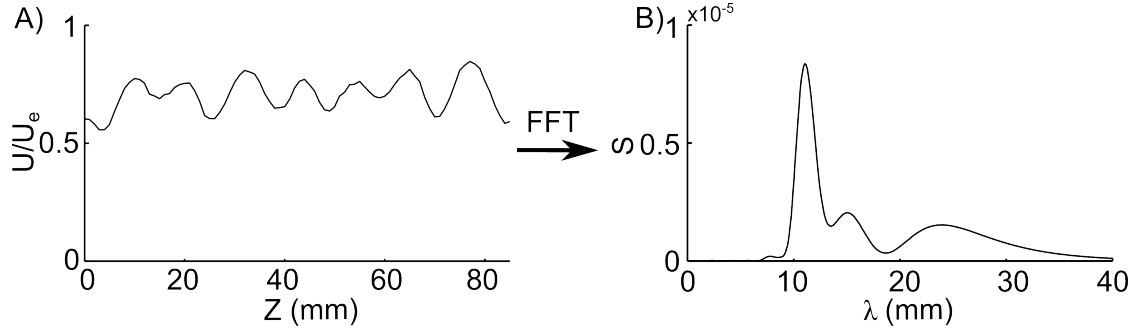


**Figure 18.** Calculation of the spatial power spectrum with the data shown in Figure 15. A) Normalized velocity at constant wall-normal location ( $Y=1\text{mm}$ ). B) Spatial power spectrum obtained from the signal shown in A.

the signal was zero-padded<sup>2</sup> to be able to distinguish different peaks in the power spectrum. Next the Fast Fourier Transform algorithm was applied in MATLAB, resulting in the spatial power spectrum shown in Figure 18B. A clear peak is shown at  $\lambda=11\text{mm}$  which is close to the chosen spanwise spacing of the roughness elements of  $11.5\text{mm}$ . Because of the small sample size for the spatial spectra, the resolution of  $\lambda$  has to be taken into account. As shown in Reibert et al. (1996) the resolution for a signal which measures a span of  $L$  is determined by

$$\Delta\lambda = \frac{\lambda^2}{L}. \quad (4.13)$$

This means that, in the current experiment, where  $L=82\text{mm}$ , a wavelength of  $11.5\text{mm}$  has a resolution of  $1.6\text{mm}$ .

### *Amplitude of bandpass filtered velocity*

The bandpass filtered velocity was determined by integrating the normalised temporal power spectra between frequencies  $f_1$  and  $f_2$  with:

$$u'_{BP} = \int_{f_1}^{f_2} S df, \quad (4.14)$$

as illustrated in Figure 19. The same definition was used in White and Saric (2005); Eppink (2014); Serpieri and Kotsonis (2016b). The amplitude of a mode which lies in the frequency band between  $f_1$  and  $f_2$  was then calculated in two different ways

<sup>2</sup><http://www.bitweenie.com/listings/fft-zero-padding> gives a clear explanation of zero-padding.

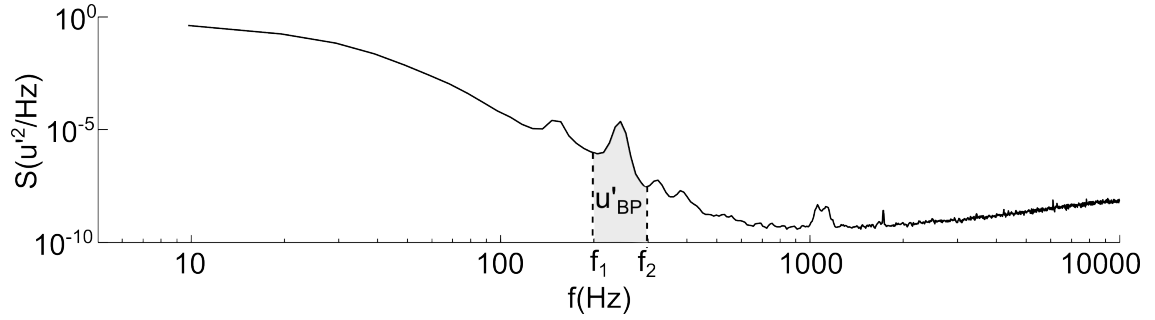


**Figure 19. Definition of the bandpass filtered velocity  $u'_{BP}$ .** The power spectrum is obtained from a time signal at  $Y=0.2\text{mm}$  and  $Z=64\text{mm}$  of the dataset shown in Figure 15.

depending on the available data. For the x-scan the amplitude was determined from a single point measurement as:

$$A_{BP,x} = \frac{\int_{f_1}^{f_2} S df}{\int_2^{10000} S df} = \frac{u'_{BP}}{u'_{rms}}. \quad (4.15)$$

Here the discrete integral was calculated with the trapezium rule. For the YZ-scan the bandpass filtered velocity,  $u'_{BP}$ , was integrated in the wall-normal and spanwise direction to obtain the amplitude  $A_{BP,YZ}$  with:

$$A_{BP,YZ} = \frac{\int_{Z_1}^{Z_2} \int_0^\delta u'_{BP} dY dZ}{\int_{Z_1}^{Z_2} \int_0^\delta u'_{rms} dY dZ}, \quad (4.16)$$

following [White and Saric \(2005\)](#). The normalisation of the amplitude was chosen such that it can be interpreted as a percentage of the total energy of the flow. It consequently, allows to compare across different data sets since the normalisation settles small differences in freestream velocity or other measurement conditions.

### ***Gradient fields***

The Reynolds-Orr equation shows that the wall-normal and spanwise shear are essential in the production term (see Chapter 1) of the disturbances. Therefore, the mean gradient fields  $\partial U/\partial Y$  and  $\partial U/\partial Z$  were calculated. Because the derivatives are sensitive to noise in the data, it was chosen to first smooth the mean velocity fields with a moving average filter from the *smooth()* function in MATLAB. Then,

the derivatives were calculated with a central difference scheme:

$$\left. \frac{\partial U}{\partial Y} \right|_{Y_i, Z_j} = \frac{U_{i+1,j} - U_{i,j}}{Y_{i+1,j} - Y_{i,j}}, \quad (4.17)$$

$$\left. \frac{\partial U}{\partial Z} \right|_{Y_i, Z_j} = \frac{U_{i,j+1} - U_{i,j}}{Z_{i,j+1} - Z_{i,j}}. \quad (4.18)$$

### *Correlation coefficient*

The correlation coefficient between bandpass filtered velocity distributions and gradient fields are calculated to understand if high intensity fluctuations coincide with high shear. Pearson's correlation coefficient for two matrices of size MxN is written as:

$$R = \frac{\sum_{i=1}^M \sum_{j=1}^N (A_{ij} - \bar{A})(B_{ij} - \bar{B})}{\sqrt{\sum_{i=1}^M \sum_{j=1}^N (A_{ij} - \bar{A})^2 (B_{ij} - \bar{B})^2}}, \quad (4.19)$$

where  $R=1$  is perfect positive correlated,  $R=0$  means there is no correlation and  $R=-1$  means perfect negative correlated.

### *Intermittency factor*

When the flow transitions from laminar to turbulent the hot-wire signal becomes intermittent. This means that the time signal shows alternating phases of laminar and turbulent flow, with low and high fluctuations respectively. Figure 20 shows hot-wire signals in a laminar and turbulent boundary layer, together with their respective power spectra. To determine which part of the flow is turbulent and which part is laminar the following algorithm, Figure 21, was applied to each hot-wire signal obtained in the x-scans. First, the analogue filtered hot-wire signal was smoothed with a moving average filter of 50 samples. Secondly, the original signal is subtracted. Finally, a sample was determined to be turbulent when it was above a certain threshold. The intermittency of the signal was then defined as:

$$\gamma = \frac{n_T}{n_{tot}}, \quad (4.20)$$

where  $n_T$  is the number of turbulent samples and  $n_{tot}$  the total number of samples in the analysed signal.

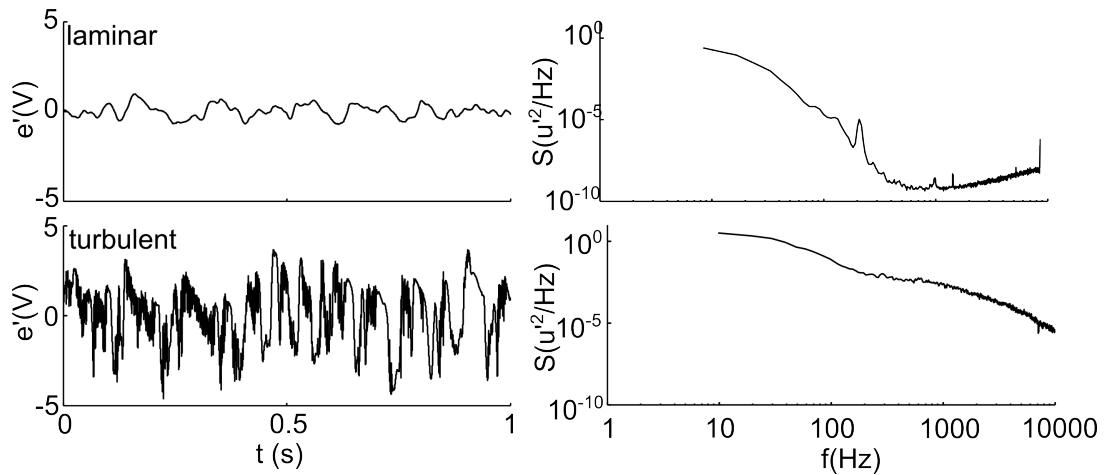


**Figure 20.** Example of a time signal and power spectrum obtained in a laminar and turbulent boundary layer.

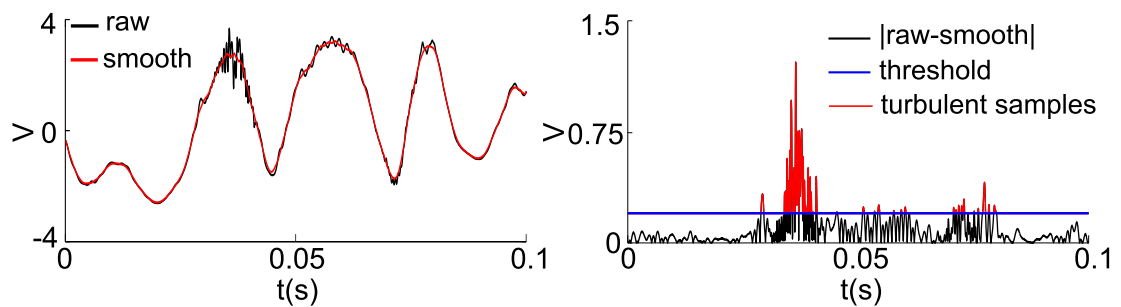


**Figure 21.** On the left a hot-wire signal which has a high frequency burst related to turbulence is shown. On the right the samples in the burst are defined by subtracting a smoothed signal from the raw signal.

## 4.6. Results

### 4.6.1. YZ-scans

The normalised time-averaged velocity fields at  $x/c=0.31$  show that the roughness elements close to the leading edge re-organise the flow which becomes more uniform in the spanwise direction, (Figure 22) as was also shown before by Reibert et al. (1996). A spanwise uniform flow was not observed in the present experiment due to the absence of the infinite swept condition unlike in the case of Reibert et al. (1996). The pressure gradient varies in the spanwise direction, as shown in Section 3.2, which results in different growth rates of the stationary modes along the span. The overall pressure distribution is not influenced by the roughness elements and therefore the time-averaged velocity fields can still be compared for different roughness distributions. To eliminate the influence of individual vortices on the results, it is chosen to study a large spanwise region. In the following analysis the results of the cylindrical

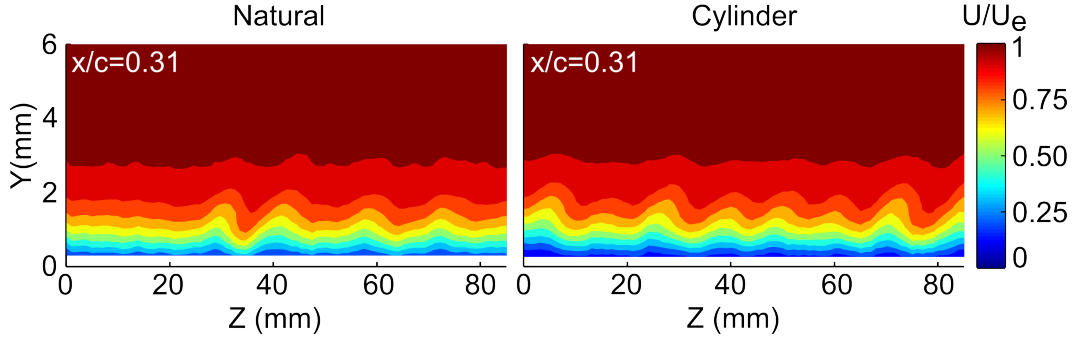


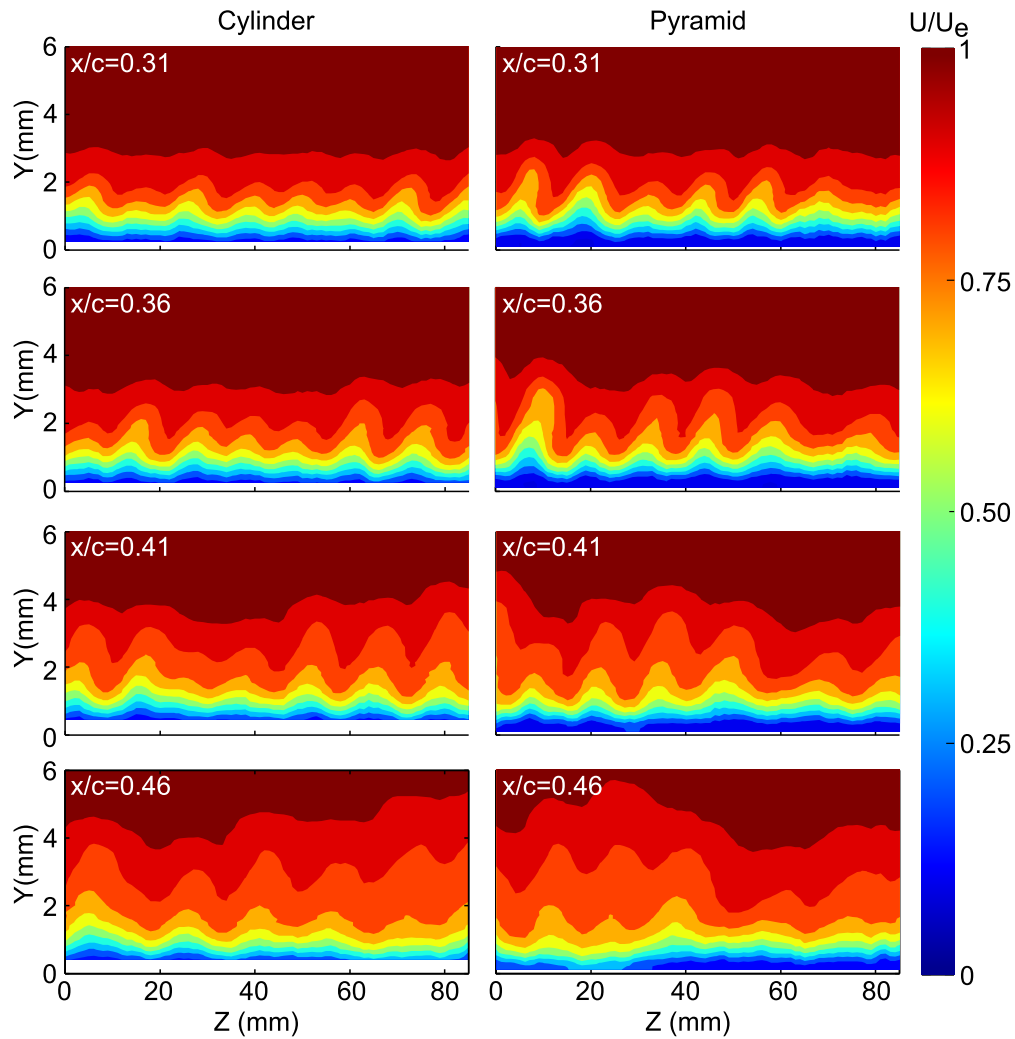
**Figure 22.** Streamwise velocity fields at the first measurement location with (right) and without (left) roughness elements placed at the leading edge.

and pyramidal roughness distributions are presented and compared.

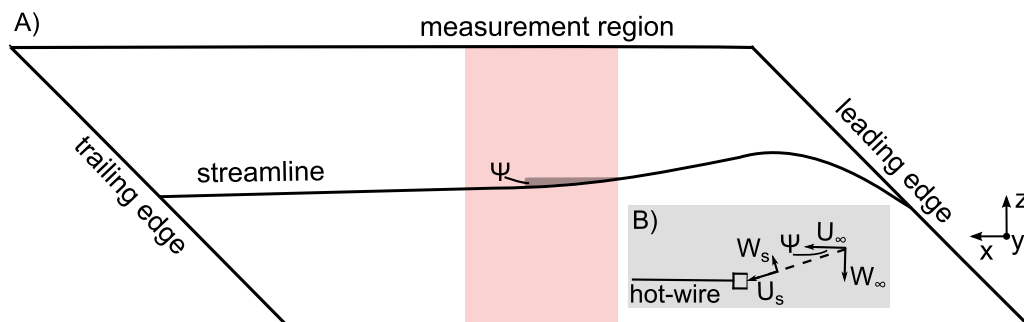
In Figure 23 the development of the vortices is shown for both roughness distributions. The stationary crossflow vortices grow downstream after which the periodic structure is less prominent, indicating that the flow is becoming turbulent. The vortices appear at different locations along the span when moving downstream which shows that the inviscid streamlines are not completely aligned with the x-axis, as illustrated in Figure 24. Since the single hot-wire is aligned with the x-axis, the streamwise velocity  $U$  is measured while the spanwise velocity,  $W$ , will not be measured due to blockage of the hot-wire prones. If the streamline angle is large the obtained results could be wrongly interpreted since then the  $W$  component of the velocity vector could not be ignored. The streamline angle,  $\Psi$ , could be estimated by manually following vortices downstream. For the cylindrical roughness elements, the two vortices at  $x/c=0.36$  at  $Z=56-80\text{mm}$  seem to appear at  $x/c=0.41$  at  $Z=50-74\text{mm}$ . From this shift in  $Z$  and the known distance in  $x$  the streamline angle can be determined. Mathematically, this is achieved by cross-correlating the negative part of the spanwise gradient fields (Figure 25) for the different  $x/c$  locations. The cross-correlation gives a most probable shift in  $Z$ ,  $\Delta Z$  and then the streamline angle is calculated with:

$$\Psi = \frac{\Delta Z \cos \Lambda}{\Delta x}, \quad (4.21)$$

where  $\Lambda$  is the geometric sweep angle in degrees. In Table 4.1 the obtained streamline angles are given for the cylindrical roughness distribution. The streamline angles are all negative and close to 6 degrees. At  $x/c=0.46$  the vortices and therewith the gradient fields are less defined resulting in odd values for the streamline angles. This shows that this cross-correlation technique to estimate the streamline angle only



**Figure 23.** Streamwise velocity fields for the cylindrical (left) and pyramidal (right) roughness distributions.

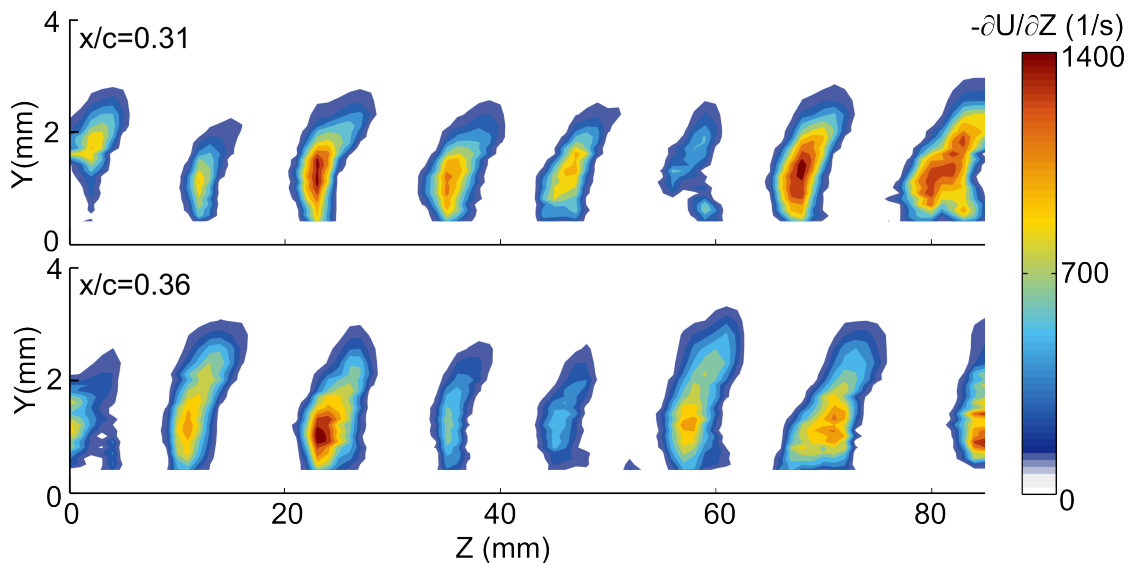


**Figure 24.** A) Sketch of streamline on swept wing model. B) Different velocity components measured by the hot-wire.

works when the vortices are well defined. The same analysis was carried out for the pyramidal roughness distribution and similar streamline angles were obtained. A streamline angle of 6 degrees is small and indicates that the hot-wire is almost

**Table 4.1.** Estimation of streamline angle  $\Psi$ .

	$x/c=0.31$	$x/c=0.36$	$x/c=0.41$	$x/c=0.46$
$x/c=0.31$	-			
$x/c=0.36$	$-6.06^\circ$	-		
$x/c=0.41$	$-6.06^\circ$	$-5.52^\circ$	-	
$x/c=0.46$	-	$3.23^\circ$	$-5.75^\circ$	-

**Figure 25.** Spanwise gradient distributions used to estimate the streamline angle,  $\Psi$ .

parallel to the streamline. The exact ratio of the crossflow velocity and streamwise velocity inside boundary layer is unknown since the crossflow velocity profile has not been measured. In previous studies the crossflow component was measured (Deyhle and Bippes, 1996; Kurian et al., 2011; Serpieri and Kotsonis, 2016b). The velocity did not exceed 8% when the stationary crossflow vortices were fully developed. Therefore, the small streamline angle in the current study ensures that the obtained results can be interpreted as streamwise velocity fields, keeping in mind that a small fraction of the velocity magnitude will be caused by the wall-normal component as explained earlier in Section 2.4.4.

The spanwise averaged velocity profiles at  $x/c=0.31$ , Figure 26, show that the mean flow is laminar. When moving downstream, the velocity profiles show more momentum close to the wall indicating transition to a turbulent boundary layer. In Figure 26 the solutions from the BL2D code<sup>3</sup>, discussed in Appendix A, are shown in red. The input for this code was the interpolated pressure distribution from the static

<sup>3</sup>Qinetic (unpublished)

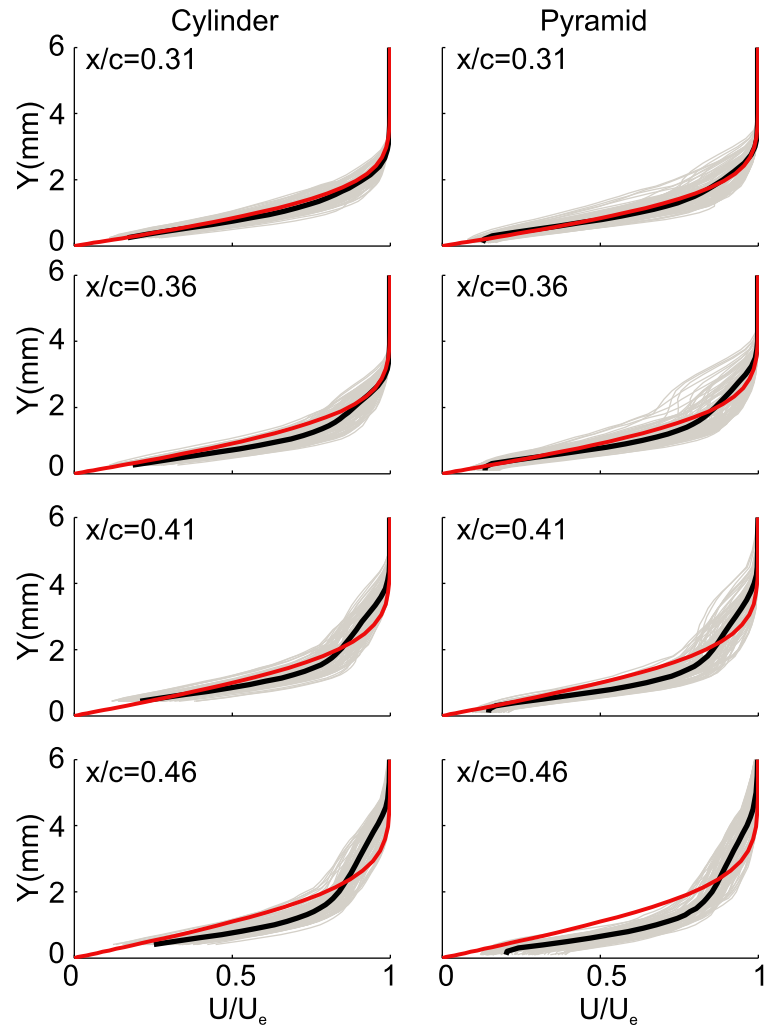


**Figure 26.** The measured streamwise velocity profiles at different spanwise locations for all chordwise locations. In light gray the spanwise averaged velocity profile are shown. In black the spanwise averaged profile and in red the velocity profiles obtained with the boundary layer code solver (BL2D) is shown.

pressure ports on the flat plate. Considering that this interpolation already introduces an error, the experimental and computational velocity profiles show reasonable agreement at the first measurement location. When moving downstream the computed results deviate from the experimental results. This is due to the mean flow distortion which creates non-linear effects, not taken into account in the numerical computations.

The stationary mode shapes, shown in Figure 27, also illustrate the onset of the non-linear effects at  $x/c=0.36$ . The secondary lobe in the upper part of the stationary mode shape indicates the roll-over of the vortex as discussed in (Reibert et al., 1996). Due to the coarse streamwise resolution of  $0.05x/c$  it is difficult to determine where the stationary modes exactly saturate and if there is a difference between this saturation location in the cylindrical and pyramidal roughness distribution.

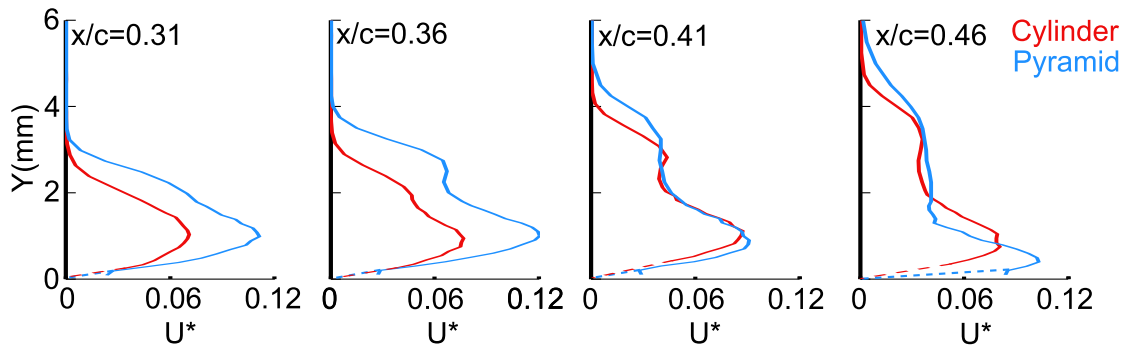


**Figure 27.** Stationary mode shapes for the different roughness distributions.

The main difference between the roughness distributions is the difference in wavelength content. To be able to focus on this aspect, the spatial power spectra were determined from the time-averaged velocity fields. In Figure 28 the spectra at  $x/c=0.31$  are shown for each wall normal location (light gray) and superimposed with the maximum at each wavelength (black). The maximum is clearly located around  $\lambda=11.5\text{mm}$  for the two cases with roughness, while for the natural case the energy is centered around  $\lambda=15\text{mm}$ . The energy for the natural case is spread over a larger area, while for the cylinder and pyramid it is more focussed around  $11.5\text{mm}$ . This is expected since in the natural flow no forcing is applied such that all unstable modes are amplified. From linear stability analysis it follows that the stationary waves with a wavelength ranging from  $9\text{-}15\text{mm}$  have a similar amplification, which is directly shown in the spatial power spectrum. It should be noted that the resolution decreases with increasing wavelength; at  $\lambda=11.5\text{mm}$  the resolution is  $1.6\text{mm}$ , at  $\lambda=20\text{mm}$  it is  $4.8\text{mm}$  and at  $\lambda=30\text{mm}$  it is  $10.8\text{mm}$ . To have further insight on the spreading of energy over the different wavelengths, the total energy was represented by the area underneath the spectrum with the trapezium rule. The area of each wavelength band was then divided by the total energy. The results did not change. The energy for the pyramidal roughness elements is larger at  $\lambda = 11.2\text{mm}$  than for the cylindrical elements. For the natural case now it is clearly shown that the energy is more spread as no selective forcing at a specific wavelength is applied. In

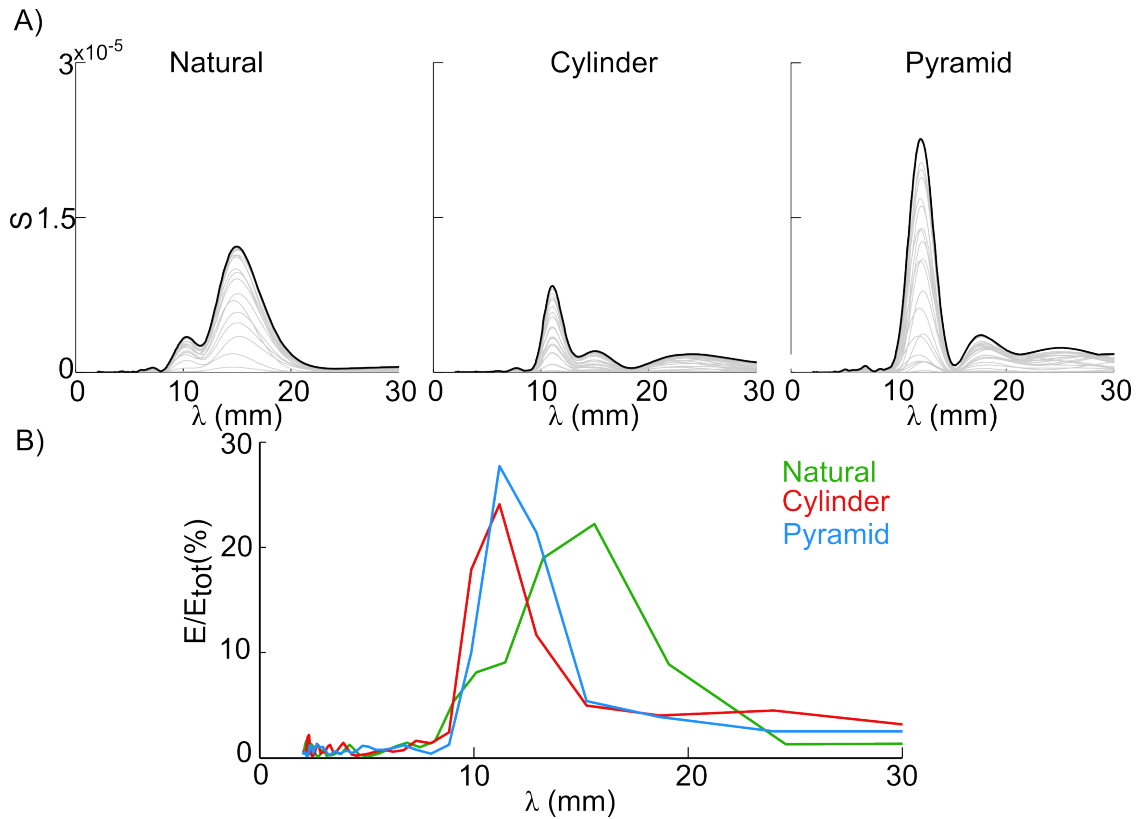


**Figure 28.** Spatial power spectra for the different roughness distributions. A) In light gray the spectra are shown for each wall normal location. In black the maximum at each wavelength is shown. B) The spatial power spectra normalized by the total energy.

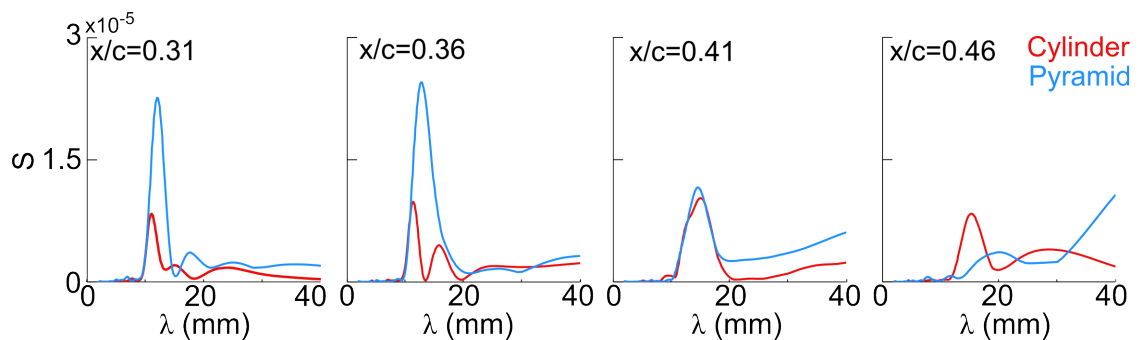


**Figure 29.** Spatial spectra for all chordwise locations.

Figure 29 the change in energy content over the different wavelengths is shown as a function of  $x/c$  locations. The trends are similar for both roughness distributions. Going downstream, the energy spreads to higher wavelengths, which indicates that the coherency of the stationary vortices diminishes when the flow becomes saturated. In previous studies this has not been mentioned since the spatial spectra are not shown in this later stage of the transition process (Reibert et al., 1996; Hunt and Saric, 2011; Eppink, 2014). At  $x/c=0.36$  two peaks are observed for the cylin-

der one around 11.5mm and one around 15mm. From the mean flow distribution in Figure 23 it is observed that at this location the vortices start merging together leading to this larger wavelength. In all spatial spectra, there is almost no energy in the modes with a wavelength of  $\lambda/2$  and  $\lambda/3$ . This is interesting since in previous crossflow studies (Reibert et al., 1996; Hunt and Saric, 2011; Eppink, 2014) these harmonics of the forced mode were observed. From Hunt and Saric (2011) the ratio between the energy in the fundamental and that of the harmonics measured at  $x/c=0.1$  depended on the Reynolds number. The Reynolds number changes the stability characteristics and at some Reynolds numbers the harmonics of the forced mode might be amplified. This indicates that the appearance of the harmonics in this study is due to the coupling of the wavelength content of the roughness distribution and the amplified modes in the natural flow. From Reibert (1996) the growth of the harmonics is only observed far downstream of the forcing, which indicates that the appearance of the harmonics is not a direct result of the forcing of the harmonics through the roughness distribution but instead caused by the non-linear interactions as predicted computationally by Reed (1988). In the current study the stronger forcing in the roughness distribution at the harmonics for the cylindrical elements compared to the pyramidal elements (see Figure 12) is not reflected in the response of the flow far downstream of the forcing. Instead, the forcing at the spanwise wavelength  $\lambda$  dominates the response of the flow. From the linear stability analysis results shown in Figure 9, it is found that only waves with a wavelength larger than 9.25mm are excited at the measured  $x/c$  locations, which means that the harmonics of the 11.5mm mode are not naturally excited. This is also observed in the spatial spectra of the naturally excited flow where there is almost no energy for modes with  $\lambda < 9$ mm. The non-linear interactions and wave doubling phenomenon, as observed in Reibert et al. (1996) and Reed (1988) have not been observed here.

From the analysis on the mean flow it is not directly clear what the effect of the wavelength content is on the transition process and therefore the fluctuating flow is analysed. Even though it is not expected that the roughness directly forces the travelling modes it does give insight in how the flow develops and eventually transitions into turbulence. The frequency bands which are dominating the flow are identified by following one vortex downstream and computing the power spectra at different locations inside the vortex. Here only the cylindrical roughness distribution will be discussed, but the same frequency bands were found for the pyramidal distribution. From the Reynolds-Orr equation (see Chapter 1) it follows that the wall-normal and spanwise shear caused by the mean velocity field are essential in the production

terms of the streamwise disturbances. Therefore, the power spectra are calculated where the wall normal shear and spanwise shear is maximal. From previous studies it has also been found that a specific type of secondary crossflow instabilities is located at the top of the vortex, which is discussed in detail in Chapter 5. For this reason the power spectrum is also calculated in one point at the top of the stationary vortex.

In Figure 30 the power spectra for the first chordwise measurement station are presented. No large differences are found in the spectra between the different locations in the vortex. Most of the energy in the flow is concentrated in a low-frequency

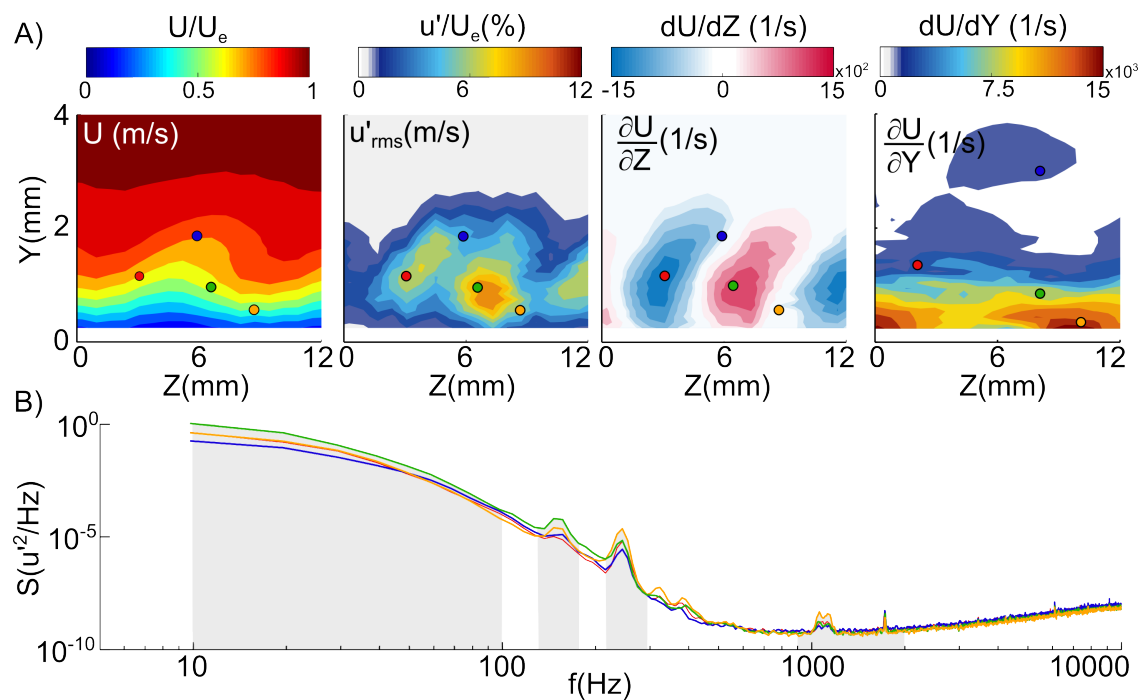


**Figure 30. Power spectra at different locations inside a stationary vortex at  $x/c=0.31$ .** A) Distribution of mean velocity, wall normal and spanwise gradient. The coloured dots represent the location where the power spectra are taken. B) Power spectra at different locations in the vortex. The color of the line corresponds to the color of the dot in A). The grey-shaded areas correspond to the frequency bands which are discussed in more detail in Figure 32.

band (10-100Hz). In Figure 31 the range between 2-100Hz is shown with a frequency resolution of 1Hz. While no distinct peaks are shown the energy content is especially large in the region upto 20Hz. A similar observation was made in crossflow studies by Kawakami et al. (1999), Eppink (2014) and Serpieri and Kotsonis (2016b), while in other studies such as White and Saric (2005) and Chernoray et al. (2005) the low-frequency band is not as high in energy. In Serpieri and Kotsonis (2016b) the low-frequency band is analysed through a proper orthogonal decomposition of tomographic PIV measurements. It is concluded that the energy in the low-frequency

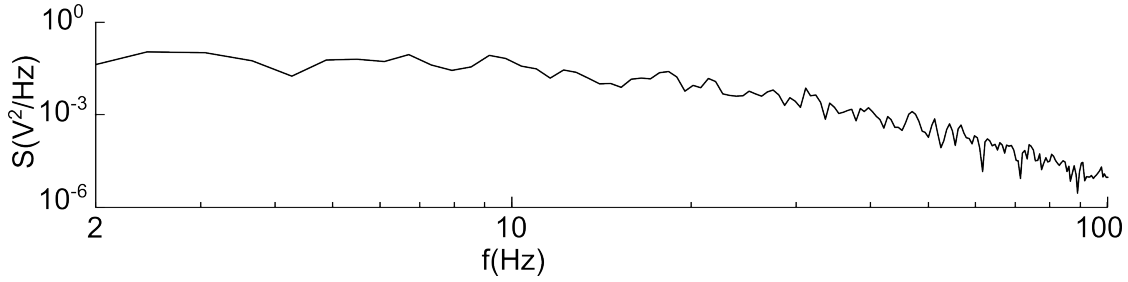


**Figure 31.** Power spectra from 2-100 Hz with  $\Delta f=1\text{Hz}$

band is caused by an oscillation of the stationary modes. While the source of the oscillations might be related to the specific experimental set-up, it is concluded that this low-frequency mode does not play any role in the transition process. In Chapter 3, it was found that, for the current set-up, the high energy in this low-frequency band is due to the blockage caused by the displacement bodies and that the fluctuations are due to acoustic noise and vibrations. In Figure 32B the spatial distribution of the low-frequency fluctuations is shown. The velocity fluctuations reach levels up to 10% of the edge velocity.

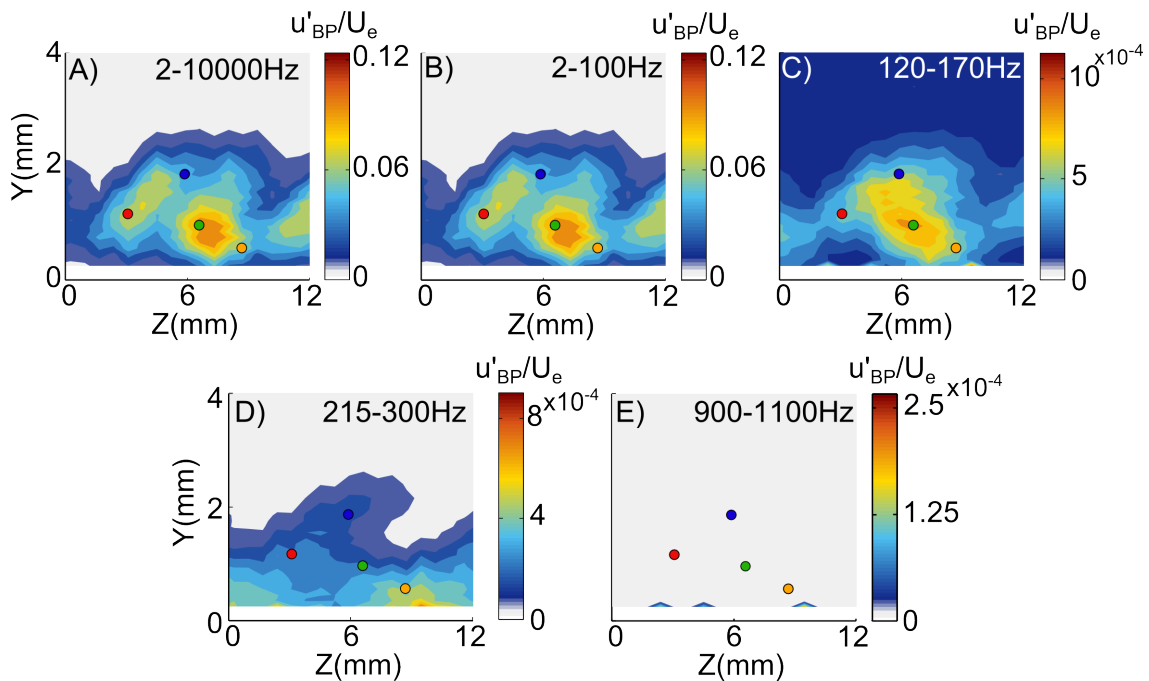


**Figure 32.** Spatial distribution of travelling waves for different frequency at  $x/c=0.31$ .

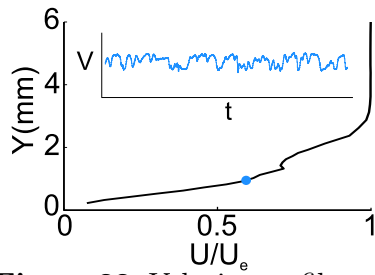


**Figure 33.** Velocity profile and time signal at maximum fluctuation level.

In a conventional flat plate boundary layer these levels of fluctuations would be defined as a fully turbulent flow (Klebanoff, 1955). However, when the mean velocity profile and time signal are analysed at the location of maximum fluctuations, as shown in Figure 33, it is clear that the flow is still laminar. Again, this confirms that the main contribution of the fluctuation energy is not attributed to travelling waves inside the boundary layer but instead is caused by

low-frequency noise inside the experimental set-up. Even though the level of fluctuations, presented in Figure 32A and 32B, seems to be larger than in previous experimental studies, the spatial distribution with respect to the time-averaged mean flow is similar (Downs, 2012; Serpieri and Kotsonis, 2016b). In these studies a region of high fluctuations is found in the upwelling and downwelling part of the vortex structure. Next to the fluctuations in the low-frequency band, other waves are identified in the power spectra shown in Figure 30. These waves could be identified as a Tollmien-Schlichting wave, a travelling primary crossflow wave or a low-frequency secondary instability. It is unlikely that these are secondary instabilities, since the mean flow is not significantly distorted yet and the crossflow vortices are still growing.

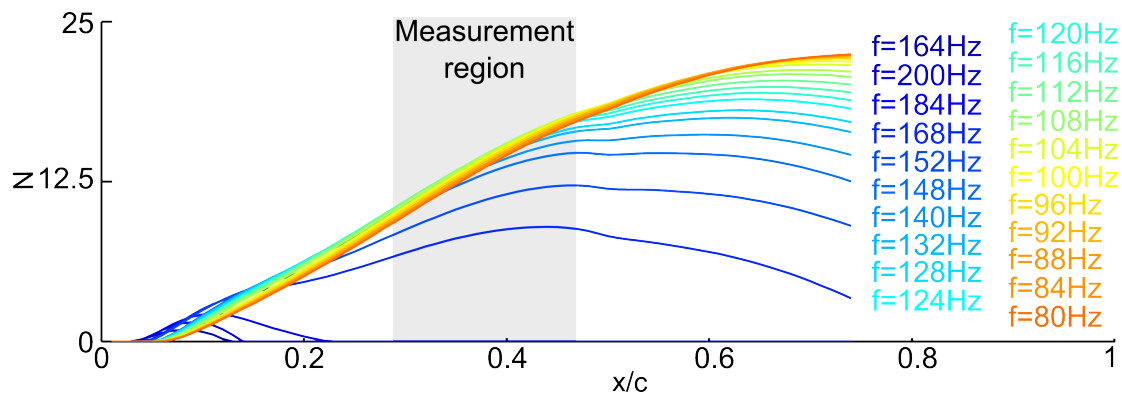


**Figure 34.** N-factor curves for the travelling crossflow waves obtained from linear stability analysis with the experimental pressure distribution.

The spatial distribution of the 120-170Hz velocity fluctuations (Figure 32C) shows that the fluctuations are aligned with the stationary vortex structures. The linear stability analysis for the travelling crossflow waves, carried out with the experimental pressure distribution, is presented in Figure 34. It is shown that in the measurement region travelling waves with frequencies from 80-200Hz are amplified. The wavelengths of the travelling waves are 15-20mm which is larger than the stationary structure. This indicates that the 120-170Hz fluctuations could be travelling

crossflow waves which are modulated by the stationary crossflow waves. The spatial distribution shows that the maximum is in the middle of the boundary layer, while for the Tollmien-Schlichting wave it would be expected to be close to the wall. Similar distributions were found by Malik et al. (1994), Deyhle and Bippes (1996), Högberg and Henningson (1998), White and Saric (2005) and Serpieri and Kotsonis (2016b). This mode is attributed to the modulation of the travelling waves due to the interaction with the stationary modes and is also referred to as a Type-III secondary instability. The mode appears due to the distortion of the mean flow, which changes the stability characteristics. From these observations it is concluded that the wave with a frequency of 120-170Hz, presented here, is a travelling crossflow wave. In a low-turbulence wind tunnel the transition process is expected to be dominated by stationary crossflow waves (Deyhle and Bippes, 1996; Downs, 2012), however, travelling crossflow waves can still be present in the flow (White and Saric, 2005; Serpieri and Kotsonis, 2016b; Eppink, 2014). As will be seen shortly, the 120-170Hz mode does not develop further, which indicates that the transition process is not caused by the travelling waves in this frequency band.

The fluctuations of the travelling wave with a frequency around 250Hz are located close to the wall in between two vortex structures as shown in Figure 32D. In these locations the contours of the time-averaged velocity  $U$  are close together, indicating high wall-normal shear. The gradient field of the mean velocity in the wall normal direction presented in Figure 30, shows an almost identical spatial structure as the fluctuation field in Figure 32D, which is also confirmed by a correlation coefficient of 0.92 between both distributions. The high correlation with the wall-normal shear indicates that the wave in this frequency band is a Tollmien-Schlichting wave. However, the linear stability analysis predicts a slightly lower frequency and later appearance of this mode. It is difficult to exactly define the nature of this mode, however, this mode does not seem to play a large role in the transition process. Another peak in the power spectrum is identified around 1000Hz. The spatial distribution of this mode, shown in Figure 30E, does not exhibit a clear coherent structure. Furthermore, no growth was observed downstream. Together these observations indicate that this frequency band is most probably due to noise and is not related to the flow. The same can be concluded for the small peak of 1600Hz. From 5kHz-10kHz there is an increase in energy. This increase is related to the cut-off frequency of the low-pass filter at 10kHz. The filter has a decay and therefore the travelling waves and noise, with a frequency slightly higher than 10kHz, can be shown in the spectrum due to aliasing.

At the second chordwise location, no significant differences in the spectra were found

compared to the first location and these are therefore not shown here. The spectra for the third chordwise location,  $x/c=0.41$ , are presented in Figure 35 and show that there is a substantial growth of a high-frequency band from 900-3000Hz. At

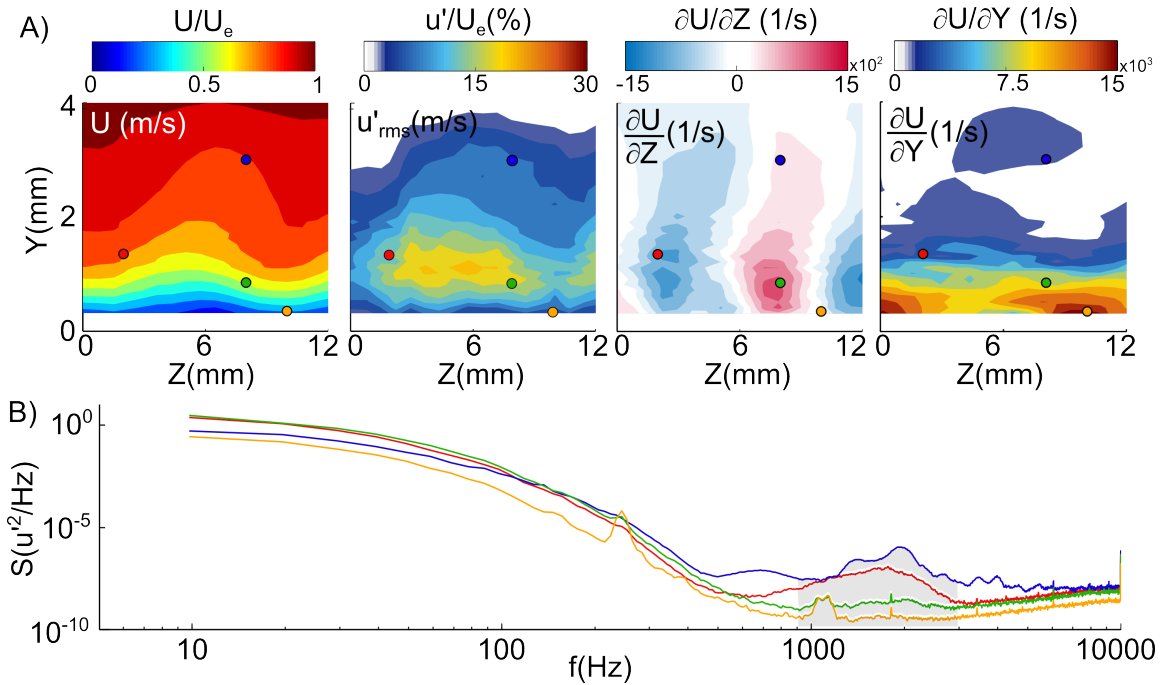


**Figure 35. Power spectra at different locations inside a stationary vortex at  $x/c=0.41$ .** A) Distribution of mean velocity, wall normal and spanwise gradient. The colored dots represent the location where the power spectra are taken. B) Power spectra at different locations in the vortex. The color of the line corresponds to the color of the dot in A). The fluctuations in the grey-shaded area are discussed in the text.

this chordwise location the mean velocity profiles are distorted (Figure 26). Based on the high-frequency, it is concluded that the increase in energy is due to the secondary instability which grows and eventually leads to a turbulent boundary layer. By comparing Figure 35 and 36A, it is observed that the magnitude of this frequency band is large in the upwelling region of the vortex. Previous studies found the Type-I secondary instability in the upwelling region of the stationary vortex which was aligned with the spanwise gradient,  $\partial U/\partial Z$  (Malik et al., 1999; Kawakami et al., 1999; White and Saric, 2005; Serpieri and Kotsonis, 2016b). Here this alignment is not so obvious. This aspect of the secondary instability will be discussed in more detail in Chapter 5. In the previous studies it was also found that, even if the dominating secondary instability is the Type-I instability, the Type-II and Type-III instabilities could still be present in the flow. In White and Saric (2005) it is suggested to analyse the fluctuating velocity in narrow frequency bands, to be able to distinguish between the different types. For this reason, the 900-3000Hz band was divided into narrow

frequency bands and the spatial distribution of each of the bands was analysed as presented in Figure 36B,C,D and E. It is shown that the fluctuations lie in the same region for each of the frequency bands, which confirms that the dominating secondary instability is the Type-I instability. Type-II instabilities with low energy levels and a similar frequency as the Type-I instability could still be present in the flow. With single hot-wire anemometry measurements it is not possible to distinguish between waves with the same frequency and the wave with the largest amplitude is detected. White and Saric (2005) showed that the roughness height changed the secondary instability mode from Type-I to Type-II. The spatial distribution of the secondary instability was similar for both the cylindrical and pyramidal roughness distribution, which suggests that the variation in wavenumber content of the distributions does not cause a different secondary instability mechanism to appear. Next

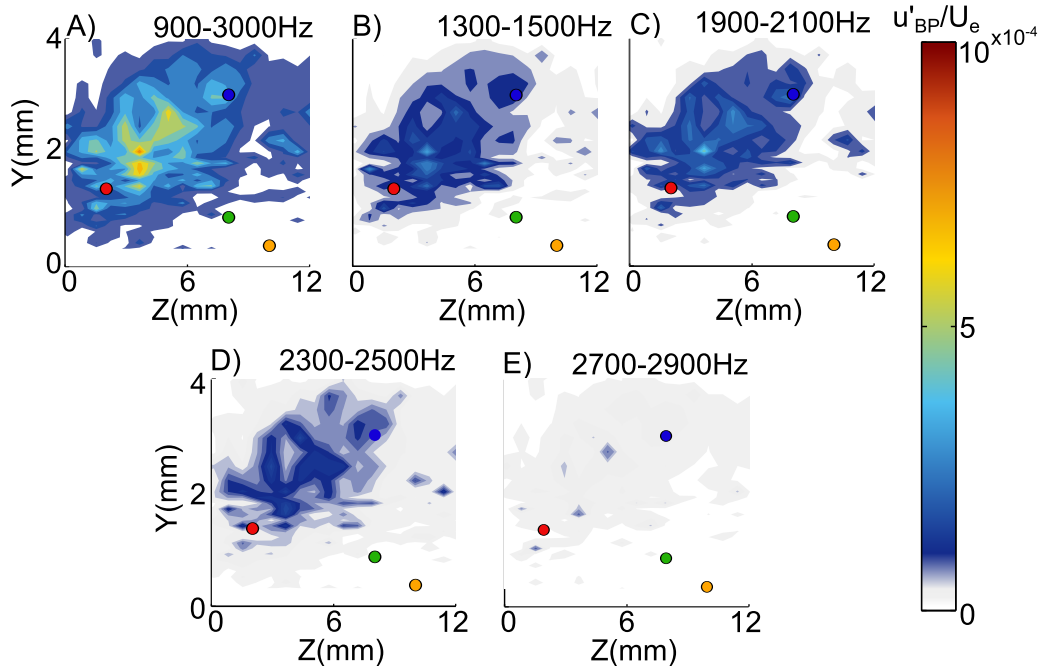


**Figure 36.** Spatial distribution of travelling waves for different frequency bands between 900-3000 Hz at  $x/c=0.40$ .

to the high-frequency travelling waves, the 250Hz mode is still clearly visible in the power spectrum at the location where the wall normal gradient is large. The energy level is very similar to the first location which indicates that the wave did not experience significant growth, furthermore the transition process is not dominated by this travelling disturbance.

The spectra at the final chordwise location, presented in Figure 37 show that the energy in the high-frequency band has grown significantly and no clear peaks can

be distinguished. The flow is almost fully turbulent at this location. The  $u'_{rms}$  has now one maximum in the middle of the structure, which seems to be a direct result of different vortices merging together.

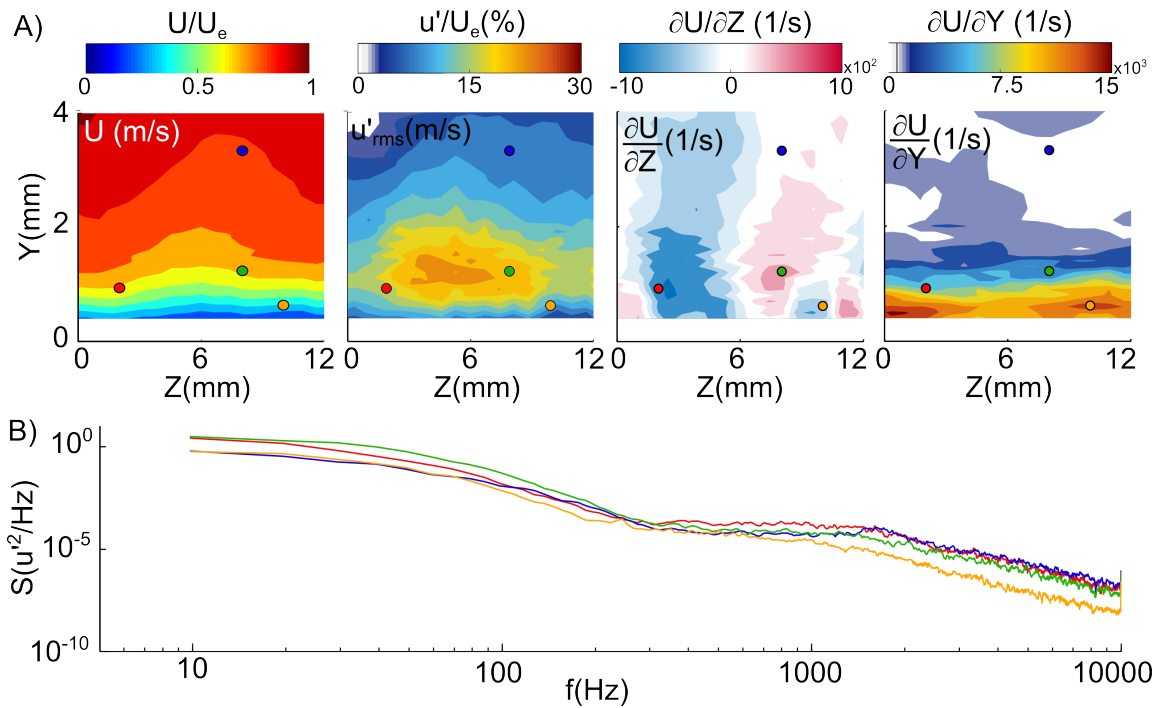


**Figure 37. Power spectra at different locations inside a stationary vortex at  $x/c=0.46$ .** A) Distribution of mean velocity, wall-normal and spanwise gradient. The colored dots represent the location where the power spectra are taken. B) Power spectra at different locations in the vortex. The color of the line corresponds to the color of the dot in A).

### 4.6.2. x-scans

In addition to the YZ-scans, the x-scans were measured to study the development of the flow in more detail and to determine at which location the flow transitions into turbulence. The x-scans were taken at constant wall-normal location at diffe-

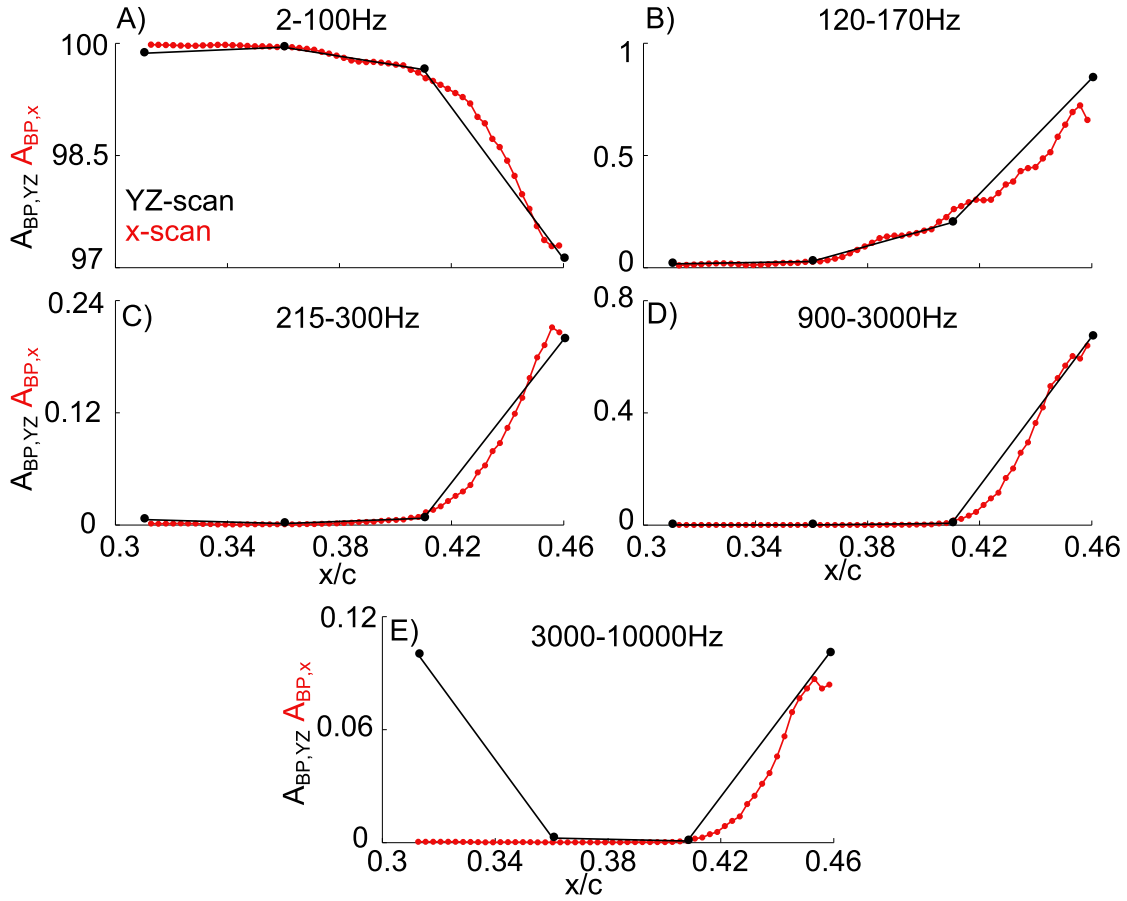


**Figure 38.** Comparison of the growth of the travelling waves obtained with the x-scan (red) and YZ-scan (black) for the cylindrical roughness distribution.

rent x-locations for three different spanwise positions (Figure 14). Due to the small streamline angle, discussed in Section 4.6.1, and the non-uniformity in the spanwise direction, the x-scan measurements cut through different stationary vortices when going downstream. Therefore, it is not evident that the one-point measurements of the x-scan represent the development of the three-dimensional flow. To determine if the x-scans can describe the development of the flow, the amplitude of the fluctuations in the dominating frequency bands, as defined in Figures 30 and 35, has been calculated for both the YZ and x-scan at each streamwise location. The results, for the cylindrical roughness distribution, are presented in Figure 38. Similar trends were obtained for the pyramidal roughness distribution. The amplitudes  $A_{BP,YZ}$  and  $A_{BP,x}$  have been calculated as described in Section 4.5. For the x-scan, each point re-

presents the amplitude averaged over the three spanwise locations. Figures 38A,B,C and D, show that the trends for the YZ-scan and x-scan are similar. Only the amplitude at the first measurement location in Figure 38E, does not match between the x-scan and YZ-scan. The spatial distribution of the fluctuations in the 3-10kHz band for the YZ-scan, revealed that at measurements close to the wall the fluctuation level was high. The power spectrum at such measurement location, presented in Figure 39, shows the high noise level in the 3kHz-10kHz frequency band. This

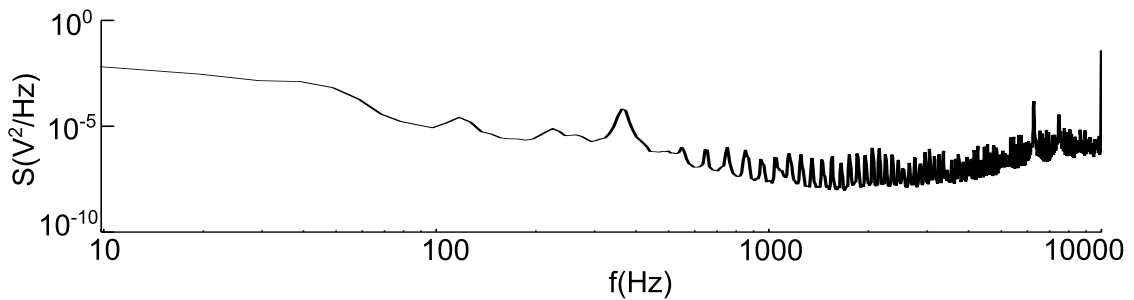


**Figure 39.** High-frequency noise on a measurement close to the wall.

suggests that the signal was probably corrupted at these locations due to probe-wall interference. At streamwise locations further downstream the noise disappeared and the amplitude becomes comparable for the x-scan and YZ-scan (Figure 38E). The similar trends for the x-scan and YZ-scan across all frequency bands, presented in Figure 38A-E, shows that the x-scans are representative for the three-dimensional development of the flow. The x-scans are therefore analysed, to compare the development of the flow for the cylindrical and pyramidal roughness distribution in more detail. In Figure 40 the amplitude of the fluctuations are shown for the cylindrical and pyramidal roughness distribution. For the 2-100Hz and 120-170Hz frequency bands the onset of growth and total growth are very similar. The relative energy in the 2-100Hz frequency band decreases, which indicates that the energy in other frequency bands increases. The energy growth in the 120-170Hz band does not represent the growth of the 120-170Hz travelling waves shown in Figure 32. Instead, it is due to the general increase in fluctuations of the flow, as is shown in Figure 35 and 37. For the frequency bands from 0.215 to 10kHz, presented in Figures 40C to F, the differences between the two roughness distributions become more apparent and the following observations are made:

- For the 0.9kHz-3kHz frequency band, the fluctuations start to grow at  $x/c=0.38$  for the pyramid and at  $x/c=0.41$  for the cylinder as shown in Figure 40E. The energy of the fluctuations becomes higher for the cylinder at  $x/c=0.42$ . The fluctuations in this frequency band are associated with the secondary instability as shown in Figure

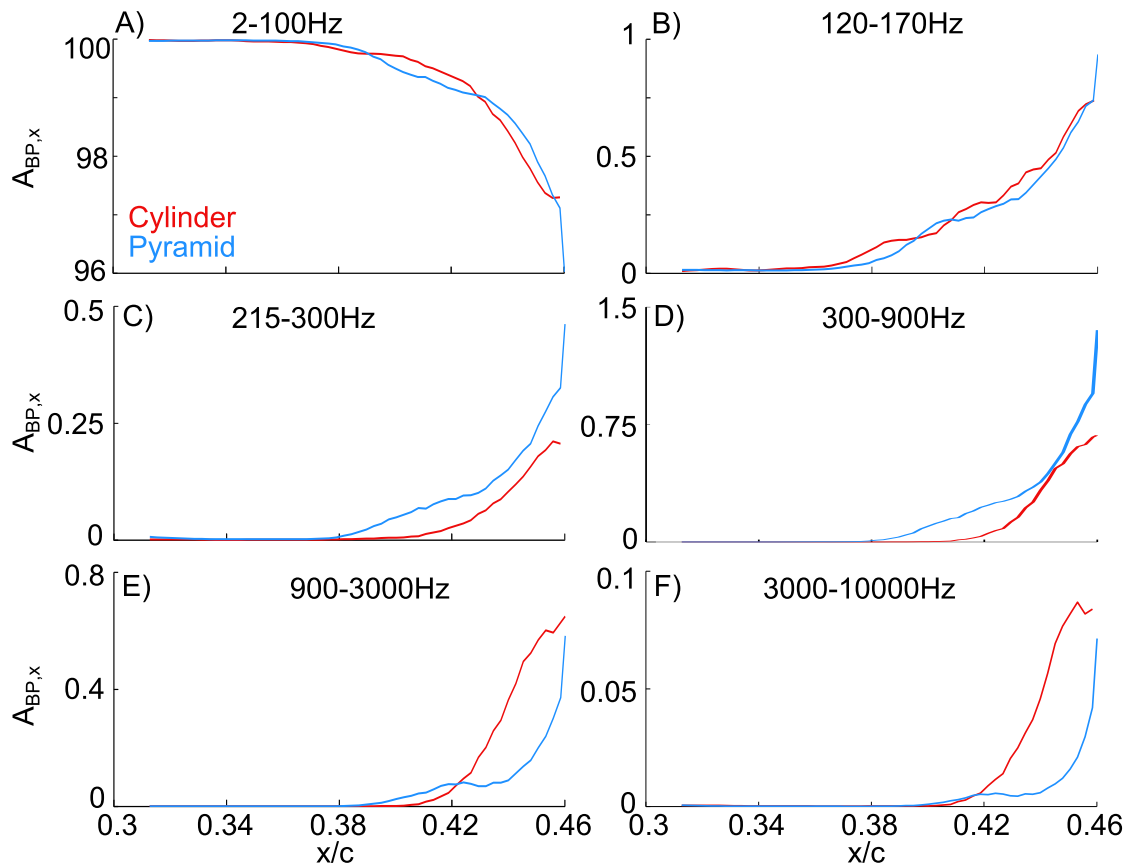


**Figure 40.** Growth of travelling waves for the cylindrical and pyramidal roughness distributions obtained with the x-scan.

35 and 36.

- The location where the fluctuations in the 215-300Hz band and 300-900Hz band start to grow is the same location as where the secondary instability starts to grow. This shows that the increase in the 215 to 900Hz fluctuations is due to the breakdown process of the flow, where eventually the energy in all frequencies increases.
- For the fluctuations in the 0.9kHz-3kHz and 3kHz-10kHz frequency band, the amplitude of the cylinder increases rapidly from  $x/c=0.41$ , which is the location where the secondary instability starts to grow. Since  $A_{BP,x}$  is the energy in a certain frequency band scaled with the total energy, the higher value for the cylinder, compared to the pyramid shown in Figure 40E and F, is attributed to the lower value in the 215-300Hz and 300-900Hz band. Another way to understand the development of the flow is by calculating intermittency function,  $\gamma$ , as described in Section 4.5. The intermittency is determined from the x-scan measurements at each streamwise location and averaged over the three spanwise locations. In Figure 41 the development of  $\gamma$  is presented for the cylinder and pyramid. The trend is similar as shown in Figure 40. The actual magnitude of  $\gamma$  depends on the chosen threshold as explained

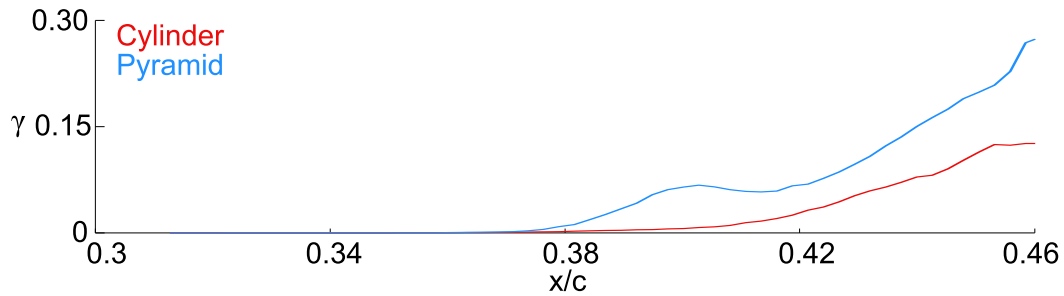


**Figure 41.** Intermittency function for different chordwise locations obtained from the x-scan.

in section 4.5, which is kept fixed for the cylinder and pyramid. It is clear that the onset of growth is earlier for the pyramid and the value remains larger going downstream. This indicates that the flow transitions earlier for the pyramidal roughness distribution.

## 4.7. Conclusions on forcing of the primary instability

In this Chapter the influence of forcing through different roughness shapes (cylinder and pyramid) on the development of the crossflow instability is studied. Roughness elements of the same height were placed at a spanwise spacing of 11.5mm. From the analysis of the mean and fluctuating flow the following conclusions are discussed:

- The stronger forcing through the pyramidal roughness distribution leads to a stronger response of the flow and larger stationary mode amplitudes as expected from Fourier theory. The spatial power spectra show that the relative energy content in the 11.5mm wavelength band is larger for the pyramid than for the cylinder.
- The stronger forcing at the harmonics through the cylindrical roughness distribution is not reflected in the response of the flow since these modes are not amplified in the natural flow.
- From the fluctuating flow it is found that the stronger forcing at the most unstable wavelength leads to earlier growth of the secondary instability and breakdown of the flow. This shows that a subtle change in roughness distribution due to shape can change the transition process from a laminar to turbulent boundary layer. The results imply that next to height measures of a surface roughness distributions the power spectral content is also of great importance.



# 5

## **Secondary instability and breakdown to turbulence**

## 5.1. Introduction

In Chapter 4 the development of the primary instability has been studied. It was found that when the mean flow is highly distorted a high-frequency secondary instability appears which causes breakdown of the flow. In this chapter the focus is on the origin and development of this secondary instability with and without forcing from the wall and freestream. The chapter starts with the literature review, after which the design of the excitation mechanisms are shown. The data analysis of the exciter data in particular is described in Section 5.5. In the last two sections the results are discussed and conclusions are drawn.

## 5.2. Background

### 5.2.1. Origin and development of the secondary instability

In the experiment of Poll (1985) the flow over a cylinder with a variable sweep angle was investigated with hot-wire measurements. In Figure 1 the time traces measured by Poll (1985) inside the boundary layer are shown for increasing Reynolds number when the sweep angle of the cylinder was  $63^\circ$ . For the lowest Reynolds number tested the flow was laminar and a fundamental wave of 1100Hz is shown. When the Reynolds number increases high frequency disturbances ride on top of these fundamental waves. Increasing the Reynolds number made the flow completely turbulent. The high-frequency riders just prior to transition were the first observation of the secondary crossflow instability.

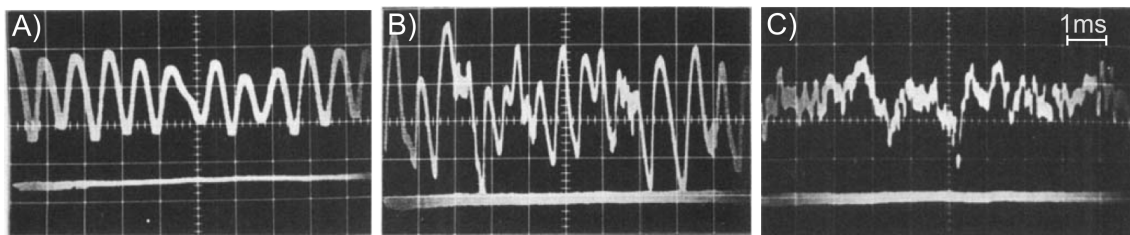


**Figure 1.** Hot-wire time traces for A)  $Re=0.9 \times 10^6$  B)  $Re=1.18 \times 10^6$  C)  $Re=1.65 \times 10^6$ . Figure taken from Poll (1985).

The first detailed measurements on the origin of the secondary instability in three-dimensional boundary layers were carried out by Kohama et al. (1991). With hot-wire measurements they found that the secondary instability appeared when the streamwise velocity profiles had multiple inflection points in the wall-normal direction, caused by the growth of the stationary crossflow instability as schematically

depicted in Figure 2.

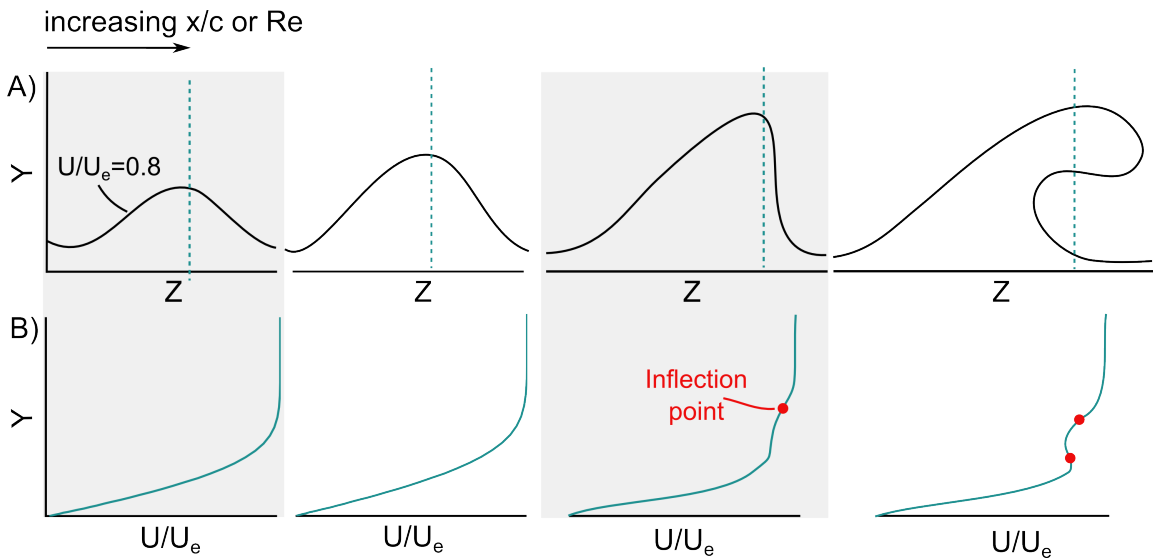


**Figure 2. Development of the primary crossflow instability leading to inflection points in the mean velocity profiles.** A) Mean velocity contour,  $U/U_e=0.8$ , contour of a stationary crossflow vortex for, from left to right, increasing streamwise location or Reynolds number. B) Mean velocity profile at the spanwise location  $Z$  corresponding to the dotted line in A.

As explained in Chapter 1 the inflection points are a source of an inviscid instability following the Rayleigh inflection-point theorem. The inviscid character of the secondary instability has been shown by Chernoray et al. (2005) who found that the secondary instability fluctuations were aligned with the critical layer. In computations by Malik et al. (1999) it has been shown there are two types of high-frequency secondary instabilities. Following the Reynolds-Orr equation, the energy production mechanisms of so-called Type-I and Type-II instabilities are the shear layer of the mean streamwise velocity in the spanwise,  $\partial U/\partial Z$ , and wall-normal,  $\partial U/\partial Y$  direction respectively. Therefore, next to the wall-normal inflection points of the streamwise velocity profile, inflection points of the streamwise velocity profile in the spanwise direction,  $U(z)$ , also have to be considered. Chernoray et al. (2005) studied the breakdown of a vortex created by a single roughness element. They found that, even though the streamwise profiles were not significantly distorted, a secondary instability was created due to the inflection point in the crossflow velocity profile. While the measurements from Chernoray et al. (2005) seem reliable it seems strange that the inflection point in the crossflow profile would cause a convective instability in the streamwise direction. Different types of secondary instabilities are presented here as isolated cases, however, in practice all modes can exist simultaneously, as has been found experimentally by Kawakami et al. (1999); White and

Saric (2005); Serpieri and Kotsonis (2016b). In these studies it was found that the breakdown process is mostly caused by Type-I instabilities located in the upwelling region of a vortex. White and Saric (2005) found that the Type-II instabilities have a frequency approximately twice as high as the Type-I instabilities. Next to the high-frequency Type-I and Type-II instabilities a low frequency Type-III instability has been identified by computational studies of Fischer and Dallmann (1991) and Janke and Balakumar (2000) and experimentally observed by Deyhle and Bippes (1996) and Serpieri and Kotsonis (2016b). This mode appears due to growing nonlinear disturbances, when the primary vortex saturates. The disturbances modify stable modes in the undisturbed mean flow to become unstable. The spatial distribution of this Type-III instability is on the downwelling side of the vortex, coinciding with the location where the  $dU/dZ$  are maximum. While the mechanisms by which the secondary instability grows have been generally understood, the location of the onset of the secondary instability has been less defined. When the primary instability starts to develop the mean flow distorts and an inflection point in the  $U(z)$  profile appears indicating that a Type-I instability should appear shortly after. However, from computational and experimental studies this has not found to be the case. Instead, the secondary instability starts to grow further downstream when the mean flow is distorted significantly, such that also the wall-normal velocity profiles have inflection points (White and Saric, 2005) and consequently the amplitude of the spanwise shear exceeds some maximum value (Bippes, 1999). Criteria to predict this critical condition are scarce. Wassermann and Kloker (2002) proposed a Reynolds number variation  $\Delta Re_{loc} = \Delta U(y_0, z_0) \frac{y_0}{\delta_1}$ , where  $(y_0, z_0)$  is the location where  $dU/dZ$  is minimum,  $\delta_1$  the displacement thickness and  $\Delta U(y, z) = U(y, z) - \bar{U}(y, z)$ , where  $\bar{U}(y, z)$  is the streamwise velocity profile averaged in the spanwise direction. They find a criterion of  $\Delta Re_{loc} \leq -0.3$  for the onset of the secondary instability. This criterion has, to the authors knowledge, not been confirmed or refuted in any follow-up studies.

Next to the origin of the secondary instability there has been discussion on the nature of the instability. First, it was thought that, analogously to a rotating disk described in Lingwood (1995), an absolute instability caused breakdown to turbulence on a swept wing. However, on a swept wing flow the group velocity vector has to be zero for a true absolute instability to exist (Koch, 2002). In experiments and computations this does not turn out to be the case and an absolute instability was not detected (White, 2000). Computations by Koch (2002) and Wassermann and Kloker (2002) confirmed that the secondary instability is a convective instability.

The characteristics of the secondary instability have been studied in experiments and computations. Experimental studies used excitation sources for example pulsed blowing and suction using a small speaker (Kawakami et al., 1999; Chernoray et al., 2005) and plasma actuators (Serpieri and Kotsonis, 2016a). In these studies the phase-averaged velocities were obtained by calculating the phase between the hot-wire and exciter signals. A tomographic PIV study by Serpieri and Kotsonis (2016b) obtained the structure of the secondary instability without any external forcing using a proper orthogonal decomposition technique. In computational studies the structure of the instability has been studied with spatial DNS (Högberg and Henningson, 1998; Wassermann and Kloker, 2002; Bonfigli and Kloker, 2007). The character of the Type-I secondary instability for the forced, unforced and computational studies are shown in Figure 3.

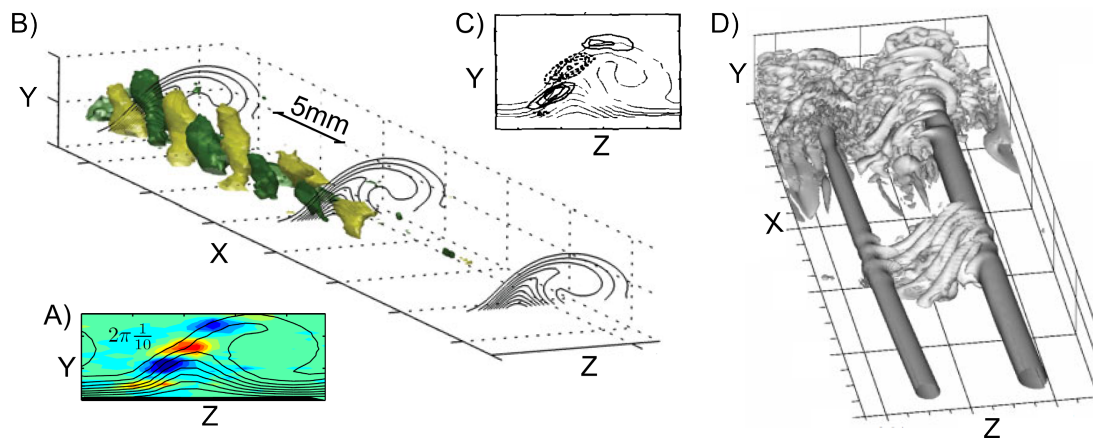


**Figure 3. Structure of the secondary instability obtained in several experimental and computational studies** A) Experimentally obtained with a plasma actuator. From Serpieri and Kotsonis (2016a). B) Experimentally obtained with tomographic PIV without forcing. From Serpieri and Kotsonis (2016b). C) Experimentally obtained with pulsed blowing and suction. From Kawakami et al. (1999). D) Computationally obtained with DNS. From Wassermann and Kloker (2002)

Visually, the structures look similar and consists of vortex structures whose vortex axis is tilted with respect to the primary crossflow axis. The wave speed and orientation of the structure can be used to compare to structure in a more quantitative manner. The wave speed of the secondary instability is calculated with  $U_{ph} = 2\pi f / \alpha_r$  where  $\alpha_r$  is the streamwise wavenumber. Normalized by the freestream velocity or edge velocity values of  $0.78U_e$  to  $0.84U_\infty$  have been found in previous experimental and computational studies (Kawakami et al., 1999; Malik et al., 1999; Serpieri and Kotsonis, 2016b). The orientation is defined with two angles, the elevation angle,  $\gamma$  and the azimuthal angle,  $\chi$ . For the elevation angle values of 12 and 21 degrees were

found in Bonfigli and Kloker (2007) and Serpieri and Kotsonis (2016b). For the azimuthal angle values in a range of 18.2 and 29.9 degrees are reported in Serpieri and Kotsonis (2016b) and Janke and Balakumar (2000). This shows that the exact orientation seems to be influenced by the experimental parameters however in general the structure compares well across studies from a quantitative point of view. In the experimental studies with forcing the focus is mostly on the initial growth of the secondary instability. An exception is Chernoray et al. (2005) who studied the development of a single vortex created by a large roughness element with phase-locked hot-wire measurements. They found that after an initial growth stage of the secondary instability, harmonics of the secondary instability appeared. The harmonics were a result of nonlinear interactions and seemed to cause breakdown. The harmonics were identified by calculating the growth rates of the secondary instability with frequency  $f_1$  and the growth rates of the velocity fluctuations with frequencies of  $2f_1$  and  $3f_1$ . It was found that the growth rate of the velocity fluctuations of  $2f_1$  and  $3f_1$  were respectively twice and thrice as high as those of the secondary instability fluctuations. This is a very common behaviour for nonlinear generated harmonics (Chernoray et al., 2005) and hence the velocity fluctuations were identified as harmonics of the secondary instability. The same method was used by White and Saric (2005) and they found that in some cases the growth rate of the velocity fluctuations with a frequency of  $2f_1$  were twice as high as the growth rate of the velocity fluctuations with a frequency of  $f_1$  and were therefore identified as harmonics. In other cases the energy for velocity fluctuations with  $2f_1$  did increase however, the growth rate did not support that these were harmonics. White and Saric (2005) concluded that these were other distinct secondary modes.

In a stationary-crossflow-dominated flow, computational, hot-wire and flow visualization studies found that the breakdown process is accompanied by the appearance of turbulent wedges (White and Saric, 2000; Wassermann and Kloker, 2002; Hunt and Saric, 2011; Duan et al., 2013; Eppink, 2014; Borodulin et al., 2017). With the exception of Borodulin et al. (2017) the origin of the wedge is observed with wall-based measures. In experimental studies naphthalene flow visualization shows the wedge due to the higher sublimation rate of the turbulent flow compared to laminar flow. In the computational studies the spanwise vorticity at the wall shows the footprint of the wedge. In these studies the origin of the wedge is found where the secondary instability fluctuations reach close to the wall on the side of the primary vortex. Borodulin et al. (2017) studied the appearance of the wedge for different external disturbances. They found that for high freestream turbulence levels, when

the transition process was dominated by the travelling crossflow waves, there was no appearance of the wedge structure, instead the transition front was uniform. Individual wedges for the breakdown of each stationary vortex are only clearly observed when the development of the flow is not uniform in the spanwise direction, due to differences in surface roughness (Hunt and Saric, 2011; Eppink, 2014). In most experimental crossflow studies, small roughness elements are placed to make the flow spanwise uniform and the vortices of the same strength. While this has advantages from an experimental point of view, it might not accurately describe the development and breakdown of crossflow vortices on an actual wing, with a spanwise pressure gradient and non-uniformities in the surface roughness. Wassermann and Kloker (2002) found that a vortex package with two vortices of unequal strength, will cause breakdown earlier than a vortex package with two equal strength vortices. They explained that this behaviour was due to the spanwise modulation, which caused larger mean flow decelerations in the stronger vortex leading to a stronger secondary instability. In contrast, Choudhari et al. (2016) suggested that for strong modulation the transition length would be increased. They found that the stronger vortex merges with the weaker vortex. They then hypothesize that when this vortex structure breaks down, the wedge has to travel a larger spanwise distance to interact with neighbouring vortices, consequently having a longer transition zone.

To summarize this section, in previous studies the secondary crossflow instability has been defined as a high-frequency travelling wave caused by the shear layers in the wall-normal and spanwise direction in the mean streamwise flow. The structure of the secondary instability has been measured experimentally with and without forcing in its early development stage. Close to breakdown the structure has not been measured. The breakdown process of the secondary instability is accompanied by a turbulent wedge structure which spreads in the spanwise direction.

### 5.2.2. Receptivity of the secondary crossflow instability

In the previous section it was shown that a small amount of forcing was used to visualize and characterize the secondary crossflow instability, without intrinsically changing the flow. Studies on the influence of different forcing mechanisms, on the growth and development of the secondary instability, are limited. Kawakami et al. (1999) studied the growth of the secondary instability for different forcing amplitudes of a speaker embedded in the swept wing model. From their findings it seemed that the saturation location and therewith transition location was influenced by the

forcing which suggests that there are receptivity mechanisms for the secondary instability. [White and Saric \(2005\)](#) studied the influence of roughness height on the development of the secondary instability by modifying the primary crossflow instability. Next to a baseline case, with roughness elements of  $18\mu\text{m}$ , roughness elements with  $54\mu\text{m}$  were tested. It was found that the high frequency secondary instability for the baseline case was a Type-I instability while for the large roughness a Type-II instability was found. The varying roughness height at the leading edge changes the development of the primary instability and, as a consequence, the development of the secondary instability. [White and Saric \(2005\)](#) also investigated the influence of sound on the secondary instability. Speakers were placed in the plenum upstream of the test section and the amplitude and frequency were varied. No influence, of sound was observed in any of the measurements. The reason for this could be the distance of the forcing to the onset of the secondary instability. When the forcing mechanism is placed at a large distance, the amplitude might have decreased when interacting with the secondary instability in the boundary layer. Since the secondary instability is a high frequency travelling wave the receptivity mechanism could be similar to those of travelling waves in general. [Schrader et al. \(2009\)](#) found that to excite the travelling crossflow waves a combination of freestream forcing and roughness had to be used. The long wavelength disturbances from the freestream scatter from the roughness elements to be able to couple with the flow. [Borodulin et al. \(2013\)](#) confirmed this with an experimental study. In this investigation the freestream disturbances consisted of vortices which were excited by a thin vibrating wire. The roughness consisted of long strips, whose length and spanwise spacing were based on the spanwise and streamwise wavenumbers of the predicted travelling crossflow waves from linear stability analysis. They found that due to the roughness the intensity of the travelling crossflow waves excited by the freestream vortices increased.

Control of the secondary instability is a relatively new subject of study. [Friederich and Kloker \(2012\)](#) controlled the developed non-linear stationary primary vortices with localized suction in their DNS study. They found that suction drew the vortices closer to the wall, consequently reducing the strength of the spanwise and wall-normal shear resulting in lower growth of the secondary crossflow instability. In the DNS study of [Dörr and Kloker \(2016\)](#) plasma actuators were used to control the secondary instability. In [Friederich and Kloker \(2012\)](#) the focus of this investigation was to modify the development of the primary crossflow vortices. By deploying plasma actuators they were able to successfully reduce the crossflow velocity such that the growth of the secondary instability was attenuated. Experimental studies

to control the secondary crossflow instability have not been carried out up to date.

### 5.3. Aim of the current study

Previous studies have focussed on the origin and characteristics of the secondary crossflow instability. It was found that there is only a limited amount of studies on the breakdown process. Experimentally, the breakdown process has been studied in detail for a single vortex created by a large roughness element (Chernoray et al., 2005), however, no cases have been found for natural occurring crossflow i.e. due to micron sized surface roughness at the leading edge. Therefore, the first aim of the current experimental investigation is to study the development and breakdown of a single crossflow vortex in detail. A small forcing amplitude is used to visualize and determine the characteristics of the secondary instability in several stages of the development. The results of this experiment are given in Section 5.6. From the literature review it was also found that there are almost no studies on the receptivity of the secondary instability. Understanding this process better is motivated by the following reasons. Firstly, in experiments forcing is used to excite the secondary instability, however, it has not been established at which forcing amplitudes the transition process might be influenced by this forcing. Secondly, disturbances might influence the development of the secondary instability and cause the flow to breakdown earlier, as discussed in the previous chapter for the primary crossflow instability. The second aim of this experiment is therefore to study possible receptivity mechanisms of the secondary instability in more detail. In order to do so experiments on wall-forcing and freestream forcing will be carried out. The results of these experiments are given in Section 5.7.

### 5.4. Design of excitation mechanism

#### 5.4.1. Wall-forcing

For wall-forcing the flow is excited through a small speaker which is placed at the non-test side of the plate, as presented in Figure 4.

Through an aperture of 0.5mm the signal of the speaker excites the flow at the test side of the plate. In previous studies, pulsed blowing and suction has shown to be a successful mechanism to excite the secondary crossflow instability (Kawakami et al., 1999; Chernoray et al., 2005). A sinusoidal wave with a chosen frequency and amplitude is sent to the speaker through LabVIEW. The frequency of the wave

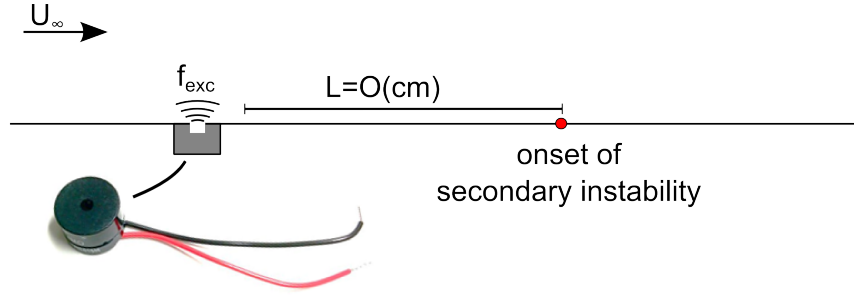


**Figure 4.** Set-up for wall-forcing of the secondary instability with pulsed blowing and suction by a small speaker.

and location of the speaker are chosen based on the development of the secondary instability without forcing. As will be shown in Section 5.6, the natural secondary instability in the flow has frequencies in a frequency band from 700-3000Hz. The forcing frequency was therefore chosen as 2kHz. The amplitude of the forcing was controlled through the voltage sent to the speaker. In order to relate the voltage to a fluctuation velocity level, boundary-layer profiles were taken at the exciter for different forcing voltages,  $F(V)$ , as presented in Figure 5.

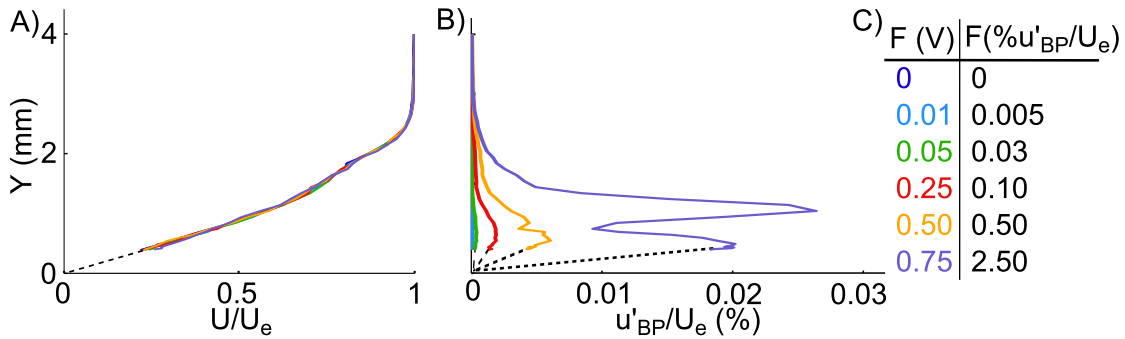


**Figure 5.** A) Mean velocity profiles for different forcing amplitudes at the location of the exciter. B) Velocity fluctuations between 1990-2010Hz for different forcing amplitudes at the location of the exciter. C) Forcing amplitude in terms of maximum fluctuations in forcing profile.

The mean velocity profile is not influenced by the forcing amplitude. However, the bandpass filtered velocity profiles between 1990-2010Hz show that the disturbance profile is influenced by the forcing amplitude. The maximum of each of the forcing profiles is defined as the forcing amplitude in terms of flow parameters and will be used throughout the thesis. It should be noted that even though the forcing amplitude is expressed in terms of the streamwise velocity fluctuations  $u'$  the forcing is in the direction which will lead to fluctuations in the  $v'$  velocity component. Since the hot-wire measures both components and they can not be separated it is chosen to keep the forcing in terms of  $u'$ . The lower forcing amplitudes are similar to those

cited in the literature (Kawakami et al., 1999; Chernoray et al., 2005), however it is not clear how the amplitudes were exactly defined in these studies. Studies with the highest forcing amplitude used in the current study, have not been found in literature before but since the forcing amplitude is 2.5% of the edge velocity, it is expected that the non-linear effects will dominate the flow shortly after the forcing is applied.

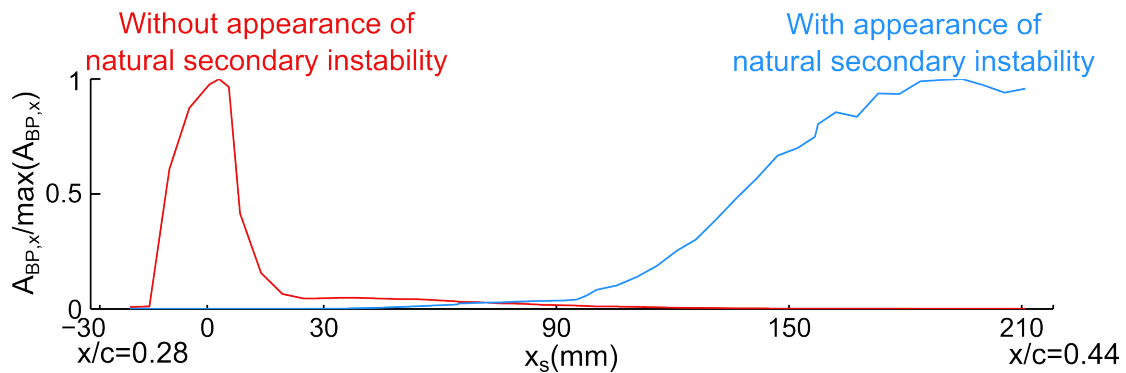


**Figure 6.** Development of the velocity fluctuations between 1900-2100Hz with (blue) and without (red) breakdown of the flow. In both cases the flow is forced at a frequency of 2000Hz at  $x_s=0$ mm.

In the initial tests it was first established that the wall-forcing was exciting the natural occurring secondary instability. This was verified by analysis of the velocity fluctuations between 1900-2100Hz for two cases. In the first case the freestream velocity was set such that the natural secondary instability appeared in the measurement region. In the second case the freestream velocity was lowered such that the flow did not break down and therefore the natural occurring secondary instability did not appear in the measurement region. The velocity fluctuations between 1900-2100Hz are shown in Figure 6 for both cases. For the case with the natural occurring secondary instability the fluctuations between 1900-2100Hz grew gradually in the measurement region. For the second case, where the natural occurring secondary instability did not appear, the velocity fluctuations between 1900-2100Hz are maximum around the exciter,  $x_s=0$ , after which their magnitude decreases. This means that for small wall-forcing the excitation did not create an instability by itself, instead the energy in the 2kHz wave dissipates. For the velocity fluctuations to grow, the natural secondary instability was a prerequisite. Next, the velocity fluctuations were analysed in the YZ-scan. The spatial distribution of the fluctuations around 2000Hz are compared with and without moderate forcing in Figure 7. The fluctuations for the forced and unforced case spatially coincide, which again indicates that the forcing excites the natural occurring secondary instability in the flow.

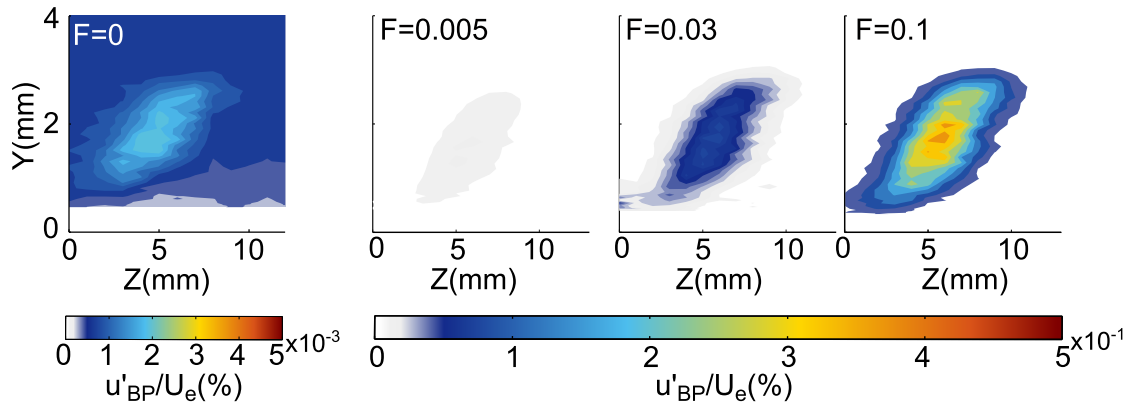


**Figure 7.** Distribution of the velocity fluctuations between 1900-2100Hz for different forcing amplitudes.

#### 5.4.2. Freestream forcing

The main set-up for freestream forcing, sketched in Figure 8, consisted of a brass pipe with a 3D-printed sleeve to be placed over a speaker, similar to the one used for wall-forcing. The sleeve was mounted in an opening at the trailing edge of the displacement body. The exciter was then attached to the sleeve from the back of the displacement body.

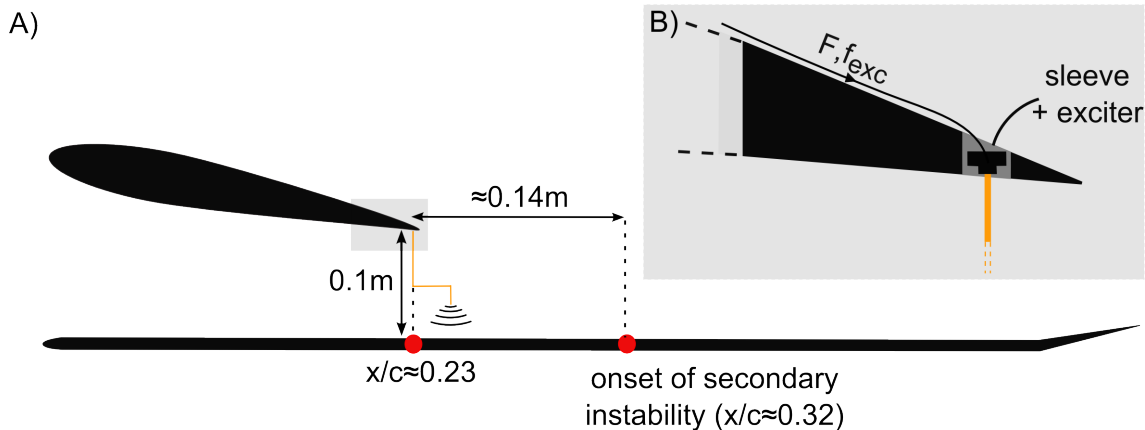


**Figure 8.** A) Overview of the freestream forcing set-up. B) Detail of the trailing edge of the displacement body which shows the placement of the sleeve, exciter and brass pipe.

Pipes with different characteristics were tested, as shown in Figure 9. Initial tests focussed on the effect of the pipe on the flow inside the boundary layer.

The power spectrum for configuration 2 (Figure 9), compared to the configuration without a pipe, is shown in Figure 10. In configuration 2 the outlet of the brass pipe is around 5mm above the edge of the boundary layer at the plate. The power spectrum in the middle of the boundary layer shows that the energy from 100-800Hz is increased at  $x/c=0.29$  which is caused by the wake of the pipe. Moving

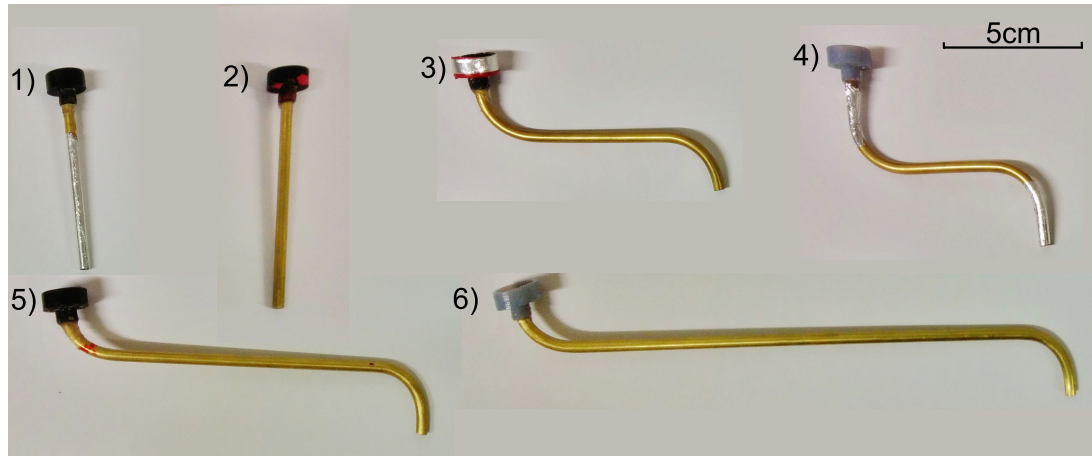


**Figure 9.** Different brass pipes used for freestream forcing.

downstream it is shown that the presence of the pipe does not alter the frequencies of the secondary instability occurring without the pipe. Similar observations were made for the other brass pipes. From this it is concluded that the obstruction caused by the pipe does not change the development of the secondary instability and therefore it is a suitable set-up to study forcing from the freestream.

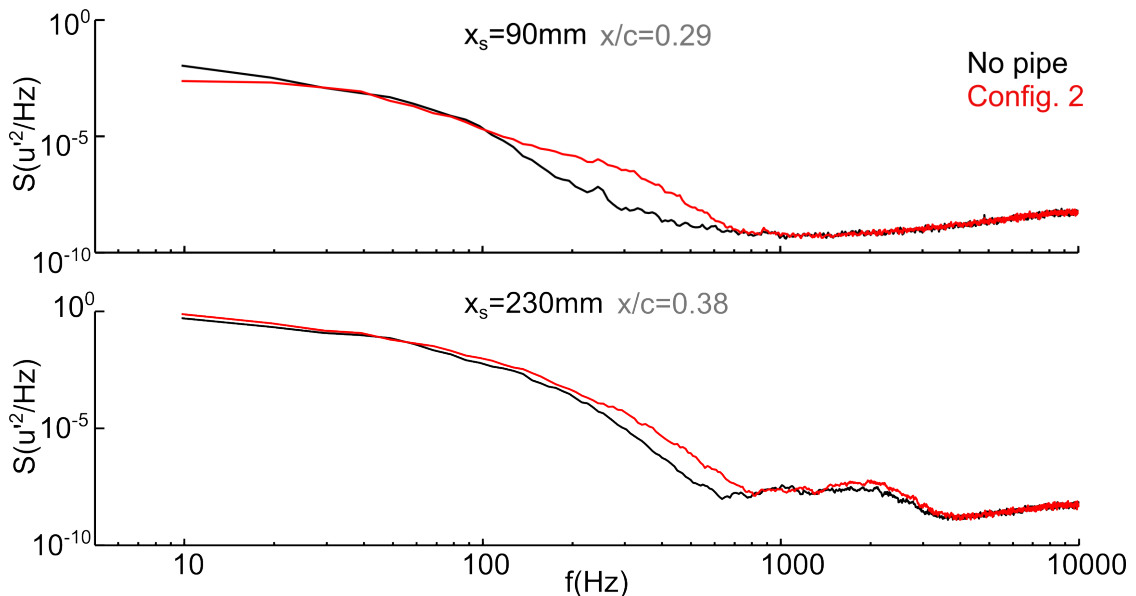


**Figure 10.** Influence of brass pipe used to direct freestream forcing at two different streamwise locations at  $Y=5\text{mm}$ .

Just as for wall-forcing, the forcing amplitudes in terms of velocity fluctuations from 1990-2010Hz were determined during a set of initial tests. The forcing from the freestream, experienced by the boundary layer, is determined at the boundary layer edge at  $Y=5\text{mm}$ . From the results of the initial tests, presented in Section 5.7, configuration 5 was chosen for further tests. Therefore the forcing amplitudes are

determined for this configuration. The pipe exit is located at around  $x/c=0.31$  and  $Y=50\text{mm}$ . The forcing profile at the pipe exit was only measured for configuration 3 and is shown in Figure 11 for an excitation amplitude of  $0.5V$ . Here the pipe exit is again around  $Y=50\text{mm}$ .

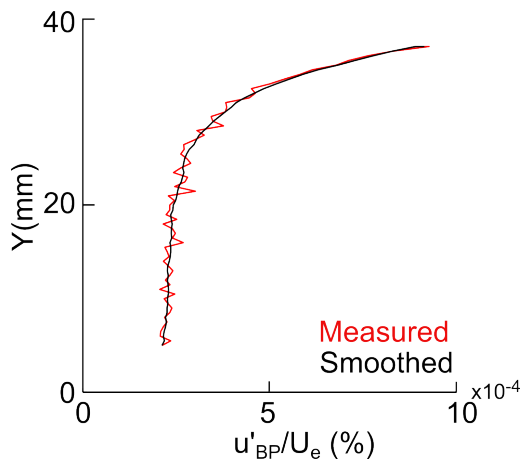


**Figure 11.** Freestream forcing profile at the exciter placed at  $Y=50\text{mm}$ .

The fluctuation level alternates to a constant level as the boundary layer edge is approached. For configuration 5 a similar shape and trend would be expected. The forcing amplitude measured from  $x/c=0.32-0.37$  for configuration 5 had a variation of around 5% around the mean value. In the tests discussed in Section 5.8 a roughness strip was placed at  $x/c=0.33$  as an additional disturbance. Therefore it is chosen to define the forcing amplitude after the roughness strip at  $x/c=0.36$  at  $Y=5\text{mm}$  about  $75\text{mm}$  downstream of the exciter. In Figure 12 the forcing amplitudes are shown. Compared to the

wall-forcing (Figure 5) the amplitudes are very small due to the definition of the forcing amplitude. For wall-forcing the forcing amplitude is determined at the wall-normal location where the velocity fluctuations, with frequencies at and close to the excitation frequency, are maximum. This is about  $1-2\text{mm}$  from the exciter where the forcing can interact with the disturbances in the boundary layer. For freestream forcing the forcing amplitude is determined at the edge of the boundary layer where the first interaction of the forcing with the disturbances inside the boundary layer could occur. Since this is about  $45\text{mm}$  from the actual exciter the fluctuations created by the exciter are convected downstream with the freestream velocity and largely reduced in amplitude when the boundary layer edge is approached.

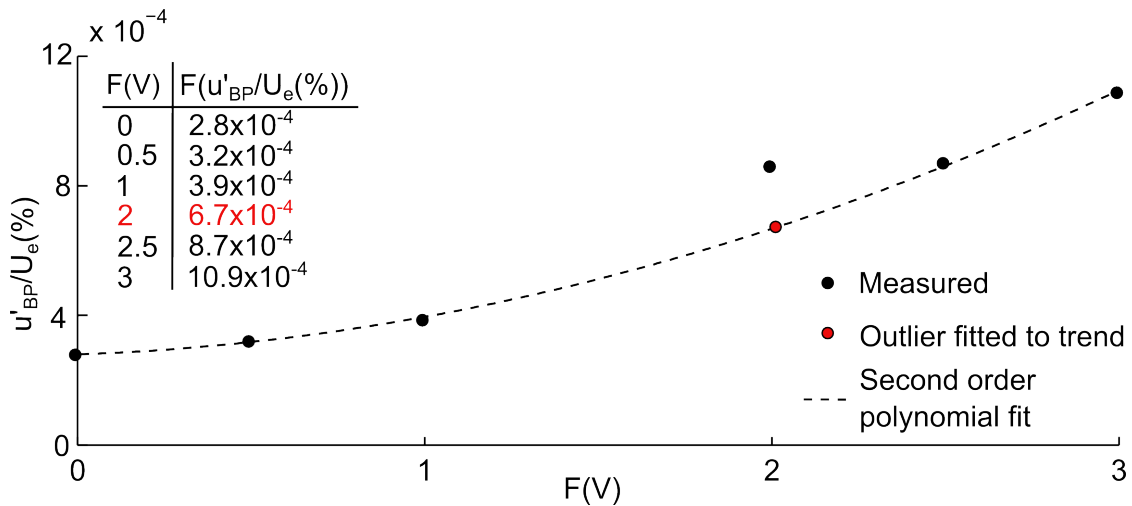


**Figure 12.** Forcing amplitude of freestream forcing in terms of velocity fluctuations between 1990 and 2010Hz measured at  $x/c=0.36$  at the edge of the boundary layer.

## 5.5. Measurements and data analysis

### 5.5.1. Coordinate systems

In the experiments the development of one crossflow vortex structure is studied in detail through hot-wire scans. In Figure 13 the different hot-wire scans and coordinate systems for the experiments is shown. All experiments discussed in this chapter were taken at a freestream velocity of 18m/s and Reynolds number of about  $1.5 \times 10^6$ .

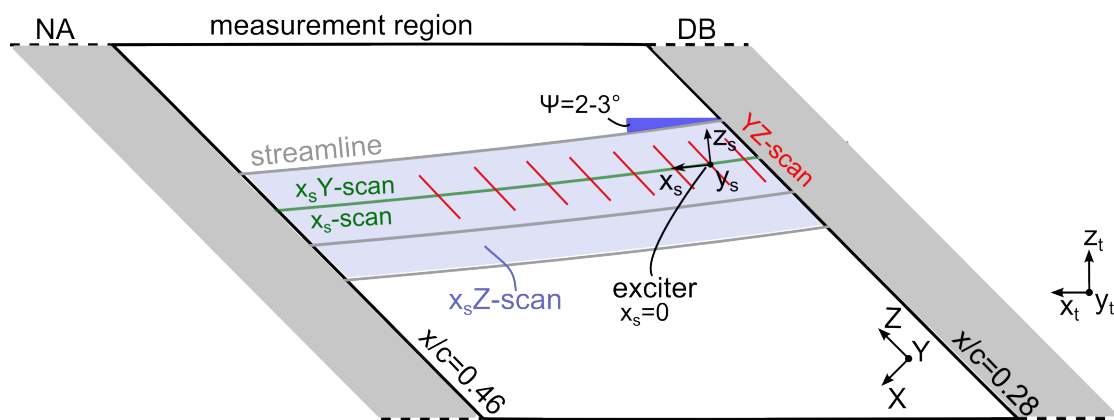


**Figure 13.** Measurement region with different coordinate systems for experiments on the secondary crossflow instability.

When the vortex was initially followed downstream, a small streamline angle,  $\Psi$ , was observed with respect to the  $x_t$ -axis. Since detailed measurements of only one vortex were taken, it was essential to follow this vortex along the streamline. Therefore, a new coordinate system was defined along,  $x_s$ , and perpendicular,  $z_s$  to the

streamline. The origin of the system is defined at the location of the exciter, which is at  $x/c=0.30$  for the wall-forcing and at  $x/c=0.31$  for freestream forcing. Different scans were carried out to understand the development of the flow in detail. The YZ-scans were taken parallel to the leading edge and in the wall-normal location, as also shown in Chapter 4. From the YZ-scans the development of the travelling and stationary crossflow waves was determined. Furthermore, the streamline angle  $\Psi$  was determined from the YZ-scans of one vortex at 8  $x/c$ -locations, by tracking the middle of the vortex at each streamwise location. In the  $x_s$ -scan the hot-wire was kept at constant wall-normal location and moved through the middle of the region where the secondary instability was located. These scans are carried out with  $\Delta x_s=1\text{mm}$  to quickly assess the development of the flow. The  $x_s$ Y-scan was taken along the same line as the  $x_s$ -scan, however, at each  $x_s$  location a boundary layer profile was obtained. These scans gave a detailed view of the onset and breakdown of the excited secondary instability. The  $x_s$ Z-scan covered a large region in the spanwise ( $\Delta Z=1\text{mm}$ ) and streamwise ( $\Delta x_s=1\text{mm}$ ) direction, while the wall-normal distance was kept constant. The Z-axis is chosen for this scan instead of the  $z_s$ -axis to be able to easily compare the Z-locations of YZ- and  $x_s$ Z-scans. This did mean that the axes for the  $x_s$ Z-scan were non-orthogonal.

To be able to compare the different  $x/c$  locations where the YZ-scans were taken with the corresponding  $x_s$  location, most figures indicate both the  $x_s$  and  $x/c$  coordinates on the x-axis.

With these scans the breakdown of different vortices could be assessed. To visualize the secondary instability in three dimensions, a  $x_s$ YZ-scan was taken. This consisted of 10 YZ-scans with  $\Delta x_s=1\text{mm}$ . In Table 5.1 an overview of the different step sizes used in each of the hot-wire scans are given.

**Table 5.1.** Overview of step sizes used for the different hot-wire scans.

	$\Delta x_s$ (mm)	$\Delta Y$ (mm)	$\Delta Z$ (mm)
$x_s$ -scan	1	-	-
$x_s$ Y-scan	1	0.005 to 0.2	-
$x_s$ Z-scan	1	-	1
YZ-scan	-	0.005 to 0.2	1
$x_s$ YZ-scan	1	0.005 to 0.2	1

In the results section, findings of two experiments are discussed. The first experiment, Test I, was carried out in January 2017. For this test, the exciter was in the middle of the studied vortex and, to obtain a more spanwise uniform flow, roughness elements with a height of  $24\mu\text{m}$  were placed at the leading edge. After that, the test section was

changed and the roughness elements were removed. For the test in June 2017, Test II, the roughness elements were reapplied at the same chordwise location, but a slightly different (a 2-3mm shift) spanwise location. This led to a different development of the vortex and secondary instability as shown in Section 5.6.

### 5.5.2. Analysis of the exciter signal

The general analysis of the results has been discussed in Chapter 2 and Chapter 4. Here the focus is on the analysis of the exciter data. To obtain the spatial structure of the secondary instability, the phase and phase-averaged velocity have been calculated.

The phase between the exciter and analogue filtered hot-wire signal was obtained by digitally filtering the hot-wire signal in MATLAB with the cut off frequencies chosen  $\pm 10\text{Hz}$  around the exciter frequency. The digitally bandpassed filtered hot-wire signal,  $\tilde{u}$ , is then cross correlated with the exciter signal,  $\tilde{E}$ ,

$$R_{\tilde{u}\tilde{E}}(\Delta m) = \sum_{m=1}^M \tilde{u}[m]\tilde{E}[m - \Delta m] \quad \Delta m = 0, \pm 1, \pm 2, \dots, \pm M, \quad (5.1)$$

where  $M$  is the number of samples of the signal. The power spectrum of  $R_{\tilde{u}\tilde{E}}$  is calculated,  $S_R$ , and from this the phase is determined with:

$$\phi(f) = \tan \left( \frac{\text{Im}(S_R(f))}{\text{Re}(S_R(f))} \right), \quad (5.2)$$

Where  $\phi(f_{exc})$  is the phase at the excitation frequency in radians.

The phase-averaged velocity can only be obtained when the measurements are phase-locked. In this experiment the exciter was continuously enabled i.e. the exciter was not started and stopped for each hot-wire measurement. Therefore, the algorithm to obtain the phase-averaged velocity consisted of two main steps, as presented in Figure 14. First the phase between the exciter signal and a reference signal,  $\cos(2\pi f_{exc}t)$ , was first determined (Figure 14A). The phase difference,  $\Delta\phi$ , in degrees was then converted to a number of samples through:

$$\Delta n = \frac{\Delta\phi}{2\pi} \frac{f_s}{f_{exc}}, \quad (5.3)$$

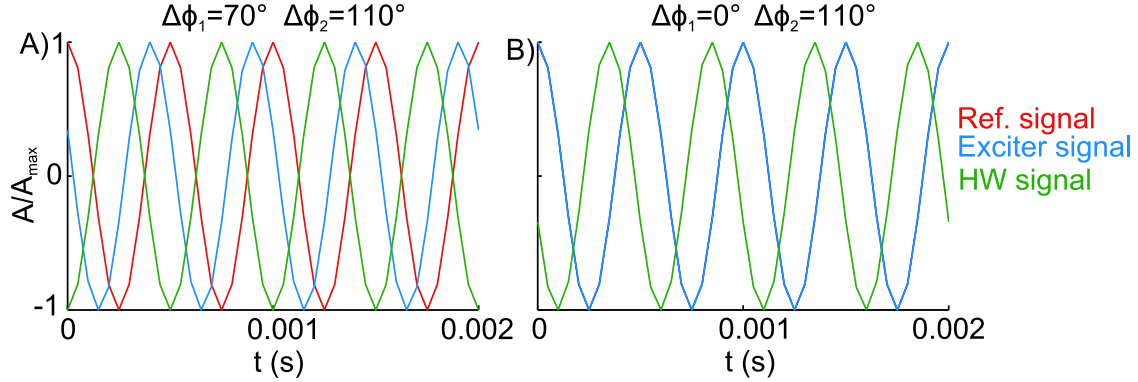


**Figure 14.** A) The phase between the reference signal and exciter signal,  $\Delta\phi_1$  and the phase between the exciter signal and hot-wire signal,  $\Delta\phi_2$ . B) Signal is shifted such that  $\Delta\phi_1=0$ .

where  $f_s$  is the sampling frequency. The exciter signal and hot-wire signal were then shifted by  $\Delta n$  to have exciter signals starting at the same phase as shown in Figure 14B. Finally, the hot-wire signal was sorted based on the phase and each block was averaged to obtain the phase-averaged velocity. The number of discrete phases,  $p_\phi$ , which could be resolved was calculated with:

$$p_\phi = \frac{f_s}{f_{exc}}, \quad (5.4)$$

and the number of samples per discrete phase with:

$$n_\phi = \frac{L}{p_\phi}. \quad (5.5)$$

For a measurement of 10 seconds, sampled at 20000 Hz, a wave excited at 2000 Hz can be resolved in 10 phases with 10000 samples per phase. The phase-averaged velocity,  $u'_{ph}$ , was determined for each hot-wire measurement to obtain the structure of the secondary instability.

## 5.6. Results: development of the secondary instability

In this section the characteristics of the secondary instability, obtained in this experiment, are first compared to previous studies in terms of structure, length-scales, orientation and velocities. After that the breakdown process is studied in more detail. The results of both Test I and II are presented, where, for both tests, one vortex was followed downstream.

### 5.6.1. Development of the mean and fluctuating flow

In Figures 15 and 16 the streamwise velocity fields are shown for Test I and Test II respectively. It is observed that the upwelling and downwelling region is more pronounced for Test II than for Test I, which indicates a stronger vortex has developed. It is thought that the difference in strength between both tests was caused by small differences in the experimental set-up, such as the location of the forcing by the roughness elements at the leading edge, as well as a small difference in the pressure distribution. The effect of the different vortex shapes and strengths is discussed throughout this section.

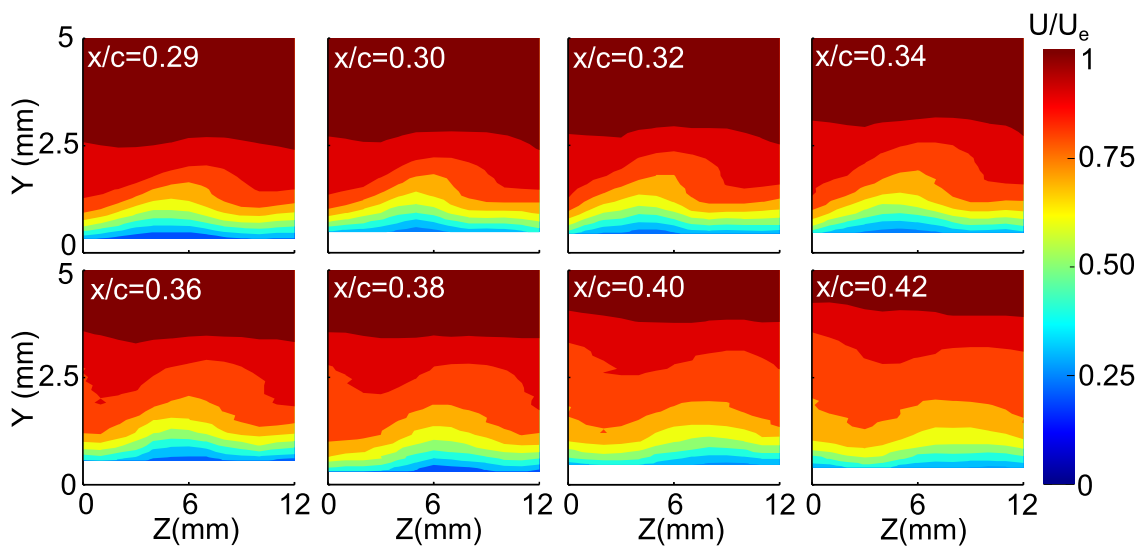


**Figure 15.** Normalized mean velocity fields of Test I for different chordwise stations.

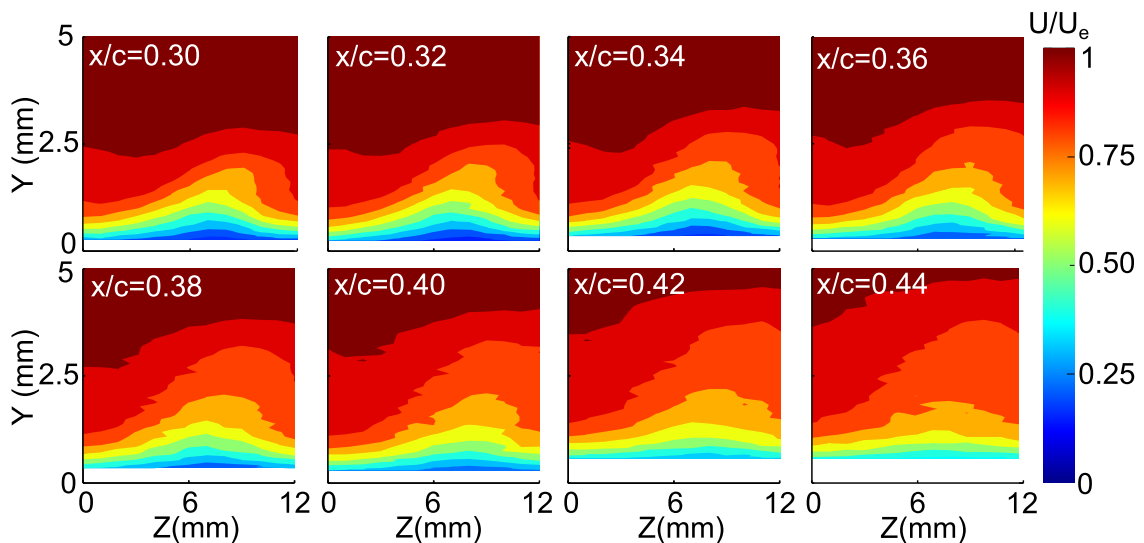


**Figure 16.** Normalized mean velocity fields of Test II for different chordwise stations.

Using a similar analysis as carried out in Chapter 4, the frequency bands with the dominant fluctuations in the early development of the crossflow instability were determined. In Figure 17 the distribution of these frequency bands are shown at  $x/c=0.3$  for both tests. The total fluctuations between 2 and 10000Hz have a simi-

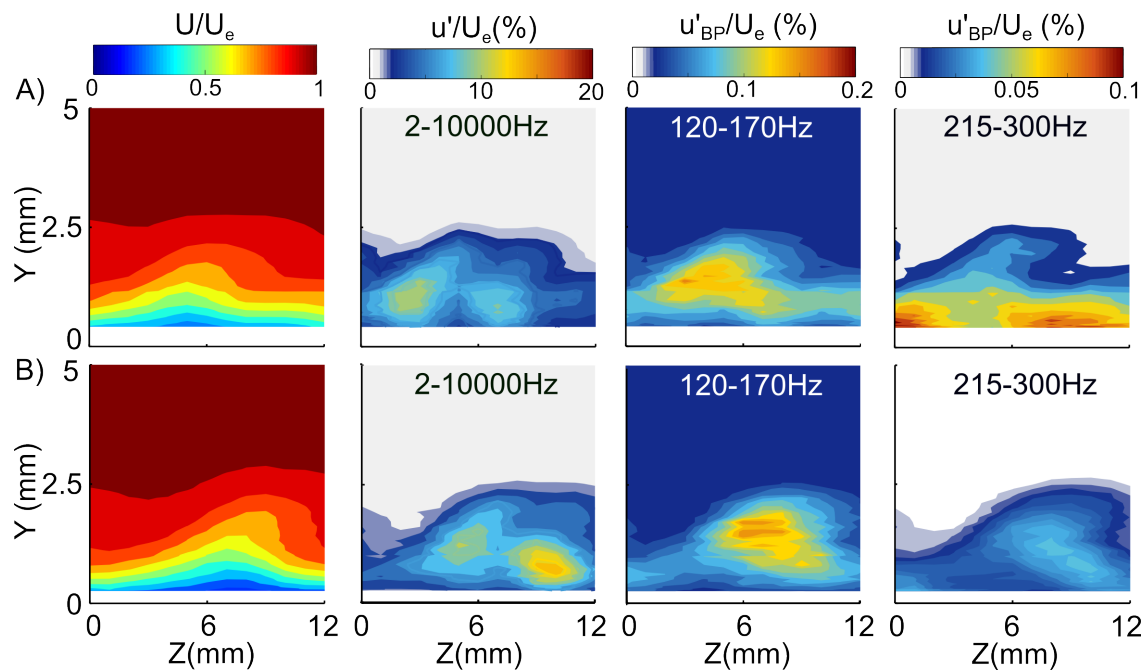


**Figure 17.** Spatial distribution of velocity fluctuations in different frequency bands at  $x/c=0.30$  for A) Test I and B) Test II.

lar distribution for both Test I and Test II. The fluctuations in Test I and II for the 120-170Hz have a similar distribution as found in Chapter 4. These fluctuations are attributed to travelling waves which are amplified following linear stability analysis and modulated by the stationary crossflow vortex. The distribution for the 215-300 Hz in Test I also resembles closely the structure found in Chapter 4. It was concluded that the origin of these fluctuations is difficult to define and that a Tollmien-Schlichting wave or travelling crossflow wave are both possibilities. For Test II the fluctuations in the 215-300Hz frequency band are located in the inner part of the structure and similar to those of the 120-170Hz structure. The frequencies are higher than those expected from linear stability analysis. It is thought that these fluctuations are caused by an interaction of the stationary waves with the present travelling crossflow waves similar to the 120-170Hz fluctuations. From the current experiment the mean flow distortion is stronger for Test II than Test I, which might explain why this instability did not appear in Test I. This shows that subtle changes in the vortex strength and shape can change the amplification of the travelling modes significantly.

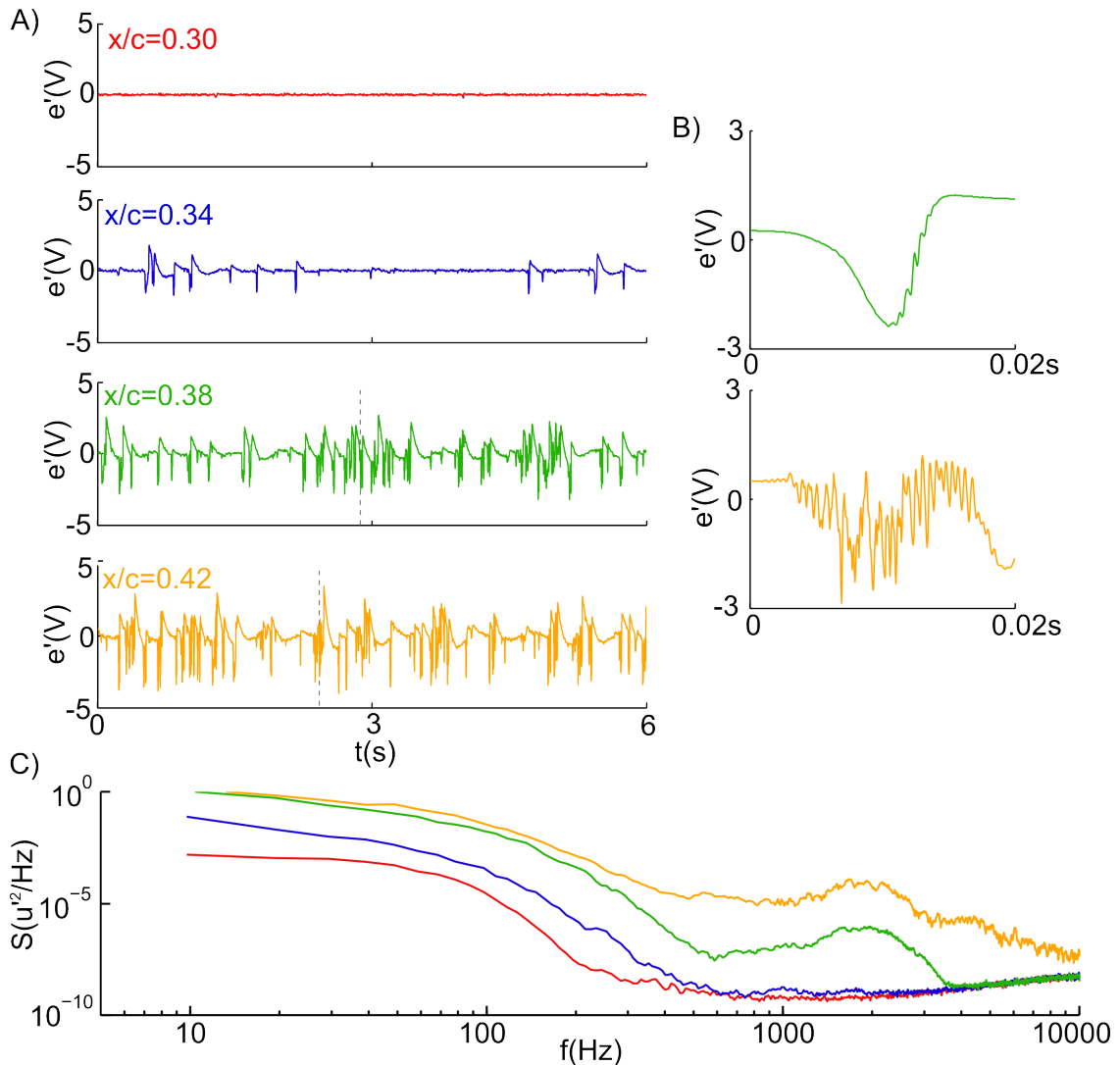


**Figure 18.** A) Fluctuating voltage signals from the hotwire for different chordwise locations. B) Detail of the time signals at  $x/c=0.38$  and  $x/c=0.42$  at the time instance shown with the dashed lines in A). C) Power spectra at different streamwise locations.

The development of the velocity fluctuations in the flow going downstream at constant wall-normal location is shown in Figure 18 for Test II. The time signal at  $x/c=0.34$  shows the appearance of spikes which become more frequent and stronger going downstream. A detail of the time signal at  $x/c=0.38$  shows the appearance of the secondary crossflow instability as a high-frequency travelling wave on top of the spike. This behaviour is similar as shown in Figure 1 where the time signal obtained by Poll (1985) is shown. In the spectra, Figure 18C, the appearance of the high-frequency waves is shown by the large increase in energy of the velocity fluctuations between 700-3000Hz. The time signal, and snapshot of the time signal, at  $x/c=0.42$  show that the high frequency fluctuations became stronger and dominate the time signal. The power spectrum shows that at  $x/c=0.42$  the flow is almost turbulent.

Similar characteristics of the time signals in the different stages of the crossflow transition process were reported by Poll (1985), Kohama et al. (1991) and Deyhle and Bippes (1996).

Figure 18 shows that the spectrum is increasingly dominated by the high-frequency secondary instability. In Figure 19 a power spectrum is shown for Test I and Test II. For both tests a frequency band from 700-3000Hz is amplified. The frequencies are similar to those found in experimental studies with similar freestream velocity and Reynolds number (Kawakami et al., 1999; White and Saric, 2005; Serpieri and Kotsonis, 2016b).

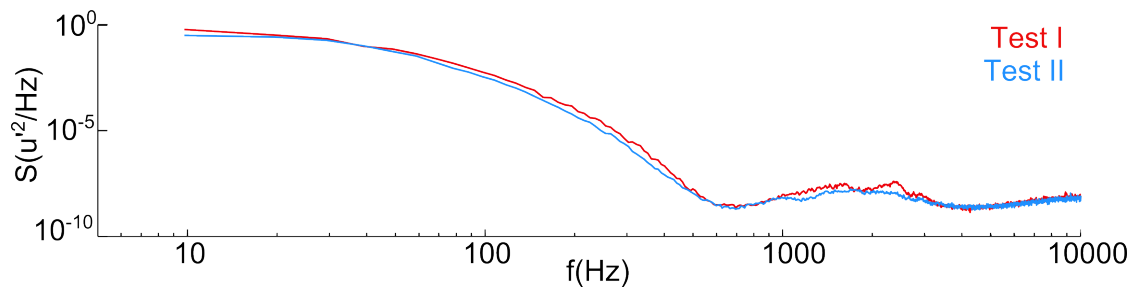


**Figure 19.** Power spectra at  $x/c=0.38$  at  $Y=2.4\text{mm}$  and  $Z=6\text{mm}$  for Test I and Test II.

Since a large band of frequencies was amplified, there was the possibility of several co-existing secondary instabilities. To study this in more detail, the velocity fluctuations from 100-6000Hz were analysed in 100Hz bands. From this, different regions of high velocity fluctuations were identified. In Figure 20 the velocity fluctuations in the relevant frequency bands are shown with the outline of the mean velocity contours at  $x/c=0.36$  for Test I. The spanwise and wall-normal gradient are shown to indicate which type of secondary instability has been developed. First, it should be noted that the maximum magnitude differs for the velocity fluctuations in each frequency band. The fluctuations between 100-300Hz are distributed in a similar way as the 120-170Hz waves at  $x/c=0.3$ . Again these are thought to be a combination of amplified travelling waves and acoustic noise which are modulated by the stationary structure. At the higher frequencies there seem to be three slightly different regions where a secondary instability develops. For 700 to 1300Hz the fluctuations are concentrated in the middle of the vortex, while for the higher frequencies there is a shift to the left side and upper part of the vortex. It is difficult to classify the instabilities as pure Type-I or Type-II instabilities. Compared to previous studies the roll-over of the vortex is less pronounced in the current experiment, due to a combination of the moderate pressure gradient over the plate and small forcing at the leading edge. Malik et al. (1999) shows that the spatial distribution of the secondary instability

coincides with the energy production term from the Reynolds-Orr which can be written as,  $-u'w'\partial U/\partial Z$  and  $-u'v'\partial U/\partial Y$ . Depending on the shape of the vortex the location of the maxima in the gradient fields do not necessarily coincide with the location of the maxima of the velocity fluctuations  $u',v'$  and  $w'$ . Since with the single hot-wire measurements the wall-normal and spanwise fluctuations are not measured, it is difficult to predict where exactly the production terms would be maximum in this experiment, however, it is expected to be in the region where the secondary instability fluctuations are large.

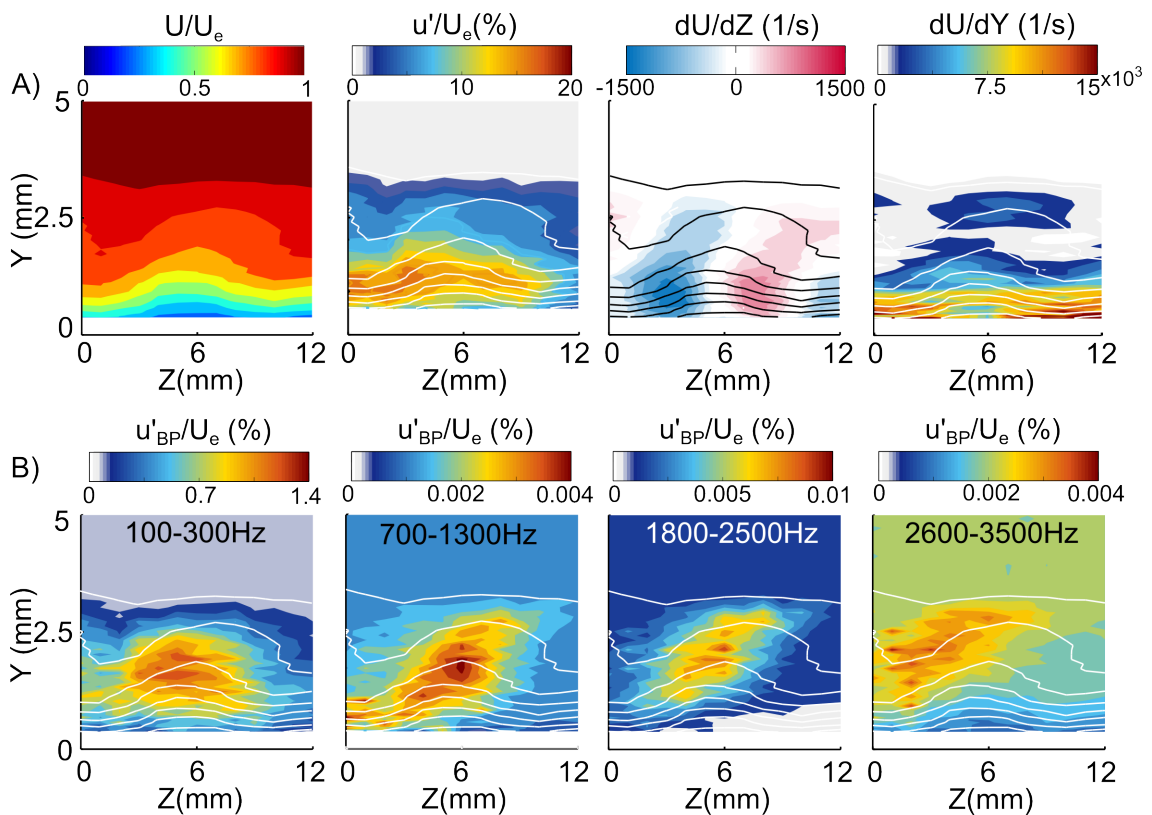


**Figure 20. Mean and fluctuating velocity for Test I at  $x/c=0.36$ .** A) Spatial distribution of the mean streamwise velocity, the total fluctuations, spanwise and wall-normal gradient. B) Spatial distribution of velocity fluctuations in different frequency bands.

The growth for the relevant travelling waves is shown in Figure 21. The growth for the 100-300Hz fluctuations is relatively small compared to the high frequency instabilities, which suggests that the secondary instabilities are responsible for the break down process. Previous research shows that the different types of instabilities have different growth rates (White and Saric, 2005). Here, it is shown the fluctuations in all three frequency bands have a similar growth curve. This indicates that even though the spatial distribution of the fluctuations in the analysed frequency bands differ, they do not seem to be originating from different mechanisms.

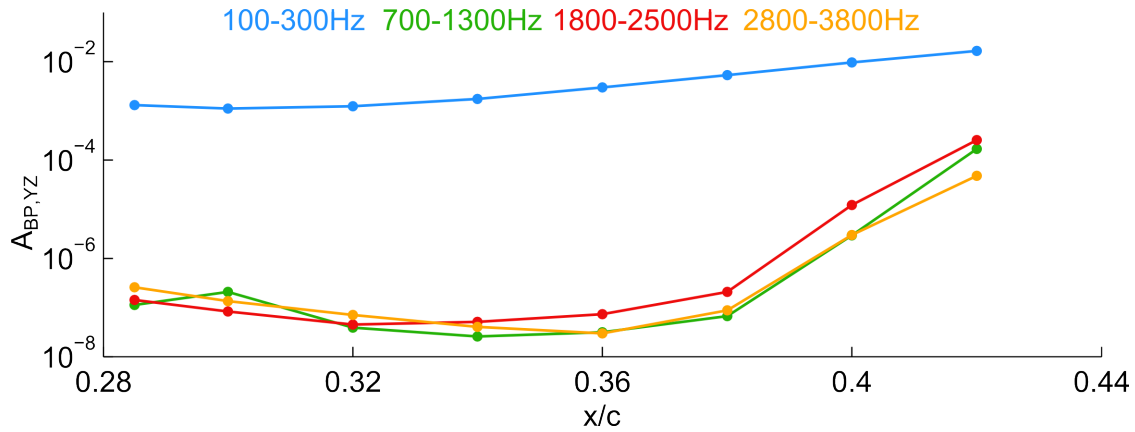


**Figure 21.** Growth of travelling waves in different frequency bands for Test I.

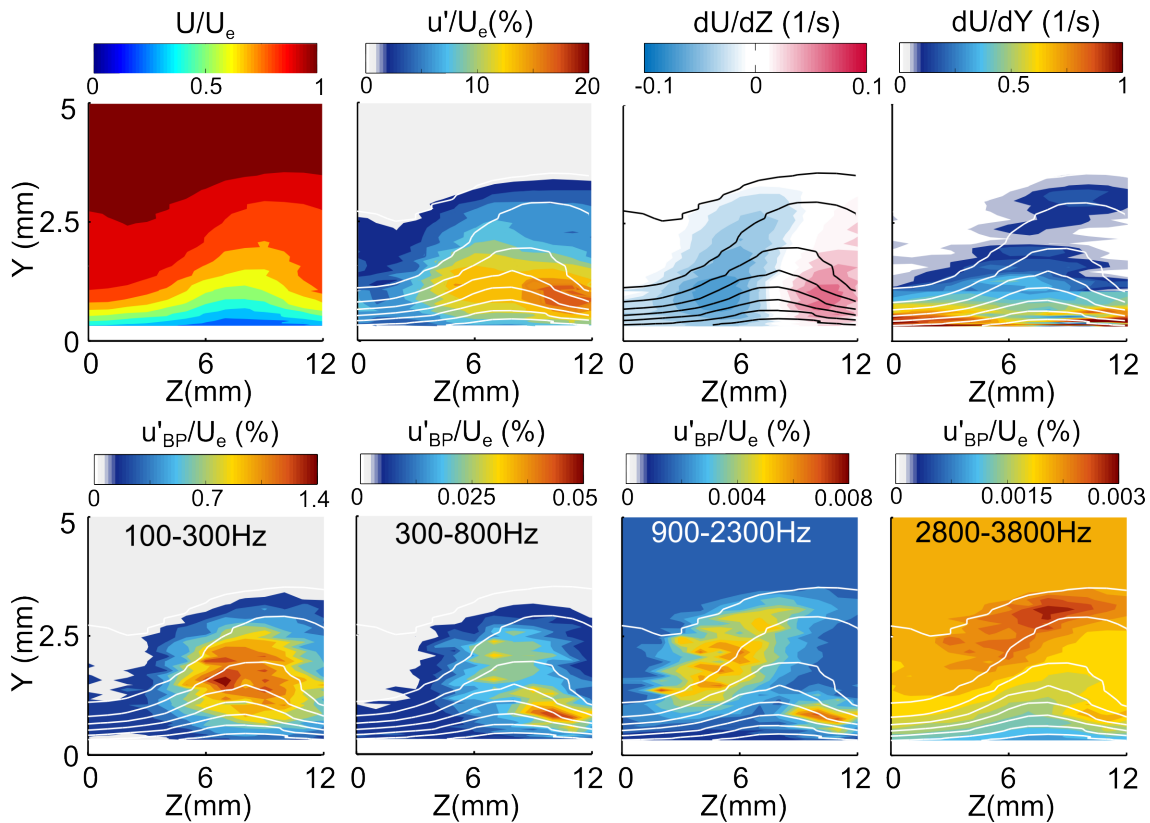


**Figure 22.** Mean and fluctuating velocity for Test II at  $x/c=0.36$ . A) Spatial distribution of the mean streamwise velocity, the total fluctuations, spanwise and wall-normal gradient. B) Spatial distribution of velocity fluctuations in different frequency bands.

For Test II the velocity fluctuations at  $x/c=0.36$  are shown in Figure 22. The fluctuations in the 100-300Hz instability are very similar to those found in Test I. For the higher frequencies again three regions were identified. For the 300-800Hz band the maximum fluctuations reside in the lower part of the vortex where the spanwise gradient is maximum and the streamwise fluctuations are as well. The fluctuations

look similar to those found at  $x/c=0.3$  at 215-300Hz, Figure 17, and could indicate that the Type-III instability developed further, spreading to higher frequencies.

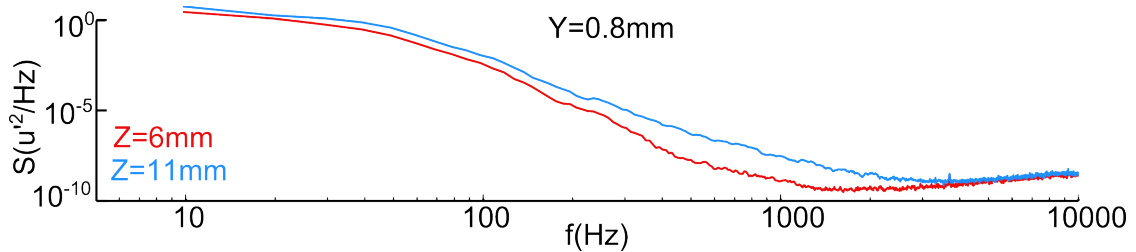


**Figure 23.** Power spectrum at  $Y=0.8\text{mm}$ ,  $Z=6\text{mm}$  and  $Z=11\text{mm}$  for  $x/c=0.36$ .

To investigate this further, the power spectrum at  $Y=0.8\text{mm}$  where these fluctuations are maximum is shown in Figure 23 at  $Z=6\text{mm}$  and  $Z=11\text{mm}$ . There is no specific frequency band amplified, instead the power from 400Hz to 4000Hz has been increased. These frequencies are higher than the Type-III frequencies of 300-500Hz found in previous studies (Serpieri and Kotsonis, 2016b). The alignment of the fluctuations with the spanwise gradient does suggest that an instability has been created by a similar mechanism as the Type-III instability. The strong fluctuations in the 900-2300Hz band, presented in Figure 22 are in the upwelling part of the vortex. While these velocity fluctuations do not exactly coincide with the maximum negative  $\partial U/\partial Z$  term, the structure does resemble those structures found in previous studies, referred to as Type-I instabilities (Malik et al., 1999; White and Saric, 2005; Serpieri and Kotsonis, 2016b). The fluctuations in the 2800-3800Hz band are located on the top of the vortex and resemble the Type-II instability found in previous studies. The growth curves of all the instabilities are shown in Figure 24. The waves in the 100-300Hz range do not exhibit strong growth while the high frequency wave show explosive growth around  $x/c=0.38$ . The strong growth of the Type-II instability starts from  $x/c=0.38$  while for the Type-I instability growth from  $x/c=0.34$  is observed. As will be shown in detail in Section 5.6.3, the flow breaks down around  $x/c=0.38$  where the velocity fluctuations of all frequencies increase. Therefore, the apparent growth for the Type-II instability is caused by the overall breakdown of the flow and it is concluded that the Type-I instability dominates the transition process.

Comparing the characteristics of the travelling waves for Test I and II shows that subtle differences in the shape and strength of the vortex can change the nature of the developing instabilities. However, when the development of the high-frequency fluctuations are considered, similar trends are observed. Up to  $x/c=0.38$  a relatively slow growth is observed after which rapid growth, note the logarithmic scale, occurs.

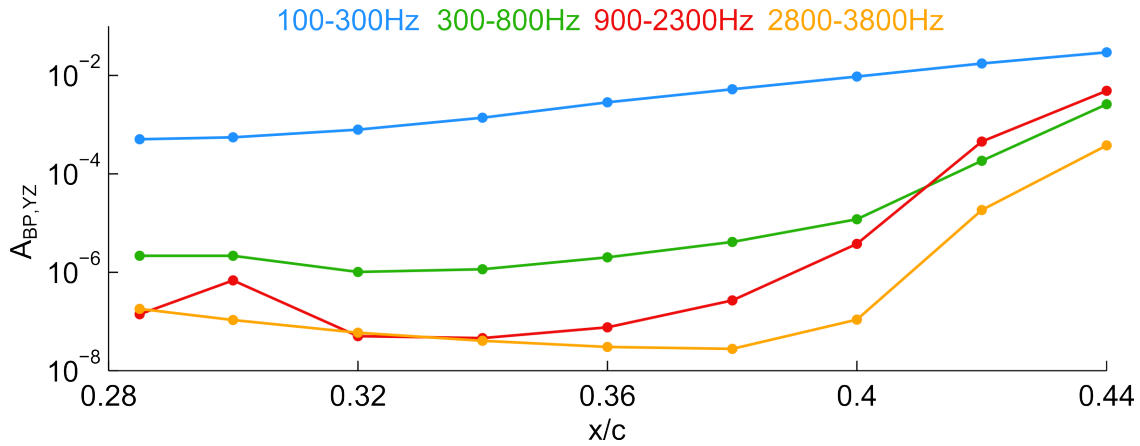


**Figure 24.** Growth of travelling waves in different frequency bands for Test II.

Similar growth curves were reported in the experiments of Kawakami et al. (1999) and White and Saric (2005), where the rapid growth is related to the breakdown of the flow and the high frequency fluctuations increase rapidly. The distribution of the fluctuations of 4kHz-10kHz are shown for Test I and II in Figure 25. Firstly, it is observed that for Test I the fluctuations are strongest on the side of the studied vortex, while for Test II the fluctuations grow from the middle. A possible explanation of this behaviour will be discussed in Section 5.6.3. Secondly, it is shown from Figure 25 that the fluctuations grow explosively from  $x/c=0.38-0.40$  which indicates breakdown of the flow. In the following two sections, the region up to and after  $x/c=0.38$  are analysed and discussed separately. First the origin of the secondary instability is discussed.

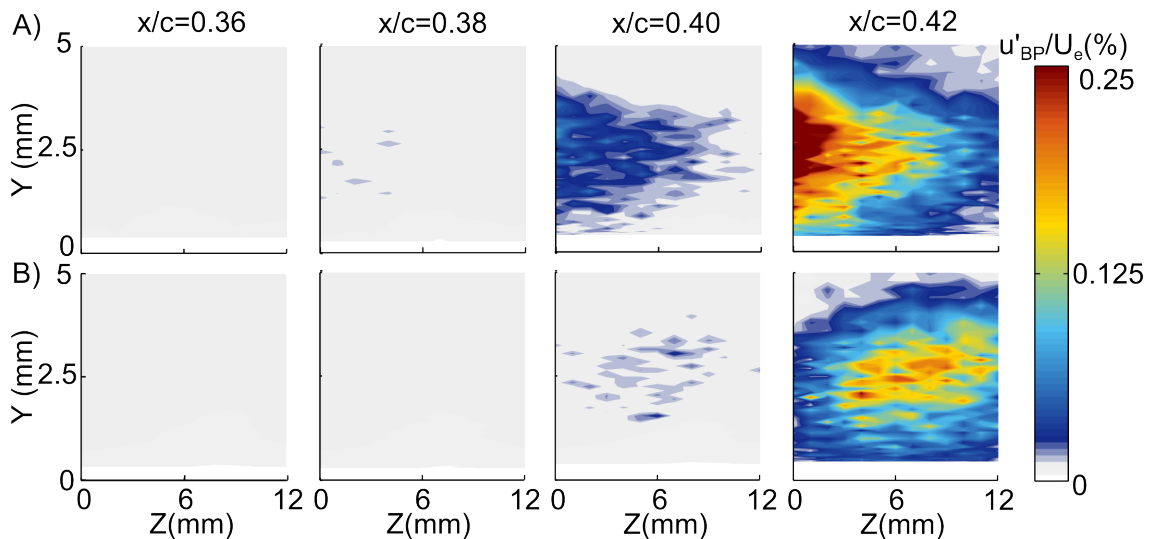


**Figure 25.** Spatial distribution of travelling waves in the frequency band from 4kHz to 10kHz for A) Test I and B) Test II.

### *Origin of the secondary instability*

From the measurements it is difficult to pinpoint the exact origin of the secondary instability. Previous studies found that the shear and the highly three-dimensional nature of the flow creates multiple inflection points which are a source for a secondary instability (Saric et al., 2003). To get an idea of the expected frequencies and wavenumbers for the current experiment, a simple and highly simplified analysis was carried out. The measured streamwise velocity profiles were approximated as piecewise linear profiles for which the stability characteristics were calculated. In Appendix the derivation of the dispersion relation between the streamwise wavenumber,  $\alpha$ , and temporal frequency  $f$  of a general piecewise linear velocity profile with four sections is given. A major limitation of this method is that it calculates the approximate stability characteristics of a Type-II instability while in this experiment the secondary instability fluctuations seem to be more aligned in the region where the spanwise gradients are large, therefore relating more to a Type-I instability. Nevertheless, since the distinction between the two types has not been as clear in this study as in previous studies, it might be expected that here the instability is caused by a combination of the gradient in the streamwise and spanwise direction. Therefore the characteristics of the Type-II secondary instability following from this analytical method might still be similar to those of the secondary instability measured in the experiments. In Figure 26 the dispersion relation for two measured velocity profiles are shown. When there is no inflection point in the velocity profile as is the case for  $Z=1\text{mm}$ ,  $\alpha_i=0$  which indicates that there are no perturbations growing in space, as would be expected from Rayleigh's inflection point theorem. At  $Z=6\text{mm}$  the velocity profile does have an inflection point which results in a region where the  $\alpha_i \neq 0$  and hence the fluctuations are convectively unstable. The results from this analysis can be compared to the results obtained from the experiment. The streamwise wavenumber,  $\alpha_r$ , could be determined from the experimental results as is shown in the next section. In Figure 26 the values obtained from Test I and Test II are indicated with the stars and are quite close to the theoretical prediction. In Figure 27 the power spectrum is shown at the streamwise location where the secondary instability starts to grow together with the theoretical prediction. The theory gives maximum growth for waves with a temporal frequency around 2kHz, as is also found in the experiments. In the experiments there the velocity fluctuations up to 4kHz show an increase in energy while in the theory waves with a frequency upto 3kHz exhibit growth.

Finally, the theoretical growth rate is compared to growth rate found in the experi-

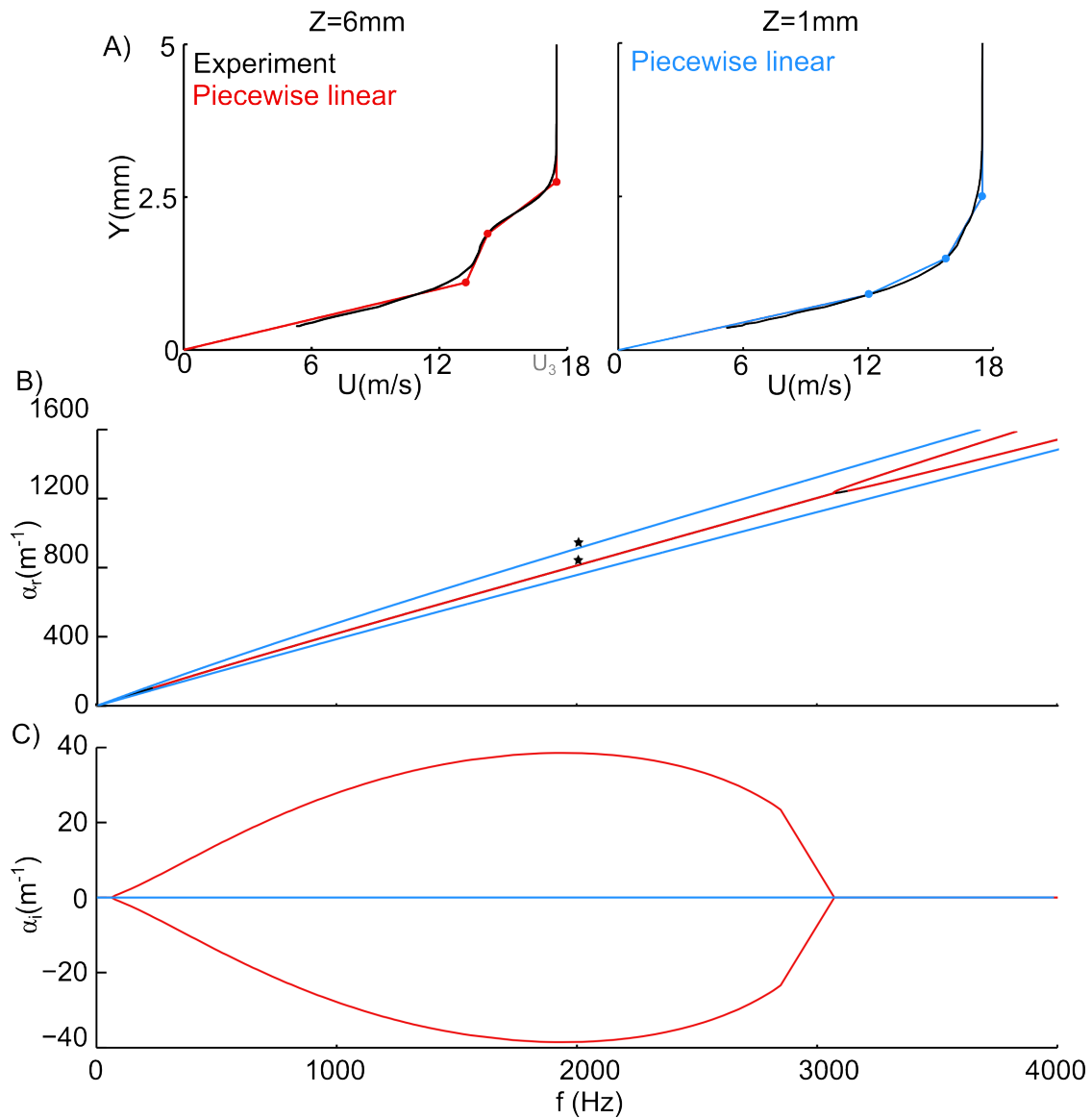


**Figure 26. Results of piecewise velocity profile analysis.** A) Experimental velocity profile at  $x/c=0.32$   $Z=6\text{mm}$  for Test II together with linear approximation. B) Real part of the wavenumber,  $\alpha_r$ , against the frequency where the red line shows the results obtained from the analysis and the stars the show the experimentally obtained results. C) Imaginary part of the wavenumber,  $\alpha_i$ , against the frequency obtained from the analysis.

ment. In Figure 28 the velocity fluctuations between 1990 and 2010Hz are shown for an x-scan without forcing. As explained in the previous section nonlinear effects start to breakdown around  $x/c=0.38$ . The logarithmic growth of the secondary instability from  $x/c=0.32$  upto  $x/c=0.37$  can be approximated with a straight line where the slope is equal to  $\alpha_r$ . With this approximation a value of  $\alpha_r$  is 35 was found. This is close to the 38 which is the value for  $\alpha_r$  found at  $f=2000\text{Hz}$  with the theoretical analysis.

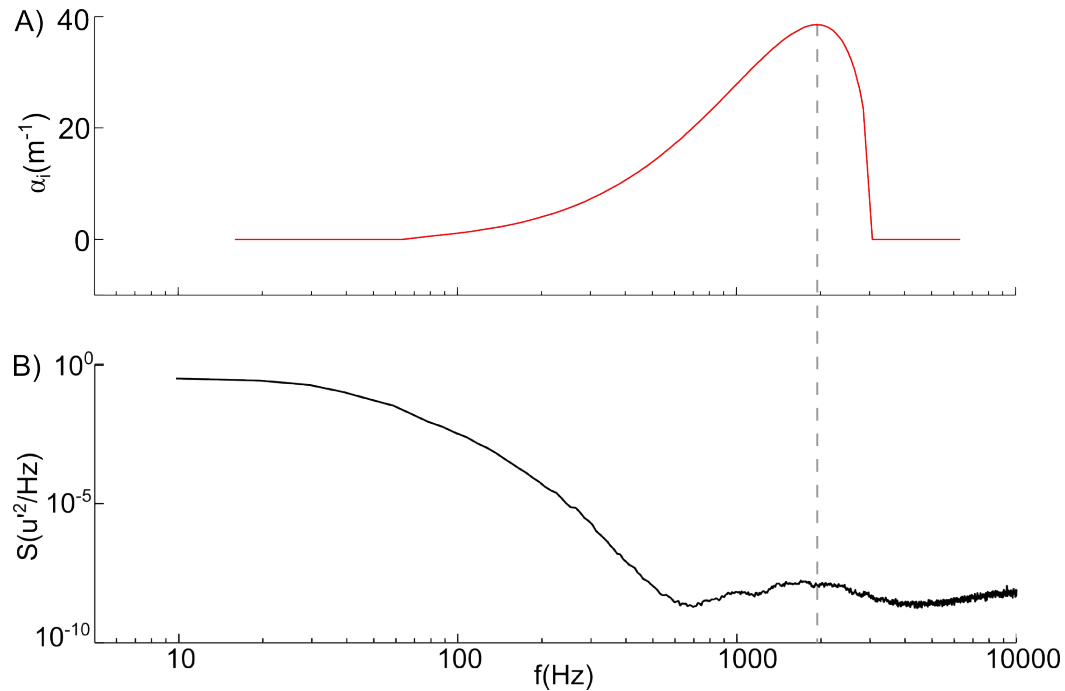


**Figure 27.** Comparison of the power spectrum obtained from the experiment together with the theoretical computed growth.

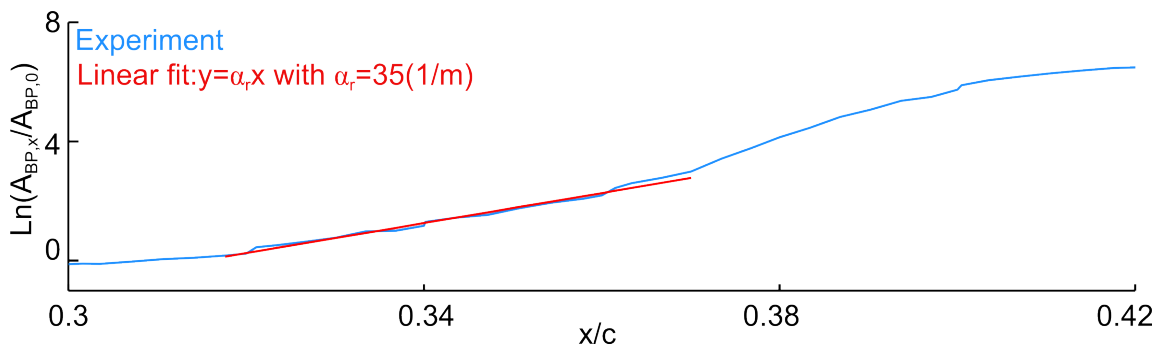


**Figure 28.** Growth of the secondary instability fluctuations for Test II together with a linear fit to compare to the theoretical analysis.

This simple analysis with the mentioned limitations, shows that the shear layers with similar characteristics as those found in the streamwise wall-normal velocity profile are a possible mechanism for the onset of the secondary instability in the current experiment.

### 5.6.2. Early development of the secondary crossflow instability

The aim of this section is to compare the characteristics of the secondary instability in the early development stage, to those found in literature. The structure of the secondary instability is visualized by exciting the flow with a frequency of 2000Hz

at  $x/c=0.30$  ( $x_s=0$ ) and a forcing amplitude of 0.03. As will be shown in Section 5.7 this forcing amplitude does not influence the transition process significantly, but is still large enough to phase lock the hot-wire and exciter signal. The distribution of the phase-averaged velocity is shown for both tests at  $x/c=0.34$  in Figure 29.

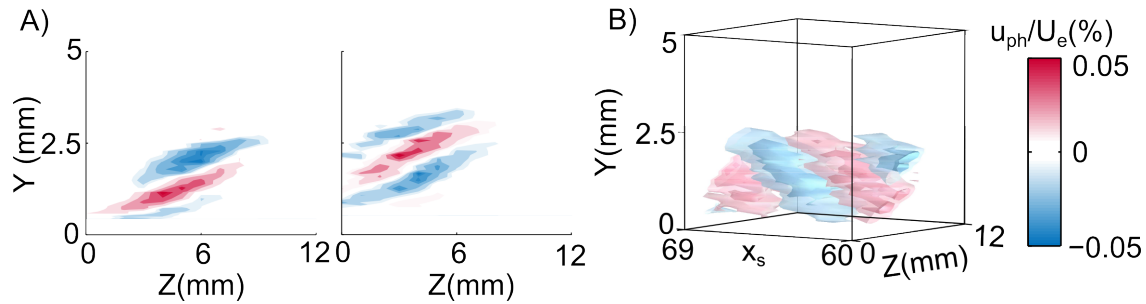


**Figure 29. Phase-averaged velocity distribution of the fluctuations at 2000Hz.** A) The distribution in the spanwise direction for Test I (left) and Test II (right). B) The three-dimensional representation of the secondary instability.

The patches of alternating positive and negative velocity resemble to the structures found in previous studies (Kawakami et al., 1999; Wassermann and Kloker, 2002; Chernoray et al., 2005; Serpieri and Kotsonis, 2016b). It is interesting to see that, even though only the structure of the streamwise velocity of the 2kHz wave is visualised, it has similar characteristics to the secondary instability vortex structures of the DNS study of Wassermann and Kloker (2002) which does not select specific frequencies. This means that the structure and distribution of the 2kHz wave is characteristic for the development of the secondary instability occurring in the flow without forcing. In Figure 30 the phase-averaged velocity distribution is shown in the stream wise and wall-normal direction. As expected the magnitude increases going downstream showing that the secondary instability becomes stronger.

From the streamwise distribution the spatial power spectrum at each wall-normal location is calculated as shown in Figure 31. It shows that the streamwise wavelengths of the secondary instability,  $\lambda_x$ , were 6.67 and 7.48mm for Test I and Test II respectively, which gives wavenumbers,  $\alpha_r$ , of 942 and 840. These wavenumbers are plotted in Figure 26 and agree well with the theoretical values from the simplified inviscid analysis.

With the wavenumber the phase speed is calculated with:

$$U_{ph} = \frac{2\pi f_{exc}}{\alpha_r}. \quad (5.6)$$

With a freestream velocity of 18m/s the normalized phase velocity is  $0.74U_\infty$  for Test I and  $0.83U_\infty$  for Test II. These values are very similar to the values found of  $0.78U_e$

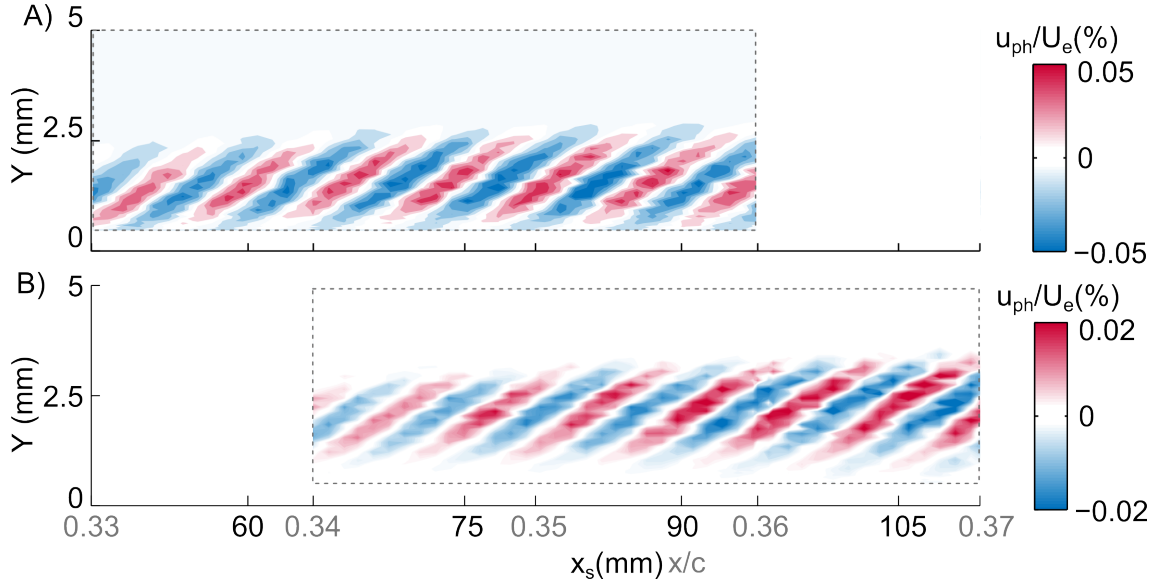


**Figure 30.** Phase-averaged velocity distribution in the streamwise and wall-normal direction for A) Test I and B) Test II. The dashed box indicates the measurement region.

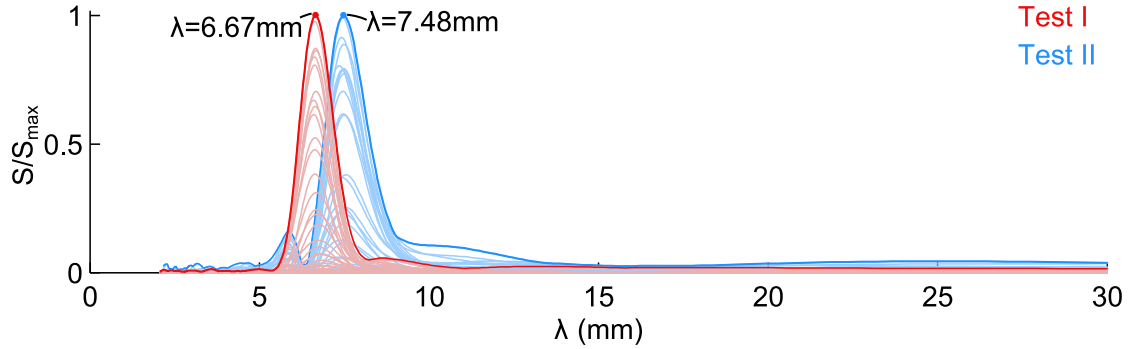


**Figure 31.** Normalized spatial power spectrum of the streamwise phase-averaged velocity distribution for Test I and Test II. In light red and blue the spectrum for each wall-normal location is shown. The bold red and blue line represent the maximum at each wavelength.

to  $0.84U_\infty$  in previous experimental and computational studies (Kawakami et al., 1999; Malik et al., 1999; Serpieri and Kotsonis, 2016b). Next, the angle between the streamwise structures and the wall, which is more or less parallel to the primary vortex axis, as defined in Figure 32A is calculated. The elevation angle,  $\gamma$ , is found by cross-correlating the phase-averaged velocity signals at two wall-normal locations as shown in Figure 32B. The shift which gives the highest correlation represents  $\Delta x_s$  and with this the angle is calculated as:

$$\gamma = \tan^{-1}\left(\frac{\Delta Y}{\Delta x_s}\right) \quad (5.7)$$

The resolution in the streamwise direction mainly determines the accuracy of this

method which, in this case, is 1mm resulting in an accuracy of about 0.3 degrees. The elevation angle calculated with this method is shown with the black lines in Figure 32C and represent the actual angle of the structures. For both Test I and Test II an angle of  $14^\circ$  was found. In Bonfigli and Kloker (2007) and Serpieri and Kotsonis (2016b) similar angles of 12 and 21 degrees were found.

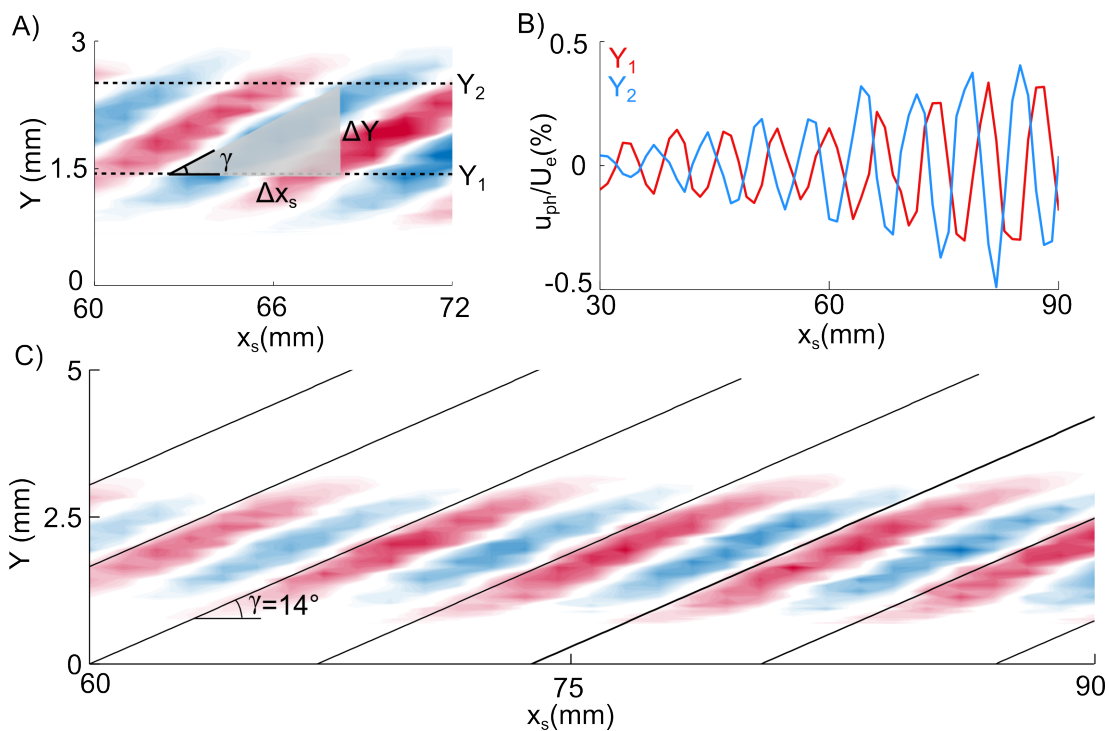


**Figure 32.** A) Definition of the elevation angle  $\gamma$ . The red and blue contours represent the phase-averaged velocity magnitude of the secondary instability. B) The signals at  $Y_1$  and  $Y_2$  are cross correlated to determine  $\Delta x_s$ . C) The phase-averaged velocity distribution where the black lines are inclined under the calculated angle  $\gamma$ .

Finally, in Figure 33 the phase structure is shown in the  $x_s$ - $Z$ -plane at constant wall-normal location of 2mm. The structure has a width of approximately 6mm, which is half of the wavelength of the stationary primary vortex, as was also reported in Kawakami et al. (1999). The azimuthal angle  $\chi$  is determined in a similar way as  $\gamma$  and found to be  $43^\circ$ . This value is much larger than the  $18.2^\circ$  angle found in the experiments by Serpieri and Kotsonis (2016b) and the  $20^\circ$  angle estimated from the figures reported in Kawakami et al. (1999). The value is more similar to the angle reported in the computations of Janke and Balakumar (2000) of  $29.9^\circ$ . The azimuthal angle is dependent on the spanwise structure of the stationary vortex. In the current investigation a clear distinction between the Type-I and Type-II instabilities could

not be made which is due to the structure of the stationary vortex. It seems that the wide range of azimuthal angle reported and found in literature depend on the different shapes of the stationary structures. For the elevation angle the spanwise structure is of less importance resulting in more similar angles found across different studies.

In this section it is shown that the main characteristics of the secondary instability studied in this experiment resemble those found in previous studies. In the next section the further development and breakdown of the secondary instability is discussed.

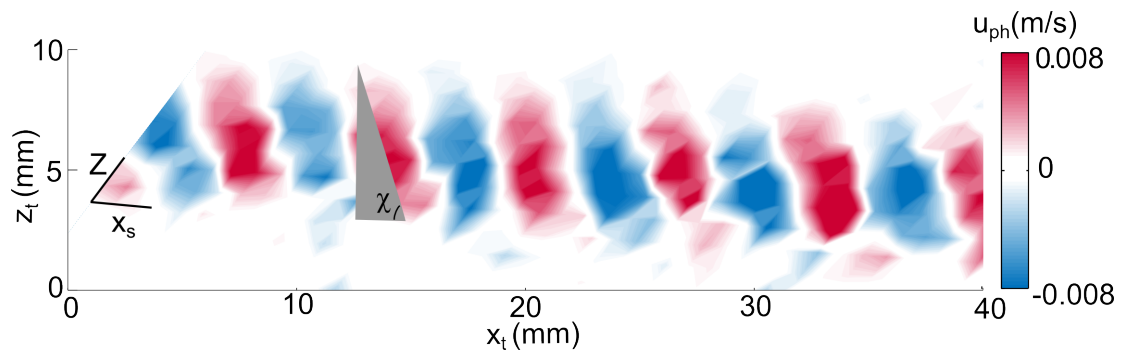


**Figure 33.** Definition of the azimuthal angle  $\chi$ .

### 5.6.3. The secondary instability in the non-linear growth stage

While studying the early development of the secondary instability the focus was on both Test I and Test II, here the focus is on the vortex followed in Test II, since more detailed measurements were carried out for this test. The mean velocity in the  $x_s Z$ -plane is presented in Figure 34A at  $Y=2\text{mm}$ .

The mean velocity distribution clearly shows streaks with high and low velocity due to the stationary vortex structure. Going downstream it is observed that the velocity in the high velocity streak slightly decreases while the velocity in the low velocity streak slightly increases. This indicates that the span wise periodicity decreases due breakdown of the stationary vortices. The orientation of the mean flow streaks is almost horizontal with respect to the  $x_s$ -axis which indicates that the streamline angle obtained from the  $YZ$ -scan, as explained in Section 5.5, was correct to within 2%. The velocity fluctuations in Figure 34B show a wedge structure. The start of the structure is difficult to define and depends on the contour lines chosen. It seems that a diverging structure is observed from  $x/c=0.36$  but the velocity fluctuations increase rapidly from  $x/c=0.38$ . The coherency of the phase structure, shown in Figure 34, disappears around  $x_s=140\text{mm}$  or  $x/c=0.39$ . As shown in Figures 24 and 25 the se-

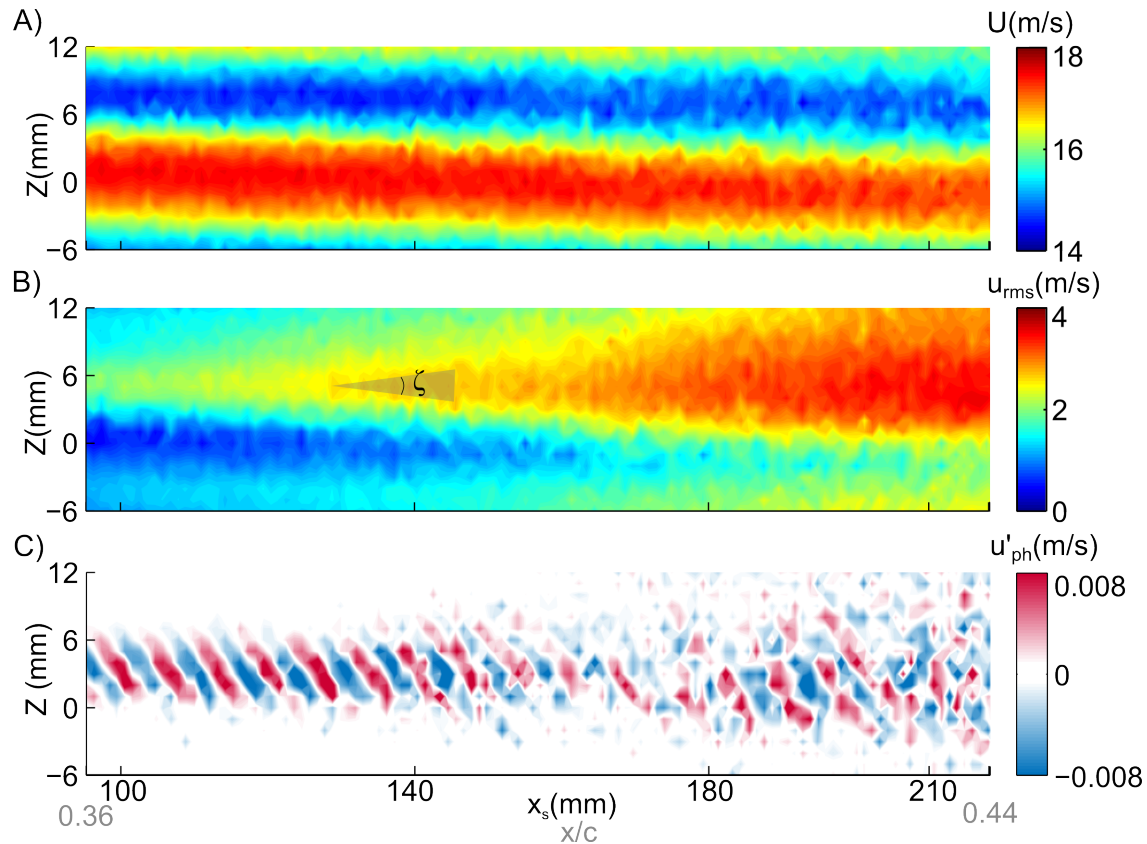


**Figure 34.** The mean velocity (A), fluctuating velocity (B) and phase-averaged velocity (C) distributions along the streamline and spanwise direction for constant wall-normal location ( $Y=2\text{mm}$ ).

condary instability start to grow with a larger growth rate around  $x/c=0.38$  and the high frequency fluctuations from 4kHz-10kHz also start to grow at this streamwise location. As discussed in section 5.2 the increase in the high frequency fluctuations is in agreement with previous studies where the appearance of the wedge has been observed in experimental and computational crossflow studies when the stationary crossflow dominated flow breaks down in turbulence (Dagenhart and Saric, 1999; Wassermann and Kloker, 2002; Borodulin et al., 2017).

### *Wedge characteristics*

The wedge spreading angle,  $\zeta$ , as defined in Figure 34 was determined from three different wedge structures. An angle of 8 degrees was found with a standard deviation of 0.4 degrees. Previous studies did not report wedge angles, however, from the figures presented in Wassermann and Kloker (2002) an angle of 10 degrees was estimated. These angles are similar to the spreading angles of turbulent spots and turbulent wedges caused by large roughness protrusions (Goldstein et al., 2017), suggesting that the physics of the spreading mechanism is similar for all these cases.

The characteristics of the velocity fluctuations through the middle of the wedge ( $Z=5\text{mm}$ ) and outside the wedge ( $Z=-3\text{mm}$ ) are shown in Figure 35 and 36 respectively. The power spectra are presented at each streamwise location with a step size of 1mm. These results were obtained without excitation at 2kHz. For  $Z=5\text{mm}$  the energy of the velocity fluctuations around 2kHz increase around  $x_s=140\text{mm}$  after which the energy of the high frequencies increases. It is noticed that there is some intermittency in space and the magnitude does not increase gradually.

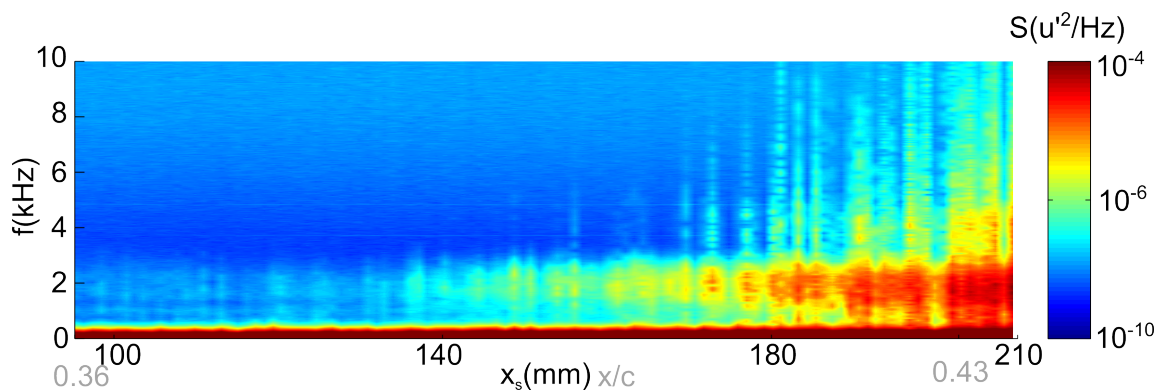


**Figure 35.** Power spectra for different streamwise locations at  $Z=5\text{mm}$  and  $Y=2\text{mm}$ .

The power spectra outside the wedge, at  $Z=-3\text{mm}$  shown in Figure 36 exhibits an even stronger intermittent behaviour in space. Some streamwise locations show high energy in the 2kHz region, while at an adjacent location the energy level is low. The energy level is significantly lower than inside the wedge which represents the local and three-dimensional signature of the breakdown process.

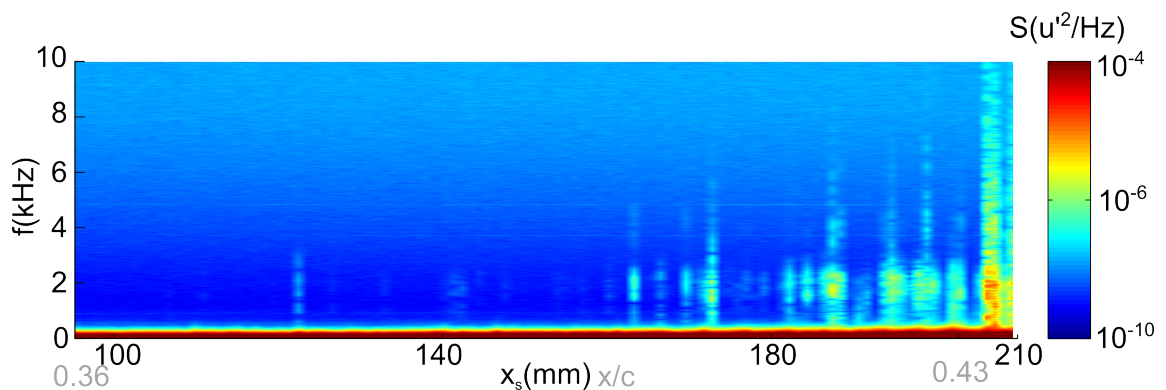


**Figure 36.** Power spectra for different streamwise locations at  $Z=-3\text{mm}$  and  $Y=2\text{mm}$ .

To better understand the intermittent behaviour in Figure 36, the time signal and power spectra in and outside a high intensity patch outside the wedge is presented in Figure 37 together with the time signal at the same streamwise location inside the

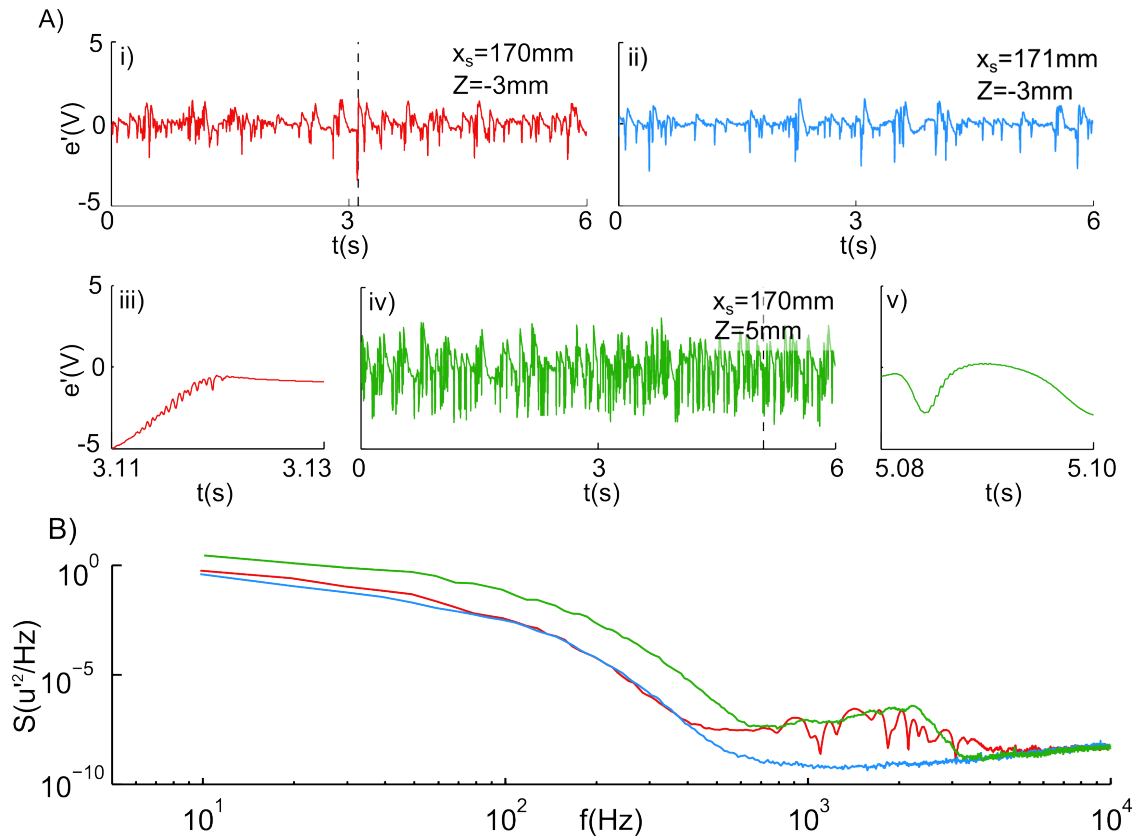


**Figure 37. Time signal and power spectra inside and outside the wedge structure.** *Ai*) Time signal outside the wedge, at  $x_s=170\text{mm}$ , where there is energy for the high frequency fluctuations. *ii*) Time signal outside the wedge, at  $x_s=171\text{mm}$ , where there is no energy for the high frequency fluctuations. *iii*) Detail of the time signal at the dashed line shown in *i*. *iv*) Time signal inside the wedge, at  $x_s=170\text{mm}$ . *v*) Detail of the time signal at the dashed line shown in *iv*. B) Power spectra of three different time signals. The color of the power spectrum corresponds to the color of the time signals shown in A.

wedge. The signals outside the wedge (37Ai and 37Aii) do not differ from each other significantly while inside the wedge the overall fluctuations are higher. At  $x_s=170\text{mm}$  a large peak is shown at  $t=3.1\text{s}$  for  $Z=-3\text{mm}$ . A closer look at the time signal (37Aiii), shows the appearance of high frequency fluctuations riding on top of the edge of the large peak. For the signal inside the wedge a large number of these peaks with a similar behaviour is found. The effect of this peak on the power spectrum shows that  $x_s=170\text{mm}$  the power spectrum is highly distorted. At  $x_s=171\text{mm}$  there is no energy in the high frequency band. It seems that the high intensity patches at  $Z=-3\text{mm}$  are directly related to the developing wedge, since they become more frequent when the wedge gains strength. Goldstein et al. (2017) among others found that the spreading of the wedge is driven from its edges. This possibly happens in the current case where the laminar flow, in close proximity to the wedge is already influenced by the wedge structure. It should be noted that the exact pattern shown in Figures 35 and

36 is not repeatable. The analysis of the time signals show that the large peaks appear randomly in the time signal. Therefore when the measurement would be carried out again the high intensity peaks could be at slightly different streamwise locations. Nevertheless, it is expected that the intermittent behaviour would be observed again.

The  $x_s$ - $Y$ -scan through the middle of the wedge at  $Z=5\text{mm}$  is shown in Figure 38. It should be noted that for this scan the secondary instability was excited with a small amount of forcing, which did not influence the onset location of the wedge. Ideally, no forcing would have been applied however, due to time limitations this measurement was not carried out. From the total fluctuations no apparent difference in structure or magnitude is shown when the wedge starts to grow. When the flow breaks down the velocity fluctuations increase over the entire frequency range. The fluctuations from 900-2300Hz in the  $x_s$ - $Y$ -plane show a diverging structure which initiates at a similar streamwise location where the wedge starts in the  $x_s$ - $Z$ -plane (Figure 38). The wedge structure in the wall-normal direction has, up to the author's knowledge, not been reported before. From previous studies with wall-based measures, the onset of breakdown is defined at the bottom of the vortex structure where the secondary instability fluctuations reach the wall. Even though, the location at the wall is probably more relevant in engineering applications, it is thought that to gain understanding in the mechanism of breakdown the region where the secondary instability fluctuations diverge towards the wall should be studied in more detail.

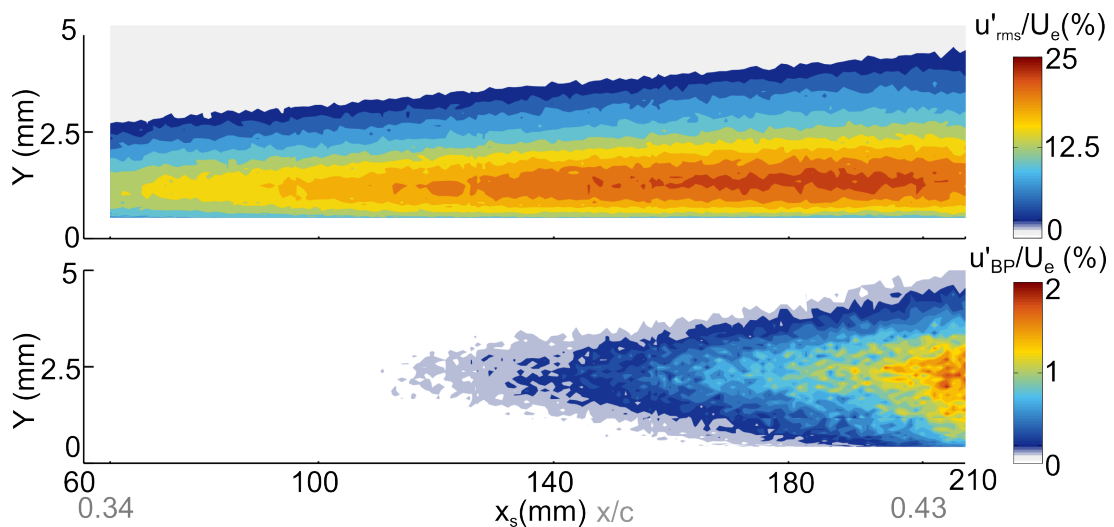


**Figure 38.** A) Total velocity fluctuations in the  $x_s$ - $Y$ -plane ( $Z=5\text{mm}$ ). B) Bandpass filtered velocity fluctuations between 900-2300Hz in the  $x_s$ - $Y$ -plane ( $Z=5\text{mm}$ ).

### *Interaction with neighbouring vortices*

When the phase-averaged velocity distributions from Test I were analysed an unusual

behaviour was found. This is shown in Figure 39 where the phase-averaged velocity distribution from Test I is compared to Test II.

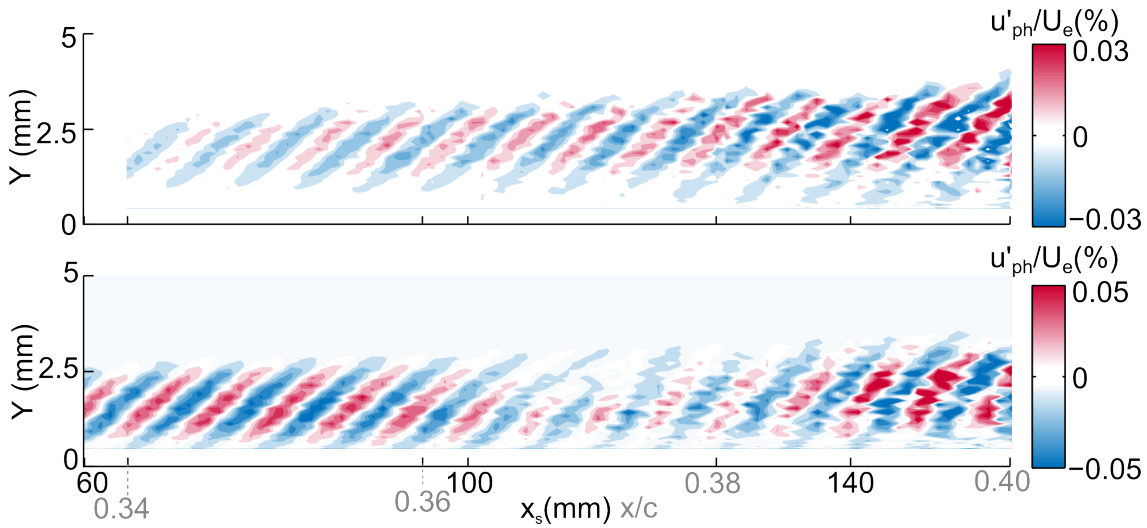


**Figure 39.** A) Phase-averaged velocity distribution in the  $x_s$ - $Y$ -plane for A) Test I and B) Test II.

Up to  $x_s=100$ mm the phase-averaged velocity distributions develop similar for both tests. After that the phase-averaged velocity decreases for Test I while for Test II a gradual increase is observed. First it was thought that an experimental error was made, however, when the phase-averaged velocity fluctuations in the  $YZ$ -plane at  $x/c=0.34$  are compared to  $x/c=0.38$  a similar behaviour has been observed, as presented in Figure 40.

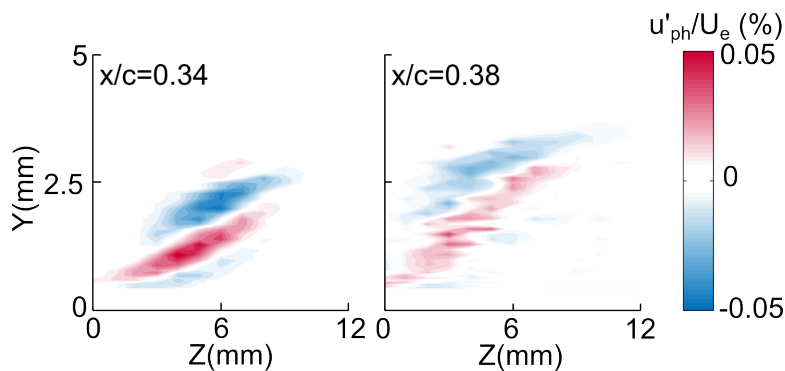


**Figure 40.** A) Phase-averaged velocity distributions in the  $YZ$ -plane for Test II at two chordwise locations.

Another hypothesis was that the decrease in phase velocity was caused by an interaction of two 2kHz waves. When these two waves are not in phase, it will appear as a lower phase-averaged velocity. This other wave could be coming from a neighbouring vortex. The bandpass filtered velocities for Test I showed that the high

amplitude fluctuations are coming from the side of the vortex instead of the middle as is also shown in Figure 25. In previous computational studies the interaction of neighbouring vortices of uneven strength have been investigated for two cases. In Wassermann and Kloker (2002) vortices with a similar wavelength but uneven strength were studied. It was found that these two vortices will cause earlier breakdown than two vortices of the same strength. In Choudhari et al. (2016) the strong modulation of stationary vortices caused different vortices to merge together leading to transition further downstream compared to vortices of the same strength. Because of the behaviour shown in Figure 39 for Test I it was chosen to study the interaction of different vortices in more detail for Test II which results are discussed in the following paragraphs.

In Figure 41 the mean velocity distribution, total fluctuations and secondary instability fluctuations are shown for the spanwise region on the left of the vortex studied in Test II. The mean velocity fields show that vortex B is weaker than vortex A and C and consequently that a fully spanwise uniform flow was not obtained. The influence of spanwise modulation of the stationary crossflow vortices on the development of the secondary instability has been studied in numerical studies by Wassermann and Kloker (2002) and Choudhari et al. (2016). In these studies the spanwise modulation causes the vortices to be of different strength, however, the wavelength of both vortices is similar. In contrast here it is found that next to the difference in strength, vortex B is more shallow and has a larger wavelength than vortex A and C. The velocity fluctuations for the dominating secondary instability (900-2300Hz), show that in vortex B no fluctuations appear. Chernoray et al. (2005) suggest that the ratio of the vortex width to the vortex height determines if a Type I or Type II mode appears. For two neighbouring modulated vortices, a Type I mode appears in the vortex with the smallest height-to-width-ratio while a Type-II mode develops in the other vortex. In the current experiment, the weaker vortex has a smaller height-to-width ratio but neither Type-I or Type-II fluctuations were observed, indicating the complete absence of a secondary instability in this vortex at this streamwise location.

The streamwise development of vortices A, B and C is shown in Figure 42 at the wall-normal location indicated in Figure 41 with the dashed line. As expected, two wedges appear in vortex A and C. The wedges appear at the same  $x_s$  location, indicating that the primary vortices developed in a similar manner. For vortex B no wedge structure has been observed, instead there are two regions where the fluctuations are growing as indicated at the start of the measurement region, which

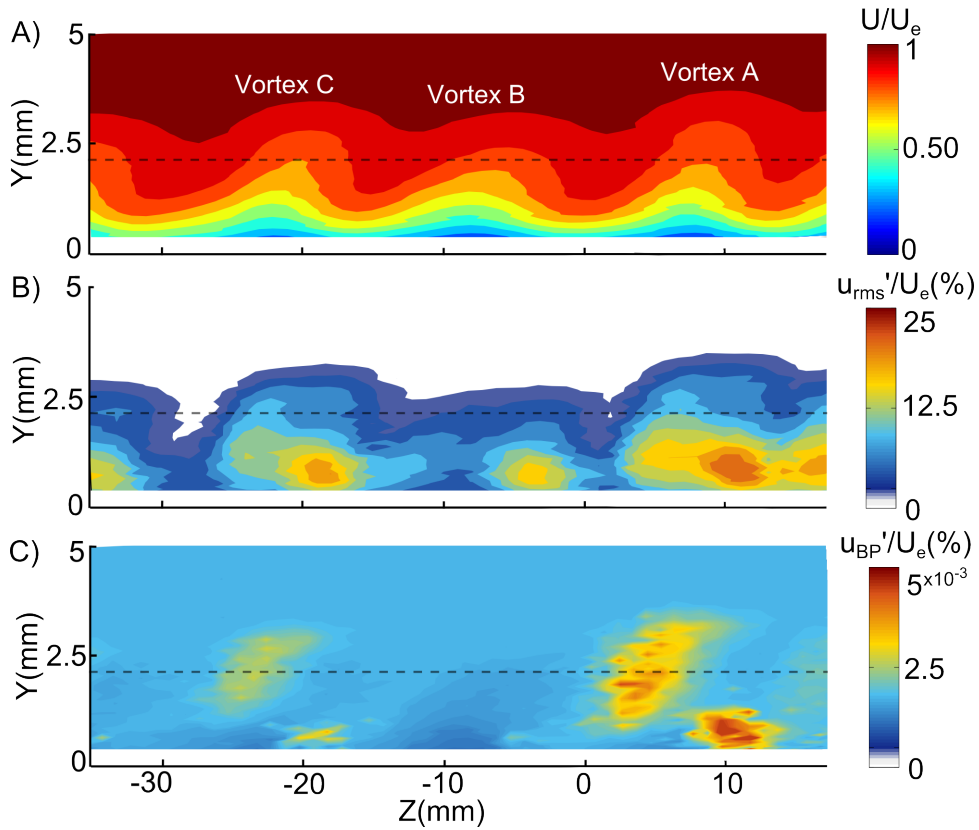


**Figure 41.** A) Mean velocity distribution at  $x/c=0.36$ . C) Total velocity fluctuations between 2Hz-10000Hz. B) Bandpass filtered velocity fluctuations between 900-2300Hz.

is also observed from Figure 41B. Around  $x_s=140$ mm the regions merge together but no large increase in amplitude as shown for vortex A and C has been observed.

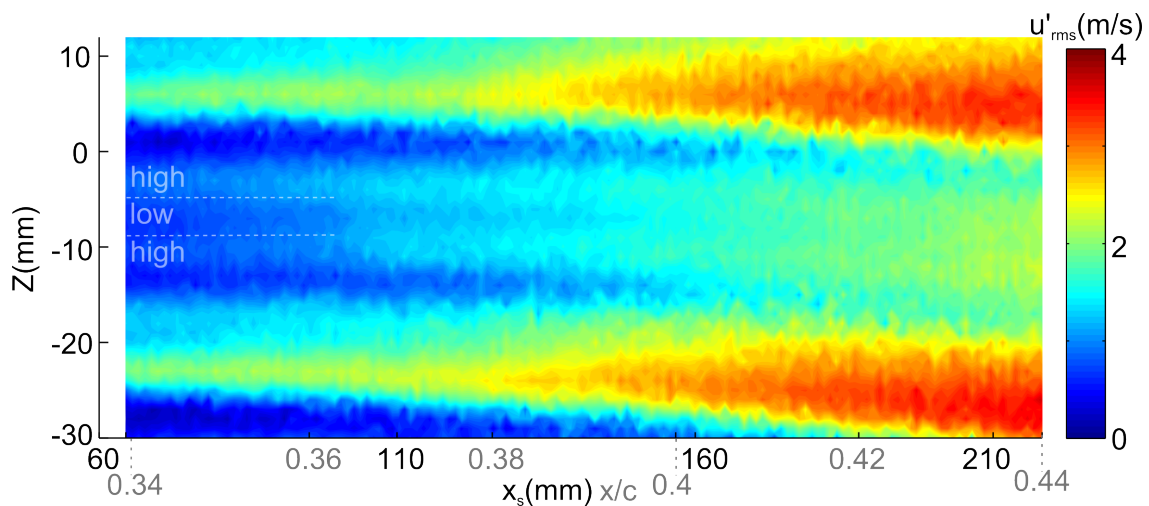


**Figure 42.** Distribution of the velocity fluctuations in the  $x_s$ - $Z$ -plane for  $Z=-26$ mm to  $Z=12$ mm.

It was found that through the middle of the wedge of vortex A and C the develop-

ment of the velocity fluctuations is the same as in Figure 35. The development of the velocity fluctuations at  $Z=-10\text{mm}$ , which is the location where the secondary instabilities in vortex B would be expected to grow, is shown in Figure 43. From  $x/c=0.42$  there is some activity around  $0.5\text{kHz}-2\text{kHz}$  but no clear continuous increase of high frequency fluctuations is shown. This indicates that in the entire measurement region the secondary instability does not appear for vortex B. Furthermore, the turbulent wedges from the stronger vortices do not seem to contaminate the weaker vortex to lead to earlier transition. If the flow would have been spanwise uniform, with three vortices of similar overall strength, it would be expected that the average breakdown location of the three vortices would be around  $x/c=0.40$ . In the current case, where the stationary crossflow vortices are modulated in the spanwise direction, the average breakdown location is further downstream since the breakdown location of vortex B is not observed up to  $x/c=0.44$ . This behaviour seems similar to what had been found in Choudhari et al. (2016). They hypothesized that transition occurs at a location further downstream, compared to a case without spanwise modulation of the stationary vortices, since the wedge structure of the large vortex has to spread a further spanwise distance to interact with neighbouring vortices. Here it is found that no secondary instability develops in the weaker vortex. Due to its large wavelength, the turbulent wedges of the neighbouring vortices do not contaminate the vortex and no breakdown is observed prior to  $x/c=0.44$ .

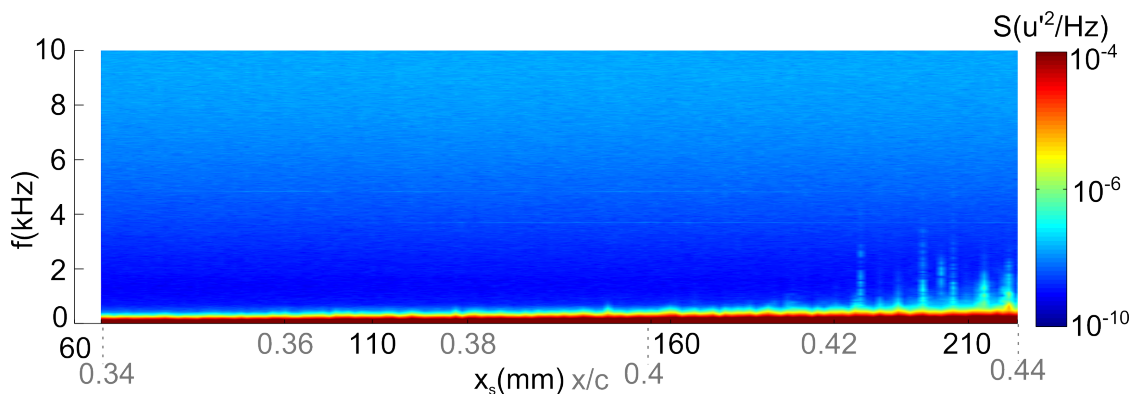


**Figure 43.** Power spectra at different streamwise locations for  $Z=-10\text{mm}$  in Figure 42.

In Figure 44 the mean velocity distribution is shown for the spanwise region on the right of the vortex studied in Test II, for  $x/c=0.36$  and  $x/c=0.40$ . The vortices are of different strength, where vortex D is the weakest and vortex E seems slightly stronger than vortex A. In contrast to vortices A,B and C, shown in Figure 41, the spanwise wavelengths of all three vortices are similar, which makes it similar to the vortex packet studied by Wassermann and Kloker (2002). The amplitude of the fluctuating component for these YZ-scans was not correctly measured due to

wrong filter settings, but the spatial distribution is expected to be correct. The total velocity fluctuations in Figure 44 show that at  $x/c=0.36$  there are no regions with strong disturbances in vortex D in comparison to vortex A and E. At  $x/c=0.40$  the regions from vortex A and E create stronger disturbances in vortex D. In Figure 44C it is shown that the secondary instability developed in vortex A and E. In vortex D there was no distinct region with high frequency fluctuations, however at some locations bursts, similar to those shown in Figure 37, were observed.

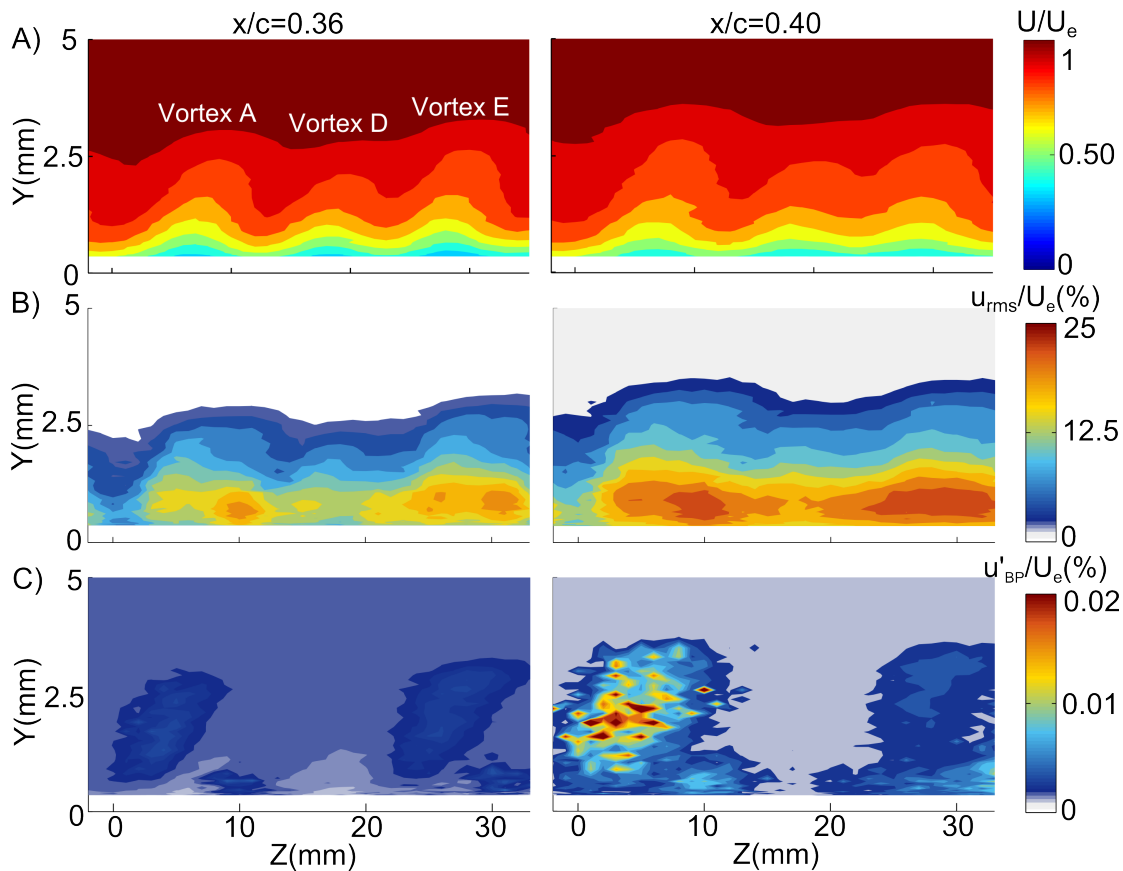


**Figure 44.** A) Mean velocity distribution. C) Total velocity fluctuations between 2Hz-10000Hz. B) Bandpass filtered velocity fluctuations between 900-2300Hz.

The streamwise development in the  $x_s Z$ -plane of vortices A, D and E is shown in Figure 45. The onset of the wedge for vortex E is about 20-30mm upstream of the onset of the wedge for vortex A. For vortex D a weaker wedge structure seems to be created around  $x/c=0.37$ , which indicates that despite its lower strength, vortex D is breaking down. This is interesting since from the mean velocity distribution at  $x/c=0.36$  this would not be expected.

The development of the fluctuations at  $Z=17$ mm, in the upwelling region of vortex D, is shown in Figure 46. At  $x/c=0.36$  the velocity fluctuations around 2kHz already have a high energy level. Going downstream an intermittent behaviour is shown

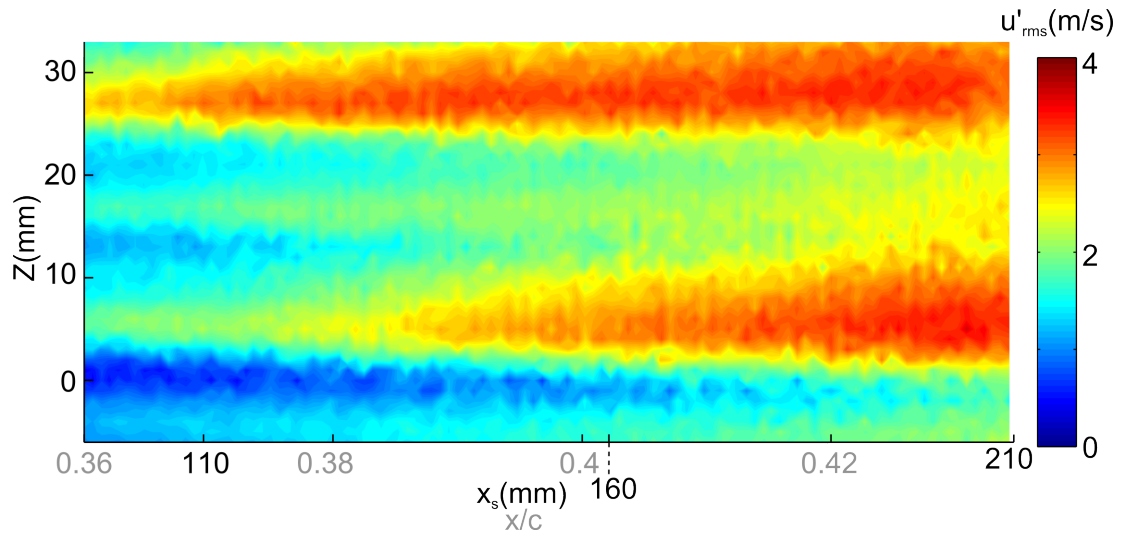


**Figure 45.** Distribution of the velocity fluctuations in the  $x_s Z$ -plane for  $Z=-6\text{mm}$  to  $Z=33\text{mm}$  ( $Y=2\text{mm}$ ).

where at some locations the energy level of the velocity fluctuations with frequencies above  $3\text{kHz}$  is significantly increased. Since the mean velocity distributions did not indicate the appearance of a secondary instability in vortex D and vortices D and E merge together, as shown in Figure 44A at  $x/c=0.40$ , it is thought that the high frequency fluctuations are due to turbulent contamination from vortex D and E.

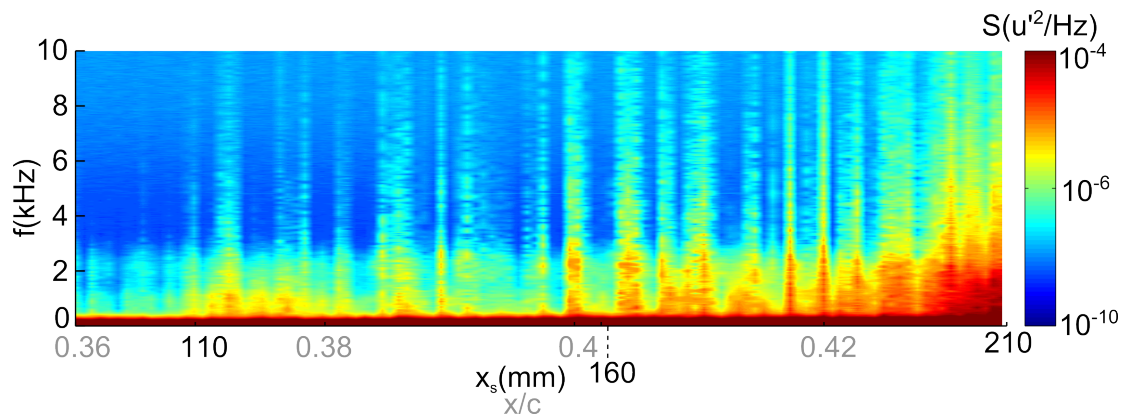


**Figure 46.** Power spectra at different streamwise locations for  $Z=17\text{mm}$  in Figure 45.

The velocity fluctuations at  $x_s=210\text{mm}$ , the measurement location furthest downstream, are shown across the span in Figure 47. The high frequency velocity fluctuations in vortex E are the strongest, which would also be expected from the wedge development shown in Figure 45. For vortices A and D no clear differences in energy levels are observed. This shows that even though vortex D was less strong than vortex A, the breakdown process occurred in a similar way, due to the influence of the neighbouring vortices. As discussed earlier Wassermann and Kloker (2002) found in

their DNS study, that, in contrast to what was found by Choudhari et al. (2016), the spanwise modulation of a stationary vortex package can lead to earlier transition than when the flow would be fully uniform. The vortex package in this study consisted of a strong and weak vortex of similar wavelength. Here a similar behaviour has been found. The development of vortices D and E show that a vortex packet with a strong and weak vortex both breakdown when they both have a similar wavelength. The development of vortices A and D show that the weaker vortex can breakdown at a similar streamwise location as the stronger vortex.

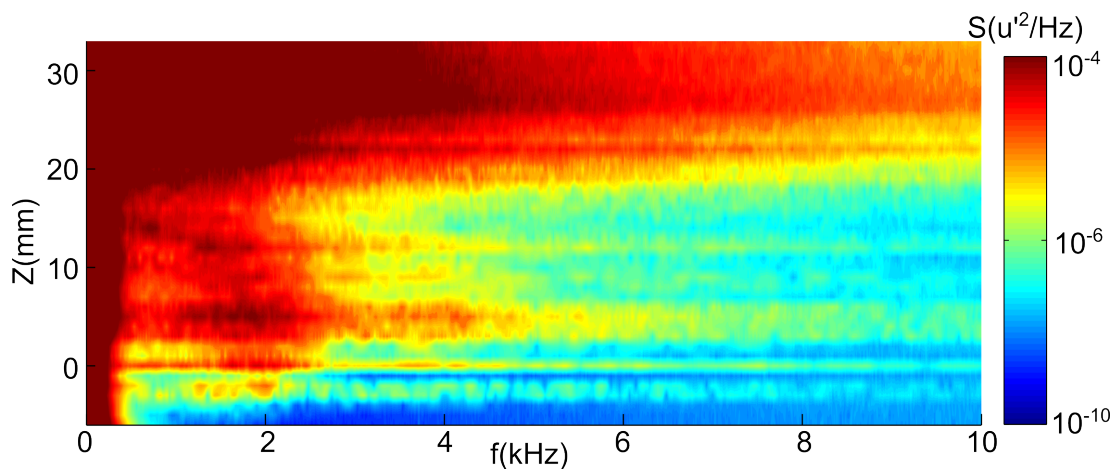


**Figure 47.** Power spectra at different  $Z$  locations for  $x_s=210\text{mm}$  in Figure 45.

This paragraph started with Figure 39 which showed an interesting behaviour of the phase averaged velocity distribution in Test I. With the analysis of the vortex packages obtained in Test II it can now be concluded that the observed decrease in phase-averaged velocity is caused by a 2kHz wave from a neighbouring vortex. After the decrease the phase-averaged velocity increases again which is an indication that the stronger wave is dominating the flow. The mean velocity distribution of Test I shown in Figure 15 shows that around  $x/c=0.38$  another vortex is coming in from the right and that they merge together further downstream similar as what was observed for vortices D and E in Test II. This is also shown for the high frequency velocity fluctuation distribution where the fluctuations are strongest on the right side of the vortex. This would explain why the development of the travelling waves in the weaker vortex of Test I, compared to Test II, is similar for both tests.

### *Structure of the secondary instability*

The streamwise distribution of the phase-averaged velocity for Test II is shown in Figure 48. From  $x_s=125\text{mm}$  ( $x/c=0.38$ ) the magnitude of the phase-averaged velocity increases rapidly and the coherency disappears, as would be expected from the

wedge development. The wavelength of the secondary instability and elevation angle does not change significantly downstream. Chernoray et al. (2005) measured and visualized the onset and breakdown of the secondary instability of a single vortex with high spatial resolution. Initially, the structure is similar, however, going downstream the breakdown into smaller structures has not been observed in Chernoray et al. (2005). The reason for this is unclear, since when the flow becomes turbulent it would be expected that structures are broken up and a more chaotic flow appears.

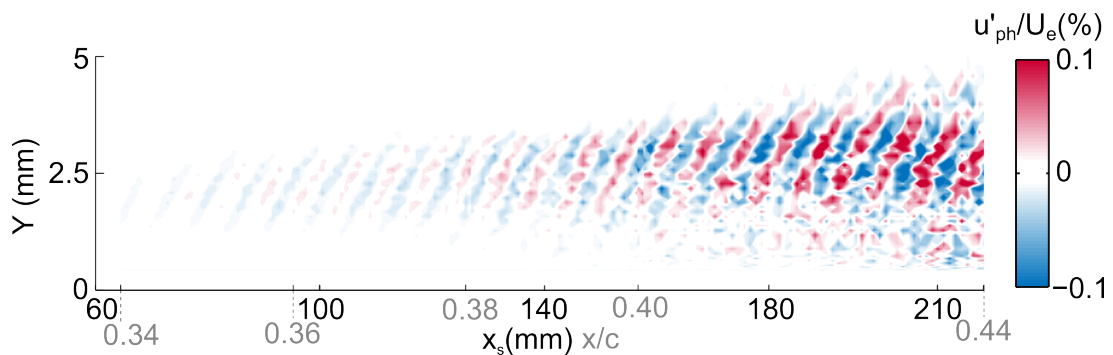


**Figure 48.** Phase-averaged velocity distribution in the wall-normal and streamwise direction for Test II ( $Z=5\text{mm}$ ).

In Figure 49A the structure in the wall-normal and spanwise plane is shown at  $x/c=0.34$ ,  $0.38$  and  $0.40$ . From  $x/c=0.34$  to  $x/c=0.38$  the phase-averaged velocity becomes stronger and a slight spreading over the vortex is observed. At  $x/c=0.40$ , which is in the middle of the wedge, the structure has spread over the entire vortex. Furthermore, the initial structure has broken down in smaller structures which is also shown in the three-dimensional representation, shown in Figure 49B. It seems that the structure has been torn apart in the spanwise direction due to the increased spanwise extent of the wedge. It is interesting that even though the flow is breaking down such coherent structure could still be detected. Wassermann and Kloker (2002) visualised the breakdown process of the secondary instability with vortical structures. The structures found in the present study at  $x/c=0.4$  could not be distinguished from numerical noise in their results which they explain as a limitation of the numerical method.

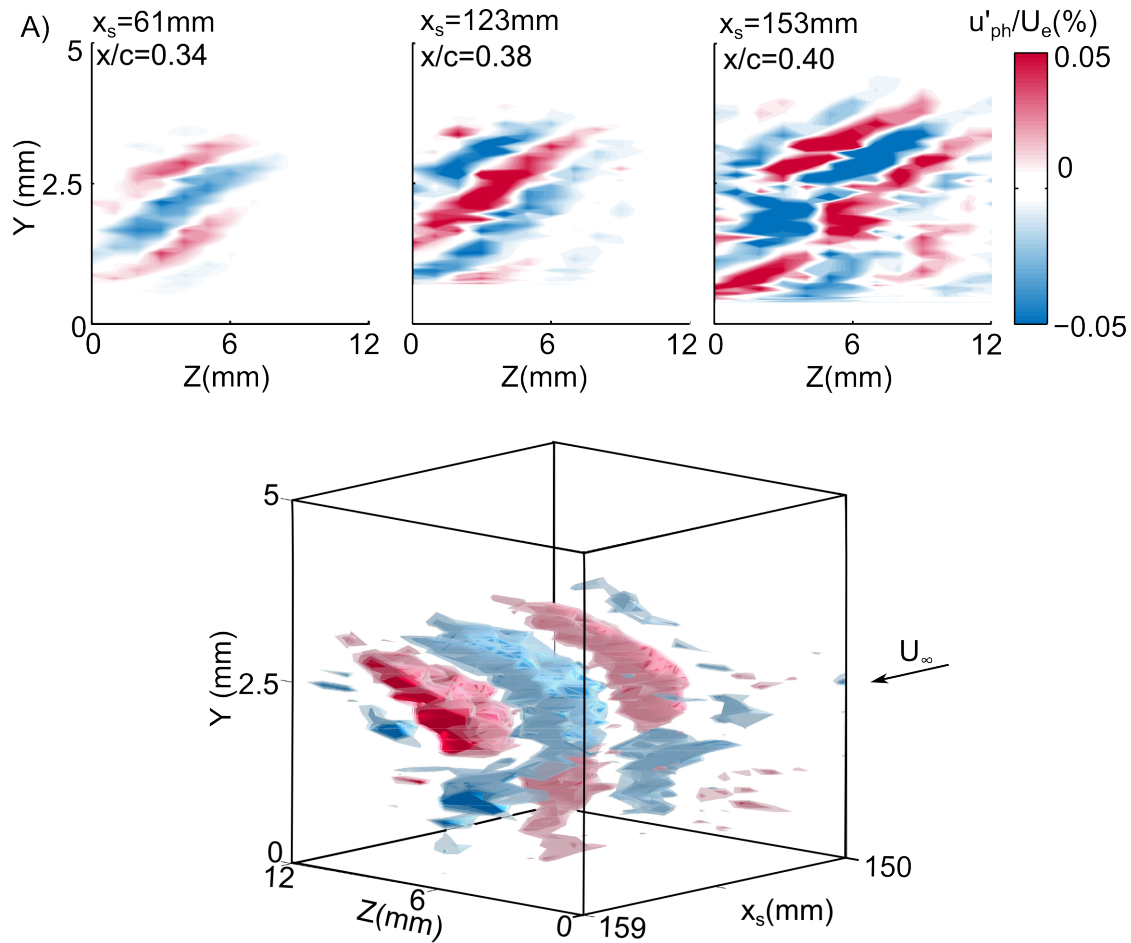


**Figure 49.** A) Phase-averaged velocity distributions in the spanwise and wall-normal plane for different chordwise locations. B) Three dimensional representation of the phase-averaged velocity distribution at  $x/c=0.4$ .

#### 5.6.4. Conclusions: development of the secondary instability

In this section the development of the secondary instability was studied in the linear and non-linear growth stage, leading to the following conclusions:

The secondary crossflow instability measured here had similar characteristics as the secondary instability found in previous studies.

- When the flow breaks down the secondary instability fluctuations spread in the wall-normal and spanwise direction. The full-spectrum velocity fluctuations show a wedge structure in the spanwise direction.
- The wedge structure, leading to breakdown of the flow, starts in the middle of the vortex where the fluctuations of the secondary crossflow instability are strongest. The location of breakdown with wall-based measures would be measured further downstream since that is where the secondary instability velocity fluctuations reach the wall.

- The results of the measurements from Test II indicate that the spanwise modulation of the stationary crossflow vortices can influence the transition location due to the interaction of neighbouring vortices. When there are three vortices with a weaker middle vortex with a larger wavelength it is found that the middle vortex does not get contaminated by the turbulent wedge of the stronger vortices on each side. This would indicate that the transition front would move downstream compared to a case where the three vortices had the same strength and wavelength. When there are three vortices with a weaker middle vortex but similar wavelength it is found that the neighbouring vortex merges with the weaker vortex leading to turbulent contamination and breakdown of the weaker vortex. This indicates that the transition front would move upstream compared to the case where the three vortices have the strength and wavelength.

## 5.7. Results: wall-forcing

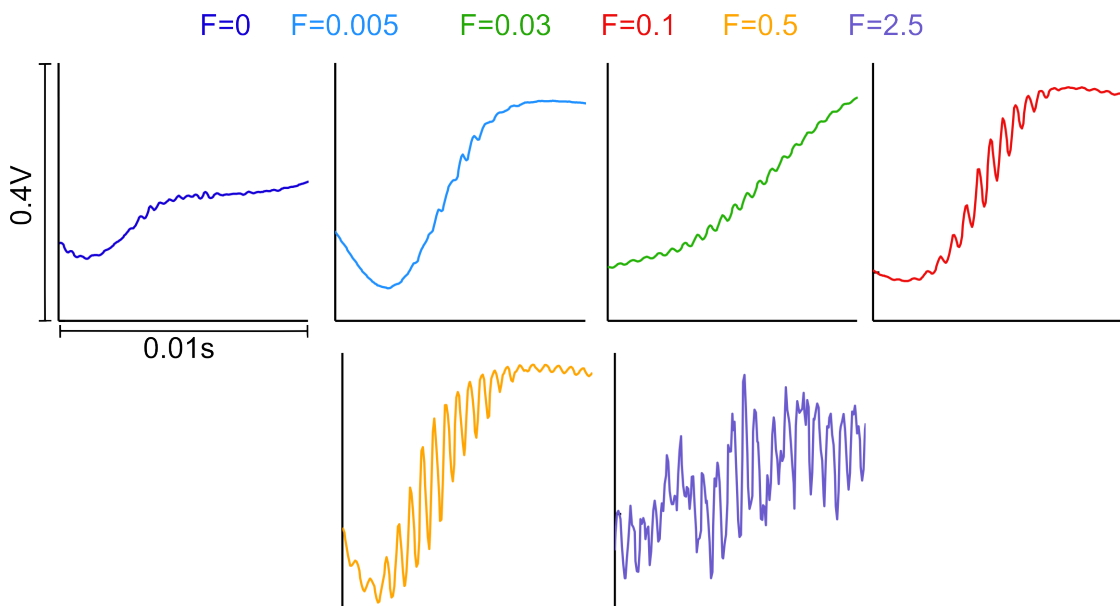


**Figure 50.** Detail of the time signal for different forcing amplitudes.

In this section the influence of wall-forcing on the development of the secondary instability is discussed. A detail of the time signal for different forcing amplitudes is shown in Figure 50. Up to  $F=0.5$  the signal is taken at  $x_s=98\text{mm}$  or  $x/c=0.36$ , while for  $F=2.5$  an earlier location is chosen since at  $x_s=98\text{mm}$  the flow broke down into turbulence. For the small forcing amplitudes the 2kHz fluctuations reside on the side of a spike as is also the case for the time signal without forcing. For  $F=2.5$  the fluctuations are present at any time in the flow, which is only observed for the

unforced case (Figure 18) when the flow is already completely broken down, giving a first indication that for the highest forcing amplitude another transition path is followed. The development of the flow is obtained from the  $x_s$ -scan and presented in Figure 51 for different forcing amplitudes. The following observations are made for each  $x_s$  and  $x/c$ -location.

- $x_s=0\text{mm}$ : For the large forcing amplitudes of 0.5 and 2.5 the second harmonic is clearly shown which indicates the forcing was non-linear. For the lower forcing the excitation signal is a pure sine wave at 2kHz since no harmonics appear. The power spectra look identical when the excitation frequency is excluded, indicating that the base flow was not dependent on the forcing at the exciter location. This agrees with the mean velocity profiles at the exciter shown in Figure 5.
- $x_s=8\text{mm}$ : The energy in the velocity fluctuations from 300Hz-10kHz has increased for  $F=2.5$  and 0.5. The harmonics are clearly shown for both cases. For  $F=0.5$  the energy distribution of the fluctuations around 2kHz is similar to those found in the natural case shown at  $x_s=64\text{mm}$ . This indicates that even though the flow is strongly forced, similar frequencies are still amplified and dominating the transition process. For  $F<0.5$  the peak around 2kHz has broadened compared to  $x_s=0\text{mm}$ , suggesting that there is some initial interaction with the natural occurring secondary instability in the flow.
- $x_s=64\text{mm}$ : For the lower forcing amplitudes ( $F<0.5$ ) the magnitudes of the  $f=2\text{kHz}$  mode and its harmonics are increased; however the rest of the spectra are identical to the case without forcing, which confirms that the forcing is limited to the fluctuations in the 2kHz range. For  $F=0.1$  the width of the 2kHz peak is limited to the band of frequencies amplified in the flow without forcing. The secondary instability is a flow structure consisting of fluctuations with a large band of frequencies (Wassermann and Kloker, 2002; White and Saric, 2005). The broadening of the peak suggests that, even though only one frequency is excited, the entire secondary instability flow structure is excited.
- $x_s=157\text{mm}$ : Turbulent power spectra are shown for both  $F=2.5$  and  $F=0.5$ . For the lower forcing amplitudes the energy level for the high frequency fluctuations is higher for  $F=0.1$  than for  $F=0.03$  to  $F=0$ , indicating that for  $F=0.1$  full transition will occur earlier.
- $x_s=248\text{mm}$ : The flow is turbulent for all forcing cases. The energy level for the low frequency fluctuations (10-100Hz) still shows an dependency on the forcing amplitude which will be discussed later in this section.

It is observed that for the flow without forcing, the high frequency fluctuations are first centered around 2kHz, however, at  $x/c=0.40$  the maximum energy is around

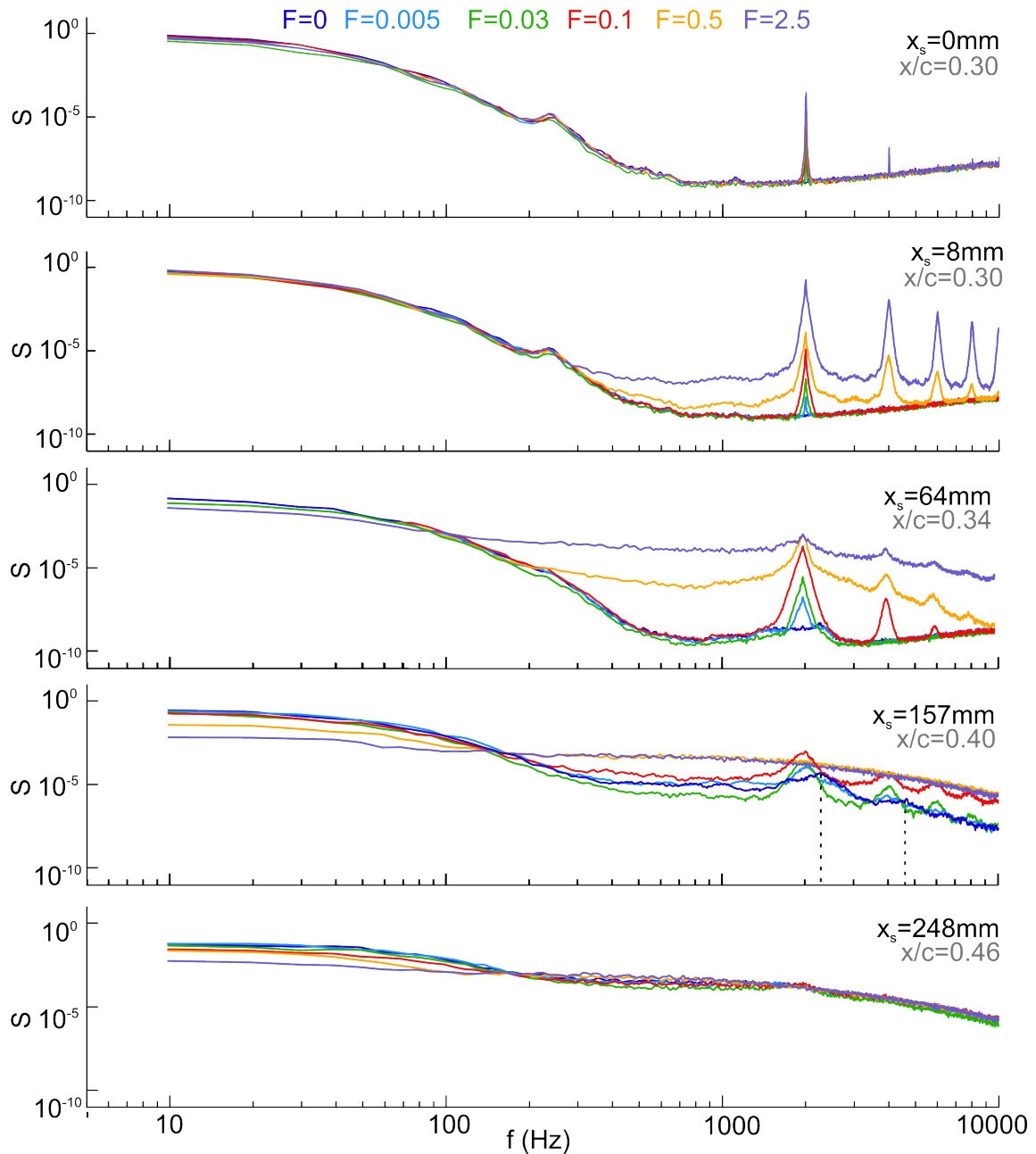


**Figure 51.** Power spectra at different chordwise locations for several forcing amplitudes. The unit of  $S(u'^2/Hz)$  is omitted here due to the limited amount of space.

2.2kHz. The second harmonic seems to grow around 4.6kHz. Therefore, forcing around 2.3kHz might have been even more effective. In previous studies the harmonics of the natural secondary instability were reported and it has been concluded that these are a product of nonlinear interactions (White and Saric, 2005; Chernoray et al., 2005). Here, the harmonics at the high forcing amplitudes seem to be due to the non-linear input, but at amplitudes below 0.5 they appear far from the excitation source indicating that they could be flow related. In Figure 52 the growth

of the fluctuations around the primary 2kHz mode and the second harmonic are shown. The amplitude  $A_{BP,x}$  is normalised by  $A_{BP,xEnd}$  which is the amplitude at

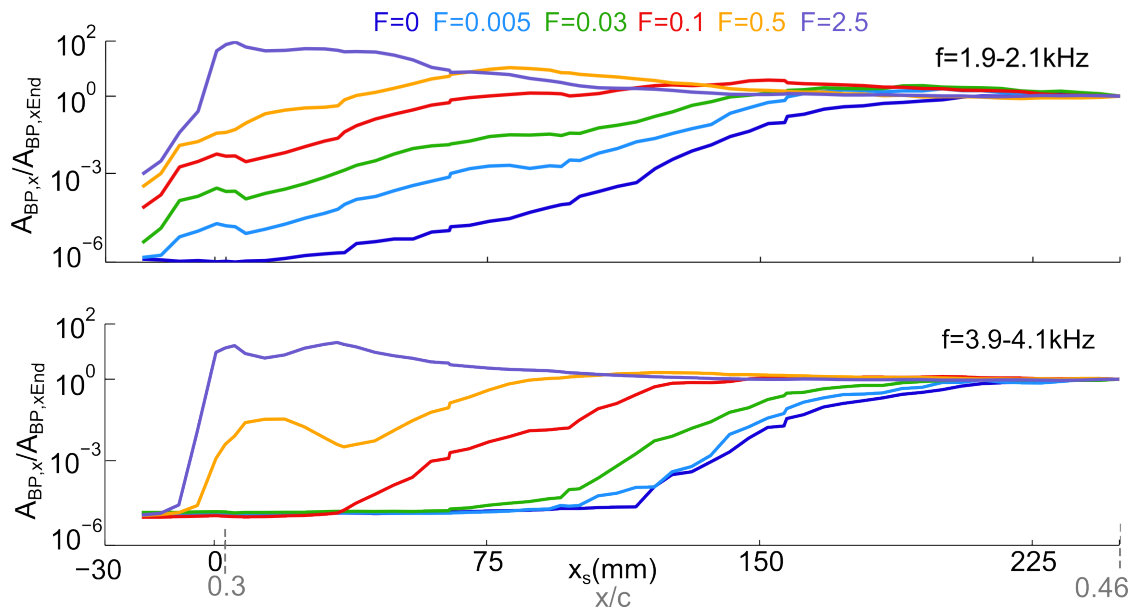


**Figure 52.** Growth of the velocity fluctuations for 1.9kHz-2.1kHz and 3.9kHz-4.1kHz for different forcing amplitudes obtained from the  $x_s$ -scan.

$x/c=0.46$  which is the final measurement location. For  $F=2.5$  the 2kHz mode shows small growth after  $x_s=0$ mm, indicating that the flow breaks down quickly after the forcing is applied. For the forcing amplitudes below  $F=0.5$  the growth curves are similar to each other, however the saturation point differs in streamwise location and amplitude. The difference in saturation location, suggests that the growth and breakdown of the secondary instability is altered by moderate wall forcing. Similar results were obtained by Kawakami et al. (1999) who studied comparable forcing amplitudes. The growth of the second harmonic (3.9-4.1kHz) shows that the location where the harmonic starts to grow is dependent on the forcing amplitude. For  $F=0.5$  the amplitude first increases when the forcing is applied and then after a short decrease it increases again. This indicates that the forcing was nonlinear but the harmonic did initially not interact with the flow which caused a decrease in amplitude after the forcing was applied. Then when the secondary instability starts to grow it interacts with the flow causing an increase again. This behaviour is very similar to what is observed close to the neutral stability point of the primary instability and indicates that such a neutral stability point also exists for the secondary instability. The growth rate of the second harmonic is about twice that of the first harmonic or fundamental. The spatial distribution of the second harmonic coincides with the fluctuations of the 2kHz mode as shown in Figure 53.

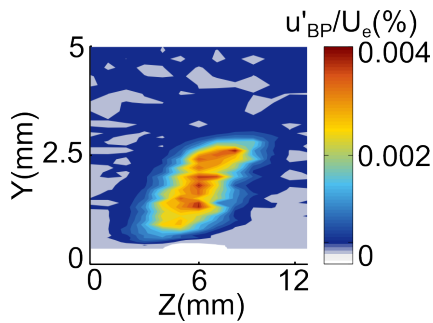


**Figure 53.** Spatial distribution of velocity fluctuations between 3.9kHz-4.1kHz for  $F=0.25$ .

The growth rate and spatial distribution both indicate that the harmonics are flow related and caused by non-linear interactions as discussed and shown by [White and Saric \(2005\)](#); [Chernoray et al. \(2005\)](#). Comparing the growth and saturation of the primary and secondary crossflow instability shows that there are similarities between both instabilities. For the primary crossflow instability the primary stationary structure saturates after which nonlinear effects of the primary structure start to play a role. When the forcing, by for example roughness, is increased the saturation amplitude stays the same however the saturation process occurs over a shorter distance. Figures 51 and 52 show a similar mechanism for the secondary instability with wall-forcing.

The growth of the total velocity fluctuations filtered between 2Hz-10kHz is shown in Figure 54.

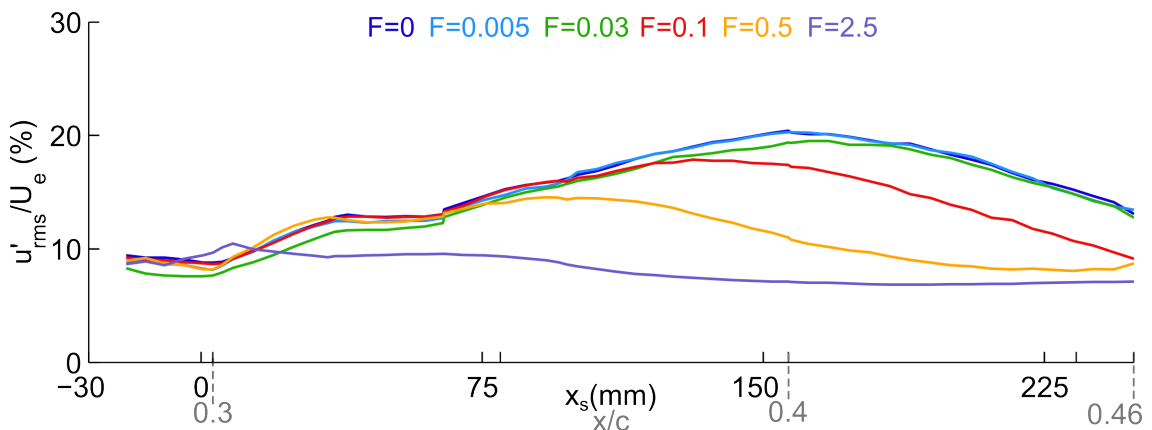


**Figure 54.** Development of the full-spectrum velocity fluctuations for different forcing amplitudes, obtained from the  $x_s$ -scan.

As mentioned before, the magnitude of the total fluctuations is dominated by a low frequency band up to 100Hz. The decrease of the total fluctuations and shift in saturation location, is not arbitrary and several hypotheses are proposed.

- With the  $x_s$ -scan measurement it is attempted to follow the streamline at constant wall-normal location. However, when actual streamline differs from the streamline followed with the hot-wire measurement, the fluctuations at different spanwise locations will be shown when going downstream. The fluctuations differ across the vortex and therefore the  $x_s$ -scan could show an apparent decrease. Even though, it

is difficult to prove if this is the case for the measurements shown, the effect should be constant for all forcing amplitudes. Therefore, it would not explain the dependence of the forcing amplitude on the saturation location shown in Figure 54.

- As discussed in Chapter 4, it has been found by [Serpieri and Kotsonis \(2016b\)](#) that the low frequency energy is related to a low frequency spanwise shift of the stationary vortices. The magnitude is related to the low frequency noise in the specific experimental set-up. When the stationary vortices would break up, it is expected that the low frequency spanwise shift will also disappear. This would consequently result in a decrease in energy of the low frequency fluctuations. In Chapter 4 it has been shown that in the current study the total velocity fluctuations are dominated by the fluctuations from 10-100Hz. The decrease observed in Figure 54 could therefore be attributed to break up of the vortices. For the flow without forcing the fluctuations saturate around  $x/c=0.40$ , which is the location where the stationary vortices becomes less coherent as presented in Figure 15. This hypothesis would indicate that the upstream shift of the saturation point with increased forcing is caused by the stationary vortices breaking down at different locations.

- The decrease in fluctuations could also be caused by the flow becoming three-dimensional. When the flow becomes turbulent the energy will spread in the wall-normal and spanwise direction which is not captured with the one point single hot-wire measurements. In this case, the upstream shift of the saturation point would still indicate a dependency of the forcing amplitude on the location where the flow becomes turbulent.

Each of the hypotheses agree that there is a dependency of the saturation location and possibly break down of the flow on the forcing amplitude. To understand how the characteristics of the secondary instability change with the forcing amplitude, the fluctuations in the YZ and  $x_s$ Y-plane are studied in detail for three different forcing amplitudes. The chosen forcing amplitudes were  $F=0.03$ ,  $F=0.1$  and  $F=2.5$  to see the effect of small, moderate and large forcing respectively.

In Figure 55 the mean velocity and phase-averaged velocity distribution are shown for the different forcing amplitudes in the YZ-plane at  $x/c=0.34$ . The mean flow and phase-averaged velocity distributions for  $F=0.03$  and  $F=0.1$  are similar, while for  $F=2.5$  the mean flow is altered. For  $F=2.5$  the modulation of the mean flow still shows the presence of a crossflow vortex however its shape and size seem to have changed by the large forcing. The phase-averaged velocity distributions for  $F=0.03$  and  $F=0.1$  are again similar and resemble closely to the phase-averaged velocity distributions found in literature [Wassermann and Kloker \(2002\)](#); [Kawakami et al. \(1999\)](#); [Serpieri and Kotsonis \(2016a\)](#). For  $F=2.5$  the flow structure is different, the

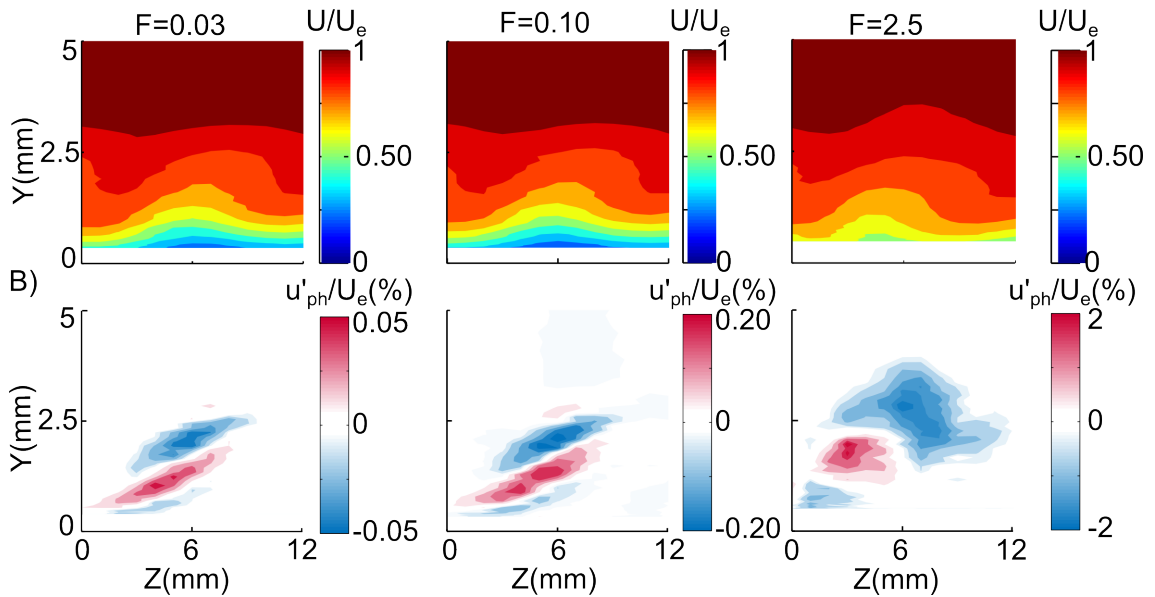


**Figure 55.** Phase-averaged velocity distribution in the YZ-plane at  $x/c=0.34$  ( $x_s=61\text{mm}$ ) for different forcing amplitudes.

distribution of the phase-averaged velocity for the different phase indicate that a large vortex structure has formed, however, from the single hot-wire measurements it is difficult to confirm this.

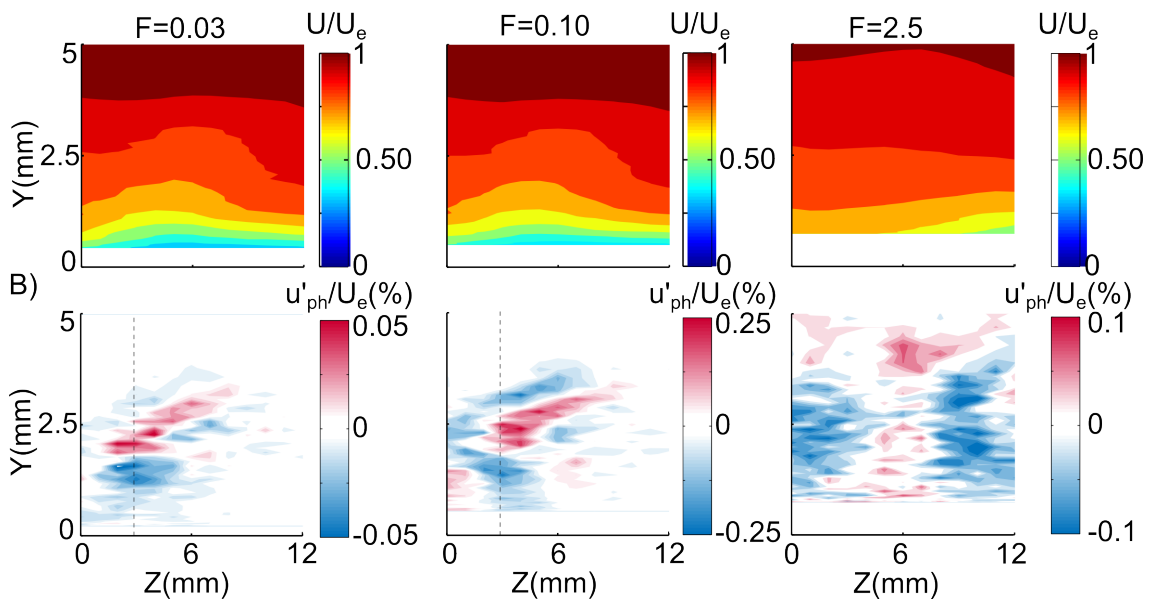


**Figure 56.** Phase-averaged velocity distribution in the YZ-plane at  $x/c=0.40$  ( $x_s=150\text{mm}$ ) for different forcing amplitudes.

For  $x/c=0.4$  the mean and phase-averaged velocity distribution is shown in Figure 56. For  $F=2.5$  the flow has now completely broken down and no vortex structure is present in the flow anymore. The phase-averaged velocity shows regions of positive

and negative velocity, however, it is difficult to define any coherent flow structures. The mean velocity distribution for  $F=0.03$  and  $F=0.10$  are again similar, where small differences in the vortex structure are observed. The phase structure is broken up in smaller structures. The structures for  $F=0.03$  and  $F=0.1$  seem to be slightly different, however, it is difficult to conclude this from the  $YZ$ -scan alone.

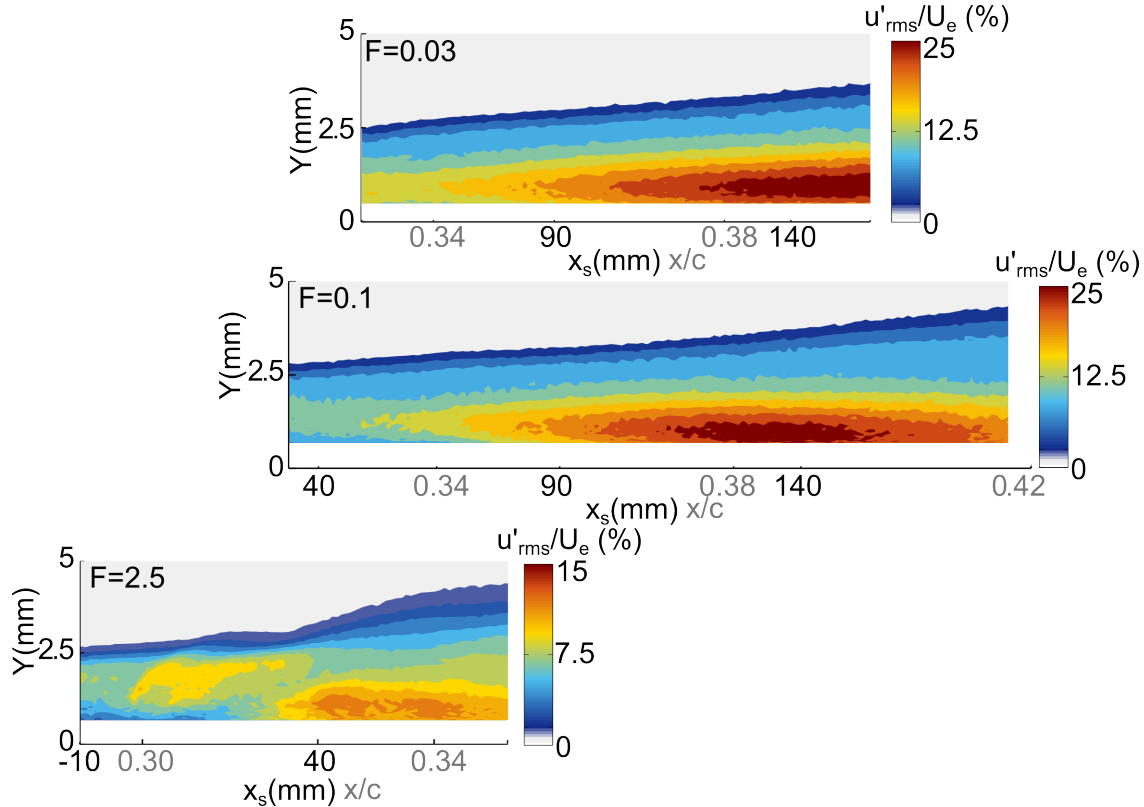


**Figure 57.** Distribution of full-spectrum fluctuations in the  $x_s$ - $Y$ -plane for different forcing amplitudes.

In Figure 57 the distribution of the total velocity fluctuations is shown in the  $x_s$ - $Y$ -plane for different forcing amplitudes. The measurement time for the full domain from  $x_s=-10$  to  $x_s=180$ mm for one forcing amplitude was approximately 20 hours. Since measurement time was limited, it was chosen to focus on specific streamwise regions for each forcing amplitude based on the streamwise location of the saturation amplitude shown in Figure 54. For  $F=2.5$ , the fluctuations increase close to the excitation location, while further downstream no strong increase is observed. A similar behaviour was found for the constant wall-normal measurement shown in Figure 54. The boundary layer thickness increases strongly around  $x_s=40$ mm ( $x/c=0.32$ ) which indicates that the boundary layer becomes turbulent. For  $F=0.03$  and  $F=0.1$  a different distribution is shown. The velocity fluctuations first increase after which a decrease is shown. For  $F=0.1$  the maximum velocity fluctuations seem to occur at

an earlier streamwise location than for  $F=0.03$  as was also observed in Figure 54. For both smaller forcing amplitudes a clear increase in boundary layer thickness is not observed which indicates that in the measurement region the flow did not become fully turbulent. In Figure 58 the phase structure in the  $x_s Y$ -plane is shown for the

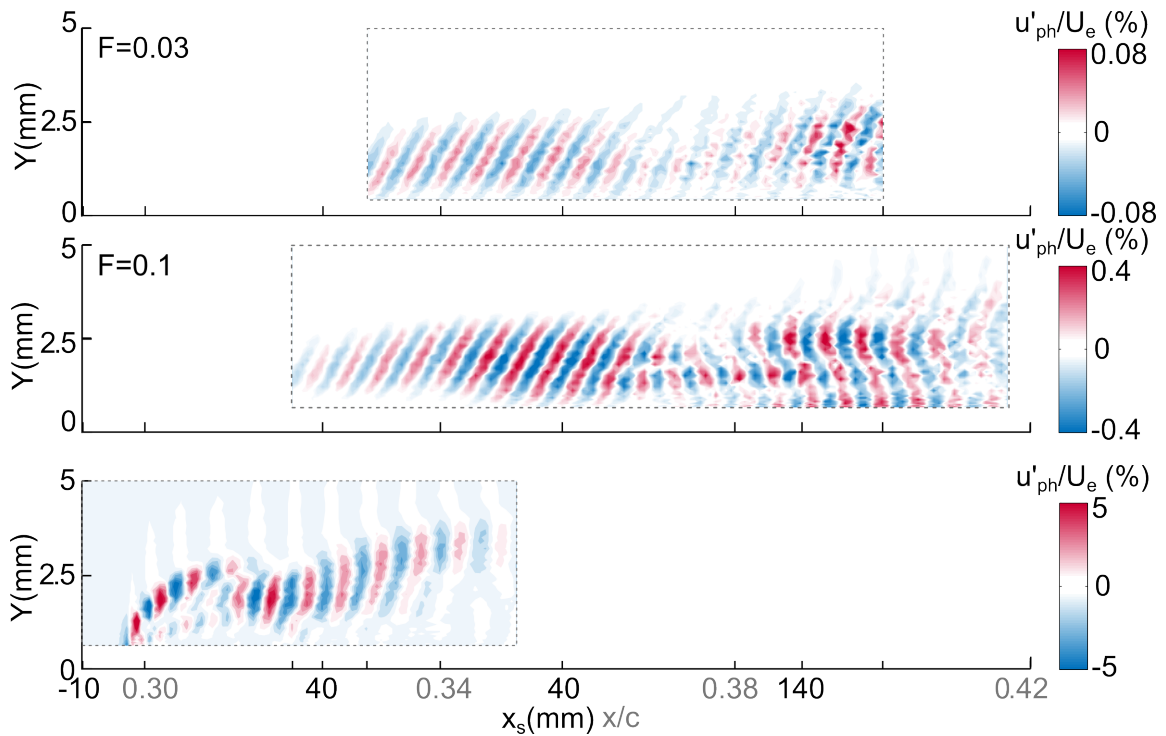


**Figure 58.** Distribution of phase-averaged velocity the  $x_s Y$ -plane for different forcing amplitudes.

different forcing amplitudes. Again, for  $F=2.5$  the phase structure exhibits characteristics which do not compare to the phase structures found in Section 5.6 or to secondary instability structures found in literature. Therefore, from the development of the spectra, distribution of velocity fluctuations and phase structures in both the spanwise and streamwise direction it is concluded that for such high forcing a different transition path is followed. The small patches close to  $x_s=0$  for  $F=2.5$  could be small vortex structures being created by the strong shear introduced by the large forcing, however, with a single hot-wire measurement these are speculations. Up to  $x_s=60\text{mm}$  the characteristics of the phase structure are very similar for  $F=0.03$  and  $F=0.1$ . After that there is the region of wedge interaction as explained in section 5.6. From here the characteristics change, for  $F=0.1$  the elevation angle changes going from positive to slightly negative, while for  $F=0.03$  no change is observed. This possibly, has to do with the wedge developing earlier for the higher forcing leading to a slightly different development and interaction with the neighbouring vortex.

The development of the dominating secondary instability, the velocity fluctuations between 1500-2500Hz, are shown in Figure 59 for  $F=0.03$  and  $F=0.1$ . As expected, the divergence of the fluctuations towards the wall starts earlier for the higher forcing amplitude. In Section 5.6 the location of divergence was related to the onset of the wedge in the  $x_s Z$ -plane. Unfortunately, the  $x_s Z$ -plane measurements were not carried out for this test, however, a similar behaviour would be expected here. Furthermore, a strong increase in fluctuations is shown around  $x/c=0.38$  for  $F=0.1$  while this is not observed for  $F=0.01$ , which again indicates an earlier onset of breakdown for  $F=0.1$ .

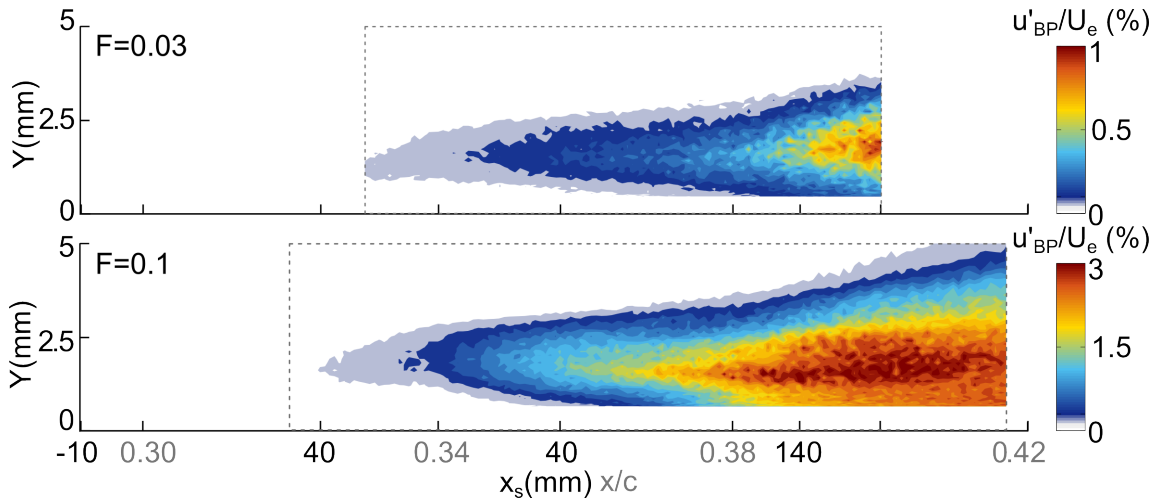


**Figure 59.** Distribution of the secondary instability fluctuations (1500-2500Hz) in the  $x_s Y$ -plane for different forcing amplitudes.

In Figure 25 The increase in energy by the high frequency velocity fluctuations indicated that the flow was breaking down. In Figure 60 the growth of these fluctuations is obtained from the  $x_s Y$ -scan for different forcing amplitudes. To account for the different initial amplitudes,  $A_{xy}$  is normalised by  $A_{xy,0}$  which is defined as:

$$A_{xy,0} = \frac{1}{\delta} \int_0^{\delta} \int_{1990}^{2010} u' df dY, \quad (5.8)$$

calculated at the location of the exciter. From Figure 60 it is shown that for  $F=0.10$  the high frequency fluctuations start to grow around  $x/c=0.34$  while for  $F=0.03$  the increase is around  $x/c=0.37$ . This agrees with the trends shown in Figure 59 and indicates again that for higher forcing the breakdown location moves upstream due to the earlier onset of nonlinear interactions.

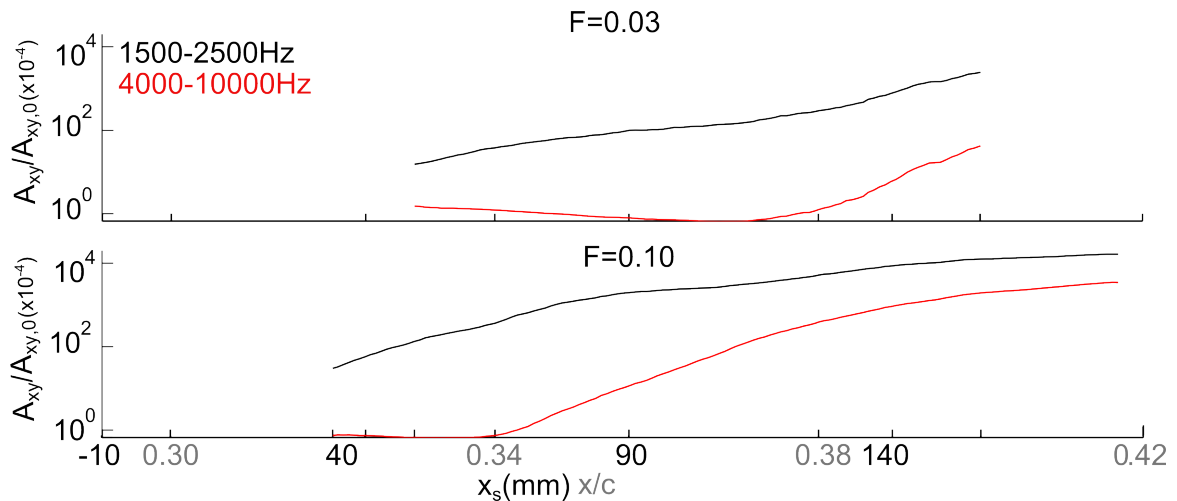


**Figure 60.** Growth of the secondary instability velocity fluctuations (1.5kHz-2.5kHz) and the high frequency velocity fluctuations (4kHz-10kHz), for  $F=0.03$  and  $F=0.10$ .

### 5.7.1. Conclusions: wall-forcing

From the experiments on the influence of wall-forcing on the development of the secondary crossflow instability the following is concluded:

- Forcing has an influence on the development of the secondary crossflow instability. From an experimental point of view this indicates that the forcing amplitude should be taken into account when forcing is used to visualize the secondary crossflow instability.
- The growth and spatial distribution of the velocity fluctuations with harmonics of the excitation frequency, indicate that these velocity fluctuations are due to nonlinear interactions and not a byproduct of the forcing.
- Large forcing, 2.5% of the freestream velocity, causes breakdown immediately where a different transition path seemed to be followed.
- From the velocity fluctuations in the flow as well as phase-averaged velocity distributions it was concluded that for smaller forcing, 0.03% to 0.5%, an increasing forcing amplitude moves the breakdown location upstream. The reason for this seems to be earlier appearance of the harmonics with increasing forcing amplitude, leading to earlier breakdown of the flow.
- The experiments show that it is possible to influence the development of the secondary instability directly. The receptivity through wall-forcing of the secondary instability and previously found for the primary instability suggests that the disturbance sources at the surface of an aeroplane wing need to be well understood. A possible reduction of these sources might lead to transition delay.

## 5.8. Results: freestream forcing

First, the various pipe configurations shown in Figure 9 were tested to understand if the secondary instability would interact with the flow. In Figure 61 the power spectra, for the third configuration from Figure 9, are shown at different distances from the exciter inside the boundary layer. Up to 120mm from the exciter the peak at 2000Hz is clearly shown, while downstream the peak diminishes. This indicates that the sound wave penetrated into the boundary layer, however, no interaction with the secondary instability took place.

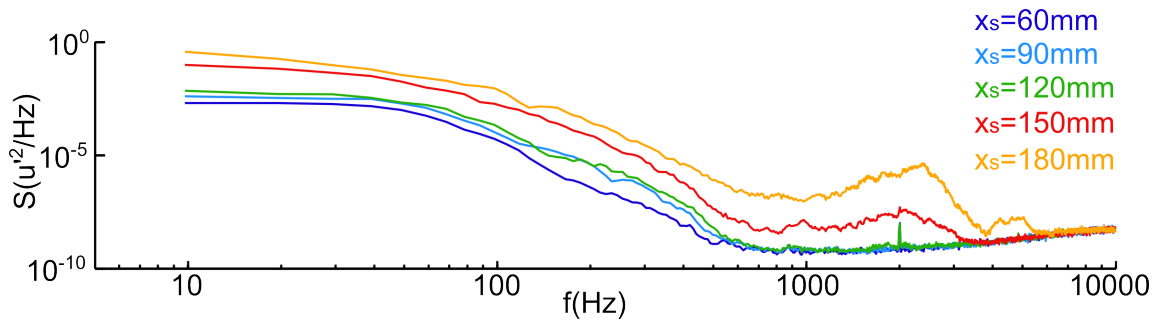


**Figure 61.** Power spectra at different distances from the exciter placed in the freestream at  $x/c=0.29$  (configuration 3) for  $F=3.9 \times 10^{-4}$ .

Placing the exciter upstream at  $x/c=0.31$ , which refers to the fifth configuration in Figure 62, shows a similar behaviour. In Figure 62 a small peak is shown at 2kHz for  $x_s=60\text{mm}$ ., after which no distinct peak is observed.

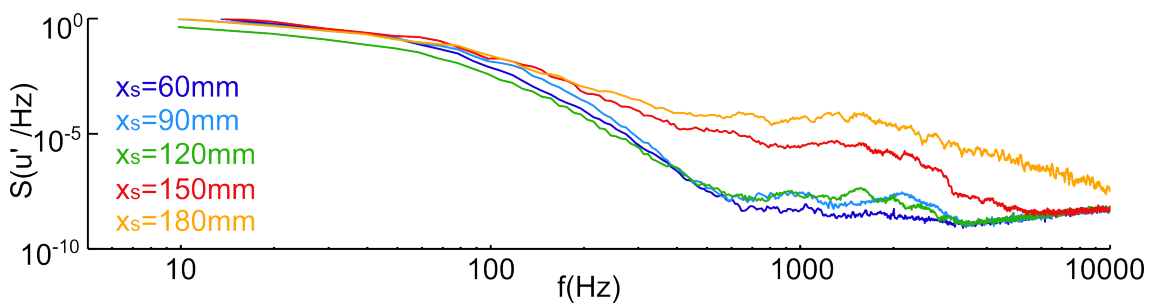


**Figure 62.** Power spectra at different distances from the exciter placed in the freestream at  $x/c=0.31$  (configuration 5) for  $F=3.9 \times 10^{-4}$ .

The results did not change for different configurations and larger forcing amplitude. This agrees with previous research that the secondary instability is not receptive to sound (White and Saric, 2005). Goldstein (1985) found that a combination of freestream acoustic waves and surface roughness couples with the spatially growing Tollmien-Schlichting wave inside the boundary layer. Choudhari (1994), Schrader

et al. (2009) and Borodulin et al. (2013) found a similar mechanism for traveling crossflow waves. Therefore, analogously to these previous studies, a small two-dimensional roughness strip ( $d=6\text{mm}$ ,  $k=150\mu\text{m}$ ) was added after the exciter at  $x/c=0.33$ . The height is large in comparison to the roughness elements placed at the leading edge, however the height ratio is similar since the boundary layer is about  $3\text{mm}$  at  $x/c=0.33$ . In Figure 63 the mean flow and power spectra with and without roughness is shown at  $x/c=0.38$ . The roughness strip changed the mean flow significantly. The secondary instability is located in the upwelling region of the vortex, indicating that the Type-I instability dominates the transition process in both cases. The power spectra show that the frequency band of the secondary instability is similar with and without roughness. From this it was concluded that even though a slightly different flow is studied with the roughness strip, the interaction of the roughness and the  $2000\text{Hz}$  sound wave could still be studied.

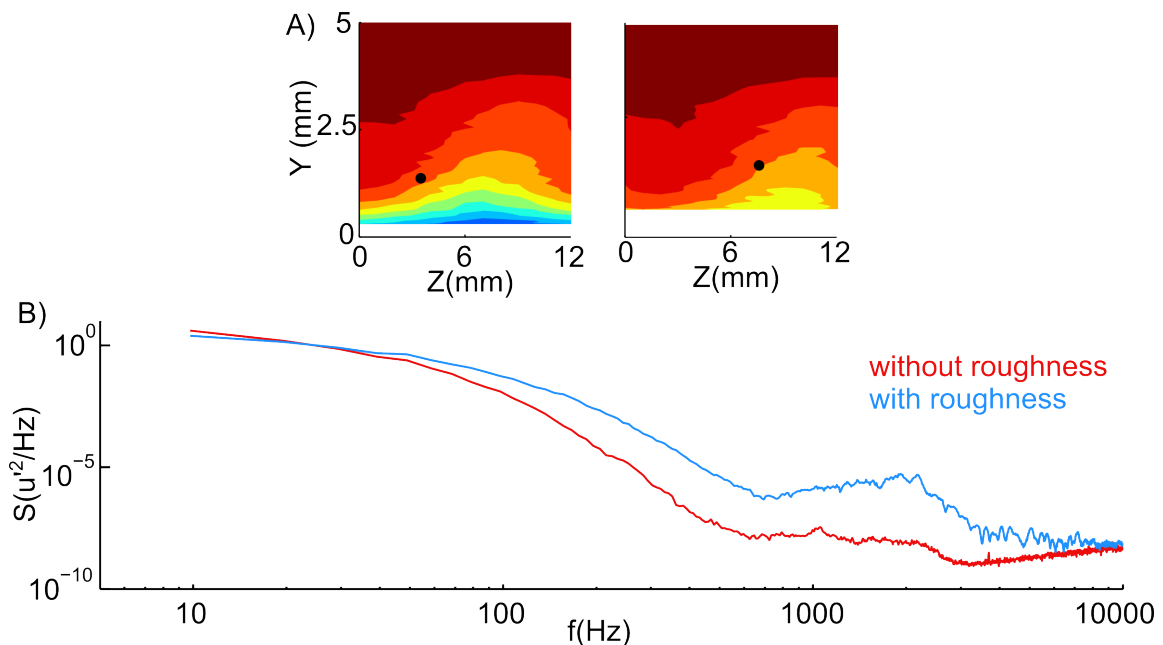


**Figure 63.** A) Mean velocity distributions for the flow without a roughness strip (left) and with a roughness strip (right). For the case with roughness the measurements were taken at a larger distance from the wall. B) Power spectra in the upwelling region of the secondary instability (indicated with the black dot in A) where the secondary instability fluctuations are high.

In Figure 64 the power spectra at different streamwise locations is shown for the flow with freestream forcing. At the locations further downstream the  $2\text{kHz}$  peak is now clearly shown which indicates there is an interaction of the freestream disturbances with the natural occurring secondary instability.

The phase-averaged velocity development shown in Figure 65 shows the same re-

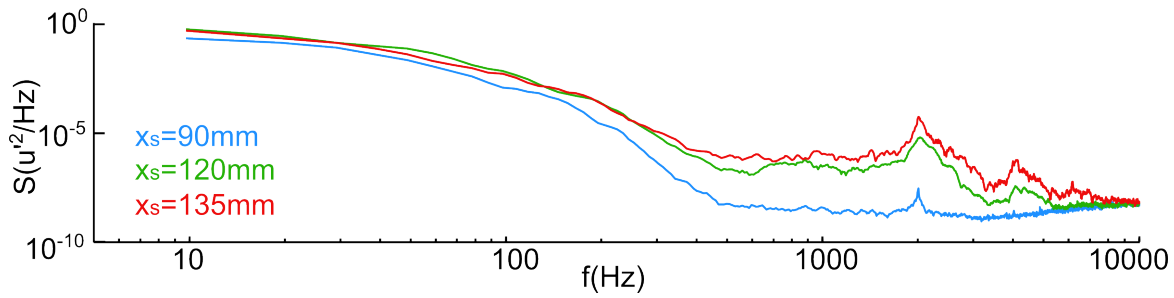


**Figure 64.** Power spectra at different distances from the exciter placed in the freestream at  $x/c=0.31$  and a roughness strip placed at  $x/c=0.33$ .

sult. The clear periodicity shown with the roughness indicates that the forcing of the freestream locked onto the secondary instability inside the boundary layer. The wavelength is approximately 6mm as also found in Section 5.6.2 for the naturally occurring instability and not the actual sound wave which has an expected wavelength of 170mm.

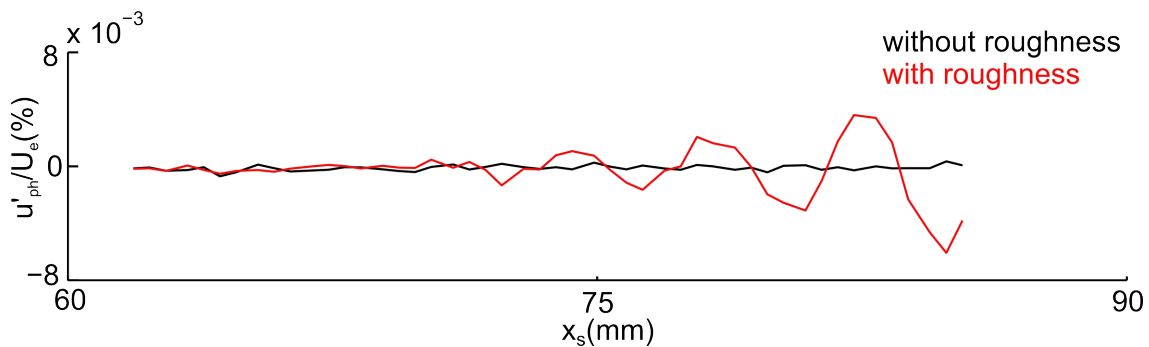


**Figure 65.** Normalized phase-averaged velocity for flow forced in the freestream at  $x/c=0.31$  with and without roughness ( $\Delta x_s=0.5\text{mm}$ ).

In Figure 66 the phase-averaged velocity for two different forcing amplitudes are shown. The larger phase-averaged velocity with increased forcing again shows there is an interaction of the sound with the fluctuations inside the boundary layer and that the phase-averaged velocity increases with increasing forcing amplitude.

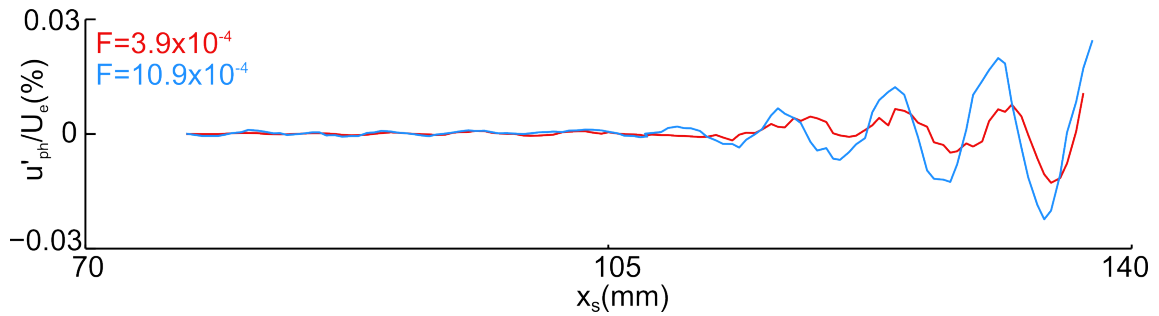


**Figure 66.** Normalized phase-averaged velocity for flow forced in the freestream at  $x/c=0.31$  for different forcing amplitudes.

Finally, a YZ-scan was taken at  $x/c=0.38$  for different forcing amplitudes as presented in Figure 67. The bandpassed filtered velocity fluctuations again increase with increased forcing. Only for the large forcing a phase structure of the secondary instability can be detected. The positive and negative streaks in the upwelling region are similar to those found for the natural occurring secondary instability.

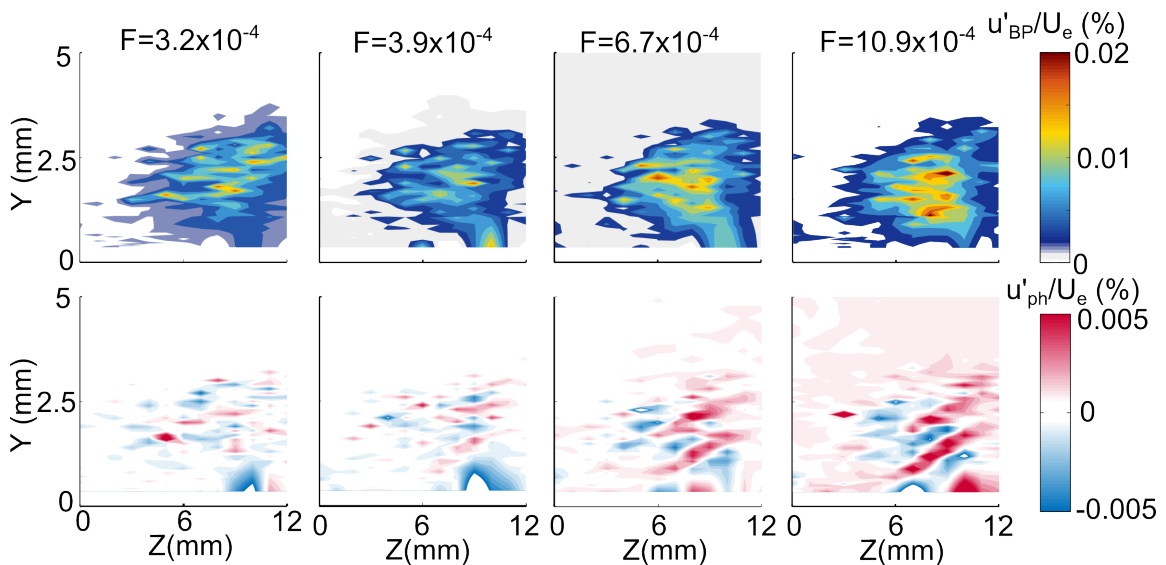


**Figure 67.** YZ-scan for different freestream forcing amplitudes at  $x/c=0.38$ . A) Bandpassed filtered velocity fluctuations between 1990 and 2010Hz. B) Phase-averaged velocity distribution.

### 5.8.1. Conclusions: freestream forcing

From the experiments on the freestream forcing the following can be concluded:

- Freestream forcing alone does not excite the secondary crossflow instability even though large forcing amplitudes were used, close to the neutral stability point of the secondary instability.

- When a small roughness strip is placed, after the location of excitation from the freestream, the freestream forcing does interact with the natural occurring secondary instability in the flow.
- The mechanism by which the freestream disturbances and roughness interact with the secondary instability, has similarities with previous receptivity mechanisms found for Tollmien-Schlichting waves and travelling crossflow waves however, the current mechanism has not been reported before.
- This study did not focus on the influence of the forcing amplitude on the breakdown location. In this experiment small forcing amplitudes were tested with respect to the edge velocity. It is expected that for larger forcing amplitudes the breakdown location would move upstream, similar to what is shown for wall-forcing.





# 6

## **Conclusions and recommendations**

## 6.1. Main objectives

In Section 1.7 the main objectives of this PhD project were outlined. The objectives were focussed on three topics namely:

- The design of an experimental model, data acquisition system and data analysis tool to study the development of the crossflow instability.
- The influence of roughness on the development of the primary crossflow instability.
- The development of the secondary crossflow instability and the influence of forcing on this instability.

In the following three sections the main conclusions of the work carried out in these areas are discussed, together with recommendations for future work. The sections on the primary and secondary crossflow instability ends with a summary of how the results compared to previous studies and how it contributed to new knowledge in the field.

## 6.2. Experimental design and data analysis

A major task of this PhD project was to design an experimental set-up, data-acquisition system and data-analysis tools to study the development of the crossflow instability. From this process the following conclusions are drawn:

*An inviscid and two-dimensional panel code in combination with boundary layer and linear stability calculations is a useful tool to design a flat plate with displacement body configuration to study the crossflow instability, provided that the trailing-edge flap is part of the computational model.*

The comparison of the pressure distribution obtained from the panel code with a full three-dimensional RANS computation showed that the magnitude of the pressure coefficient for the panel code was slightly higher, however, the pressure gradient was comparable. This led to similar stability characteristics for both computational models in the region where three-dimensional effects were small.

*Pressure belts are a viable alternative to measure the pressure distribution compared to static-pressure ports.*

In previous studies the pressure belt was used to measure the pressure distribution on an experimental model, however, a direct comparison of the pressure coefficients obtained from the static-pressure ports and the pressure belt was not carried out

(Eppink, 2014; Rivers et al., 2001). In the current experiment, the pressure coefficients were measured with both methods and showed good comparison between the pressure coefficients from the pressure belt and static pressure ports. In the leading edge region no static-pressure ports were placed but the shape of the pressure distribution obtained with the pressure belt compared well with the three-dimensional RANS computation. The attachment line pressure, which was located close to the leading edge in this experiment, could not be obtained reliably with the pressure belt. However, the flexibility of the pressure belt to measure the pressure distribution at any spanwise and streamwise location is a large advantage over the static pressure ports.

***The automated data acquisition system developed in LabVIEW allowed the efficient capture of large volumes of hot-wire data.***

In the current project the experiments were carried out in six time slots of two to three weeks, over a period of three years. Since time was limited it was essential to use the available time as efficiently as possible. Therefore, a large part of the first year was spent developing to develop the LabVIEW system. While the control of the traverse system motors was implemented by other people from the research group (Barry Crowley and Marco Placidi), Isabella Fumarola and I implemented the velocity control of the wind tunnel through LabVIEW. This led to a system which could easily run 48 hours without interruption taking the data necessary to describe the development of the primary and secondary crossflow instability in detail.

***The data-processing system in MATLAB allowed rapid assessment of the data taken in the wind tunnel.***

The final system consisted of a separate pre- and post-processing step. The results were automatically organised and summarised in a pdf file with a Python script to quickly understand the measurements and to be able to compare across measurements. Furthermore, when a significant adjustment was made in any of the scripts to analyse the data, the data sets of all experimental sessions would be automatically re-analysed to ensure consistency throughout all data sets. The comparison was made by assessing the images of different data-analysis procedures side by side as well as comparing random chosen values for both procedures.

The following recommendations related to the experimental design are given:

- In the current experiment a displacement body with a swept-flat-plate configuration was chosen to study the crossflow instability. When designing the set-up the

variable orientation and location of the displacement body were seen as a large advantage compared to the swept wing configuration. Furthermore, the laser correction method to follow a curved wall was not developed yet, such that a flat plate was ideal as a measurement surface. In practice the displacement body orientation stayed fixed and the developed laser system would allow the hot-wire to follow a curved surface such as a swept wing, eliminating the main advantages of the displacement body set-up. The main disadvantage of the displacement body was the blockage of the traverse system such that it was not possible to measure close to the leading edge. Therefore for the current wind-tunnel and traverse set-up in future experiment it might be preferred to use a swept wing instead of the displacement body arrangement. Alternatively, the traverse system could be redesigned such that it would allow to measure in between the flat plate and displacement body.

- In the experiments a single hot-wire was used to measure the streamwise velocity. Even though, it was possible to measure the stationary crossflow waves indirectly with this method and to characterize the breakdown process, it would have been informative to measure the crossflow velocity profiles as well. These data could have been obtained with two separate measurements of a wire which is at a 45 degrees angle with the freestream.

### 6.3. Experiments on forcing of the primary instability

A cylindrical and pyramidal roughness distribution with the same height were tested, to understand the influence of the wavelength content of the roughness distribution on the development of the primary crossflow instability. The roughness elements were placed at  $\lambda=11.5\text{mm}$ , which corresponds to the most amplified stationary crossflow wave following linear stability analysis. By calculating the Fourier coefficients of both roughness distributions it was found that the pyramidal roughness distribution had slightly higher forcing at  $\lambda$  while forcing at  $\lambda/n$  was small compared to the cylindrical roughness distribution. From the experimental results the following conclusions were drawn:

***Larger forcing at  $\lambda$  leads to a stronger response of the flow.***

In the experiment the stationary crossflow amplitude was larger for the pyramidal roughness distribution. Furthermore, the relative energy content for waves with a wavelength of 11.5mm was larger for the pyramidal roughness distribution compared to the cylindrical roughness distribution. This indicated that the forcing of the primary mode correlated with the spectral content of the roughness.

***Larger forcing at  $\lambda/n$  does not necessarily lead to a stronger response of the flow.***

In the current experiment it followed from linear stability analysis that stationary crossflow waves with a wavelength below 9mm were not amplified. Since the span-wise spacing of the roughness elements was 11.5mm the forcing at 5.75mm, 3.83mm, 2.88mm, i.e.  $\lambda/2$ ,  $\lambda/3$  and  $\lambda/4$ , did not have an influence on the development of the stationary crossflow waves. Reibert et al. (1996) has shown that when more than one stationary crossflow mode is forced the non-linear interactions between the different modes can lead to earlier transition. Therefore the conclusion in the current experiment implies that to correctly predict development of the crossflow instability, the coupling between the wavelength content of the roughness distribution and that of the naturally amplified crossflow modes should be taken into account, instead of the coupling with only the most amplified mode, as is current practice.

The following recommendations related to the forcing of the primary crossflow instability are given:

- In the current experiment two roughness distributions at one Reynolds number were tested. In future experiments the Reynolds number could be changed to change the wavelengths of the naturally amplified crossflow modes. Consequently, this would change the coupling between the roughness distribution and flow resulting in a different response of the flow.
- A range of roughness distributions with different wavelength content could be tested to understand the exact coupling between the flow and roughness distribution in more detail. An idea of two roughness distributions is shown in Figure 1. These roughness distributions have the same volume and height only their wavelength content will be different which could lead to a different response of the flow.

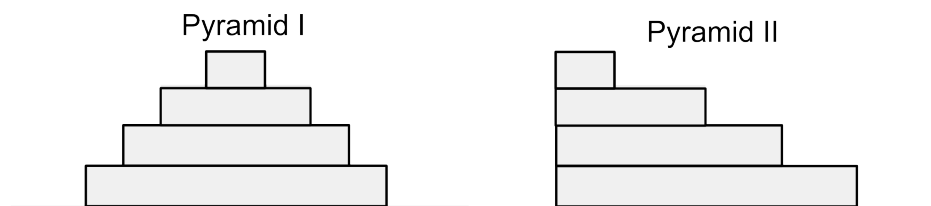


**Figure 1.** Idea for roughness distributions to study in future experiments.

- The response of the flow could only be measured from  $x/c=0.29$ . In future experiments it would be preferred to measure closer to the roughness distributions. This

would also allow to compare more directly to computational studies which often study the receptivity process at the location of the roughness elements.

- In industry the focus is often the roughness height instead of the wavelength content in relation to the naturally amplified crossflow modes. This study and also previous experimental and computational studies (Reibert et al., 1996; Wassermann and Kloker, 2002; Mughal and Ashworth, 2013) show that the wavelength content should be taken into account to correctly predict the response of the flow and transition location.

The experiments on the primary crossflow instability confirmed the theory that the response of the flow is related to the Fourier spectrum of the roughness distribution, put forward in previous computational studies (Bertolotti, 2000). While previous experimental studies confirmed this theory with cylindrical roughness elements (Radeztsky et al., 1999; Reibert et al., 1996), here it is shown directly by using different shapes of roughness elements. Furthermore, from the literature review it followed that in previous studies the importance of the forcing of the harmonics in the roughness distribution was dependent on the Reynolds number and therewith the modes naturally amplified in the flow (Hunt and Saric, 2011). In the current investigation it is shown that the stronger forcing of the harmonics does not lead to a stronger response of the flow since these modes are not naturally amplified.

## 6.4. Experiments on forcing of the secondary instability

The experiments on the secondary crossflow instability focussed on three topics; the characteristics of the secondary instability in the different growth stages of this instability, the influence of wall-forcing on the development of the secondary instability and the influence of freestream forcing on the secondary instability. The results of the experiments on the characteristics of the secondary instability led to the following conclusions:

*The secondary instability in this experiment could not be classified as a pure Type-I or Type-II instability.*

In previous experimental studies where this clear distinction could be made, the streamwise pressure gradient was strong from the leading edge to the streamwise location where transition occurred. This led to vortices where the roll-over behavi-

our prior to breakdown was clearly observed. In the current experiment the pressure gradient was weaker and therefore this roll-over behaviour was not observed, leading to a different spatial distribution of the secondary instability with respect to the underlying mean flow. This shows that the pure Type-I and Type-II classification might not be sufficient to specify the characteristics of the secondary crossflow instability.

***The characteristics of the secondary instability in its early development stage agreed with those found in previous studies.***

This implies that even though the mechanism by which the secondary instability was created was different than in previous studies, the actual flow structure and orientation of the secondary instability was not altered.

***With a simple analytical method, based on the shear layer in the wall-normal direction, the range of temporal frequencies and spatial wave-numbers could be predicted.***

The results of the pure inviscid analysis were consistent with the belief that the secondary instability is an inviscid instability as stated in previous studies. Furthermore, this analysis, together with the spatial distribution of the secondary instability, confirmed that the origin of the secondary instability in this experiment was related to the shear layer in the wall-normal direction as well as in the spanwise direction.

***The spanwise modulation of the primary crossflow vortices changes the physics of the breakdown process.***

In most experimental studies on the crossflow instability a spanwise uniform flow is studied to simplify the experimental procedure. The observations of vortex interaction between vortices of different strength and wavelengths show that this simplification omits part of the physics occurring on current swept aeroplane wings where the strength of the vortices will not be spanwise uniform.

Next to these conclusions the following observations were made:

- When the flow breaks down the secondary-instability fluctuations spread as a wedge in the spanwise and wall-normal direction.
- The wedge structure, leading to breakdown of the flow, starts in the middle of the vortex where the fluctuations of the secondary crossflow instability are strongest. The location of breakdown with wall-based measures would be measured further downstream since that is where the secondary instability velocity fluctuations reach

the wall.

- When breakdown occurs the main flow structure of the secondary instability breaks up in two smaller structures.

While the single hot-wire measurements did not lead to a full physical explanation of these observations, it is thought that the data obtained in the current experiment could be compared to future DNS studies to understand the observed phenomena.

The following conclusions related to the forcing of the secondary crossflow instability were made:

***Wall-forcing has an influence on the development of the secondary instability.***

For smaller forcing ( $0.03\%U_\infty$  to  $0.5\%U_\infty$ ) the breakdown location moves upstream. For large forcing ( $2.5\%U_\infty$ ) the flow breaks down immediately and a different transition path seemed to be followed.

***The secondary instability saturates after which harmonics appear due to nonlinear interactions.***

When the forcing is increased the streamwise location where the harmonics appears moves upstream. This sequence seems similar to the primary crossflow instability which first grows linearly after which it saturates and nonlinear effects between different modes occur.

***The experiments on wall-forcing show that the secondary instability is receptive to environmental disturbances.***

During flight there might be a similar source of forcing such as vibrations or noise which could influence the growth of the secondary instability. Furthermore, from an experimental point of view it is important to take into account the forcing amplitude when using wall-forcing to visualize the structure of the secondary crossflow instability.

***Freestream forcing with a single tone does not excite the secondary instability directly.***

In the current experiment the distance from the excitation mechanism to the neutral stability point of the secondary instability and the amplitude of forcing were altered but no interaction was found.

*A small roughness strip causes the freestream forcing to interact with the natural occurring secondary instability.*

This mechanism has not been observed in previous studies for the secondary crossflow instability. The mechanism has analogies with receptivity mechanisms found for Tollmien-Schlichting waves and travelling crossflow waves (Goldstein, 1985; Schrader et al., 2009).

The following recommendations related to the experiments on the secondary instability are given:

- Wall-forcing is important for both the primary and secondary instability and therefore needs to be understood in more detail. Experiments with different amplitudes and frequencies could be carried out. Furthermore, instead of tonal excitation, the influence of white noise could be investigated to have closer similarity to actual sound. Furthermore, since it is possible to move transition upstream by increasing the forcing amplitude, there might be a possibility to delay transition with wall-forcing.
- The mechanism by which roughness and freestream disturbances excite the secondary instability should be studied in more detail. Even though, the flow breaks down shortly after the secondary instability appears without forcing, strong receptivity of the secondary instability to roughness and acoustic disturbances could lead to even earlier transition leading to an increase in friction drag. To avoid this, it could indicate that next to the leading edge region, there should be a second region on an aeroplane wing where strong requirements on the surface roughness should hold.

The experiments on the secondary instability started with confirming previous studies after which a new area was investigated. While the secondary instability found in this study could not be classified as a pure Type-I or Type-II instability, the wavelength, wave speed and elevation angle of the instability in its early growth stage, all agreed with those found in previous investigations (Kawakami et al., 1999; Wassermann and Kloker, 2002; Serpieri and Kotsonis, 2016b). The structure of the secondary crossflow instability in the nonlinear growth stage has not been reported before and might help to understand the physics of the breakdown process over a swept wing more thoroughly. In previous investigations it was found that wall-forcing could be used to excite the secondary instability (Kawakami et al., 1999; Chernoray et al., 2005; Serpieri and Kotsonis, 2016a) however a detailed study on the influence of wall-forcing had not been carried out before. Excitation of the secondary instability from the freestream had not been effective in previous studies White and Saric

(2005). While it was thought that this had to do with the location where the forcing was applied, this did not turn out to be the case. Instead, with freestream forcing close to the onset of the natural occurring secondary instability similar results as in previous studies were obtained and the secondary instability was not excited. In previous studies a small roughness was added on the experimental model to increase the receptivity from freestream forcing to Tollmien-Schlichting waves and the travelling crossflow instability (Goldstein, 1985; Schrader et al., 2009; Borodulin et al., 2013). Here it was shown for the first time that when a roughness strip this also occurs for the secondary crossflow instability.





# Appendices

# A

# Computational analysis

## A.1. Linear stability analysis

Linear stability analysis is carried out to understand how the instabilities grow on the flat plate. In Figure 1 an overview of the steps taken in the analysis are shown. First, pressure distributions from the computations or experiment are smoothed,

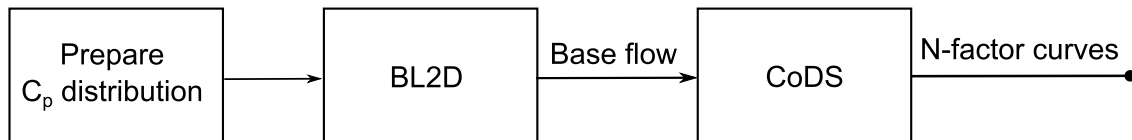


Figure 1. Flow chart for TAU analysis.

and outlier points are removed. The pressure distribution together with the flow conditions and model dimensions, are the input for the BL2D code. In this code the compressible laminar boundary layer equations for swept-tapered or infinite swept wing are solved<sup>1</sup>. From the BL2D code the mean velocity profiles in the streamwise and spanwise direction are obtained. This is the input for CoDS<sup>1</sup>, which solves the three dimensional linear stability equations (see Chapter 1). The assumptions in this analysis are the following:

- The flow is independent of the spanwise direction. Therefore the spanwise growth rate of the instabilities in the  $\beta_i=0$ .
- The wavelength  $\lambda$  defined as  $\sqrt{\alpha_r^2 + \beta_r^2}$  is constant with  $x$ . This condition is chosen since the wavelength is an important parameter in the design of the roughness elements as discussed in more detail in Chapter 4.

---

<sup>1</sup>QinetiC (unpublished)

From CoDS the most unstable eigenmodes at each chordwise location are found and are identified as Tollmien-Schlichting waves or crossflow waves depending on the direction of their wavenumber vector. For Tollmien-Schlichting waves the vector is aligned with the streamline, while for the cross flow waves the vector is perpendicular to the streamline. When the most unstable eigenmodes are calculated, N-factor curves are obtained. The N-factor curves are used to determine if the transition process is dominated by Tollmien-Schlichting waves or crossflow waves. Furthermore, the wavelength of the most unstable stationary crossflow wave is obtained.

## A.2. DLR-TAU analysis

The DLR-TAU software was used to resolve the three-dimensional flow around the designed experimental model. In the DLR-TAU code, the Reynolds Averaged Navier Stokes (RANS) equations are solved on an unstructured hybrid grid (Gerhold et al., 1997), i.e. different sizes and shapes grid cells are used to fill up the computational domain. The computations were performed at the Airbus Group Innovations facility in Bristol. The first goal of the computations was, to compare the pressure distributions obtained from the experiment and the two-dimensional panel code, with the pressure distribution obtained in a full three-dimensional flow solver. Secondly, the goal was to identify three-dimensional flow effects such as flow separation. In this computation the wind tunnel, together with the flat plate and two displacement bodies were modelled with a total of 11 million grid cells. At the inlet plane, a constant total pressure and density were described. On the wind tunnel walls a turbulent boundary layer of 0.01m was prescribed, 0.2m upstream of the leading edge of the plate. This was estimated from boundary layer measurements at the bottom tunnel wall, with a miniature Pitot tube. In the experiment the flow was laminar on approximately 50% of the test side of the flat plate, however, as a first approximation, the flow over the flat plate was computed as fully turbulent. The turbulent effects are modelled with the negative Spalart-Allmaras model, a one equation eddy-viscosity model. In Figure 2 the flow chart of the computational analysis is shown. First, the model was assembled in SolidWorks and imported in RAVEN (corvidTec) to prepare the model for the meshing stage. Next, the initial surface and volume mesh were generated with SOLAR (Leatham et al., 2000) and the quality of the mesh was visually checked in ParaView. Here, detail was especially given to the leading edge region of the flat plate, since small changes in the leading edge shape, could change the location of the stagnation point and the pressure distribution significantly. In Figure 3 details from the final mesh in the leading edge region are shown. The generated

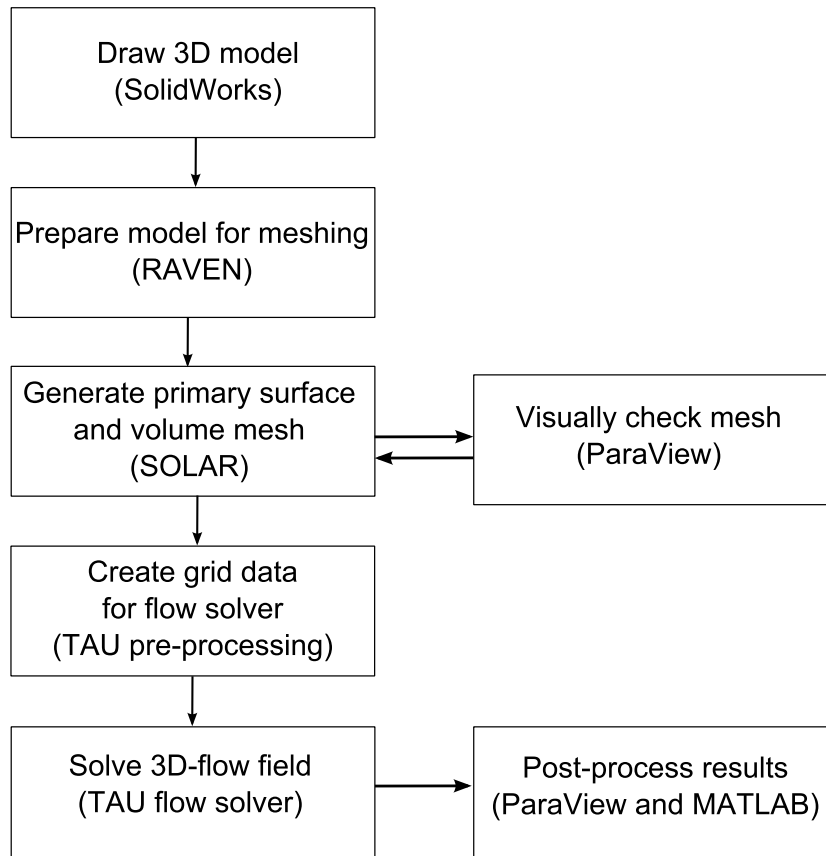


**Figure 2.** Flow chart for TAU analysis

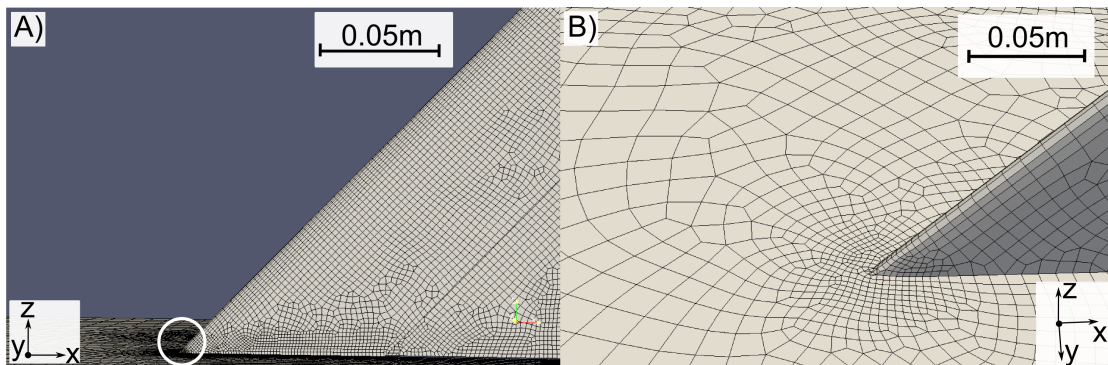
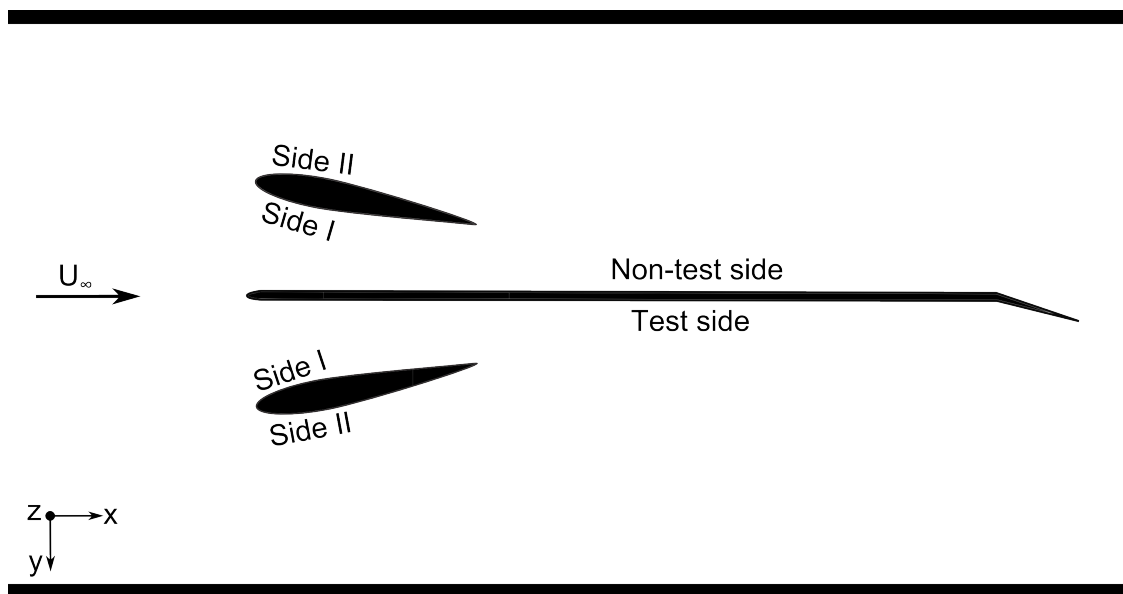


**Figure 3.** Mesh details on the flat plate and leading edge.

mesh went to a pre-processing procedure of TAU, which computed data necessary for the TAU flow solver. The TAU flow solver used a multigrid method with three steps, where in each step a finer grid was generated. The results were post-processed in ParaView and MATLAB. The initial idea was to test a wide range of flap angles, to understand how this would alter the pressure distribution on the flat plate. However, the computations turned out to be time-consuming to set-up and therefore only one flap angle of about  $25^\circ$  was tested. This angle is about 5 degrees higher than

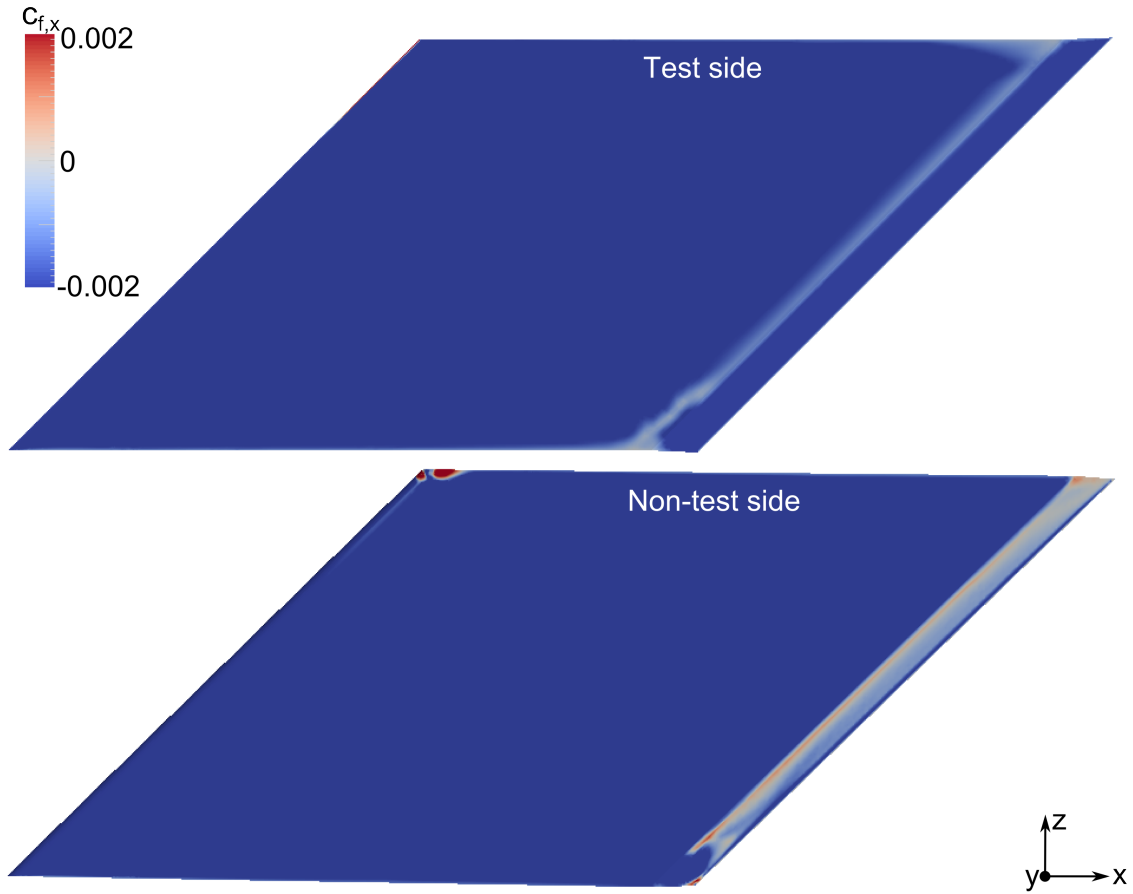
the angles used in the experiment, however, the pressure distribution for this flap angle was measured with the pressure belt such that a comparison could be made (Section 3.2). In this section the results of the computation are discussed and the pressure distribution is compared to the 2D panel code. In Section 3.2 the results are compared to the experimental pressure distribution.

Figure 4 shows a schematic of the set-up viewed from the top, to define the front and back of the flat plate and displacement bodies. In Figure 5 the streamwise friction



**Figure 4.** Mesh details on the flat plate and leading edge viewed from the top.

coefficient is presented for the front and back of the plate. A positive friction coefficient indicates that the flow is reversed and flow separation occurred. The friction coefficient is negative on the test side of the plate. At the back of the plate flow separation occurs at the flap for almost the entire height of the plate. This is expected since the flap angle tested is high, creating a strong adverse pressure gradient. The friction coefficient for the displacement body placed on the test side of the plate is shown in Figure 6. At the back of the displacement body, which is facing the plate, no flow separation occurs. At side II of the displacement body, there is separation on the leading edge, at the junction between the attachment line on the displacement body and the wall of the tunnel. The flow does stay attached at the trailing edge of the body. This is important from an experimental point of view, since a separated wake on the trailing edge could interact with the boundary layer on the plate.



**Figure 5.** Streamwise friction coefficient at the front and the back of the plate.

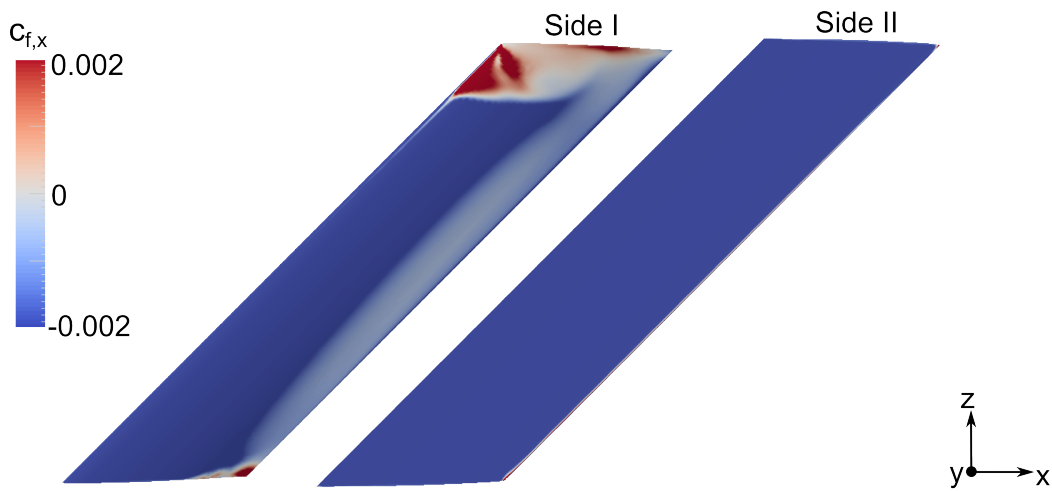


**Figure 6.** Streamwise friction coefficient at both sides of the displacement body placed at the test-side of the plate.

The pressure coefficient,  $C_{p,\tau}$  is determined with:

$$C_{p,\tau} = \frac{p_s - p_{s,\infty}}{\frac{1}{2}\rho U_\infty^2}, \quad (\text{A.1})$$

where  $p_s$  is the static pressure at the location where  $C_{p,TAU}$  is evaluated,  $p_{s,\infty}$  the static pressure at the reference location and  $U_\infty$  is the reference velocity. Initially, it was thought that this reference velocity was set at the inlet of the computational domain.

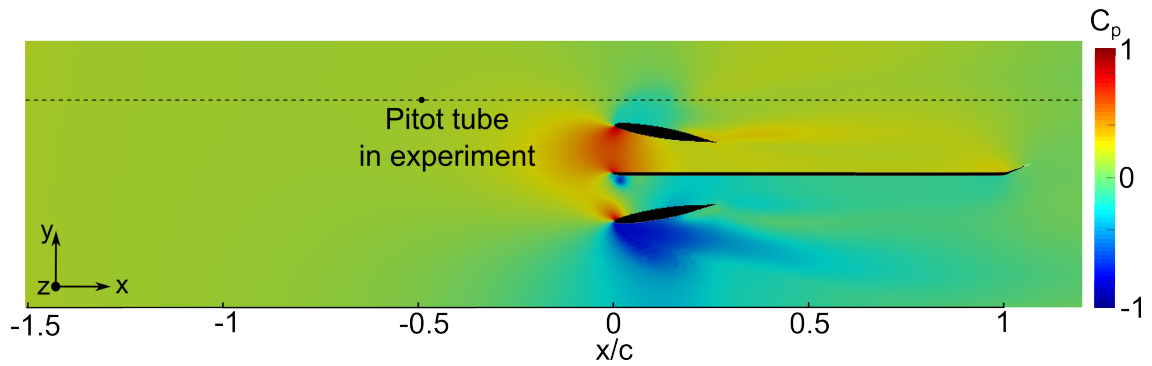


**Figure 7.** Pressure distribution around the flat plate at the ceiling of the wind tunnel.

However, the pressure distribution at the ceiling of the wind tunnel, presented in Figure 7, it was observed that the pressure coefficient did not equal zero at the start of the computational domain. The pressure distribution along the entire computational domain at the location of the Pitot tube, presented in Figure 8, shows that  $C_p=0$  at the outlet of the domain.

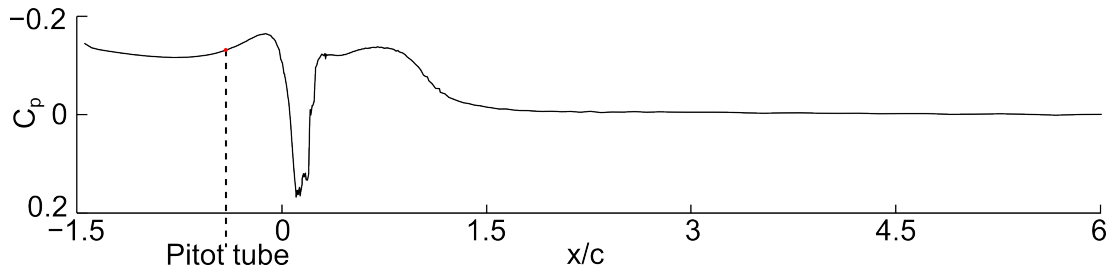


**Figure 8.** Pressure coefficient in the streamwise direction along the dotted line shown in Figure 7.

In the experiment the freestream environment is defined at the inlet and therefore the pressure coefficient from TAU,  $C_{p,\tau}$ , is corrected to represent the reference conditions at the location of the Pitot tube. The correction is determined by assuming isentropic flow such that the total pressure at the reference location used in TAU denoted with,  $\infty$  is equal to the total pressure at the Pitot tube:

$$p_{s,\infty} + \frac{1}{2}\rho U_\infty^2 = p_{s,Pitot} + \frac{1}{2}\rho U_{Pitot}^2 \quad (\text{A.2})$$

If now the static pressure  $p_s$  is added to both sides of the equation it can be shown

that the corrected pressure coefficient  $C_p$  is determined with:

$$C_p = 1 - \left( \frac{U_\infty}{U_{Pitot}} \right)^2 (1 - C_{p,\tau}). \quad (\text{A.3})$$

To obtain the ratio between  $U_\infty/U_{Pitot}$  the pressure coefficient at the Pitot tube was determined from Figure 8 and equal to 0.13. Assuming isentropic flow the ratio between is determined with:

$$C_{p,Pitot} = 1 - \left( \frac{U_{Pitot}}{U_\infty} \right)^2, \quad (\text{A.4})$$

and equal to 1.072. This value is used in Equation A.3 to obtain the corrected pressure coefficient.

In Figure 9 the corrected pressure coefficient on the front and the back of the plate are presented.

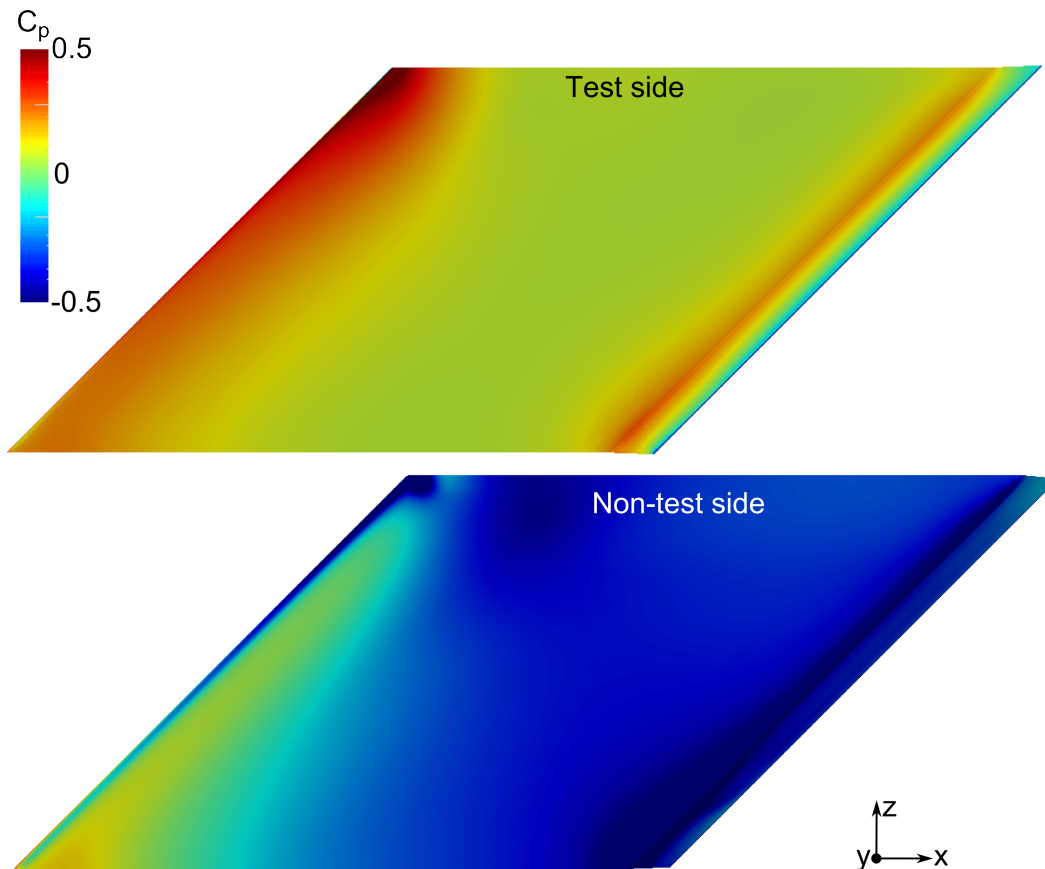


**Figure 9.** Pressure coefficient on both sides of the flat plate.

The pressure decreases in the chordwise direction, due to the converging channel created by the displacement bodies. Towards the trailing edge of the plate the pressure

increases, due to the angle of the trailing edge flap. The pressure coefficient varies in the leading edge region, indicating the presence of three-dimensional effects. To see this effect more clearly the pressure coefficient at  $z/H=0.1$  to  $z/H=0.9$  in 0.1 steps is extracted along the streamwise direction (Figure 10), where  $H$  is the height of the wind tunnel. The location of the attachment line is determined as the location

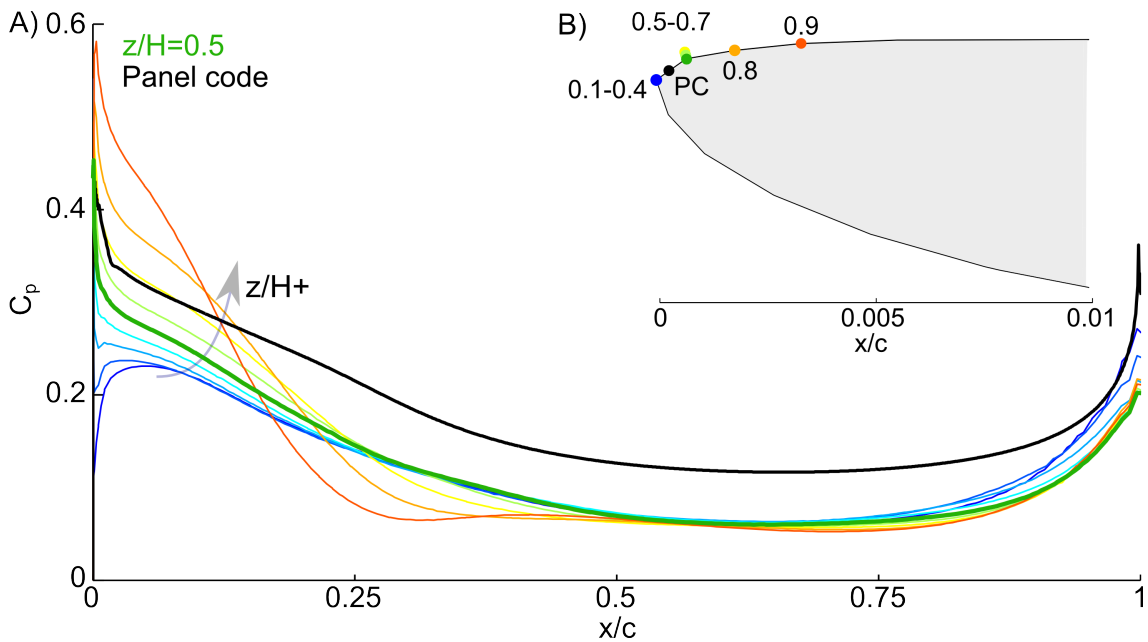


**Figure 10. Pressure distribution on the plate and location of the attachment line.** A) Pressure distribution for different  $z/H$  locations (color) computed with TAU and the panel code (black). B) Location of the attachment line on the leading edge for different  $z/H$  locations (color) and with the panel code (black).

where the pressure is maximum. At the lower part of the plate ( $z/H=0.1-0.4$ ) the attachment line is at  $x/c=0$  while the stagnation point moves to the front part of the plate for from  $z/H=0.5$ . From the attachment line pressure coefficient,  $C_{p,AL}$ , the effective sweep angle is calculated with:

$$\Lambda_{eff} = \cos^{-1} \left( \sqrt{C_{p,AL}} \right), \quad (\text{A.5})$$

where it is used that in a two-dimensional flow the stagnation pressure is equal to 1. The attachment line pressure changes from  $C_{p,AL}=0.58$  at the bottom of the plate, to  $C_{p,AL}=0.45$  in the middle of the plate to  $C_{p,AL}=0.53$  at the top of the plate which corresponds to  $\Lambda_{eff}=40.4^\circ$  to  $\Lambda_{eff}=47.8^\circ$  and  $\Lambda_{eff}=43.3^\circ$  degrees respectively. In the absence of three-dimensional effects, an effective sweep angle of 45 degrees would be expected, which is reasonably close to the value found in the computations at the middle of the plate.

Next, the pressure distribution in the middle of the plate,  $z/H=0.5$ , is compared to the pressure distribution from the two dimensional inviscid panel code, as presented in Figure 10 with the black line. The pressure distribution from the two-dimensional panel code is transformed to its three-dimensional equivalent by using:

$$C_{p,3D} = C_{p,2D} \cos(\Lambda_{eff})^2, \quad (\text{A.6})$$

where  $\Lambda_{eff}=47.8^\circ$  degrees obtained from the TAU computations. In Figure 10 it is shown that the magnitude of the pressure coefficient obtained with the panel code is slightly lower for the pressure distribution obtained with TAU. The viscous effects cause this lower pressure distribution through two mechanisms. First of all, the growing boundary layers on the plate, displacement body and tunnel walls will change the effective shape of the bodies. Secondly, flow separation on the flap, which is not modelled in the inviscid panel code, makes the flap less effective leading to a more accelerated flow and consequently a lower pressure.

Even though, the magnitude of the pressure coefficient is lower, the trend and gradient for both pressure distributions is similar. The linear stability analysis results, presented in Figure 11, show that the growth of the crossflow and Tollmien-Schlichting waves is similar. The wavelengths of the stationary crossflow waves and the neutral stability point were similar for both cases as well.

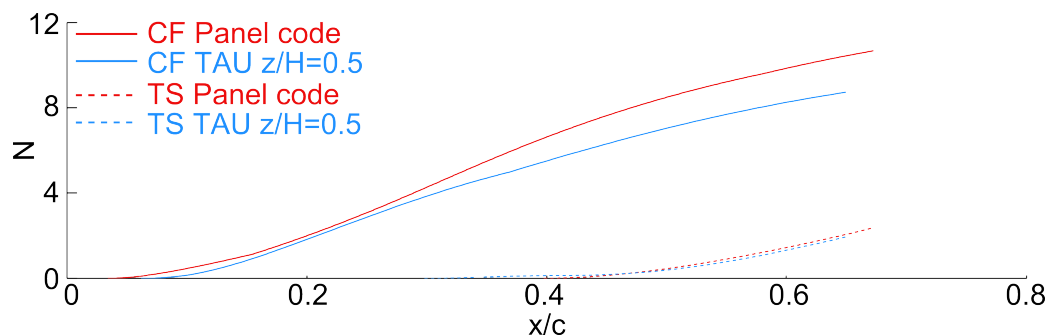


**Figure 11.** N-factor curves for stationary crossflow waves obtained from the pressure distributions of the panel code and DLR-TAU code.

Comparing the computation time of around 20 hours for TAU to 20 seconds for the panel code, it is concluded that the panel code is a useful tool to get a first approximation of the pressure distribution and stability characteristics at a location on the plate where three-dimensional effects are minimal.

### A.3. Piecewise linear velocity profiles

To estimate the frequencies of the secondary instability the piecewise linear velocity profile technique was employed to the measured streamwise velocity profiles. This crude technique was used before computational methods were available and are not expected to give exact agreement with the experiment (Schmid and Henningson, 2001). Here the technique will be explained and a dispersion relation for an arbitrary piecewise linear velocity profile will be given.

As explained before in Chapter 1 the Orr-Sommerfeld can be taken in the limit of large Reynolds numbers to obtain Rayleighs equation:

$$(U - c) \left( \frac{d^2 v}{dy^2} - \alpha^2 v \right) - \frac{d^2 U}{dy^2} v = 0, \quad (\text{A.7})$$

where  $c = \omega/\alpha$  and for temporally and spatially unstable flow,  $\omega$  and  $k$  are complex respectively.

For a piecewise linear velocity profile the second derivative in  $U$  becomes zero simplifying the equation. Here the velocity profile is given with:

$$U(y) = \begin{cases} a_1 y & \text{for } 0 \leq y \leq y_1 \\ a_2 y + b_2 & \text{for } y_1 < y \leq y_2 \\ a_3 y + b_3 & \text{for } y_2 < y \leq y_3 \\ 1 & \text{for } y > y_3 \end{cases} \quad (\text{A.8})$$

as shown in Figure 12 For each segment Rayleighs equation is solved. The general solution for each segment reads:

$$\begin{aligned} v_1 &= Ae^{-\alpha y} + Be^{\alpha y} \rightarrow v_1 = B(e^{\alpha y} - e^{-\alpha y}), \\ v_2 &= Ce^{-\alpha y} + De^{\alpha y}, \\ v_3 &= Fe^{-\alpha y} + Ge^{\alpha y}, \\ v_4 &= He^{-\alpha y} + Le^{\alpha y} \rightarrow v_4 = He^{-\alpha y}, \end{aligned}$$

where the boundary conditions  $v=0$  at  $y=0$  and  $v=0$  as  $y \rightarrow \infty$  are applied for  $v_1$  and  $v_4$ . To find the constants  $A, B, C, D, F, G$  and  $H$ , the

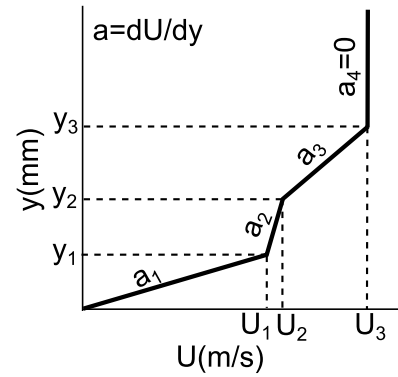


**Figure 12.** Parameters on two panels determining the influence coefficients.

jump conditions are applied at  $y_1$ ,  $y_2$  and  $y_3$ . The first jump condition writes:

$$\left[ \left[ (U - c) \frac{dv}{dy} - \frac{dU}{dy} v \right] \right] = 0, \quad (\text{A.9})$$

and represents that the pressure is constant over the jump. The second jump condition writes:

$$\left[ \left[ \frac{v}{U - c} \right] \right] = 0, \quad (\text{A.10})$$

and represents that the point where the condition is applied is a material surface. For a derivation of the jump conditions Schmid and Henningson (2001) can be consulted. Each of the jump equations is now applied for  $y_1$ ,  $y_2$  and  $y_3$  to get a system of equations which can be written as:

$$\begin{pmatrix} \gamma_1 c + \beta_1 & \gamma_2 c + \beta_2 & 0 \\ 0 & \gamma_5 c + \beta_5 & \gamma_6 c + \beta_6 \\ \beta_7 & \beta_8 & \gamma_9 c + \beta_9 \end{pmatrix} \begin{pmatrix} B \\ D \\ G \end{pmatrix} = \begin{pmatrix} 0 \\ 0 \\ 0 \end{pmatrix} \quad (\text{A.11})$$

Where  $\gamma_1$  to  $\gamma_9$  and  $\beta_1$  to  $\beta_9$  are a function of  $k$ . For brevity, here the procedure for  $y_1$  is written out. Jump condition 1 writes:

$$\begin{aligned} \frac{v_1}{U_1 - c} &= \frac{v_2}{U_1 - c} \rightarrow v_1 = v_2, \\ B(e^{\alpha y_1} - e^{-\alpha y_1}) &= C e^{-\alpha y_1} + D e^{\alpha y_1}, \\ C &= B(1 - e^{2\alpha y_1}) + D e^{2\alpha y_1}. \end{aligned}$$

The second jump condition writes:

$$\begin{aligned} (U_1 - c)(B(k e^{\alpha y_1} + k e^{-\alpha y_1}) - a_1 B(e^{\alpha y_1} - e^{-\alpha y_1})) &= \\ (U_1 - c)(D k e^{\alpha y_1} - C k e^{-\alpha y_1}) - a_2 (C e^{-\alpha y_1} + D e^{\alpha y_1}) & \end{aligned}$$

Combining the equations for both jump conditions results in:

$$B((U_1 - c)k(2e^{\alpha y_1} + (a_2 - a_1)(e^{\alpha y_1} - e^{-\alpha y_1})) - 2Dk e^{\alpha y_1}(U_1 - c)) = 0 \quad (\text{A.12})$$

Which corresponds to the first row of the matrix. Applying the jump conditions for

$y_2$  and  $y_3$  the coefficients of the matrix described in A.11 write:

$$\begin{aligned}
 \gamma_1 &= -2ke^{\alpha y_1} \\
 \gamma_2 &= 2ke^{\alpha y_1} \\
 \gamma_5 &= -2ke^{\alpha y_2} \\
 \gamma_6 &= 2ke^{\alpha y_2} + 2k\frac{a_2 - a_3}{a_3}e^{k(2y_3 - y_2)} \\
 \gamma_9 &= \frac{2k}{a_3}e^{2\alpha y_3} \\
 \beta_1 &= 2U_1ke^{\alpha y_1} + (a_2 - a_1)(e^{\alpha y_1} - e^{-\alpha y_1}) \\
 \beta_2 &= -2U_1ke^{\alpha y_1} \\
 \beta_5 &= 2U_2ke^{\alpha y_2} \\
 \beta_6 &= -2kU_2e^{\alpha y_2} + 2U_3k\frac{a_3 - a_2}{a_3}e^{k(2y_3 - y_2)} + (a_3 - a_2)(e^{\alpha y_2} - e^{k(2y_3 - y_2)}) \\
 \beta_7 &= e^{2\alpha y_1} - 1 \\
 \beta_8 &= e^{2\alpha y_2} - e^{2\alpha y_1} \\
 \beta_9 &= \frac{-2U_3k}{a_3}e^{2\alpha y_3} - e^{2\alpha y_2} + e^{2\alpha y_3}
 \end{aligned}$$

To find the non-trivial solutions of the system described by A.11 the determinant has to be equal to 0, which gives

$$f(k) = a\omega^3 + b\omega^2 + g\omega + h = 0 \quad (\text{A.13})$$

where  $c = \omega/k$  has been substituted. The coefficients  $a, b, d$  and  $f$  write:

$$\begin{aligned}
 a &= \frac{1}{k^3}\gamma_1\gamma_5\gamma_9 \\
 b &= \frac{1}{k^2}(\gamma_1\gamma_5\beta_9 - \gamma_1\beta_5\gamma_9 - \gamma_6\gamma_1\beta_8 + \gamma_2\gamma_6\beta_7 + \beta_1\gamma_5\gamma_9) \\
 g &= \frac{1}{k}(\gamma_1\beta_5\beta_9 - \gamma_1\beta_6\beta_8 + \gamma_5\beta_9\beta_1 + \beta_5\gamma_9\beta_1 - \gamma_6\beta_1\beta_8 + \beta_2\gamma_6\beta_7 + \beta_6\gamma_2\beta_7) \\
 h &= \beta_5\beta_9\beta_1 - \beta_6\beta_1\beta_8 + \beta_6\beta_2\beta_7
 \end{aligned}$$

For the temporal stability problem  $\omega$  is found in terms of  $k$ . In order to do so the roots of the third order polynomial in Equation A.13 are calculated with the

following equations:

$$\begin{aligned} r_1 &= -\frac{1}{3a} \left( b + C_1 + \frac{\Delta_0}{C_1} \right) \\ r_2 &= -\frac{1}{3a} \left( b + C_2 + \frac{\Delta_0}{C_2} \right) \\ r_3 &= -\frac{1}{3a} \left( b + C_3 + \frac{\Delta_0}{C_3} \right) \end{aligned}$$

where,

$$\begin{aligned} C_1 &= \left( \frac{1}{2} (\Delta_1 + \sqrt{\Delta_1^2 - 4\Delta_0^3}) \right)^{\frac{1}{3}} \\ C_2 &= C_1 \left( -\frac{1}{2} + \frac{1}{2} \sqrt{3}i \right) \\ C_3 &= C_1 \left( -\frac{1}{2} - \frac{1}{2} \sqrt{3}i \right) \end{aligned}$$

and

$$\begin{aligned} \Delta_0 &= b^2 - 3ag \\ \Delta_1 &= 2b^3 - 9abg + 27a^2h. \end{aligned}$$

For the spatial stability problem Newton's method was employed to find a complex  $k$  for a given  $\omega$ . After each iteration a new  $k$  is determined with:

$$k_{n+1} = k_n - \frac{f(k_n)}{f'(k_n)} \quad (\text{A.14})$$

The derivative  $f'(k_n)$  is determined analytically by first calculating the derivatives of  $\gamma_1$  to  $\gamma_9$  and  $\beta_1$  to  $\beta_9$  and then using the chain rule to calculate the derivatives of  $a, b, g$  and  $h$ .

To verify the derivation of the function  $f(k)$  first a temporal stability problem was solved, which dispersion relation was given in [Schmid and Henningson \(2001\)](#). The profile is described with:

$$U(y) = \begin{cases} 2by & \text{for } 0 \leq y \leq 1/2 \\ 2(1-b)y + (2b-1) & \text{for } 1/2 < y \leq 1 \\ 1 & \text{for } y > 1 \end{cases} \quad (\text{A.15})$$

This profile has three segments instead of four for the derived equations. Therefore

one extra segment is added resulting in:  $a_1=a_2=2b$ ,  $b_2=0$ ,  $a_3=2(1-b)b_3 = (2b - 1)$ ,  $y_1=0.25$   $y_2=0.5$ ,  $y_3=1$ ,  $U_1=0.5b$ ,  $U_2=b$  and  $U_3=1$ . The solutions with  $b=0.4$  for the real and complex  $c$  are shown in Figure 13 and are equivalent to Figure 2.9 in Schmid and Henningson (2001).

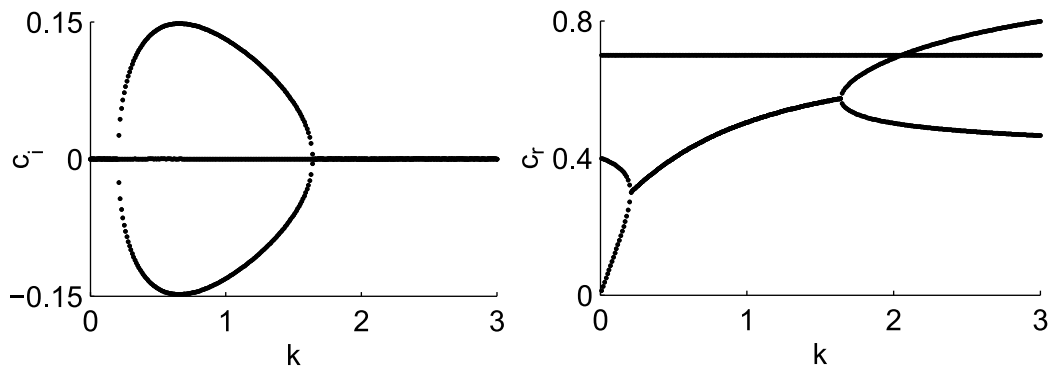


**Figure 13.** N-factor curves for stationary crossflow waves obtained from the pressure distributions of the panel code and DLR-TAU code.

As expected from the equations for the roots of the third order polynomial there are two bifurcation points. At these points the system only has one solution. In the region where  $c_i$  has two solutions the perturbations of the form  $e^{ik(x-ct)}$  can grow in time and therefore the system is unstable. In the region where  $c_i=0$  the system is stable again and the perturbations are described as waves with wavenumber  $k$  and temporal frequency  $c_r$ , where again due to the quadratic form of the equations there are two solutions.

# B

# Hess-Smith panel code

## B.1. Introduction

The panel code was used to design the displacement body which is placed above and below the flat plate. First, a simple code was written with one aerofoil, after which the code was extended to more bodies such to describe the entire experimental set-up. In this appendix the principle of the panel code will be discussed, together with the validation of the written code. Finally, improvements of the initial code are described.

## B.2. Principle of panel code

The two-dimensional panel code follows the classic Hess Smith method ([Hess and Smith, 1967](#)), which is described in detail in [Mason \(1995\)](#). In this method, the contour of a body is divided in several panels, where each panel has a distributed source and vortex. In Figure 1A the lay-out for an aerofoil with an angle of attack is shown. In total there are  $N+1$  nodes which results in  $N$  panels and  $N$  control points. This means that there are  $N+1$  unknowns; the strengths of  $N$  sources and the strength of one vortex.

Since there are  $N+1$  unknowns,  $N+1$  equations are needed to solve the system. For each panel the flow tangency condition should be valid, which states that there is no flow normal to the panel. The flow tangency condition is written as:

$$\mathbf{V} \cdot \mathbf{n} = 0, \tag{B.1}$$

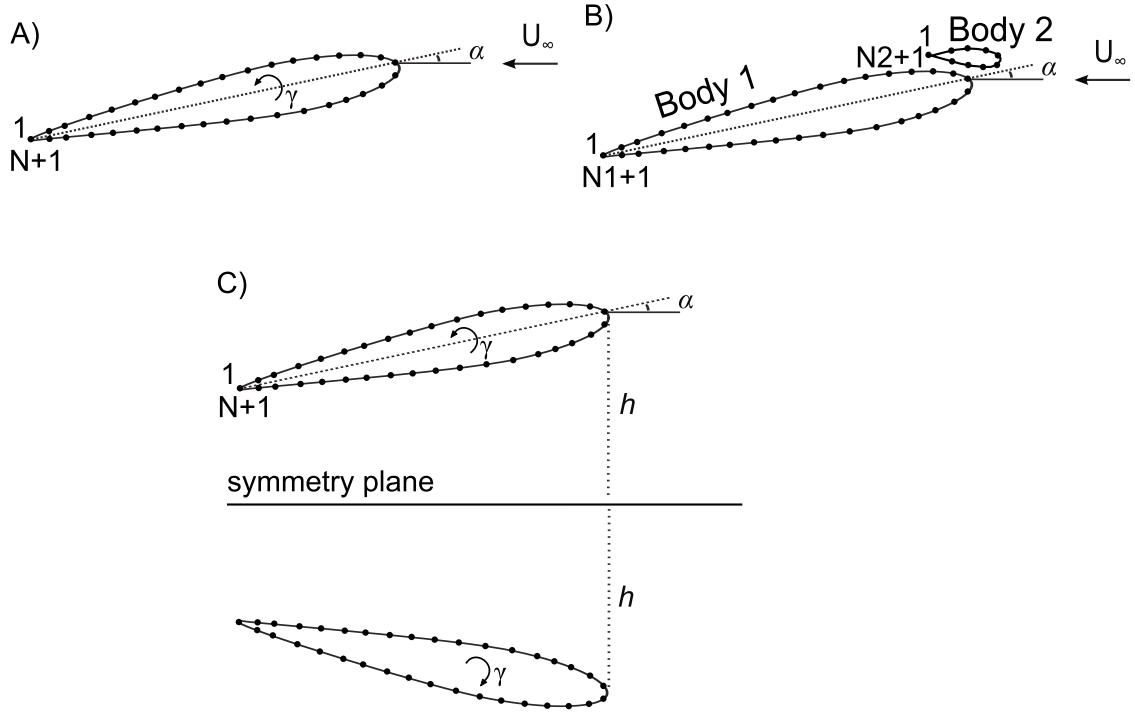


**Figure 1. Different lay-outs of the panel code.** A) One body. B) Two bodies. C) One body with methods of images.

where  $\mathbf{V}$  is the velocity vector with the streamwise velocity  $u$  and normal velocity  $v$  and  $\mathbf{n}$  the unit vector normal to the panel. The final equation is the Kutta condition, which states that the flow leaves the trailing edge smoothly and writes:

$$\mathbf{V} \cdot \mathbf{t}|_1 = -\mathbf{V} \cdot \mathbf{t}|_N, \quad (\text{B.2})$$

where  $t$  is the unit vector tangential to the panel. The subscripts  $_1$  and  $_N$  denote the first and N-th panel. In order to write down these equations expressions for the velocity components are needed. Following potential flow theory, the velocity at a control point  $i$  is written as the sum of the contributions of sources, vortices and free stream velocity as:

$$u_i = U_\infty + \sum_{j=1}^N q_j u_{s_{ij}} + \gamma \sum_{j=1}^N u_{v_{ij}} \quad (\text{B.3})$$

and

$$v_i = V_\infty + \sum_{j=1}^N q_j v_{s_{ij}} + \gamma \sum_{j=1}^N v_{v_{ij}}, \quad (\text{B.4})$$

where  $U_\infty$  and  $V_\infty$  are the free stream velocities in the streamwise and normal direction,  $q_j$  the source strength at panel  $j$  and  $\gamma$  is the vortex strength which has the same value at each panel.

The influence coefficients are given by  $u_{s_{ij}}, u_{v_{ij}}, v_{s_{ij}}$  and  $v_{v_{ij}}$ . They describe how a panel  $j$  with source  $q_j$  and vortex  $\gamma$ , influences the velocity on a panel with control point  $i$ . The velocities  $u_s$  and  $v_s$  induced by a source  $q_j$ , distributed on panel  $j$  write:

$$u_s = \int_{x=0}^{x=l} \frac{q_j}{2\pi} \frac{x_i^* - x}{(x_i^* - x)^2 + y_i^{*2}} dx, \quad (\text{B.5})$$

and

$$v_s = \int_{x=0}^{x=l} \frac{q_j}{2\pi} \frac{y_i^*}{(x_i^* - x)^2 + y_i^{*2}} dx. \quad (\text{B.6})$$

With the constant source strength  $q_j$  and integrating the expressions the influence coefficients  $u_{s,ij}$  and  $v_{s,ij}$  are obtained and write:

$$u_{s,ij} = -\frac{1}{2\pi} \ln\left(\frac{r_{i,j+1}}{r_{i,j}}\right) \quad (\text{B.7})$$

and

$$v_{s,ij} = \frac{\beta_{i,j}}{2\pi}. \quad (\text{B.8})$$

Similarly, for a vortex the induced velocity components are written as:

$$u_v = \int_{x=0}^{x=l} \frac{\gamma}{2\pi} \frac{y_i^*}{(x_i^* - x)^2 + y_i^{*2}} dx \quad (\text{B.9})$$

and

$$v_v = \int_{x=0}^{x=l} -\frac{\gamma}{2\pi} \frac{x_i^* - x}{(x_i^* - x)^2 + y_i^{*2}} dx. \quad (\text{B.10})$$

From this it is found that  $u_{v_{ij}} = v_{s_{ij}}$  and  $v_{v_{ij}} = -u_{s_{ij}}$ . After a coordinate transformation to the global coordinate system, a linear system of equations is derived which can be written as:

$$Aq = b, \quad (\text{B.11})$$

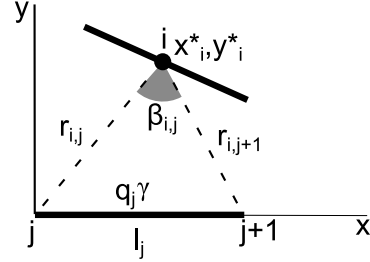


**Figure 2.** Parameters on two panels determining the influence coefficients.

where  $A$  is the matrix with Equation B.1 and B.2 for each panel,  $q$  a vector with the unknown sources and vortex and  $b$  a vector with all the known parameters such as the contribution of the freestream.

## B.3. Definition of matrix A for different cases

The panel code is easily extended for multiple bodies or for using the method of images. The only variable is the matrix  $A$  written in Equation B.11. In this section the structure of matrix  $A$  is given for the lay-outs of the panel code shown in Figure 1.

### B.3.1. Single body

The single body arrangement is sketched in Figure 1A. In total there are  $N$  control points and  $N$  panels which results in the following system:

$$\begin{pmatrix} A_{1,1} & A_{1,2} & \cdots & \cdots & A_{1,N+1} \\ A_{2,1} & A_{2,2} & \cdots & \cdots & A_{2,N+1} \\ \vdots & \vdots & \ddots & \cdots & \vdots \\ A_{N,1} & A_{N,2} & \cdots & \ddots & A_{N,N+1} \\ A_{N+1,1} & A_{N+1,2} & \cdots & \cdots & A_{N+1,N+1} \end{pmatrix} \begin{pmatrix} q_1 \\ q_2 \\ \vdots \\ q_N \\ \gamma \end{pmatrix} = \begin{pmatrix} b_1 \\ b_2 \\ \vdots \\ b_N \\ b_{N+1} \end{pmatrix}$$

For a single body each entry  $A_{i,j}$  represents the influence of panel  $j$  on control point  $i$  on the body. Row  $A(1:N,j)$  represents the flow tangency condition while row  $A(N+1,j)$  represents the Kutta condition. Column  $A(i,N+1)$  represents the influence of the vortex,  $\gamma$ .

### B.3.2. Two bodies

For two bodies the number of unknowns increases because now there are two sets of sources. In Figure 1B the lay-out for two bodies is shown. The system of equations is written as:

$$\begin{pmatrix} A^{B1B1} & A^{B1B2} \\ A^{B2B1} & A^{B2B2} \end{pmatrix} \begin{pmatrix} q^{B1} \\ q^{B2} \end{pmatrix} = \begin{pmatrix} b^{B1} \\ b^{B2} \end{pmatrix}$$

With:

$$A^{B1B1} = \begin{pmatrix} A_{1,1} & A_{1,2} & \cdots & \cdots & A_{1,N1+1} \\ A_{2,1} & A_{2,2} & \cdots & \cdots & A_{2,N1+1} \\ \vdots & \vdots & \ddots & \cdots & \vdots \\ A_{N1,1} & A_{N1,2} & \cdots & \ddots & A_{N1,N1+1} \\ A_{N1+1,1} & A_{N1+1,2} & \cdots & \cdots & A_{N1+1,N1+1} \end{pmatrix}$$

$$A^{B1B2} = \begin{pmatrix} A_{1,N1+2} & A_{1,N1+3} & \cdots & \cdots & A_{1,N1+N2+2} \\ A_{2,N1+2} & A_{2,N1+3} & \cdots & \cdots & A_{2,N1+N2+2} \\ \vdots & \vdots & \ddots & \cdots & \vdots \\ A_{N1,N1+2} & A_{N1,N1+3} & \cdots & \ddots & A_{N1,N1+N2+2} \\ A_{N1+1,N1+2} & A_{N1+1,N1+3} & \cdots & \cdots & A_{N1+1,N1+N2+2} \end{pmatrix}$$

$$A^{B2B1} = \begin{pmatrix} A_{N1+2,1} & A_{N1+2,2} & \cdots & \cdots & A_{N1+2,N1+1} \\ A_{N1+3,1} & A_{N1+3,2} & \cdots & \cdots & A_{N1+3,N1+1} \\ \vdots & \vdots & \ddots & \cdots & \vdots \\ A_{N1+N2+1,1} & A_{N1+N2+1,2} & \cdots & \ddots & A_{N1+N2+1,N1+1} \\ A_{N1+N2+2,1} & A_{N1+N2+2,2} & \cdots & \cdots & A_{N1+N2+2,N1+1} \end{pmatrix}$$

$$A^{B2B2} = \begin{pmatrix} A_{N1+2,N1+2} & A_{N1+2,N1+3} & \cdots & \cdots & A_{N1+2,N1+N2+2} \\ A_{N1+3,N1+2} & A_{N1+3,N1+3} & \cdots & \cdots & A_{N1+3,N1+N2+2} \\ \vdots & \vdots & \ddots & \cdots & \vdots \\ A_{N1+N2+1,N1+2} & A_{N1+N2+1,N1+3} & \cdots & \ddots & A_{N1+N2+1,N1+N2+2} \\ A_{N1+N2+2,N1+2} & A_{N1+N2+2,N1+3} & \cdots & \cdots & A_{N1+N2+2,N1+N2+2} \end{pmatrix}$$

The total matrix  $A$  is of size  $N1+N2+2 \times N1+N2+2$  and the submatrices represent the following:

$A^{B1B1}$  represents the influence of the sources and vortices of Body 1 on Body 1 and is therefore of size  $N1+1 \times N1+1$ .

$A^{B1B2}$  represents the influence of the sources and vortices of Body 2 on Body 1 and is therefore of size  $N1+1 \times N2+1$ .

$A^{B2B1}$  represents the influence of the sources and vortices of Body 1 on Body 2 and is therefore of size  $N2+1 \times N1+1$ .

$A^{B2B2}$  represents the influence of the sources and vortices of Body 2 on Body 2 and is therefore of size  $N2+1 \times N2+1$ .

Adding more bodies will make the matrix A consist of more submatrices. With three bodies there would be 9 submatrices, with four bodies 16 etc.

### B.3.3. Standard method of images

In the method of images a body is mirrored, where a streamline is created at the line of symmetry (Figure 1C). Each body has the same number of panels and control points. In this case the system of equations is written as:

$$\begin{pmatrix} A_{1,1}^B + A_{1,1}^I & \cdots & \cdots & \cdots & A_{1,N+1}^B + A_{1,N+1}^I \\ A_{2,1}^B + A_{2,1}^I & \ddots & \cdots & \cdots & A_{2,N+1}^B + A_{2,N+1}^I \\ \vdots & \vdots & \ddots & \cdots & \vdots \\ A_{N,1}^B + A_{N,1}^I & \cdots & \cdots & \ddots & A_{N,N+1}^B + A_{N,N+1}^I \\ A_{N+1,1}^B + A_{N+1,1}^I & \cdots & \cdots & \cdots & A_{N+1,N+1}^B + A_{N+1,N+1}^I \end{pmatrix} \begin{pmatrix} q_1^B \\ q_2^B \\ \vdots \\ q_N^B \\ \gamma^B \end{pmatrix} = \begin{pmatrix} b_1^B \\ b_2^B \\ \vdots \\ b_N^B \\ b_{N+1}^B \end{pmatrix}$$

Here, each entry has the influence of the panels  $j$  on the body and image, on control point  $i$ . Since the two bodies are identical the strength of sources  $q_j$  is identical. For  $\gamma$  the sign changes on the image body which is included in the last column of the matrix.

### B.3.4. Method of images with a single body

The experimental set-up consists of two displacement bodies and a flat plate. In the panel code the two displacement bodies are modelled with the method of images and the flat plate is modeled as a single body (Figure 3). For this case the system

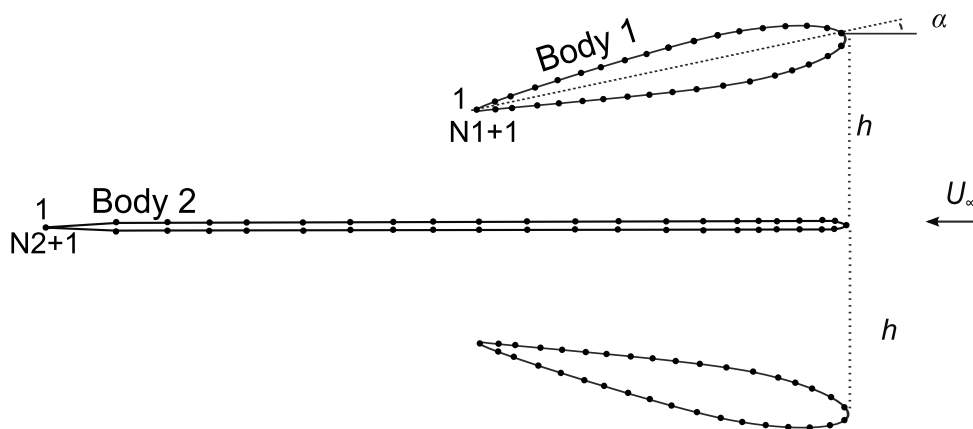


Figure 3. Panel code set-up for the method of images with one body.

is written as:

$$\begin{pmatrix} A^{B1B1,B} + A^{B1B1,I} & A^{B1B2} \\ A^{B2B1,B} + A^{B2B1,I} & A^{B2B2} \end{pmatrix} \begin{pmatrix} q^{B1} \\ q^{B2} \end{pmatrix} = \begin{pmatrix} b^{B1} \\ b^{B2} \end{pmatrix}$$

Here the additional terms represent the influence of the sources and vortices of the image. The total size of the matrix does not change compared to the two bodies case since the number of unknowns stays the same.

## B.4. Validation of panel code

The panel code was validated through different methods. The single body panel code was validated with the pressure distribution of a NACA0012. The results are presented in Figure 4. The values obtained from XFOIL and the panel code are virtually identical, which confirms that the panel code is correct for the single body arrangement shown in Figure 1A. Next, the panel code with the method of images,

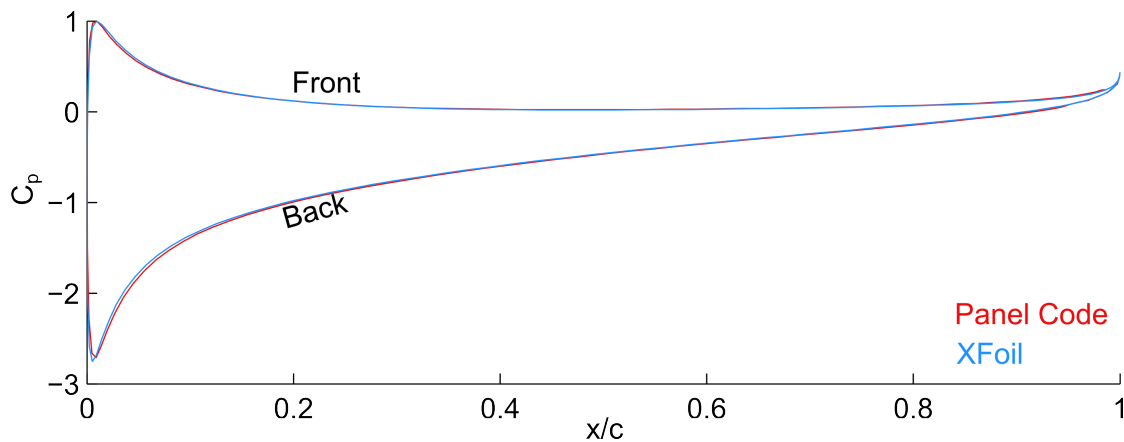
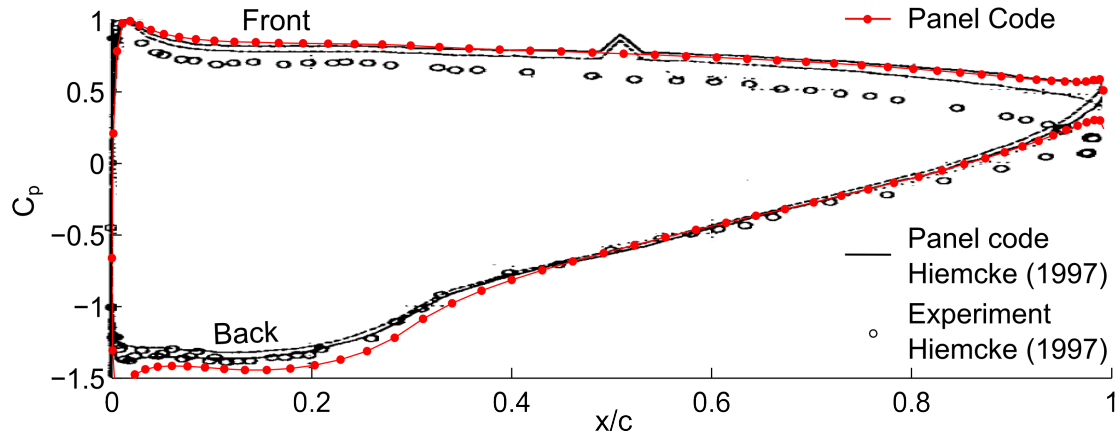


Figure 4. Comparison of panel code with XFOIL.

as defined in Figure 1C, was validated with an experimental study carried out by Hiemcke (1997). In Figure 5 it is presented that the pressure distributions for both panel codes are almost identical. Furthermore, there is a small discrepancy with the experiment where the pressure coefficient is lower compared to the panel code at the top of the displacement body. In the panel code viscous effects such as boundary layer growth are not taken into account. The boundary layer growth in the experiment changes the effective shape of the aerofoil and therewith the pressure distribution.



**Figure 5.** Comparison of the panel code with the method of images to panel code and experimental study carried out by (Hiemcke, 1997).

## B.5. Improvements of panel code

Throughout the project the panel code was improved by increasing the leading edge resolution, and by adding a flap angle and tunnel walls to the model. Here the influence of each of these additions is discussed.

### B.5.1. Flap angle, $\alpha_f$

The purpose of the trailing edge flap is to ensure that the stagnation point is at the top of the plate. In Figure 6 the influence of changing the flap angle, on the location of the stagnation point at the leading edge is shown. As expected, the stagnation point moves gradually from the back to the front of the plate with increasing flap angle.

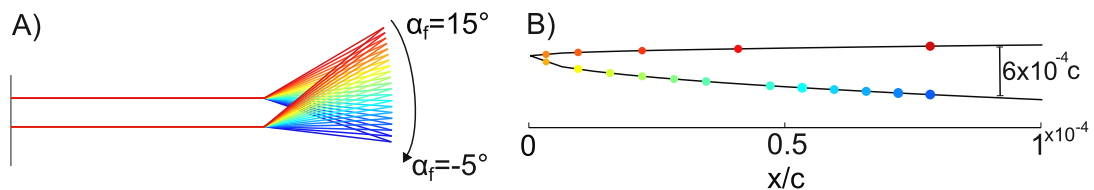


**Figure 6.** Influence of flap angle on the location of the stagnation point. A) Definition of the tested flap angles. B) Location of the stagnation point on the leading edge where the colour corresponds to the flap angle.

The pressure at the front of the plate increases with increasing flap angle (Figure 7). Increasing the flap angle is equivalent to giving the plate a small negative angle of attack, increasing the pressure at the front while decreasing the pressure at the bottom of the plate.

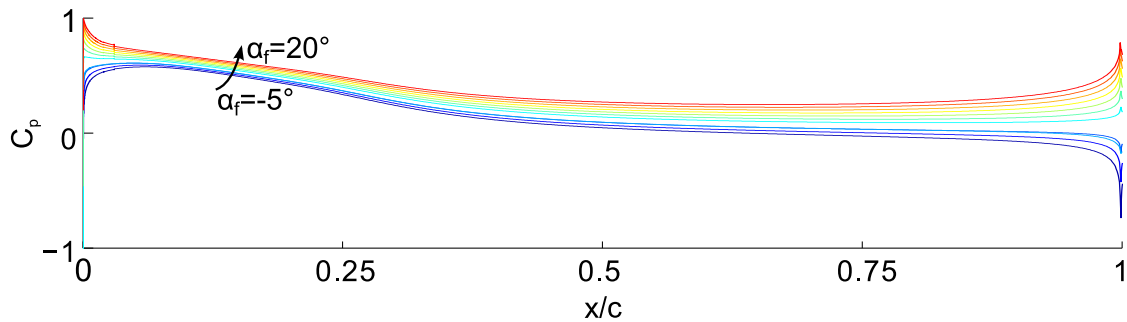


Figure 7. Pressure distribution over the plate for different flap angles.

### B.5.2. Increased resolution at leading edge

The validation of the panel code was carried out with aerofoils. These aerofoils have a leading edge nose radius, around 10% of the chord length. For the flat plate, the radius is around 0.4% of the chord length, therefore a change in resolution of control points at the leading edge can easily lead to a different shape and pressure coefficients. In Figure 8 the influence of the leading edge resolution on the stagnation pressure and location are shown. When the leading edge is described with a high resolution, the suction peak becomes larger since the leading edge becomes sharper, leading to larger velocity gradients. When a low resolution leading edge is used, the location of the stagnation point changes and the stagnation pressure decreases. For the three-dimensional linear stability analysis, the stagnation pressure determines the sweep angle and it is therefore important to have enough points at the leading edge to describe the stagnation pressure correctly.

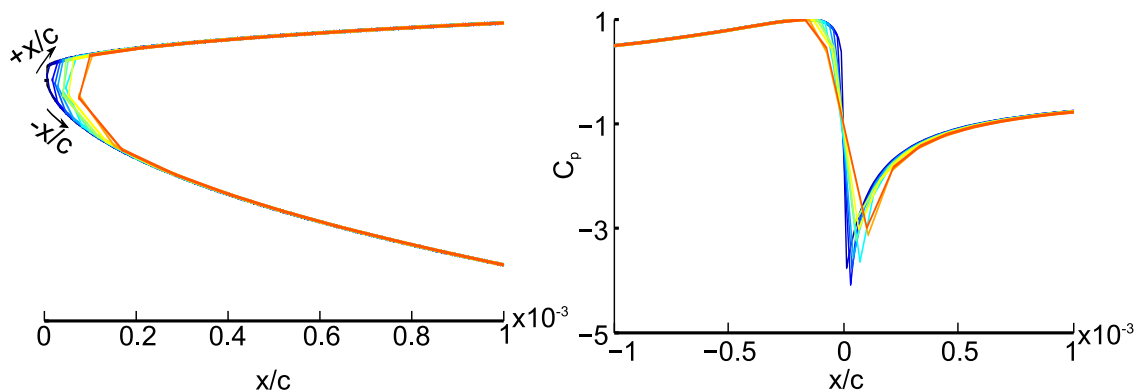


Figure 8. Influence of leading edge resolution on the pressure distribution. A) Shape of the leading edge through the distribution of the control points. B) Pressure distribution at the leading edge of the flat plate.

# C LabVIEW system

The main user interface of the developed LabVIEW system is shown in Figure 2. In each part of the interface different tasks can be carried out such as starting a hot-wire scan, carrying out a hot-wire calibration or changing the position of the hot-wire. The goal of the LabVIEW system was to automate large part of the data acquisition and switch between the different tasks smoothly.

The overall architecture to achieve this is shown in Figure 1. The state machine consists of a while loop with inside it a case structure. Each case of the case structure is assigned to a different task. At the end of each case structure it is decided to which case structure it should go next. With this system in place it was possible to carry out a large number of tasks without interference of the user.

In this PhD project the data acquisition system was built from scratch together with three other members of the research group.

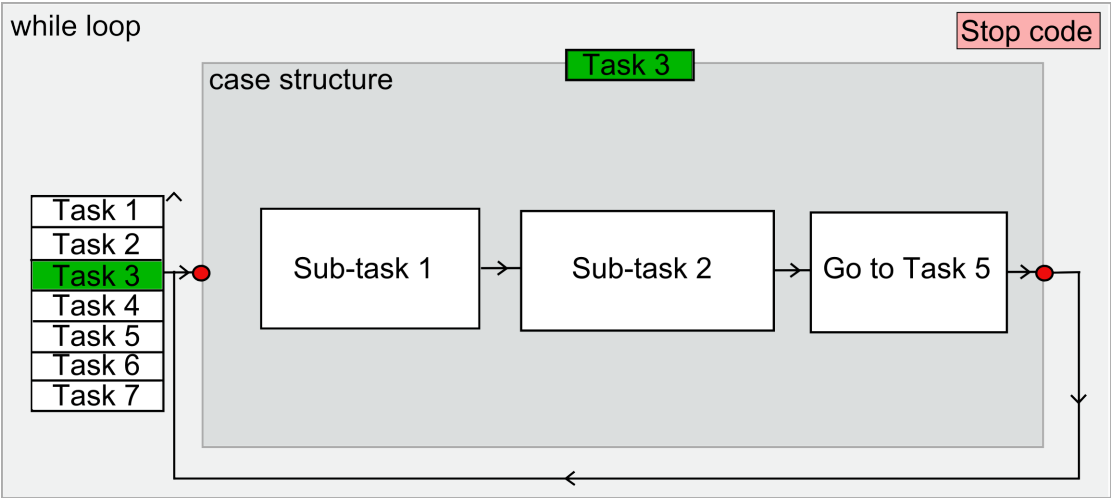


Figure 1. State machine structure to switch between different tasks.

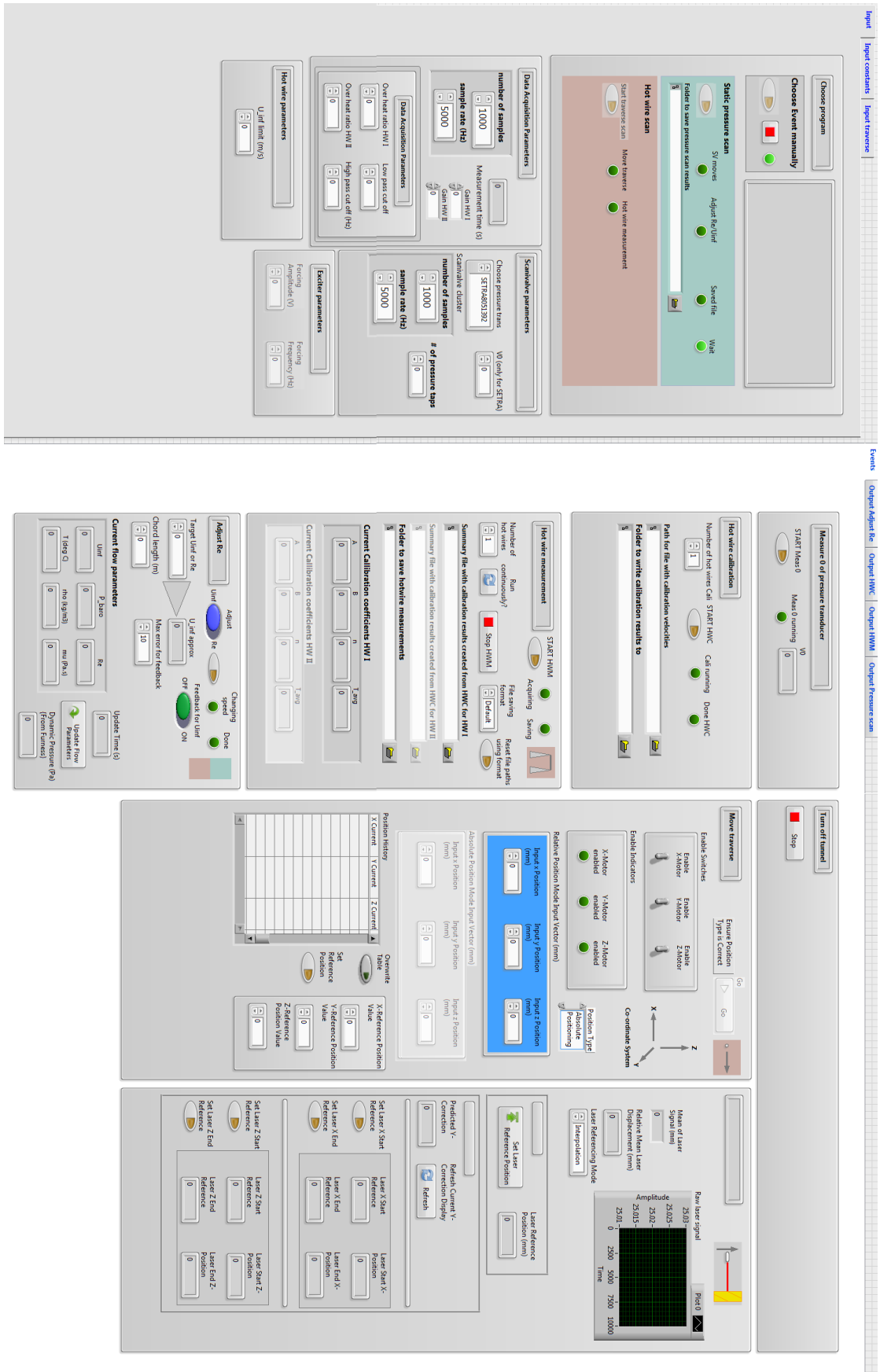
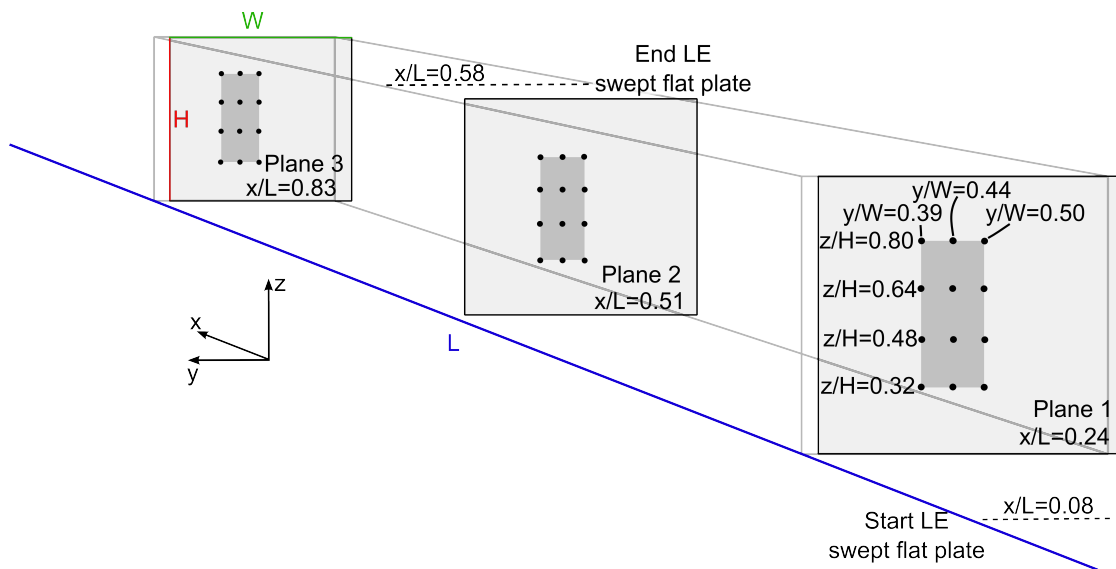


Figure 2. Overview of LabVIEW user interface

# D

## Freestream disturbance measurements

The free stream turbulence measurements are carried out in the empty wind tunnel for different locations as described in Chapter 3 and shown again in Figure 1. In this appendix the results of the measurements are given.



**Figure 1.** Locations at which free-stream turbulence measurements are taken.

**Table D.1.** Tu (%) at  $x/L=0.24$  for different  $y$  and  $z$  locations.

$y/W=0.50$					
$z/H$	$U_\infty=10$ m/s	12 m/s	14 m/s	16 m/s	18 m/s
0.32	0.0122	0.0097	0.0094	0.0083	0.0078
0.48	0.0121	0.0098	0.0093	0.0082	0.0079
0.64	0.0119	0.0097	0.0092	0.0081	0.0079
0.80	0.0141	0.0103	0.0097	0.0086	0.0083
$y/W=0.44$					
$z/H$	$U_\infty=10$ m/s	12 m/s	14 m/s	16 m/s	18 m/s
0.32	0.0121	0.0096	0.0092	0.0083	0.0078
0.48	0.0120	0.0098	0.0094	0.0083	0.0079
0.64	0.0117	0.0098	0.0092	0.0082	0.0079
0.80	0.0128	0.0103	0.0097	0.0086	0.0082
$y/W=0.39$					
$z/H$	$U_\infty=10$ m/s	12 m/s	14 m/s	16 m/s	18 m/s
0.32	0.0121	0.0097	0.0093	0.0083	0.0078
0.48	0.0121	0.0098	0.0094	0.0085	0.0078
0.64	0.0118	0.0098	0.0092	0.0082	0.0078
0.80	0.0125	0.0102	0.0096	0.0085	0.0082

**Table D.2.** Tu (%) at  $x/L=0.51$  for different  $y$  and  $z$  locations.

$y/W=0.50$					
$z/H$	$U_\infty=10$ m/s	12 m/s	14 m/s	16 m/s	18 m/s
0.32	0.0120	0.0098	0.0093	0.0084	0.0079
0.48	0.0122	0.0098	0.0093	0.0082	0.0079
0.64	0.0119	0.0098	0.0092	0.0082	0.0077
0.80	0.0141	0.0109	0.0101	0.0089	0.0494
$y/W=0.44$					
$z/H$	$U_\infty=10$ m/s	12 m/s	14 m/s	16 m/s	18 m/s
0.32	0.0120	0.0098	0.0092	0.0083	0.0078
0.48	0.0121	0.0098	0.0093	0.0083	0.0078
0.64	0.0119	0.0101	0.0092	0.0082	0.0209
0.80	0.0137	0.0107	0.0101	0.0088	0.0495
$y/W=0.39$					
$z/H$	$U_\infty=10$ m/s	12 m/s	14 m/s	16 m/s	18 m/s
0.32	0.0120	0.0097	0.0092	0.0082	0.0078
0.48	0.0122	0.0098	0.0094	0.0082	0.0078
0.64	0.0119	0.0098	0.0092	0.0082	0.0494
0.80	0.0131	0.0106	0.0099	0.0090	0.0500

**Table D.3.** Tu (%) at  $x/L=0.83$  for different  $y$  and  $z$  locations.

$y/W=0.50$					
$z/H$	$U_\infty=10$ m/s	12 m/s	14 m/s	16 m/s	18 m/s
0.32	-	-	-	-	-
0.48	0.0127	0.0100	0.0095	0.0083	0.0081
0.64	0.0127	0.0099	0.0094	0.0085	0.0080
0.80	0.0168	0.0122	0.0111	0.0099	0.0096
$y/W=0.44$					
$z/H$	$U_\infty=10$ m/s	12 m/s	14 m/s	16 m/s	18 m/s
0.32	-	-	-	-	-
0.48	0.0127	0.0099	0.0094	0.0082	0.0080
0.64	0.0127	0.0100	0.0094	0.0083	0.0079
0.80	0.0163	0.0118	0.0110	0.0099	0.0096
$y/W=0.39$					
$z/H$	$U_\infty=10$ m/s	12 m/s	14 m/s	16 m/s	18 m/s
0.32	0.0128	0.0100	0.0095	0.0083	0.0080
0.48	0.0128	0.0099	0.0095	0.0083	0.0080
0.64	0.0127	0.0099	0.0094	0.0083	0.0079
0.80	0.0149	0.0114	0.0108	0.0098	0.0096

# E

# Uncertainty analysis

## E.1. Error propagation

The errors calculated in this section follow the ISO uncertainty model (JCGM, 2008). The standard uncertainty of a function  $f$ , depending on variables  $x_1, x_2$  to  $x_N$  is:

$$\Delta f^2 = \sum_{i=1}^N \left( \frac{\partial f}{\partial x_i} \right)^2 \Delta x_i^2. \quad (\text{E.1})$$

When  $f$  is a linear function of the variables  $x$ , such as  $f = x_1 + x_2 + \dots + x_N$  the equation writes:

$$\Delta f^2 = \sum_{i=1}^N \Delta x_i^2. \quad (\text{E.2})$$

If  $f$  is a product of different variables, such as  $f = x_1^{p_1} x_2^{p_2} \dots x_N^{p_N}$  the equation writes:

$$\left( \frac{\Delta f}{f} \right)^2 = \sum_{i=1}^N \left( \frac{p_i \Delta x_i}{x_i} \right)^2. \quad (\text{E.3})$$

The uncertainty of a stochastic variable is calculated as a standard deviation. To relate the standard deviation to an interval the expanded uncertainty is defined as:

$$\Delta F = k_c \Delta f, \quad (\text{E.4})$$

where  $k_c$  is the coverage factor. Depending on the probability distribution of the measured variable and the preferred confidence level,  $k_c$  takes different values. In this Appendix the intervals are determined for a normal and rectangular distribution.

For a confidence level of 95%, the coverage factors are 1.96 and  $1/\sqrt{3}$  respectively (JCGM, 2008).

## E.2. Pressure measurements

The pressure coefficient,  $C_p$ , is calculated with:

$$C_p = \frac{P_1}{\frac{1}{2}\rho U_\infty^2}. \quad (\text{E.5})$$

Using Equation E.3 the relative error for  $C_p$  is determined as:

$$\frac{\Delta C_p}{C_p} = \sqrt{\left(\frac{\Delta P_1}{P_1}\right)^2 + \left(\frac{\Delta \rho}{\rho}\right)^2 + \left(\frac{2\Delta U_\infty}{U_\infty}\right)^2}. \quad (\text{E.6})$$

The density,  $\rho$  is calculated with  $\rho = \frac{P_2}{RT}$  so therefore the relative error for  $\rho$  is:

$$\frac{\Delta \rho}{\rho} = \sqrt{\left(\frac{\Delta P_2}{P_2}\right)^2 + \left(\frac{\Delta T}{T}\right)^2}. \quad (\text{E.7})$$

Finally, the velocity is calculated with:

$$U_\infty = \sqrt{\frac{2P_3}{\rho}}, \quad (\text{E.8})$$

which gives a relative error for  $U_\infty$  as:

$$\frac{\Delta U_\infty}{U_\infty} = \sqrt{\left(\frac{\frac{1}{2}\Delta P_3}{P_3}\right)^2 + \left(\frac{\frac{1}{2}\Delta \rho}{\rho}\right)^2}. \quad (\text{E.9})$$

With the reference values and errors given in Table E.1, the error for the pressure coefficient  $C_p$  is about 0.75%.

**Table E.1.** Uncertainties in pressure coefficient calculations.

Variable, x	Ref. value	$\Delta x$	$k_c$	$\Delta X/x$
$P_1$	31Pa	0.2Pa	$1/\sqrt{3}$	0.37%
$P_2$	101325Pa	55Pa	$1/\sqrt{3}$	0.03%
$P_3$	154Pa	0.2Pa	1.96	0.02%
$T$	20°C	0.1°C	$1/\sqrt{3}$	0.29%

### E.3. Hot wire measurements

The hot-wire measures a voltage,  $E$ , which is converted to a velocity  $U$ . The total uncertainty in  $U$  is the sum of the uncertainties caused by the calibration, data acquisition and experimental conditions (Jørgensen, 2001). The uncertainties in the calibration are caused by the accuracy of the velocity measurement with the Pitot tube. This error,  $\Delta U_{PT}$  is determined for each velocity on the calibration curve with Equation E.9 and the total error,  $\Delta U_1$  is then determined with:

$$\Delta U_1 = k_c \frac{1}{N-1} \sum_{i=1}^N \sqrt{\left( \Delta U_{PT,i} - \Delta \bar{U}_{PT} \right)^2}, \quad (\text{E.10})$$

where  $N$  is the number of measured velocities and  $\Delta U_{PT}$  the average error. For a reference calibration, an error of  $\Delta U_1=0.04$  m/s has been calculated. The curve fit between the estimated velocity,  $U_{est}$ , and measured velocity,  $U_{meas}$ , is another uncertainty in the calibration. This error is determined as:

$$\Delta U_2 = k_c \frac{1}{N-1} \sum_{i=1}^N \sqrt{\left( U_{meas,i} - U_{est,i} \right)^2}. \quad (\text{E.11})$$

With a coverage factor of 1.96,  $\Delta U_2=0.0088$  m/s. Another error is made when, the voltage is converted from an analogue to digital signal with an A/D board. The resolution of the A/D board gives an error in the measured voltage  $E$  and consequently in the velocity  $U$  with:

$$\Delta U_3 = k_c \frac{E_{range}}{2^n} \frac{\partial U}{\partial E}. \quad (\text{E.12})$$

In Table E.2 the error is calculated for the given values. After the calibration is car-

**Table E.2.** Uncertainty due to resolution of A/D board.

$E_{range}$ (V)	n	$\partial U/\partial E$ (m/s/V)	$k_c$	$\Delta U_3$ (m/s)
10	16	27	$1/\sqrt{3}$	0.0024

ried out, the hot-wire is moved to the measurement location with the traverse system. This minimises errors due to rotation of the hot-wire, as reported in (Jørgensen, 2001). Furthermore, each hot-wire measurement is corrected for a difference in calibration and ambient temperature such that this error can also be neglected. The

total error in  $U$  is calculated with Equation E.2 and writes:

$$\Delta U = \sqrt{\Delta U_1^2 + \Delta U_2^2 + \Delta U_3^2}. \quad (\text{E.13})$$

With an average velocity of 10m/s measured inside the boundary layer an uncertainty of 0.5% has been found.

# Bibliography

- Anderson, Jr, J. D.** (1997). *The Infancy of Aerodynamics: To Lilienthal and Langley*, page 87198. Cambridge Aerospace Series. Cambridge University Press.
- Atkin, C.** (2004). Performance trade-off studies for a retrofit hybrid laminar flow control system. *2nd AIAA Flow Control Conference*, 2004-2215.
- Atkin, C.** (2008). Laminar flow control: Leap or creep? *38th Fluid Dynamics Conference and Exhibit*, 2008-3986.
- Bertolotti, F. P.** (2000). Receptivity of three-dimensional boundary-layers to localized wall roughness and suction. *Physics of Fluids (1994-present)*, 12(7):1799–1809.
- Bippes, H.** (1990). Instability features appearing on swept wing configurations. In **Arnal, D. and Michel, R.**, editors, *Laminar-Turbulent Transition*, International Union of Theoretical and Applied Mechanics, pages 419–430. Springer Berlin Heidelberg.
- Bippes, H.** (1999). Basic experiments on transition in three-dimensional boundary layers dominated by crossflow instability. *Progress in Aerospace Sciences*, 35(4):363 – 412.
- Bippes, H. and Muller, B.** (1990). Disturbance growth in an unstable three-dimensional boundary layer. In **Cebeci, T.**, editor, *Numerical and Physical Aspects of Aerodynamic Flows IV*, pages 345–358. Springer Berlin Heidelberg.
- Bonfigli, G. and Kloker, M.** (2007). Secondary instability of crossflow vortices: validation of the stability theory by direct numerical simulation. *Journal of Fluid Mechanics*, 583:229–272.
- Borodulin, V., Ivanov, A., and Kachanov, Y.** (2017). Swept-wing boundary-layer transition at various external perturbations: Scenarios, criteria, and problems of prediction. *Physics of Fluids*, 29(9):094101.

- Borodulin, V. I., Ivanov, A. V., Kachanov, Y. S., and Roschektaev, A. P.** (2013). Receptivity coefficients at excitation of cross-flow waves by free-stream vortices in the presence of surface roughness. *Journal of Fluid Mechanics*, 716:487527.
- Bracewell, R. N.** (1986). *The Fourier transform and its applications*. McGraw-Hill New York.
- Braslow, A.** (1960). Review of the effect of distributed surface roughness on boundary-layer transition. Technical Report Report 254, Advisory group for aeronautical research and development.
- Braslow, A.** (1999). *A history of suction-type laminar-flow control with emphasis on flight research*. Number Monographs in aerospace history, 13. NASA History Office, Office of Policy and Plans, NASA Headquarters.
- Bruun, H.** (1995). *Hot-wire anemometry-principles and signal analysis*. Oxford science publications.
- Brynjell-Rahkola, M., Shahriari, N., Schlatter, P., Hanifi, A., and Henningson, D.** (2017). Stability and sensitivity of a cross-flow-dominated falkner–skan–cooke boundary layer with discrete surface roughness. *Journal of Fluid Mechanics*, 826:830–850.
- Carpenter, A.** (2010). *In-flight receptivity experiments on a 30-degree swept-wing using micron-sized discrete roughness elements*. PhD thesis, Texas A & M University.
- Chernoray, V. G., Dovgal, A. V., Kozlov, V. V., and Löfdahl, L.** (2005). Experiments on secondary instability of streamwise vortices in a swept-wing boundary layer. *Journal of Fluid Mechanics*, 534:295–325.
- Choudhari, M.** (1994). Roughness-induced generation of crossflow vortices in three-dimensional boundary layers. *Theoretical and Computational Fluid Dynamics*, 6(1):1–30.
- Choudhari, M., Li, F., and Paredes, P.** (2016). Influence of stationary crossflow modulation on secondary instability. *46th AIAA Fluid Dynamics Conference*, 2016-3788.
- Crouch, J. and Ng, L.** (2000). Variable n-factor method for transition prediction in three-dimensional boundary layers. *AIAA journal*, 38(2):211–216.

- Crouch, J. D.** (1992). Localized receptivity of boundary layers. *Physics of Fluids A*, 4(7):1408–1414.
- Dagenhart, J.** (1992). *Crossflow stability and transition experiments in a swept-wing flow*. PhD thesis, Virginia Polytechnic Institute and State University, Blacksburg, Virginia.
- Dagenhart, J. and Saric, W.** (1999). Crossflow stability and transition experiments in swept-wing flow. Technical Report 209344, NASA.
- Deyhle, H. and Bippes, H.** (1996). Disturbance growth in an unstable three-dimensional boundary layer and its dependence on environmental conditions. *Journal of Fluid Mechanics*, 316:73–113.
- Dörr, P. and Kloker, M.** (2016). Transition control in a three-dimensional boundary layer by direct attenuation of nonlinear crossflow vortices using plasma actuators. *International Journal of Heat and Fluid Flow*, 61:449–465.
- Downs, R.** (2012). *Environmental influences on crossflow instability*. PhD thesis, Texas AM University, College Station, Texas.
- Drela, M.** (1989). Xfoil: An analysis and design system for low Reynolds number airfoils. In *Low Reynolds number aerodynamics*, pages 1–12. Springer.
- Duan, L., Choudhari, M. M., Li, F., and Wu, M.** (2013). Direct numerical simulation of transition in a swept wing boundary layer. *43rd AIAA Fluid Dynamics Conference*, 2013-2617.
- Eppink, J.** (2014). *The interaction of crossflow instabilities and a backward facing step in swept boundary layer transition*. PhD thesis, Tufts University, Medford, MA.
- Fischer, T. and Dallmann, U.** (1991). Primary and secondary stability analysis of a three-dimensional boundary-layer flow. *Physics of Fluids A: Fluid Dynamics (1989-1993)*, 3(10):2378–2391.
- Fransson, J. H., Brandt, L., Talamelli, A., and Cossu, C.** (2004). Experimental and theoretical investigation of the nonmodal growth of steady streaks in a flat plate boundary layer. *Physics of Fluids*, 16(10):3627–3638.
- Freymuth, P.** (1977). Frequency response and electronic testing for constant-temperature hot-wire anemometers. *Journal of Physics E: Scientific Instruments*, 10(7):705.

- Friederich, T. and Kloker, M.** (2012). Control of the secondary cross-flow instability using localized suction. *Journal of Fluid Mechanics*, 706:470–495.
- Gaster, M.** (1962). A note on the relation between temporally-increasing and spatially-increasing disturbances in hydrodynamic stability. *Journal of Fluid Mechanics*, 14:222–224.
- Gaster, M.** (1965). A simple device for preventing turbulent contamination on swept leading edges. *Journal of Royal Aeronautical Society*, 69:788–789.
- Gaster, M.** (1967). On the flow along swept leading edges. *The Aeronautical Quarterly*, 18.
- Gerhold, T., Friedrich, O., Evans, J., and Galle, M.** (1997). Calculation of complex three-dimensional configurations employing the dlr-tau-code. *AIAA paper*, 167:1997.
- Goldhammer, M. and Plendl, B.** (2013). Surface coatings and drag reduction. Technical Report Aero magazine, Boeing.
- Goldstein, D., Chu, J., and Brown, G.** (2017). Lateral spreading mechanism of a turbulent spot and a turbulent wedge. *Flow, Turbulence and Combustion*, 98(1):21–35.
- Goldstein, M. E.** (1983). The evolution of tollmien sclichting waves near a leading edge. *Journal of Fluid Mechanics*, 127:59–81.
- Goldstein, M. E.** (1985). Scattering of acoustic waves into tollmien-schlichting waves by small streamwise variations in surface geometry. *Journal of Fluid Mechanics*, 154:509–529.
- Gowree, E.** (2014). *Influence of attachment line flow on form drag*. PhD thesis, City, University of London.
- Gray, W.** (1952). The effect of wing sweep on laminar flow. Technical Report Aero 255, Royal Aircraft Establishment.
- Gregory, N., Stuart, J. T., and Walker, W. S.** (1955). On the stability of three-dimensional boundary layers with application to the flow due to a rotating disk. *Philosophical Transactions of the Royal Society of London A: Mathematical, Physical and Engineering Sciences*, 248(943):155–199.

- Hagen, G.** (1839). Über die bewegung des wassers in engen cylindrischen röhren. *Annalen der Physik*, 122(3):423–442.
- Hagen, G.** (1854). *Über den einfluss der temperatur auf die bewegung des wassers in Röhren*-. Druckerei der Königl. akademie der wissenschaften.
- Hanson, R., Buckley, H., and Lavoie, P.** (2012). Aerodynamic optimization of the flat-plate leading edge for experimental studies of laminar and transitional boundary layers. *Experiments in Fluids*, 53(4):863–871.
- Herbert, T.** (1997). Parabolized stability equations. *Annual review of fluid mechanics*, 29(1):245–283.
- Hess, J. and Smith, A.** (1967). Calculation of potential flow about arbitrary bodies. *Progress in Aerospace Sciences*, 8:1–138.
- Hiemcke, C.** (1997). Naca 5312 in ground effect: wind tunnel and panel code studies. *15th Applied Aerodynamics Conference*, 1997-2320.
- Högberg, M. and Henningson, D.** (1998). Secondary instability of cross-flow vortices in falknerskancooke boundary layers. *Journal of Fluid Mechanics*, 368:339–357.
- Hunt, L.** (2012). *Boundary-layer receptivity of three-dimensional roughness arrays on a swept wing*. PhD thesis, Texas AM University, College Station, Texas.
- Hunt, L. E. and Saric, W. S.** (2011). Boundary-layer receptivity of three-dimensional roughness arrays on a swept wing. *41st AIAA Fluid Dynamics Conference and Exhibit*, 2011-3881.
- Janke, E. and Balakumar, P.** (2000). On the secondary instability of three-dimensional boundary layers. *Theoretical and Computational Fluid Dynamics*, 14(3):167–194.
- JCGM** (2008). Evaluation of measurement data; guide to the expression of uncertainty in measurement. Technical report, JCGM.
- Jørgensen, F. E.** (2001). *How to measure turbulence with hot-wire anemometers: a practical guide*. Dantec dynamics.
- Joslin, R.** (1998). The effect of wing sweep on laminar flow. Technical Report 208705, NASA.

- Kawakami, M., Kohama, Y., and Okutsu, M.** (1999). Stability characteristics of stationary crossflow vortices in three-dimensional boundary layer. *37th AIAA Aerospace Sciences Meeting and Exhibit*, 1999-811.
- Klebanoff, K.** (1955). Characteristics of turbulence in boundary layer with zero pressure gradient. Technical Report Report 1247, NACA.
- Koch, W.** (2002). On the spatio-temporal stability of primary and secondary crossflow vortices in a three-dimensional boundary layer. *Journal of Fluid Mechanics*, 456:85–111.
- Kohama, Y., Saric, W., and Hoos, J.** (1991). A high-frequency secondary instability of crossflow vortices that leads to transition. In *Proc. RAS Conf on Boundary-Layer Transition and Control, Cambridge, UK*, pages 4–14.
- Kurian, T., Fransson, J. H. M., and Alfredsson, P. H.** (2011). Boundary layer receptivity to free-stream turbulence and surface roughness over a swept flat plate. *Physics of Fluids*, 23(3):–.
- Kurz, H. and Kloker, M.** (2016). Mechanisms of flow tripping by discrete roughness elements in a swept-wing boundary layer. *Journal of Fluid Mechanics*, 796:158–194.
- Kurz, H. B. and Kloker, M. J.** (2014). Receptivity of a swept-wing boundary layer to micron-sized discrete roughness elements. *Journal of Fluid Mechanics*, 755:62.
- Leatham, M., Stokes, S., Shaw, J., Cooper, J., Appa, J., and Blaylock, T.** (2000). Automatic mesh generation for rapid-response navier-stokes calculations. In *Fluids Conference and Exhibit*, Denver, CO.
- Lin, N., Reed, H., and Saric, W.** (1992). Effect of leading-edge geometry on boundary-layer receptivity to freestream sound. In *Instability, Transition, and Turbulence*, pages 421–440. Springer.
- Lingwood, R.** (1995). Absolute instability of the boundary layer on a rotating disk. *Journal of Fluid Mechanics*, 299:17–33.
- Malik, M. R., Li, F., and Chang, C.** (1994). Crossflow disturbances in three-dimensional boundary layers: nonlinear development, wave interaction and secondary instability. *Journal of Fluid Mechanics*, 268:1–36.

- Malik, M. R., Li, F., Choudhari, M. M., and Chang, C.** (1999). Secondary instability of crossflow vortices and swept-wing boundary-layer transition. *Journal of Fluid Mechanics*, 399:85–115.
- Malik, M. R. and Poll, D. I. A.** (1985). Effect of curvature on three-dimensional boundary-layer stability. *AIAA Journal*, 23.
- Mason, W.** (1995). Incompressible potential flow using panel methods. [http://www.dept.aoe.vt.edu/~mason/Mason\\_f/CAtxtChap4.pdf](http://www.dept.aoe.vt.edu/~mason/Mason_f/CAtxtChap4.pdf). Accessed: Several times from 2014-2017.
- Matsubara, M. and Alfredsson, P.** (2001). Disturbance growth in boundary layers subjected to free-stream turbulence. *Journal of fluid mechanics*, 430:149–168.
- Morkovin, M., Reshotko, E., and Herbert, T.** (1994). Transition in open flow systems-a reassessment. *Bull. Am. Phys. Soc*, 39(9):1882.
- Mughal, M. S. and Ashworth, R. M.** (2013). Uncertainty quantification based receptivity modelling of crossflow instabilities induced by distributed surface roughness in swept wing boundary layers. *43rd AIAA Fluid Dynamics Conferenct*, 2013-3106.
- Nitschke-Kowsky, P.** (1987). Experimental studies on the stability and transition of three-dimensional boundary layers. Technical Report Technical Memorandum 88539, NASA.
- Pfenninger, W.** (1977). Laminar flow control laminarization. In *AGARD special course on concepts for drag reduction*.
- Placidi, M., van Bokhorst, E., and Atkin, C.** (2017). Advanced laminar flow enabling technologies (alfet): Technical report. Technical report, City, University of London.
- Poll, D. I. A.** (1979). Transition in the infinite swept attachment line boundary layer. *The Aeronautical Quarterly*, 30.
- Poll, D. I. A.** (1985). Some observations of the transition process on the windward face of a long yawed cylinder. *Journal of Fluid Mechanics*, 150:329–356.
- Radeztsky, R., Reibert, M., and Saric, W.** (1999). Effect of isolated micron-sized roughness on transition in swept-wing flows. *AIAA Journal*, 37:1370–1377.

- Reed, H. and Saric, W.** (1989). Stability of three-dimensional boundary layers. *Annual Review of Fluid Mechanics*, 21(1):235–284.
- Reed, H. and Saric, W.** (2014). Sensitivity and receptivity: 1) leading edge receptivity to sound and vorticity of 2d geometries. In *von Karman Institute for Fluid Dynamics Lecture series*.
- Reed, H. L.** (1988). Wave interactions in swept-wing flows. *The Physics of fluids*, 30(11):3419–3426.
- Reibert, M. S.** (1996). *Nonlinear stability, saturation, and transition in crossflow-dominated boundary layers*. PhD thesis, Arizona State University, Ann Arbor, MI.
- Reibert, M. S., Saric, W. S., Carillo, R. B. J., and Chapman, K. L.** (1996). Experiments in nonlinear saturation of stationary crossflow vortices in a swept-wing boundary layer. *34th Aerospace Sciences Meeting and Exhibit*, 1996-0184.
- Reynolds, O.** (1883). An experimental investigation of the circumstances which determine whether the motion of water shall be direct or sinuous, and of the law of resistance in parallel channels. *Philosophical Transactions of the Royal Society of London*, 174:pp. 935–982.
- Riedel, H. and Sitzmann, M.** (1998). In-flight investigations of atmospheric turbulence. *Aerospace Science and Technology*, 2(5):301–319.
- Rivers, N., van Dam, C., Brown, P., and Rivers, R.** (2001). Flight investigation of the pressure-belt tubing size pressure distributions. Technical Report NASA TM-2001-209857, National Aeronautics and Space Administration.
- Rizzetta, D., Visbal, M., Reed, H., and Saric, W.** (2010). Direct numerical simulation of discrete roughness on a swept-wing leading edge. *AIAA journal*, 48(11):2660–2673.
- Ruban, A.** (1985). On tollmien-schlichting wave generation by sound. In *Laminar-Turbulent Transition*, pages 313–320. Springer.
- Saric, W.** (1994). Görtler vortices. *Annual Review of Fluid Mechanics*, 26(1):379–409.
- Saric, W.** (2008). Introduction into linear stability analysis. In *RTO-EN-AVT-151 Advances in laminar-turbulent transition modeling*, VKI Lecture series. NATO.

- Saric, W., Reed, H., and White, E.** (2003). Stability and transition of three-dimensional boundary layers. *Annual Review of Fluid Mechanics*, 35(1):413–440.
- Saric, W. and Yeates, L.** (1985). Generation of crossflow vortices in a three-dimensional flat-plate flow. In *Laminar-Turbulent Transition*, pages 429–437. Springer.
- Saric, W. S., Carillo, R. J., and Reibert, M.** (1998). Leading-edge roughness as a transition control mechanism. *36th Aerospace Sciences Meeting and Exhibit*, 1998-0781.
- Scarano, F.** (2012). *Experimental aerodynamics*. TU Delft.
- Schlichting, H.** (1933). Berechnung der anfachung kleiner störungen bei der platten-strömung. *Zeitschrift fr Angewandte Mathematik und Mechanik*, 13:171–174.
- Schmid, P. and Henningson, D.** (2001). *Stability and Transition in Shear Flows*. Number v. 142 in Applied Mathematical Sciences. Springer New York.
- Schrader, L. U., Brandt, L., and Henningson, D. S.** (2009). Receptivity mechanisms in three-dimensional boundary-layer flows. *Journal of Fluid Mechanics*, 618:209–241.
- Schubauer, G. and Skramstad, H.** (1948). Laminar-boundary-layer oscillations and transition on a flat plate. Technical Report NACA report 909, NACA.
- Serpieri, J. and Kotsonis, M.** (2016a). Spatio-temporal characteristics of secondary instabilities in swept wing boundary layers. *46th AIAA Fluid Dynamics Conference*, 2016-3792.
- Serpieri, J. and Kotsonis, M.** (2016b). Three-dimensional organisation of primary and secondary crossflow instability. *Journal of Fluid Mechanics*, 799:200–245.
- Serpieri, J., Venkata, S., and Kotsonis, M.** (2017). Conditioning of cross-flow instability modes using dielectric barrier discharge plasma actuators. *Journal of Fluid Mechanics*, 833:164–205.
- Smith, A. and Gamberoni, N.** (1956). Transition, pressure gradient and stability theory. Technical Report Technical Report ES-26388, Douglas Aircraft Company.

- Squire, H. B.** (1933). On the stability for three-dimensional disturbances of viscous fluid flow between parallel walls. *Proceedings of the Royal Society of London. Series A, Containing Papers of a Mathematical and Physical Character*, 142(847):pp. 621–628.
- Tempelmann, D., Schrader, L., Hanifi, A., Brandt, L., and Henningson, D.** (2012). Swept wing boundary-layer receptivity to localized surface roughness. *Journal of Fluid Mechanics*, 711:516–544.
- Tollmien, W.** (1929). Über die entstehung der turbulenz. 1. mitteilung. Technical report, Nachrichten von der Gesellschaft der Wissenschaften zu Göttingen.
- Tropea, C., Yarin, A. L., and Foss, J.,** editors (2007). *Springer Handbook of Experimental Fluid Mechanics*. Springer-Verlag Berlin Heidelberg, 1 edition.
- Tufts, M. W., Reed, H., and Saric, W.** (2014). Design of an infinite-swept-wing glove for in-flight discrete-roughness-element experiment. *Journal of Aircraft*, 51(5):1618–1631.
- van Ingen, J.** (1956). A suggested semi-empirical method for the calculation of the boundary layer transition region. Technical report, Delft University of Technology.
- van Ingen, J.** (2008). The e-n method for transition prediction. historical review of work at tu delft. *38th Fluid dynamics conference and exhibit*, 2008-3830.
- Wassermann, P. and Kloker, M.** (2002). Mechanisms and passive control of crossflow-vortex-induced transition in a three-dimensional boundary layer. *Journal of Fluid Mechanics*, 456:49–84.
- White, E.** (2000). *Breakdown of crossflow vortices*. PhD thesis, Arizona state University.
- White, E. and Saric, W.** (2000). Application of variable leading-edge roughness for transition control on swept wings. *AIAA paper*, 283:2000.
- White, E. B. and Saric, W. S.** (2005). Secondary instability of crossflow vortices. *Journal of Fluid Mechanics*, 525:275–308.
- Woodruff, M., Saric, W., and Reed, H.** (2011). Receptivity measurements on a swept-wing model. *AIAA Pap. No*, 2011-3882.